

Diss. ETH No. 17169 and  
ETHZ-IPP Internal Report 2007-01



# MEASUREMENT OF DIFFRACTIVE $\phi$ MESON PHOTOPRODUCTION AT HERA WITH THE H1 FAST TRACK TRIGGER

A dissertation submitted to the  
SWISS FEDERAL INSTITUTE OF TECHNOLOGY  
ZURICH  
for the degree of  
DOCTOR OF NATURAL SCIENCES

presented by  
**NIKLAUS E. BERGER**

Dipl. Phys. ETH  
born on April 10, 1978  
citizen of Niederurnen (GL)  
and Salez-Sennwald (SG)

accepted on the recommendation of  
Prof. Dr. Ralph Eichler, examiner and  
Prof. Dr. Günther Dissertori, co-examiner

2007



## Abstract

A new measurement of diffractive  $\phi$  meson photoproduction is performed with the H1 experiment at the electron-proton collider HERA. In the kinematic range  $30 < W_{\gamma p} < 90$  GeV and  $0.2 < |t| < 1.5$  GeV<sup>2</sup>, cross sections are determined double differentially in  $W_{\gamma p}$  and  $t$ . From these data, the pomeron trajectory in elastic  $\phi$  meson photoproduction is determined to be

$$\alpha(t) = 1.15 \pm 0.05(\text{stat.})_{-0.03}^{+0.04}(\text{syst.}) + t \cdot (0.16 \pm 0.09(\text{stat.})_{-0.02}^{+0.04}(\text{syst.}))\text{GeV}^{-2}.$$

A combined fit with data from fixed target experiments and the ZEUS collaboration yields the most precise trajectory measurement using  $\phi$  mesons to date,

$$\alpha(t) = 1.122 \pm 0.008 + t \cdot (0.150 \pm 0.017) \text{ GeV}^{-2}.$$

The spin density matrix elements, which provide information on the helicity structure of the interaction, are extracted using measurements of angular distributions of the  $\phi$  meson decay products and are found to be in agreement with expectations from  $s$ -channel helicity conservation.

The presented cross section measurement was made possible by the Fast Track Trigger (FTT). This new trigger based on signals from selected wire layers of the H1 central drift chamber provides information to the first three trigger levels of the H1 experiment. The first level performs a coarse two-dimensional track reconstruction within 2  $\mu\text{s}$ , whilst the second trigger level reconstructs the event vertex along the beam line, performs a precise three-dimensional track fit and determines invariant masses of track pairs in 20  $\mu\text{s}$ . The third trigger level reconstructs final states from up to 48 tracks and allows for particle identification using information from the calorimeter and the muon system within 100  $\mu\text{s}$ .

## Zusammenfassung

Mit dem H1-Experiment am Elektron-Proton-Beschleuniger HERA wird eine neue Messung diffraktiver  $\phi$ -Meson-Photoproduktion durchgeführt. Im kinematischen Bereich  $30 < W_{\gamma p} < 90$  GeV und  $0.2 < |t| < 1.5$  GeV<sup>2</sup> werden Wirkungsquerschnitte doppelt-differenziell in  $W_{\gamma p}$  und  $t$  gemessen. Aus diesen Daten bestimmt sich die Pomeron-Trajektorie in elastischer  $\phi$ -Meson-Photoproduktion zu

$$\alpha(t) = 1.15 \pm 0.05(\text{stat.})_{-0.03}^{+0.04}(\text{syst.}) + t \cdot (0.16 \pm 0.09(\text{stat.})_{-0.02}^{+0.04}(\text{syst.}))\text{GeV}^{-2}.$$

Eine gemeinsame Anpassung mit Daten von Experimenten mit ruhendem Target und der ZEUS-Kollaboration liefert die bisher genaueste Messung der Trajektorie mit Hilfe von  $\phi$ -Mesonen:

$$\alpha(t) = 1.122 \pm 0.008 + t \cdot (0.150 \pm 0.017) \text{ GeV}^{-2}.$$

Aus der Messung der Winkelverteilung der  $\phi$ -Meson-Zerfallsprodukte werden drei Elemente der Spindichtematrix bestimmt. Diese sind verträglich mit  $s$ -Kanal-Helizitätserhaltung.

Die vorliegende Messung wurde durch den schnellen Spurtrigger (Fast Track Trigger, FTT) ermöglicht. Dieser neue Trigger leitet aus Signalen von ausgewählten Drahtlagen der zentralen Spurkammer von H1 Informationen für die ersten drei Triggerstufen des H1 Experimentes ab. Auf der ersten Stufe wird innert 2  $\mu\text{s}$  eine grobe, zweidimensionale Spurkonstruktion durchgeführt. In 20  $\mu\text{s}$  rekonstruiert die zweite Stufe den Ereignis-Vertex entlang der Strahllinie, führt eine präzise, dreidimensionale Spuranpassung durch und bestimmt die invariante Masse von Spurpaaren. Auf der dritten Stufe werden innert 100  $\mu\text{s}$  aus bis zu 48 Spuren Endzustände rekonstruiert und mit Hilfe von Informationen aus dem Kalorimeter und dem Myon-System Teilchen identifiziert.

*Je n'ai fait celle-ci plus longue que parce que je  
n'ai pas eu le loisir de la faire plus courte.*

BLAISE PASCAL [1]

*If we knew what it was we were doing, it  
would not be called research, would it?*

ALBERT EINSTEIN

# Contents

Contents	5
<b>I Diffractive <math>\phi</math> Meson Production at HERA</b>	<b>11</b>
<b>1 Introduction</b>	<b>13</b>
<b>2 Theory of Diffractive Vector Meson Production</b>	<b>17</b>
2.1 Diffraction of Hadronic Waves . . . . .	17
2.1.1 Diffraction of Light . . . . .	17
2.1.2 The Wave Nature of Matter . . . . .	19
2.1.3 Diffraction of Hadrons . . . . .	20
2.1.4 Characteristics of Hadronic Diffraction . . . . .	21
2.1.5 The Photon as a Hadron . . . . .	21
2.2 Kinematics . . . . .	21
2.2.1 Kinematics of 2-2 Reactions . . . . .	21
2.2.2 Kinematics of $ep$ Scattering . . . . .	22
2.2.3 Kinematics of Diffractive Reactions . . . . .	23
2.2.4 Helicity . . . . .	24
2.2.5 Photon Flux . . . . .	25
2.3 $\mathcal{S}$ Matrix Theory . . . . .	26
2.3.1 The $\mathcal{S}$ Matrix . . . . .	26
2.3.2 From the $\mathcal{S}$ Matrix to Cross Sections . . . . .	27
2.3.3 Unitarity and the Optical Theorem . . . . .	27
2.3.4 Analyticity . . . . .	28
2.3.5 Crossing . . . . .	28
2.3.6 Theorems . . . . .	29
2.4 The Meson Exchange Picture of Strong Interactions . . . . .	29
2.4.1 Pion Exchange . . . . .	29
2.4.2 Single Meson Exchange and Unitarity . . . . .	30
2.5 Regge Theory . . . . .	30
2.5.1 Complex Angular Momentum . . . . .	30
2.5.2 Regge Phenomenology . . . . .	31
2.6 The Pomeron . . . . .	33
2.7 Diffraction and QCD . . . . .	34
2.7.1 The Pomeron in QCD . . . . .	34
2.7.2 Strings and the Pomeron . . . . .	36

<b>3</b>	<b>The <math>\phi</math> Meson</b>	<b>37</b>
3.1	The Discovery of the $\phi$ Meson . . . . .	37
3.2	Mass and Width of the $\phi$ Meson . . . . .	38
3.3	$\phi$ Meson Decays . . . . .	39
3.4	The $\phi$ Meson in the Quark Model . . . . .	40
<b>4</b>	<b>The H1 Detector at HERA</b>	<b>43</b>
4.1	The HERA Accelerator at DESY . . . . .	43
4.2	The H1 Detector at HERA . . . . .	44
4.3	The Central Tracking System of H1 . . . . .	45
4.3.1	The Central Inner Proportional Chamber (CIP) . . . . .	46
4.3.2	The Central Jet Chamber (CJC) . . . . .	49
4.3.3	Track Reconstruction . . . . .	51
4.4	Calorimetry at H1 . . . . .	54
4.4.1	The Liquid Argon Calorimeter . . . . .	54
4.4.2	The Spaghetti Calorimeter . . . . .	55
4.5	Luminosity Measurement at H1 . . . . .	55
4.6	Forward Instrumentation at H1 . . . . .	55
4.6.1	The FTi2 Scintillating Detector . . . . .	55
4.6.2	The Forward Muon Detector (FMD) . . . . .	55
4.6.3	The Forward Tagging System (FTS) . . . . .	56
4.6.4	The Plug Calorimeter . . . . .	56
4.7	The Trigger at H1 . . . . .	56
4.7.1	Overview . . . . .	56
4.7.2	Level 1 . . . . .	57
4.7.3	Level 2 . . . . .	57
4.7.4	Readout and Level 3 . . . . .	58
4.7.5	Event-building and Level 4 . . . . .	58
<b>5</b>	<b>Monte Carlo Modelling of Diffractive <math>\phi</math> Meson Production</b>	<b>59</b>
5.1	The DIFFVM Generator . . . . .	60
5.1.1	From Electrons to Photons to Vector Mesons . . . . .	60
5.1.2	Pomeron Exchange . . . . .	60
5.1.3	Proton Dissociation . . . . .	61
5.1.4	Helicity Distributions . . . . .	61
5.2	Kinematical Distributions . . . . .	61
5.2.1	$\phi$ Meson Mass . . . . .	61
5.2.2	Momentum Transfer at the Proton Vertex $t$ and Photon-Proton Centre of Mass Energy $W$ . . . . .	62
5.3	Detector Simulation with H1SIM and GEANT . . . . .	63
5.3.1	Simulation of Nuclear Interactions with GEISHA . . . . .	64
<b>6</b>	<b>Trigger and Data Selection</b>	<b>65</b>
6.1	Triggers for $\phi$ Photoproduction . . . . .	65
6.1.1	A FTT Based $\phi$ Trigger for Level 1 . . . . .	65
6.1.2	A FTT Based $\phi$ Trigger for Level 2 . . . . .	67
6.1.3	The Level 4 $\phi$ Finders . . . . .	67

6.2	Run Selection . . . . .	68
6.2.1	Run Selection for s12 . . . . .	68
6.2.2	Run Selection for s51 . . . . .	68
6.2.3	Common Run Selection . . . . .	68
6.3	Luminosity Determination . . . . .	69
6.4	Reconstruction of Kinematic Quantities . . . . .	69
6.4.1	Energy Loss Corrections . . . . .	69
6.4.2	Kinematic Variables and their Resolution . . . . .	71
6.5	Event Selection . . . . .	78
6.5.1	Event Properties . . . . .	78
6.5.2	Track Properties . . . . .	79
6.6	Kinematic Phase Space and Binnings . . . . .	80
6.6.1	Phase Space for the Pomeron Analysis . . . . .	80
6.6.2	Phase Space for the $t$ -Dependence Measurement . . . . .	82
<b>7</b>	<b>Event Selection with Specific Energy Loss</b>	<b>85</b>
7.1	The Bethe-Bloch Equation . . . . .	85
7.2	Detector effects influencing the $dE/dx$ measurement and their correction . . . . .	86
7.2.1	Path length . . . . .	86
7.2.2	Saturation . . . . .	87
7.2.3	Threshold effects . . . . .	87
7.3	$dE/dx$ Calibration . . . . .	87
7.3.1	Fitting procedure . . . . .	88
7.3.2	Resolution determination . . . . .	89
7.4	Likelihood Determination . . . . .	89
<b>8</b>	<b>Acceptance and Efficiencies</b>	<b>93</b>
8.1	Visible Cross Section Definition . . . . .	93
8.2	Acceptance . . . . .	94
8.3	Reconstruction Efficiency . . . . .	96
8.3.1	Energy Loss . . . . .	96
8.3.2	In-Flight Decays of Kaons . . . . .	96
8.3.3	Nuclear Interactions . . . . .	97
8.3.4	Track Finding Efficiency . . . . .	98
8.3.5	Vertex Fitting Efficiency . . . . .	99
8.4	Selection Efficiency . . . . .	99
8.4.1	Efficiency of the $dE/dx$ Selection . . . . .	99
8.5	Trigger Efficiency . . . . .	101
8.5.1	Single Track Efficiency of the FTT . . . . .	101
8.5.2	Efficiency of the Global FTT Trigger Elements . . . . .	103
8.5.3	CIP Efficiency . . . . .	105
8.5.4	Veto Efficiencies . . . . .	106
8.6	Overall Efficiency . . . . .	106
<b>9</b>	<b>Separation of Elastic and Proton Dissociative Events</b>	<b>109</b>
9.1	Treatment of Detector Noise . . . . .	110

9.2	Simulation of Forward Detectors . . . . .	111
9.2.1	The Forward Muon Detector . . . . .	111
9.2.2	The Forward Tagging System . . . . .	111
9.2.3	The Plug Calorimeter . . . . .	113
9.3	Tagging Efficiencies . . . . .	113
9.4	Unfolding Procedure . . . . .	113
<b>10</b>	<b>Cross Section Determination</b>	<b>117</b>
10.1	Fitting the $\phi$ Shape . . . . .	117
10.2	Cross Section Calculation . . . . .	118
10.2.1	Cross Section Differential in $t$ . . . . .	118
10.2.2	$W$ Dependence of Cross Section . . . . .	120
10.3	Systematic Uncertainties . . . . .	120
<b>11</b>	<b>Helicity Analysis</b>	<b>125</b>
11.1	Helicity Angles and their Reconstruction . . . . .	125
11.2	Angular Dependence of Cross Sections . . . . .	130
11.3	Spin Density Matrix Elements . . . . .	136
<b>12</b>	<b>Results and Discussion</b>	<b>137</b>
12.1	Double-Differential Cross Sections . . . . .	137
12.2	Pomeron Trajectory . . . . .	137
12.2.1	Note on the Errors of the ZEUS Measurement . . . . .	143
12.3	An Alternative Trajectory Fit . . . . .	143
12.3.1	Cross Section Model . . . . .	143
12.3.2	Data Sets and Treatment of Errors . . . . .	144
12.3.3	Fit Results . . . . .	144
12.4	Cross Section Differential in $W$ . . . . .	148
12.5	Conclusion and Outlook . . . . .	150
	<b>List of Symbols</b>	<b>153</b>
<b>II</b>	<b>A Fast Track Trigger for the H1 Experiment</b>	<b>155</b>
<b>13</b>	<b>Overview of the Fast Track Trigger</b>	<b>157</b>
13.1	Triggers for HERA II physics . . . . .	157
13.2	Conceiving the Fast Track Trigger . . . . .	158
13.3	Key Technologies for the Fast Track Trigger . . . . .	159
13.3.1	Field Programmable Gate Arrays . . . . .	159
13.3.2	Content Addressable Memories . . . . .	159
13.3.3	Digital Signal Processors . . . . .	160
13.3.4	5 Gbit/s Low Voltage Differential Signaling Links . . . . .	160
13.4	The Level 1 Fast Track Trigger . . . . .	161
13.4.1	Digitisation and Hit Finding . . . . .	161
13.4.2	Track Segment Finding . . . . .	164
13.4.3	The Front End Module . . . . .	165

13.4.4	Track Segment Merging	166
13.4.5	Track Segment Linking	169
13.4.6	Level 1 Trigger Decision	169
13.5	The Level 1 $z$ -Vertex Trigger	170
13.5.1	Finding Track Segments in $r$ - $z$	170
13.5.2	Linking $z$ Segments and Trigger Decision	171
13.6	The Level 2 Fast Track Trigger	171
13.6.1	Track Segment Verification and Track Parameter Lookup	171
13.6.2	Track Segment Linking	174
13.6.3	The Multipurpose Processing Board	174
13.6.4	Data Transmission in the Level 2 System	176
13.6.5	Vertex Determination	176
13.6.6	Track Segment Fitting	176
13.6.7	Invariant Mass Determination	178
13.6.8	Level 2 Trigger Decision	178
13.7	The Level 3 Fast Track Trigger	178
13.7.1	Data Transmission and Distribution	178
13.7.2	Physics Algorithms	179
13.8	Data Acquisition and Slow Control	179
<b>14</b>	<b>Level 2 <math>z</math> Vertex Finder</b>	<b>183</b>
14.1	Drift Chamber Based $z$ Vertex Determination	183
14.2	A Robust $z$ Vertex Finder	184
14.2.1	Overview of the Algorithm	184
14.2.2	Track Segment Preparation	184
14.2.3	Extrapolation	184
14.2.4	Histogramming and Vertex Determination	184
<b>15</b>	<b>A FPGA Based Invariant Mass Determination</b>	<b>189</b>
15.1	Triggering on Reconstructed Final States	189
15.2	Strategies for an Invariant Mass Cut	189
15.3	Floating Point Operations on a FPGA	190
15.4	Steps of the Calculation	191
15.4.1	Track Parameter Determination	191
15.4.2	Track Dispatching	192
15.4.3	Invariant Mass Calculation	192
15.5	Implementation Details	193
15.5.1	Sine and Cosine Lookup	193
15.5.2	Inversion	193
15.5.3	Control of the Data Flow	194
<b>16</b>	<b>Performance of the Fast Track Trigger</b>	<b>197</b>
16.1	Performance of the Level 1 FTT	197
16.1.1	Hit, Segment and Track Finding Efficiencies	197
16.2	Performance of the Level 2 FTT	199
16.2.1	Track Finding Efficiencies	199
16.2.2	Performance of the L2 $z$ Vertex Finder	201

16.2.3 Resolution . . . . .	201
16.3 Performance of the Level 2 Invariant Mass Finder . . . . .	205
16.4 Performance of the Level 3 FTT . . . . .	205
<b>17 A Graphical User Interface for the FTT</b>	<b>209</b>
17.1 Introduction . . . . .	209
17.1.1 A Short History of the FTT Graphical User Interface . . . . .	209
17.1.2 Demands on the FTT Graphical User Interface . . . . .	210
17.2 Technical Implementation of the GUI . . . . .	211
17.2.1 LabView . . . . .	211
17.2.2 Threads and Message Queues . . . . .	211
17.2.3 FTT Communication Scheme . . . . .	211
17.2.4 Configuration and Customisation . . . . .	212
17.2.5 Three Layer Structure . . . . .	212
17.2.6 Communication Layer . . . . .	213
17.2.7 Message Handling Layer . . . . .	213
17.2.8 User Interface Layer . . . . .	214
17.3 Selected Functionalities of the User Interface . . . . .	214
17.3.1 Display of Log Messages . . . . .	214
17.3.2 Instructing the Shift Crew . . . . .	218
17.3.3 Monitoring of Synchronisation . . . . .	219
17.3.4 Setting of Calibration Constants . . . . .	219
17.3.5 Steering Readout . . . . .	220
17.3.6 Configuring Crates . . . . .	222
17.3.7 Interfacing to the MPB Message System . . . . .	222
17.3.8 Emulating Parts of the FTT . . . . .	222
<b>A Corrections to the Specific Energy Loss</b>	<b>223</b>
A.1 Threshold Correction . . . . .	223
A.2 $dE/dx$ Calibration Parameters . . . . .	224
<b>B Cross Section Tables</b>	<b>227</b>
<b>List of Figures</b>	<b>229</b>
<b>List of Tables</b>	<b>235</b>
<b>List of Acronyms</b>	<b>237</b>
<b>Bibliography</b>	<b>239</b>
<b>Acknowledgments</b>	<b>253</b>
<b>Curriculum Vitae</b>	<b>255</b>

## Part I

# A Measurement of Diffractive $\phi$ Meson Production at HERA



# Chapter 1

## Introduction

*Ob ich vorwärtskomme in dem ich scheitere oder indem ich nur ein bisschen dazugewinne, ich selbst werde immer daraus lernen... und die Welt um mich herum wird gewachsen sein.*

ALBERTO GIACOMETTI [2]

FISH 2: *Makes you think doesn't it?*

FISH 4: *I mean... what's it all about?*

FISH 5: *Beats me.*

EXCERPT FROM FISH DIALOGUE IN [3]

The quest for an understanding of the fundamental building blocks of matter and their interactions has been captivating the interest of scientists and philosophers for millennia. In the second half of the twentieth century, a new level of understanding has been gained. The theoretical framework of quantum field theory [4] and the harvest from huge advances in experimental techniques have come together in the formulation of the *Standard Model of Particle Physics*.

In the *Standard Model*, matter is built from three families of fermions (particles with half-integer spin). The interactions between matter particles are described by the exchange of bosons (particles with integer spin). The fundamental interactions are the strong interaction, mediated by gluons and the electroweak interaction (which, at low energies is split into the electromagnetic interaction carried by photons and the weak interaction carried by the  $W$  and  $Z$  particles [5, 6]). The fourth fundamental interaction, gravitation, escapes a description within the framework of quantum field theory. On the level of fundamental particles, it is however negligibly weak compared to the other three forces and thus omitted from the following discussion. Within each of the matter families, there are two quarks, which participate in all interactions, an electron-type particle, which couples to the electromagnetic and weak bosons and a neutrino, which only feels the weak force. For every particle, there is an antiparticle with opposite quantum numbers.

The predictions of the standard model have been successfully tested in many experiments with high precision. The only predicted building block that has not yet been observed is the Higgs boson, which plays a crucial rôle in the unification of the weak and electromagnetic force and is responsible for the masses of elementary particles. Nevertheless, the standard model is not believed to be the final theory of matter and forces, as it does not incorporate gravitation and depends on a rather large number of arbitrary parameters, which have to be tuned with great precision in order to obtain the observed particle masses and couplings.

The resolution of these issues lies at the heart of much of the research in fundamental physics today. On the other hand, there are areas safely rooted within the standard model where a deep understanding is still lacking. One such area is the study of strong interactions at low energy and momentum scales.

The strong interaction is successfully described by the theory of *Quantum Chromo Dynamics* (QCD) which describes the interactions between quarks and gluons. The non-abelian structure of this theory gives rise to a very rich phenomenology, most notably including a self-coupling of the force carriers, the gluons. This self-coupling leads to a decrease of the strong coupling constant with increasing momentum scale<sup>1</sup> (asymptotic freedom, [7,8]). For smaller momenta, corresponding to larger distances, the strength of the force increases and confines the quarks into bound states, the hadrons. Theoretical predictions in quantum field theory are usually based on perturbative expansions in the coupling strength. For large couplings, these expansions fail to converge, leading to a loss of computability. We are thus faced with the situation that we have a precise understanding of the dynamics at very short distances, but have to rely on phenomenological models to make predictions involving extended objects such as hadrons.

Soft interactions (interactions with no hard scale such as momentum or mass allowing for a perturbative expansion) dominate the total hadron-hadron cross sections. Whilst their properties are not amenable to perturbative calculations, *Regge Theory* [9,10] provides a theoretical framework successfully describing a wealth of data. It is of particular interest to study the transition from the soft Regge regime to the perturbative QCD regime.

The exclusive production of vector mesons from real or virtual photons interacting with protons is ideally suited to study this transition [11–15]. With the HERA collider, several scales can be probed over a wide range. One of them is the vector meson mass. Whilst the light  $\rho^0$  mesons [16–27] and the relatively heavy  $J/\psi$  mesons [20,26,28–44] have been studied in great detail, the  $\phi$  meson [22,45–48] is experimentally more difficult to access, especially for low transverse momenta, where the cross section is largest. The  $\phi$  meson is built from a strange and an anti-strange quark, which do not appear as valence quarks in the proton. The interaction between the  $\phi$  meson and the proton thus cannot be mediated by other mesons but only by an object with the quantum numbers of the vacuum called *pomeron*. This fact makes the  $\phi$  meson an unique probe for the properties of interactions where a pomeron is exchanged.

One part of the work described in this thesis has been the author's contribution to the construction and commissioning of the *Fast Track Trigger* for the H1 experiment at HERA. This device is described in detail in the second part of his thesis, starting on page 157. This trigger has been heavily used for the analysis of diffractive  $\phi$  meson production presented in the first part of this work.

The next chapter gives an overview of the theory of diffractive vector meson production, introducing diffraction in particle physics in analogy to diffraction in optics. The definition of the relevant kinematic variables is then followed by an overview of Regge theory. The chapter concludes by providing some links between the Regge theory picture and the QCD picture.

Chapter 3 introduces the object of this study, namely the  $\phi$  meson. In the following chapter, the HERA accelerator and the H1 detector are described. One further important tool, the Monte Carlo simulations of both the physics process and the detector are described in chapter 5.

A detailed account of the analysis of  $\phi$  meson production is given in chapters 6 - 12. It starts with the triggers and selection cuts applied, followed by a chapter on particle identification using ionisation energy loss. Acceptance and efficiency are discussed in chapter 8,

---

<sup>1</sup>High momenta correspond to high resolution or short distances.

---

followed by a description of the separation of elastic and proton dissociative events. The cross section measurement is elucidated in chapter 10. An analysis of the angular structure of the interaction is presented in chapter 11. The first part of this thesis then concludes with a presentation and discussion of the results of the performed measurements.



## Chapter 2

# Theory of Diffractive Vector Meson Production

*Dans le système de l'émission, il semble que rien ne devrait être plus simple que le phénomène des ombres portées, (...) et cependant rien n'est plus compliqué.*

AUGUSTIN-JEAN FRESNEL [49]

*In theory there is no difference between theory and practice. In practice there is.*

YOGI BERRA

## 2.1 Diffraction of Hadronic Waves

### 2.1.1 Diffraction of Light

The term diffraction was coined by the Jesuit Francesco Maria Grimaldi [50] in the 17<sup>th</sup> century. He observed that light let into his study through a small slit formed a larger image on the back wall than what would be expected for light travelling along straight lines. In addition he observed that the shadow of a rod held into his beam of light was wider than the expected geometrical shadow and bordered by several coloured bands.

The diffraction of light was explained by Augustin-Jean Fresnel in 1818 [49] assuming that light propagates as waves. Poisson, in an attempt to demonstrate the absurdity of this idea, predicted a bright spot in the centre of the shadow of a circular obstacle using Fresnel's theory. The subsequent observation of this spot by Arago convinced Poisson and won Fresnel the *grand prix des sciences mathématiques* in 1819.

#### Diffraction as a Fourier Transform

An object induced into the path of light will cause the light to diffract around its edge. We would like to construct the diffraction pattern seen on a distant screen<sup>1</sup>. The setup

---

<sup>1</sup>By Babinet's Principle, the diffraction pattern caused by a shape is the same as the one produced by a screen with a hole in the same shape.



where  $\mathbf{a}$  is the two-dimensional vector  $(x', y')$  and  $\mathbf{q}$  is the two-dimensional momentum transfer  $(kx/r, ky/r)$  so that

$$|\mathbf{q}| = k \sin \theta. \quad (2.6)$$

We can now decompose  $S$  into a part that leaves the incoming wave unperturbed and a part responsible for diffraction

$$S(\mathbf{a}) = 1 - \Gamma(\mathbf{a}) \quad (2.7)$$

$\Gamma(\mathbf{a})$  is the *profile function* of the diffracting object. In equation (2.5),  $\frac{A_0 e^{ikr}}{r}$  represents an outgoing spherical wave. The diffraction pattern observed depends on the factor multiplying this spherical wave, the scattering amplitude  $f(\mathbf{q})$ . This scattering amplitude is proportional to the Fourier transform of the profile function and vice versa, thus

$$\Gamma(\mathbf{a}) = \frac{1}{2\pi i k} \int f(\mathbf{q}) e^{-i\mathbf{q}\cdot\mathbf{a}} d^2\mathbf{q}. \quad (2.8)$$

*Diffraction encodes the shape of an illuminated object in a diffraction pattern.* It thus allows the study of small objects (elementary particles) with macroscopic screens (detectors), if some kind of illumination with short enough wavelength is available.

If the diffracting object is a sphere with radius  $R$ , the scattering amplitude is found to be

$$f(\mathbf{q}) = ikR^2 \frac{J_1(qR)}{qR}, \quad (2.9)$$

where  $J_1$  is a Bessel function of the first kind. This result was first obtained by Airy [53], the resulting diffraction pattern is called Airy disc and is shown in figure 2.2.

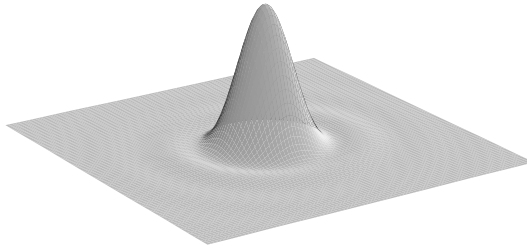


FIGURE 2.2: *The diffraction pattern generated by a circular aperture/obstacle.*

### 2.1.2 The Wave Nature of Matter

The advent of quantum mechanics in the first half of the 20<sup>th</sup> century finally resolved the century-old dispute on the true nature of light. Light consists neither of particles nor of waves<sup>3</sup>, but shares characteristics of both. This *wave-particle-duality* also applies to matter, as suggested by de Broglie [54]: massive particles behave as waves with wavelength

$$\lambda = \frac{h}{p} \quad (2.10)$$

where  $h = 2\pi\hbar$  is Planck's constant and  $p$  the momentum of the particle. Alternatively, the wave number  $k$  is given by

$$k = \frac{p}{\hbar} = \frac{\sqrt{E^2 - m^2 c^4}}{\hbar c}, \quad (2.11)$$

<sup>3</sup>One of the main advocates for the particle hypothesis was Newton, whilst the wave picture had two of its strongest advocates in Young and Fresnel.

where  $E$  is the energy and  $m$  the mass of the particle and  $c$  is the speed of light. From here onwards, natural units will be used, where  $c$  and  $\hbar$  are set to 1.

If particles are waves, they should also exhibit “optical” phenomena such as diffraction. De Broglie’s hypothesis was indeed confirmed in 1927 by Davison and Germer [55] who observed diffraction of electrons on the lattice of a crystal of nickel. Diffraction of light, electrons, atoms and cats on a double slit played an important role as thought experiments in the early days of quantum mechanics. Recent technological advances have made it possible to physically carry out interference experiments with objects as large as a  $C_{60}$  molecule [56].

### 2.1.3 Diffraction of Hadrons

Diffraction interactions of sub-atomic particles (see [57] for a review) were first observed in interactions of cosmic rays in nuclear emulsion [58, 59] where they showed up as large anisotropies in hadronic reactions. Good and Walker presented the idea of diffractive dissociation in 1960:

A phenomenon is predicted, in which a high-energy particle beam undergoing diffractive scattering from a nucleus will acquire components corresponding to various products of the virtual dissociations of the incident particle (...) [60].

The conditions for the applicability of the Fraunhofer approximation are always given in high energy hadron collisions:

- *Short wavelength condition:* The typical dimension of a hadron is  $R \approx 1$  fm. For  $kR > 10$  to be fulfilled,  $p$  has to be larger than 2 GeV.
- *Large distance condition:* The typical size of a detector is centimetres, compared to a femtometer for a hadron.  $R/D \approx 10^{-13}$ .
- *Fraunhofer condition:* Even at very high momenta,  $kR \lesssim 10^5$ , so that  $kR^2/D \approx 10^{-8}$ .

The idea that the optical analogue is indeed justified for hadron scattering is borne out beautifully by differential cross sections obtained in hadron nucleon scattering [51, 61], see figure 2.3. The diffraction patterns of nuclei and hadrons very closely resemble those of black discs. This in turn confirms that the strong interaction is indeed strong (hadrons are “black”) and short ranged (hadrons have a sharp edge).

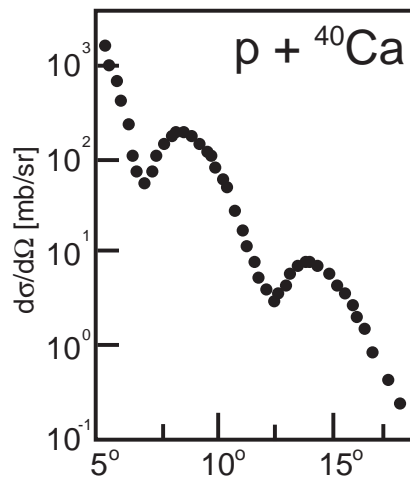


FIGURE 2.3: *Differential cross section for the scattering of protons off  $^{40}\text{Ca}$  nuclei. Adapted from [51] as measured by [61].*

### 2.1.4 Characteristics of Hadronic Diffraction

Diffraction interactions of hadrons have the following characteristics:

- A strong forward peak with a rapid falloff. In the words of Good and Walker:
 

“Since at high energy, the diffraction pattern is very narrow, this represents a distinctive feature of the reaction, and could be used to identify it.” [60]
- A slow (logarithmic) variation of the cross section with momentum (the profile function is only weakly dependent on momentum).
- No exchange of quantum numbers (except angular momentum<sup>4</sup> between the projectile and the target. This manifests itself in large rapidity gaps (regions devoid of particle production), as there is no flow of colour in the interaction.

In the optical analogy, the width of the forward peak is the Fourier conjugate of the size of the probed hadron. A wider forward peak corresponds to a smaller probed object. Indeed, in interactions where the target dissociates (i.e. the actual interaction is only with a part of the target), the diffractive peak is wider than in the case where the target stays intact.

### 2.1.5 The Photon as a Hadron

The electron-proton collider HERA allows the study of interactions between photons emitted by the electron and the proton. As any quantum mechanical particle, the photon has to be regarded as a superposition of a bare photon state and all possible fluctuations into other particles. If the target is a hadron such as a proton, the (strongly interacting) fluctuations into quark-antiquark pairs (virtual mesons) will dominate the cross-section [15]. Indeed, photon-hadron cross sections show all the features of hadron-hadron cross sections, but are suppressed by a factor proportional to  $\alpha_{em}$ , the coupling of the photon to charged particles.

The typical time/length (Ioffe length, [62]) over which a fluctuation exists, is long compared to the time scale of the interaction (the size of the proton respectively). Thus the quark-antiquark pair has time to form a bound state: Light mesons with the same quantum numbers as the photon dominate the virtual state. The hadronic part of the photon has consequently been modelled as a superposition of the vector mesons known at the time (1962) in the *Vector Dominance Model* (VDM, [63]). This model has been extended to the *generalised Vector Dominance Models* (gVDMs [14, 64, 65]) as heavier vector mesons ( $J/\Psi$  and  $\Upsilon$ ) were discovered.

## 2.2 Kinematics

### 2.2.1 Kinematics of 2-2 Reactions

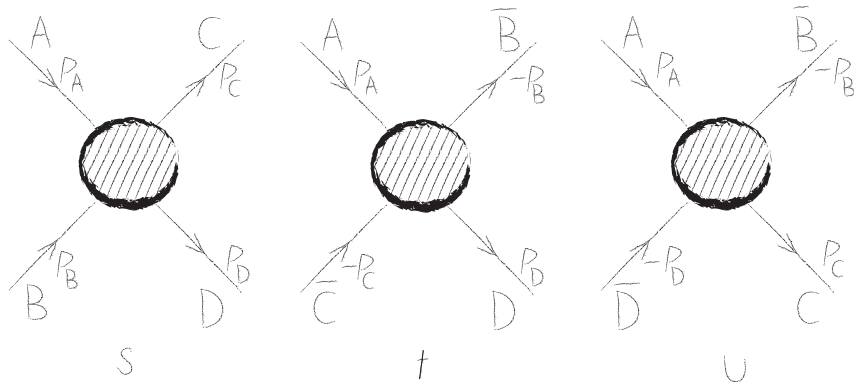
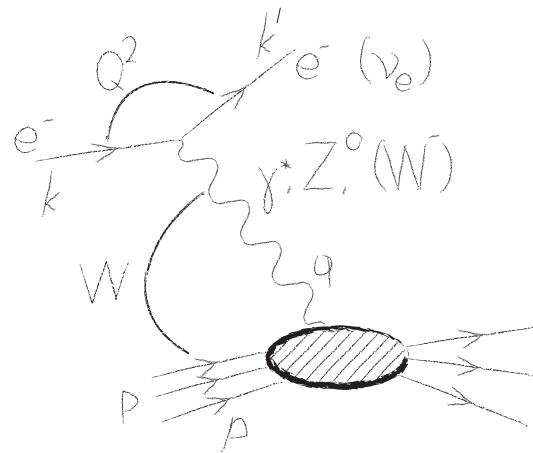
The kinematics of scattering reactions of the type  $A + B \rightarrow C + D$  (where  $C$  and  $D$  can also be systems of particles) can be described by the three Mandelstam variables  $s$ ,  $t$  and  $u$ . If the 4-momenta  $p_A$  to  $p_D$  are assigned to  $A$  to  $D$  (see figure 2.4), they are

$$s = (p_A + p_B)^2 = (p_C + p_D)^2 \quad (2.12)$$

$$t = (p_A - p_C)^2 = (p_B - p_D)^2 \quad (2.13)$$

$$u = (p_A - p_D)^2 = (p_B - p_C)^2. \quad (2.14)$$

<sup>4</sup>In principle, also parity can be exchanged (Odderon exchange), but no evidence for this process has been seen experimentally.


 FIGURE 2.4:  $s$  and  $t$  and  $u$  channel 2-2 reactions.

 FIGURE 2.5: Generic diagram for  $ep$  scattering, showing the kinematic variables.

Energy-momentum conservation implies that only two of these variables (we usually use  $s$  and  $t$ ) are independent

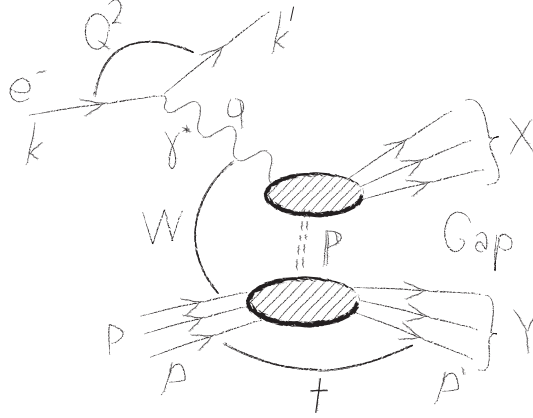
$$s + t + u = \sum_{i=1}^4 m_i^2, \quad (2.15)$$

where  $m_i$  are the masses of the four particles (particle systems). Depending on which particles are part of the initial and final state, the process is said to occur in the  $s$ ,  $t$  or  $u$  channel.

### 2.2.2 Kinematics of $ep$ Scattering

The scattering of electrons and protons at HERA can be described by the exchange of a virtual boson, which can be a photon or a  $Z^0$  (neutral current, electron in the final state) or a  $W$  (charged current, neutrino in the final state). The following Lorentz invariant quantities are used to describe this process (see figure 2.5):

- $Q^2 = -q^2 = -(k - k')^2$ : The negative squared 4-momentum transfer at the electron vertex which determines the virtuality of the exchanged boson (which for the kinematic

FIGURE 2.6: *Generic diffractive reaction.*

regime studied in this thesis is almost exclusively a photon). If the photon is quasi-real, the production regime is known as *photoproduction* ( $\gamma p$ ), whilst for large  $Q^2$  we speak of *Deep Inelastic Scattering* (DIS). For the present analysis, the acceptance of the backward calorimeter defines an experimental boundary at  $Q^2 = 2.5 \text{ GeV}^2$  below which the scattered electron escapes undetected through the beam pipe and the process is classified as photoproduction.

- $s = (k + p)^2$ : The squared  $ep$  centre of mass energy.
- $x = \frac{Q^2}{2pq}$ : Bjorken's  $x$ , the fraction of the proton momentum taking part in the interaction with the photon (in the parton picture: the fraction of the proton momentum carried by the struck quark).
- $y = \frac{pq}{pk}$ : "Inelasticity": Fraction of the incoming electron's energy carried by the photon in the proton rest frame.
- $W^2 = (p + q)^2$ : The photon-proton centre of mass energy squared (corresponds to  $s$  for hadron-hadron scattering, if the photon is considered as the hadronic projectile).

These quantities are not all independent, but linked via (neglecting the electron and proton masses)

$$Q^2 = xys \quad (2.16)$$

$$W^2 = ys - Q^2. \quad (2.17)$$

### 2.2.3 Kinematics of Diffractive Reactions

Diffractive interactions are characterised by a colourless exchange  $\mathbb{P}$  leading to two hadronic systems  $X$  and  $Y$  separated by a *large rapidity gap*<sup>5</sup>(see figure 2.6). Thus the following additional kinematic variables can be introduced:

- $t = -(p' - p)^2$ : The squared momentum transfer at the proton vertex.
- $M_X$ : Mass of the "photon remnant", for this thesis the mass of the  $\phi$  meson.

<sup>5</sup>The rapidity is defined as  $\frac{1}{2} \ln \frac{E+p_z}{E-p_z}$ , where  $p_z$  is the longitudinal momentum. For massless particles, this is the same as the pseudorapidity  $\eta = -\ln \tan \frac{\vartheta}{2}$ , where  $\vartheta$  is the polar angle.

- $M_Y$ : Mass of the “proton remnant”; or the proton mass in the elastic case<sup>6</sup>.
- $x_{\mathbb{P}} = \frac{(p-p')q}{pq}$ : The fraction of the proton’s momentum carried by  $\mathbb{P}$ .
- $\beta_{\mathbb{P}} = \frac{Q^2}{2q(p-p')}$ : The fraction of the  $\mathbb{P}$  momentum interacting with the photon.

$x$ ,  $x_{\mathbb{P}}$  and  $\beta$  are related by

$$x = \beta x_{\mathbb{P}}. \quad (2.18)$$

## 2.2.4 Helicity

Helicity  $\lambda$  is the projection of the particle’s spin onto its direction of motion. One of the questions to ask in order to understand the nature of diffractive vector meson photoproduction is whether the vector meson retains the photon helicity in the interaction. If the helicity remains the same, this is called *s*-channel helicity conservation (SCHC). In vector dominance models it is always fulfilled, whilst models based on perturbative QCD (see section 2.7) predict helicity flips. The transition amplitude for a photon of helicity  $\lambda_\gamma$  to produce a  $\phi$  meson of helicity  $\lambda_\phi$  is denoted  $M_{\lambda_\gamma\lambda_\phi}$ . As both the photon and the vector meson have spin one, they can have either positive (+), zero (0) or negative (-) helicity. For the quasi-real photons in photoproduction, the contribution from longitudinal polarisation (helicity zero) is negligible (see also section 2.2.5). Consequently, there are six remaining amplitudes  $M_{++}$ ,  $M_{+0}$ ,  $M_{+-}$ ,  $M_{-+}$ ,  $M_{-0}$  and  $M_{--}$ , of which three are independent, as for symmetry reasons

$$M_{++} = M_{--} \quad (2.19)$$

$$M_{+-} = M_{-+} \quad (2.20)$$

$$M_{+0} = M_{-0}. \quad (2.21)$$

The relation between the electron and the photon helicity cannot be probed in photoproduction as the electron is not detected. Thus three elements of the spin density matrix are accessible in the present measurement (see [66] for a definition of the matrix elements as parts of a hermitian decomposition of the full spin density matrix). They can be expressed as bilinear combinations of the helicity amplitudes<sup>7</sup>:

$$r_{00}^{04} = \frac{|M_{+0}|^2}{|M_{++}|^2 + |M_{+0}|^2 + |M_{+-}|^2} \quad (2.22)$$

$$\text{Re}(r_{00}^{04}) = \frac{1}{2} \frac{M_{++}M_{+0}^* - M_{+-}M_{+0}^*}{|M_{++}|^2 + |M_{+0}|^2 + |M_{+-}|^2} \quad (2.23)$$

$$r_{1-1}^{04} = \frac{1}{2} \frac{M_{++}M_{+-}^* - M_{+-}M_{++}^*}{|M_{++}|^2 + |M_{+0}|^2 + |M_{+-}|^2}. \quad (2.24)$$

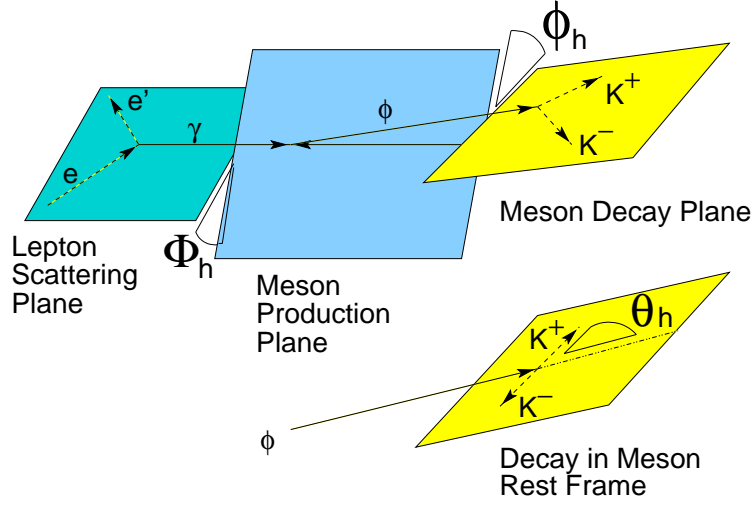
If SCHC holds, the only nonzero amplitude is  $M_{++}$  and consequently  $r_{00}^{04}$ ,  $\text{Re}(r_{00}^{04})$  and  $r_{1-1}^{04}$  are all zero.

The helicity structure of the interaction can be tested by measuring the so-called helicity angles  $\theta_h$ ,  $\phi_h$ ,  $\psi_h$  and  $\Phi_h$ . These angles are defined as follows (see also figure 2.7):

- $\Phi_h$ : The angle between the electron scattering plane and the vector meson production plane as measured in the proton rest frame;

<sup>6</sup>As usual, a second convention exists, where  $X$  and  $Y$  are interchanged.

<sup>7</sup>The conventions on helicity amplitudes and spin density matrix elements tend to maximise the cluttering with indices.

FIGURE 2.7: The helicity angles  $\Phi_h$ ,  $\phi_h$  and  $\theta_h$ .

- $\phi_h$ : The angle between the vector meson production plane and its decay plane as measured in the vector meson rest frame;
- $\theta_h$ : The decay angle of the positive decay particle with regard to the outgoing proton direction in the vector meson rest frame.
- $\psi_h$ : The difference between  $\phi_h$  and  $\Phi_h$ .

The spin density matrix elements determine the angular distribution [66]:

$$\frac{1}{\sigma} \frac{d^2\sigma}{d\cos\theta_h d\phi_h} = \frac{3}{4\pi} \left( \frac{1}{2} (1 - r_{00}^{04}) + \frac{1}{2} (3r_{00}^{04} - 1) \cos^2\theta_h \right) - \sqrt{2} \text{Re}(r_{00}^{04}) \sin 2\theta_h \cos\phi_h - r_{1-1}^{04} \sin^2\theta_h \cos 2\phi_h. \quad (2.25)$$

### 2.2.5 Photon Flux

In electron-proton scattering at HERA,  $ep$  cross sections are measured. In the case of diffractive vector meson photoproduction, the interest is however in  $\gamma p$  cross sections, which are also the quantities predicted by theoretical models. In the Weizsäcker-Williams method [67–70], the electromagnetic field of the fast moving electron is understood as a flux of virtual photons. It thus becomes possible to express the  $ep$  cross section as the  $\gamma p$  cross section folded with the photon flux:

$$\sigma_{ep} = \int_y \int_{Q^2} \sigma_{\gamma p}(W^2, Q^2) \mathcal{F}_\gamma(y, Q^2) dy dQ^2. \quad (2.26)$$

As opposed to real photons which always have transverse polarisation, virtual photons can also be longitudinally polarised. Introducing a longitudinal and a transverse cross section  $\sigma_{\gamma p}^L$  and  $\sigma_{\gamma p}^T$ , the  $ep$  cross section can then be decomposed into a longitudinal and a transverse part,

$$\sigma_{ep} = \int_y \int_{Q^2} (\sigma_{\gamma p}^T(W^2, Q^2) \mathcal{F}_\gamma^T(y, Q^2) + \sigma_{\gamma p}^L(W^2, Q^2) \mathcal{F}_\gamma^L(y, Q^2)) dy dQ^2. \quad (2.27)$$

For  $Q^2 \ll E_e$  and neglecting the electron and proton mass, the differential flux can be expressed as

$$\mathcal{F}_\gamma^T(y, Q^2) = \frac{\alpha_{em}}{2\pi} \frac{1}{yQ^2} \left( 1 + (1-y)^2 - 2m_e^2 \frac{y^2}{Q^2} \right) \quad (2.28)$$

$$\mathcal{F}_\gamma^L(y, Q^2) = \frac{\alpha_{em}}{\pi} \frac{1}{yQ^2} (1-y), \quad (2.29)$$

where  $\alpha_{em}$  is the electromagnetic coupling constant. This is the Weizsäcker-Williams approximation, also known as equivalent photon approximation. Note that the flux decreases with  $1/Q^2$  and that the longitudinal flux vanishes as  $y \rightarrow 1$ . For vector meson production, the longitudinal flux is of less importance, as the production of longitudinal vector mesons is suppressed compared to transverse vector mesons. The flux of transverse photons is obtained by integrating the differential flux over the phase space under consideration

$$\Phi^T = \int_{y_{min}}^{y_{max}} \int_{Q_{min}^2}^{Q_{max}^2} d\mathcal{F}_\gamma^T. \quad (2.30)$$

Relating  $y$  and  $W$ , the  $ep$  cross section can be expressed as a function of the average  $W$  and  $Q^2$ :

$$\sigma_{ep} \approx \Phi^T \cdot \sigma_{\gamma p} (\langle W \rangle, \langle Q^2 \rangle), \quad (2.31)$$

where  $\sigma_{\gamma p} = \sigma_{\gamma p}^T \left( 1 + \frac{\mathcal{F}_\gamma^L}{\mathcal{F}_\gamma^T} \frac{\sigma_{\gamma p}^L}{\sigma_{\gamma p}^T} \right) \approx \sigma_{\gamma p}^T$ .

## 2.3 S Matrix Theory

Before the advent of Quantum Chromo Dynamics (QCD), the most promising route to an understanding of hadronic interactions seemed to be  $S$ -matrix theory [71–73] and in particular Regge theory, where additional analyticity properties are demanded. Even though these theoretical inroads never led to a complete understanding of the strong force and were mostly replaced by QCD, their very general ansatz ensures that the insights gained remain valid to this day.

### 2.3.1 The S Matrix

In quantum field theory, the time evolution operator  $U$  from time  $t = -\infty$  to  $t = +\infty$  is given by the Dyson series

$$S \equiv U(-\infty, +\infty) = \mathbf{1} + \sum_{n=1}^{\infty} \frac{i^n}{n!} \int d^4x_1 \dots d^4x_n \mathcal{T} (H_{int}(x_1) \dots H_{int}(x_n)), \quad (2.32)$$

where  $H_{int}$  is the interaction Hamiltonian and  $\mathcal{T}$  the time ordered product. This time evolution operator is known as scattering matrix ( $S$ -matrix for short) and it is the operator which transforms an initial state  $|i\rangle$  of a scattering process to a final state  $|f\rangle$ :

$$S|i\rangle = |f\rangle. \quad (2.33)$$

The initial and final states represent free (non-interacting) particles and are defined at the times  $t = -\infty$  and  $t = +\infty$  respectively. The transition probability from a particular initial state  $|i\rangle$  to a final state  $|f\rangle$  is by definition

$$P_{i \rightarrow f} = |\langle f|S|i\rangle|^2. \quad (2.34)$$

A full knowledge of the  $S$  matrix is thus equivalent to a complete understanding of the dynamics of the scattering process.  $S$  has the following properties:

- *Relativistic invariance*: To ensure Lorentz invariance of the theory, the  $S$  matrix elements can only depend on Lorentz-invariant combinations of kinematic variables.
- *Linearity*: This follows from the superposition principle of quantum mechanics.
- *Unitarity*: Is a consequence of the conservation of probability.

Two more properties are usually postulated, namely

- *Analyticity*
- *Crossing symmetry*.

The following sections 2.3.2 to 2.3.6 discuss these properties and their consequences.

### 2.3.2 From the $S$ Matrix to Cross Sections

Subtraction of unity (no interaction) from the  $S$  matrix yields the transition matrix  $T$

$$S = \mathbf{1} + iT \quad (2.35)$$

the individual elements of the  $S$  matrix are then

$$S_{if} \equiv \langle f|S|i \rangle = \delta_{if} + i\langle f|T|i \rangle = \delta_{if} + iT_{if}. \quad (2.36)$$

$T_{if}$  necessarily contains a  $\delta$ -function to ensure the conservation of 4-momentum ( $p_i = p_f$ ), this can be extracted to yield the scattering amplitude  $A$ :

$$S_{if} = \delta_{if} + i(2\pi)^4 \delta^4(p_f - p_i) A(i \rightarrow f). \quad (2.37)$$

By Fermi's golden rule, the differential cross section of a scattering process is given by

$$d\sigma = \frac{1}{\Phi} |A(i \rightarrow f)|^2 d\Pi \quad (2.38)$$

where  $\Phi$  is the flux of incoming particles and  $d\Pi$  is the Lorentz-invariant phase space available to the final state particles.

In the case of an exclusive two-body reaction, the differential cross section in  $t$  is in the large  $s$  limit [74]:

$$\frac{d\sigma}{dt} \simeq \frac{1}{16\pi s^2} |A(s, t)|^2. \quad (2.39)$$

### 2.3.3 Unitarity and the Optical Theorem

Conservation of probability requires the  $S$  matrix to be unitary

$$S^\dagger S = S S^\dagger = \mathbf{1}. \quad (2.40)$$

Rewriting this condition for the transition matrix  $T$  yields

$$(1 - iT^\dagger)(1 + iT) = \mathbf{1} \quad (2.41)$$

and thus

$$i(T^\dagger - T) = T^\dagger T. \quad (2.42)$$

If we now take the matrix elements of equation (2.42) between the initial and final states  $|i\rangle$  and  $|f\rangle$  of the scattering process and sum over all intermediate states  $|n\rangle$  we obtain

$$i\langle f|T^\dagger - T|i\rangle = \sum_{\{n\}} \langle f|T^\dagger|n\rangle \langle n|T|i\rangle, \quad (2.43)$$

in short

$$2 \operatorname{Im} T_{if} = \sum_{\{n\}} T_{fn}^* T_{in}. \quad (2.44)$$

If we write this in terms of the scattering amplitudes  $A$ , we obtain

$$2 \operatorname{Im} A(i \rightarrow f) = \sum_{\{n\}} \int d\Pi_n A^*(f \rightarrow n) A(i \rightarrow n), \quad (2.45)$$

where  $d\Pi_n$  is the  $n$ -particle phase space measure. In the special case of identical initial and final states

$$|i\rangle = |f\rangle, \quad (2.46)$$

namely elastic forward (momentum transfer squared  $t = 0$ ) scattering, we obtain

$$2 \operatorname{Im} A_{el}(t = 0) = \sum_n \int d\Pi_n |A(i \rightarrow n)|^2. \quad (2.47)$$

Comparing with equation (2.38) we realise that the right hand side corresponds to the total cross section times the flux of incident particles  $\Phi$ , which at high energies  $\sqrt{s}$  equals  $2s$ . We thus obtain the *Optical Theorem*

$$\sigma_{tot} = \frac{2}{\Phi} \operatorname{Im} A_{el}(t = 0) \underset{s \rightarrow \infty}{\simeq} \frac{1}{s} \operatorname{Im} A_{el}(t = 0); \quad (2.48)$$

the total cross section is proportional to the imaginary part of the forward scattering amplitude. This theorem links the total cross section, which comprises a sum over an infinite number of matrix elements to a single such element.

### 2.3.4 Analyticity

The  $S$  matrix elements are postulated to be analytical functions of the kinematic variables, i.e.  $A(s, t)$  is the real boundary value of a holomorphic function of  $s$  and  $t$  continued to complex values. The singularities of  $A$  are poles and cuts, corresponding respectively to the exchange of one or multiple particles. Single particle exchange in the  $s$ - ( $t, u$ -) channel leads to a pole at  $s = m^2$  ( $t = m^2$ ,  $u = m^2$ ), where  $m$  is the particle mass. Multiple particle exchange leads to branch points at  $s = (2m)^2$ ,  $s = (3m)^2$ , etc. (and correspondingly for the  $t$  and  $u$  channels).

### 2.3.5 Crossing

In relativistic field theory, an incoming particle of momentum  $p$  can be viewed as an outgoing anti-particle of momentum  $-p$ . This operation of *crossing* relates the  $s$ ,  $t$  and  $u$  channels. The crossing postulate of  $S$  matrix theory states that the amplitude for processes related by crossing or a  $CPT$  (charge, parity and time reversal) transformation (and their inverse, if time reversal symmetry  $T$  is assumed) is the same. In other words, the same function of  $s$ ,  $t$  and  $u$  describes all these processes for different domains of  $s$ ,  $t$  and  $u$ .

### 2.3.6 Theorems

From  $S$  matrix theory, several very general theorems can be derived. The beauty of these results is that they are completely independent of the underlying dynamics of the interaction because they only depend on the properties of the  $S$  matrix. For proofs of the theorems see e.g. [74] or [75].

- *The Froissart-Martin bound* [76,77] states that the total cross section cannot grow faster than  $\ln^2 |s|$ , i.e.

$$\sigma_{tot} \leq C \ln^2 |s|, \quad \text{as } s \rightarrow \infty \quad (2.49)$$

where the constant  $C$  is theoretically found to be larger than  $\pi/m_\pi$  ( $m_\pi$  being the pion mass). If  $s$  is measured in  $\text{GeV}^2$ ,  $C > 60$  mb.

- *The Pomeranchuk theorem* [78] states that at high energy, the cross sections for particle-particle- and particle-antiparticle-scattering become equal

$$\sigma_{tot}(ab) \underset{s \rightarrow \infty}{=} \sigma_{tot}(a\bar{b}). \quad (2.50)$$

Whilst delivering these very general and powerful results,  $S$ -matrix theory in its most general form fails to predict details of the dynamics of strong interactions or existence of particular particles. With additional assumptions about the exchanges, however, cross section predictions become possible, as described in the following sections.

## 2.4 The Meson Exchange Picture of Strong Interactions

### 2.4.1 Pion Exchange

The study of strong interactions had its origin in the profound mystery of which macroscopically unobserved force could hold a nucleus composed of positively charged protons and neutral neutrons together despite of the electrostatic repulsion. In 1935 Hideki Yukawa postulated a force mediated by the exchange of a massive particle [79]. From the range of the force ( $t$ -channel exchange) he predicted the mass of the particle (resonance in the  $s$ -channel) to be about 200 times the electron mass. Such a particle was soon thereafter discovered by Anderson and Neddermeyer [80,81] (and independently by Street and Stevenson<sup>8</sup> [82]) studying cloud chamber photographs of cosmic ray interactions. The discoverers, but e.g. also Heisenberg and Euler [83], were quick to identify this particle, then dubbed “mesotron” with Yukawa’s carrier of the strong force. An ingenious experiment carried out in the basement of a gymnasium in Rome during World War II by Conversi, Pancini and Piccioni [84–86] however demonstrated the leptonic (non strongly interacting) nature of this mesotron, which is nowadays known as muon. This of course again created the need for a carrier of the strong force. Bohr tried to revive the mesotron as force carrier by demeaning the results of the Piccioni experiment as the “Pinocchio effect” [87]. Others continued the search for Yukawa’s particle with improved experimental techniques. The group of Powell met with success when examining films exposed to cosmic radiation on the Pic du Midi [88] and the Jungfrauoch [89]. In these exposures, they found traces of a strongly interacting particle of intermediate mass, which is nowadays known as the pion.

So for a short time, things were in a happy state, theory and experiment in beautiful accord, as the mystery of nuclear cohesion seemed to be solved. This was however not to last, as soon thereafter a plethora of additional strongly interacting particles (hadrons) was discovered. Among them were particles of higher spin, which leads to trouble in the calculation of cross sections.

<sup>8</sup>The experiment of Street and Stevenson was the first particle physics experiment using a sophisticated trigger with coincidences and veto anti-coincidences.

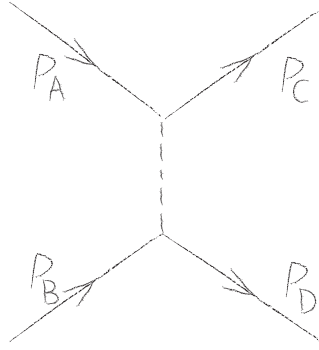


FIGURE 2.8:  $t$ -channel scattering  $AB \rightarrow CD$  mediated by the exchange of a meson (dashed line).

### 2.4.2 Single Meson Exchange and Unitarity

From partial wave decomposition it follows that the scattering amplitude for the exchange of a meson of spin  $J$  in the  $t$ -channel (see figure 2.8) is

$$A_{mes}(s, t) \sim A_J(t)P_J(\cos \theta_t) \quad (2.51)$$

where  $P_J$  is the Legendre Polynomial of  $J^{th}$  order and ( $m$  is the mass of the scattered particles, assumed to be equal)

$$\cos \theta_t = 1 + \frac{2t}{s - 4m^2}. \quad (2.52)$$

The exchanged meson leads to a pole in the partial wave amplitude  $A_J$ , thus

$$A_{mes}(s, t) \sim \frac{P_J(\cos \theta_t)}{t - M^2}, \quad (2.53)$$

where  $M$  is the mass of the exchanged meson. If we study the behaviour of  $A_{mes}(s, t)$  for  $s \rightarrow \infty$  at fixed  $t$  and use that  $P_J(z) \xrightarrow{z \rightarrow \infty} z^J$ , we obtain

$$A_{mes}(s, t) \underset{s \rightarrow \infty}{\sim} s^J. \quad (2.54)$$

Using equation 2.38, we thus obtain for the cross section (the incoming particle Flux  $\Phi$  is proportional to  $s$ )

$$\sigma \underset{s \rightarrow \infty}{\sim} s^{2J-1} \quad (2.55)$$

which, at high enough energy  $s$ , violates the Froissart-Martin bound and thus unitarity. The concepts of *Regge Theory* save unitarity whilst conserving the idea of  $t$ -channel exchange.

## 2.5 Regge Theory

### 2.5.1 Complex Angular Momentum

The original idea of Regge [9, 90] was to apply the concept of complex angular momenta to quantum-mechanical potential scattering. There, the bound states of a spherically symmetric potential have a well defined angular momentum and energy. These bound states appear

as poles of the partial wave amplitude (and thus of the  $S$ -Matrix)  $a_J(t)$  for a given integer  $J$  and an energy  $t$ . Regge analytically continued  $a_J(t)$  to complex values of  $J$ , thus obtaining an interpolating function  $a(J, t)$ , which reduces to  $a_J(t)$  for integer  $J$ . The singularities of  $a(J, t)$  are the *Regge Poles* located at values defined by a relation

$$J = \alpha(t), \quad (2.56)$$

where the function  $\alpha(t)$  is known as a *Regge Trajectory*. The energies of the bound states correspond to the  $\alpha(t)$  values for physical, i.e. integer  $J$ .

The full power of Regge theory becomes apparent when it is combined with  $S$ -matrix theory. This application of complex angular momentum to particle physics is due to Chew and Frautschi [10] and Gribov [91]. Here, a Regge trajectory is a family of resonances with increasing spin<sup>9</sup> but otherwise identical quantum numbers. If these ( $s$ -channel) resonances are exchanged in the  $t$  channel, one can treat them collectively as a *Reggeon* ( $\mathbb{R}$ ). The reggeon exchange is determined by the residue of the corresponding pole in the complex angular momentum plane and the function  $\alpha(t)$ . It is a puzzling experimental fact<sup>10</sup> that  $\alpha(t)$  ( $t = m^2$ ) is linear to a very good approximation for all known trajectories. It can thus be written as

$$\alpha(t) = \alpha(0) + \alpha' t, \quad (2.57)$$

where  $\alpha(0)$  is called the *intercept* and  $\alpha'$  the *slope*. See figure 2.9 for some mesonic trajectories.

### 2.5.2 Regge Phenomenology

Regge theory describes a two-body scattering process  $AB \rightarrow CD$  in terms of the exchange of Regge trajectories (Reggeons). The amplitude for the exchange of a single reggeon in the  $t$ -channel (figure 2.10) is given by

$$A(s, t) = \beta(t)\eta(t)s^{\alpha(t)}, \quad (2.58)$$

where  $\beta$  is the residue of the Regge pole and  $\eta$  the signature factor which selects either even or odd spins along the trajectory. The properties of the  $S$ -matrix lead to the expectation that the Regge pole residue  $\beta(t)$  factorises into two couplings at the vertices (Regge factorisation):

$$\beta(t) = g_{AC}(t)g_{BD}(t). \quad (2.59)$$

This factorisation property allows to relate cross sections for different processes, e.g.

$$d\sigma^2(AB \rightarrow CD) = d\sigma(AA \rightarrow CC)d\sigma(BB \rightarrow DD). \quad (2.60)$$

From the optical analogy on the other hand we know that  $\beta(t)$  is the Fourier transformation of the profile function of the target as seen by the projectile (where target and projectile can be exchanged). If the profile function is a Gaussian,  $\beta(t)$  will again have a Gaussian form. Also the Fourier transformation of a black disk profile is approximately a Gaussian for small  $t$ .  $\beta(t)$  can thus be described by an exponential

$$\beta(t) = \beta(0)e^{b_0 t/2}, \quad (2.61)$$

<sup>9</sup>In fact there are two trajectories for each set of quantum numbers, one interpolating between resonances of even spin, the other between those of odd spin.

<sup>10</sup>Neither Regge theory nor Quantum Chromodynamics has been successful at explaining the linearity of  $\alpha(t)$ . The only theoretical framework in which linear trajectories appear naturally is (hadronic) string theory [92–94].

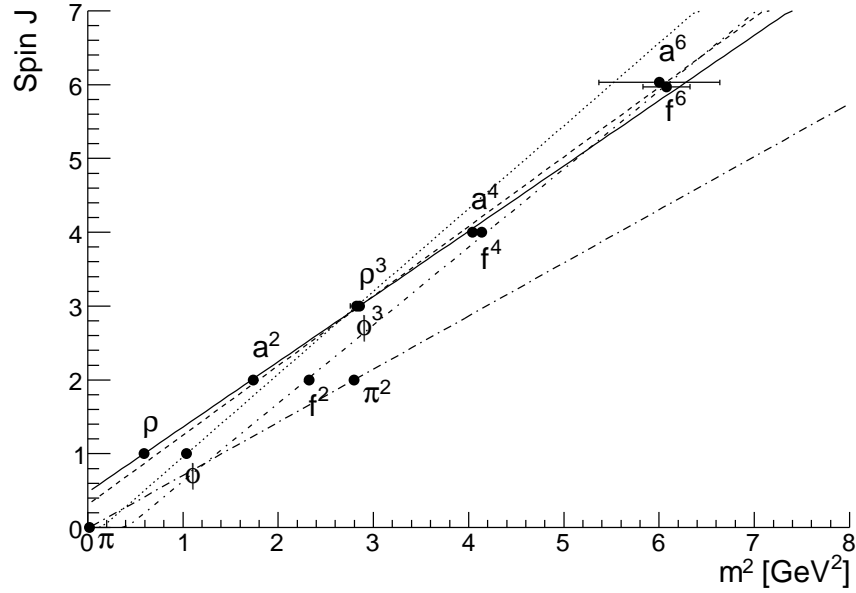


FIGURE 2.9: The so-called Chew-Frautschi plot, depicting some mesonic trajectories in the spin-mass $^2$  plane. The  $\rho$  trajectory is shown as continuous line, the  $a$  trajectory as a dashed, the  $\phi$  trajectory as a dotted line whilst the  $f$  and  $\pi$  trajectories are shown with dot-dashed lines.

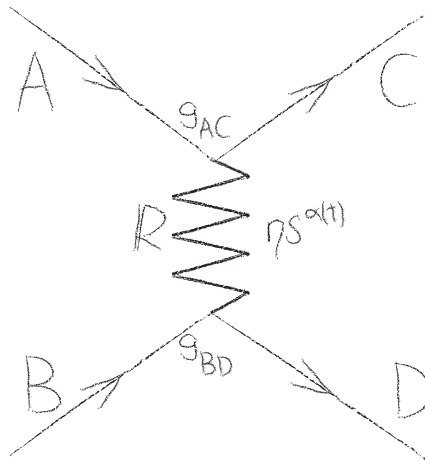


FIGURE 2.10:  $t$ -channel scattering  $AB \rightarrow CD$  mediated by the exchange of a reggeon  $\mathbb{R}$ .

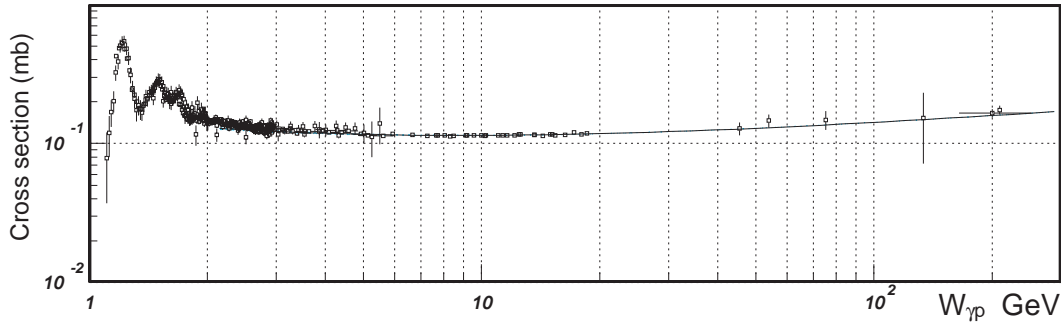


FIGURE 2.11: Total  $\gamma p$  cross section as a function of the centre of mass energy  $W_{\gamma p}$ . Adapted from [95].

corresponding to a two-dimensional Gaussian profile in  $p$ , as  $t = p_T^2 = p_x^2 + p_y^2$ . From equation (2.58) we can obtain the total cross section via the optical theorem

$$\sigma_{tot} \underset{s \rightarrow \infty}{\sim} \frac{1}{s} \text{Im}A(s, t=0) \underset{s \rightarrow \infty}{\sim} s^{\alpha(0)-1}. \quad (2.62)$$

For the elastic cross section we obtain, using equation (2.39),

$$\frac{d\sigma_{el}}{dt} \sim s^{2\alpha(0)-2} e^{-b|t|} \quad (2.63)$$

with

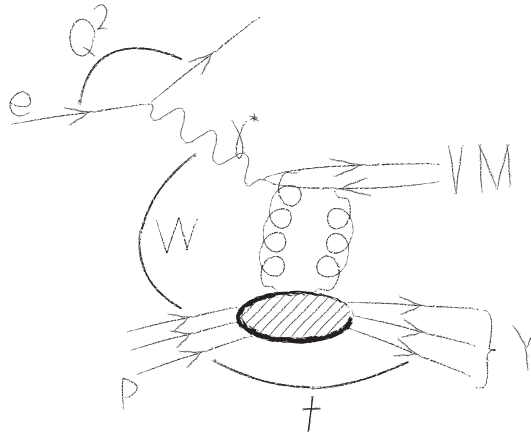
$$b = b_0 + 2\alpha' \ln(s). \quad (2.64)$$

The intercept of the trajectory thus controls the variation of the cross section with energy  $s$ , whilst  $\alpha'$  leads to a *shrinkage* of the forward peak with increasing energy. This shrinkage is not present in the optical analogy, but an observed fact and its prediction thus one of the achievements of Regge Theory.

## 2.6 The Pomeron

All trajectories associated with mesonic or baryonic resonances have intercepts which are much smaller than 1 (usually about 0.5) and thus a decrease of the total cross section with energy is expected. This is in agreement with the data up to a few GeV centre of mass energy, where the cross section begins to flatten and then to rise slowly (see figure 2.11). To explain this behaviour seen in all hadronic cross sections and to stay in agreement with the Pomanchuk theorem, a trajectory with the quantum numbers of the vacuum and an intercept slightly larger than 1 is introduced. First dubbed *Pomeranchukon*, the name was soon shortened to *Pomeron* ( $\mathbb{P}$ ) by the editors of the Physical Review.

Single pomeron exchange will necessarily violate unitarity at very high energies, since every power law violates the Froissart-Martin bound, but up to today it has been extremely successful phenomenologically. It is claimed, that the exchange of multiple pomerons cures the unitarity problem [96–98]. The consequences of multi-pomeron exchange could be observed as an enhanced shrinkage of the diffractive peak at the Large Hadron Collider (LHC) [99]. The correct prediction of the total  $\gamma p$  cross section at HERA energies before the start of HERA by Donnachie and Landshoff [100, 101] is one of the great triumphs of


 FIGURE 2.12: *Two gluon exchange picture of vector meson production.*

Regge theory. From fits to total cross sections in various reactions, Donnachie and Landshoff have determined the “canonical” values for the (so-called *soft*)  $\mathbb{P}$  trajectory [13, 101]

$$\alpha_{\mathbb{P}}(t) = 1.0808 + 0.25t. \quad (2.65)$$

Cudell *et al.* [102] arrive at a slightly higher intercept of  $\alpha_{\mathbb{P}}(0) = 1.0964^{+0.0115}_{-0.0091}$  by fitting proton-proton and proton-antiproton total cross sections.

Diffractive vector meson production provides a complementary test of Regge models to total cross sections. Whilst earlier HERA data from  $\rho$  [21, 23–25, 27],  $\omega$  [103] and  $\phi$  [47] photoproduction show no disagreement with the soft pomeron predictions, the much heavier  $J/\Psi$  mesons show a completely different behaviour, namely a steep increase of the cross section with  $W_{\gamma p}$ . This has been explained by the existence of a second *hard* pomeron [13, 104] or by a dipole pomeron [12], but can also be seen as an indication for the existence of a hard scale and the applicability of perturbative Quantum Chromo Dynamics (pQCD).

## 2.7 Diffraction and QCD

The quark model of hadrons [105, 106] and Quantum Chromo Dynamics (QCD) provide an elegant framework for the understanding of hadrons. Hadrons are built up of quarks bound by gluons, the force carriers of the strong force. The non-abelian structure of QCD lets the gluons also carry the “colour” charge of the strong interaction. Gluons can thus interact with other gluons, leading to an apparent increase of the strong force with distance. This increase has two important consequences, namely that no free coloured objects can be observed (“confinement”) and that perturbative methods, where the coupling is assumed to be weak, are not applicable for large distances.

### 2.7.1 The Pomeron in QCD

The qualitative understanding of the pomeron in QCD is that it is an object with no valence quarks. To lowest order, pomeron exchange corresponds to the exchange of two gluons (see figure 2.12), as proposed in [107, 108]. The two-gluon model gives the correct colour and parity of the exchange, but fails in describing the energy dependence of cross sections. Higher order effects thus have to be included; the pomeron consists of interacting gluons (see figure

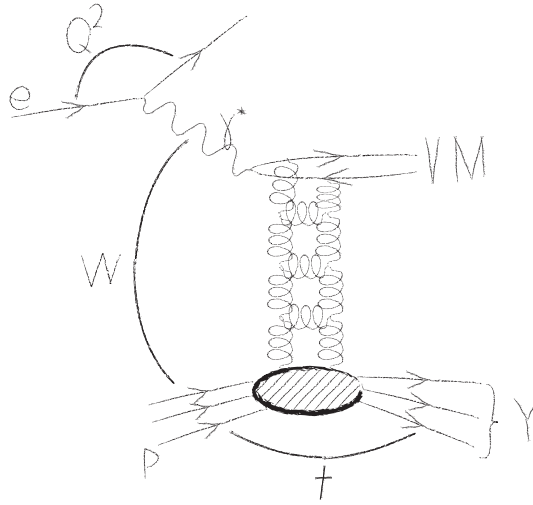


FIGURE 2.13: *Gluon ladder picture of diffractive vector meson exchange.*

2.13). The pomeron trajectory can be continued to the  $s$ -channel region and it is found to cross states which are candidates for being glue-balls (particles consisting of bound valence gluons) [109, 110]. Quantitative predictions for diffractive exchanges become possible, as soon as a hard scale such as a large  $Q^2$ ,  $|t|$  or vector meson mass<sup>11</sup> is present. There, the pomeron is treated as a ladder of gluons (“QCD Pomeron”). If  $s$  is much larger than  $|t|$ , this gluon ladder can be described by the Balitzky, Fadin, Kuraev, Lipatov (BFKL) evolution equation. The phenomenology of this *BFKL-Pomeron* [111] differs markedly from soft pomeron predictions; there is little or no shrinkage and a much steeper energy dependence, well confirmed in hard scale data.

Several BFKL-based calculations have been performed to predict diffractive vector meson production cross sections. In [112, 113] a calculation with  $t$  as a hard scale was performed – a comparison to H1 data in [16] shows that it is able to describe the  $t$  dependence of the cross section but has some problems in explaining the helicity structure. In [114],  $Q^2$  provides the hard scale; the calculation has been used in a H1 measurement of elastic  $J/\psi$  production and shows the sensitivity of these measurements to the gluon distribution in the proton. The calculation in [115] focuses on helicity effects with  $Q^2$  as a hard scale.

Other calculations use the colour dipole approach [116–119], where the virtual vector meson is treated as a colour dipole moving through the colour field of the proton. These models are able to describe a wide variety of data with few free parameters, see e.g. [120].

All QCD based approaches have in common that they require a hard scale in order to be predictive. Soft hadronic interactions, such as those measured in this thesis, are up to now only amenable to the methods of Regge theory.

Albeit there being successful theoretical approaches to “soft” diffraction and “hard” diffraction, it is by no means clear what tools have to be applied in the transition region and where this transition is about to occur. From both a theoretical but also from a purely aesthetical point of view it is highly desirable to find a common picture (a *universal pomeron*) to describe both regimes.

<sup>11</sup>The vector meson mass alone as a hard scale is a claim much disputed theoretically [12] and also not completely in agreement with the data – e.g. there is significant shrinkage seen for  $J/\Psi$  photoproduction [28].

### 2.7.2 Strings and the Pomeron

One possible inroad to such a common picture is the conjecture that string theories on a suitable higher dimensional background space are dual to strongly interacting quantum field theories in lower dimensions (the so called AdS/CFT duality<sup>12</sup> [121–123]).

This duality has been used to study the pomeron trajectory in [124]. In string theory, the pomeron is the Regge trajectory of the graviton and thus is expected to have an intercept of 2 (the graviton is a massless spin-2 particle). The intercept is however lowered by higher order corrections, bringing it into better agreement with experiment. The pomeron trajectory derived from a combination of string and BFKL techniques resembles the canonical soft pomeron for large positive values of  $t$  and becomes flat (BFKL-like) for large negative  $t$ , thus at least qualitatively linking the soft and hard regimes. The behaviour in the small  $t$  region is however dependent on confinement effects, which brake the conformal symmetry and thus invalidate the duality.

---

<sup>12</sup>AdS stands for Anti-de-Sitter, specifying properties of the metric in the extra dimensions and CFT stands for Conformal Field Theory (scale invariant field theory).

## Chapter 3

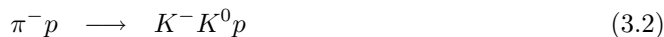
# The $\phi$ Meson

*Your eyes will see strange sights and your mind  
imagine confusing things.*

PROVERBS 23:33

### 3.1 The Discovery of the $\phi$ Meson

First indications of resonant structures in the  $\bar{K}K$  system were seen in a 1962 bubble chamber experiment [126] at the Brookhaven Alternating Gradient Synchrotron (AGS) studying the reactions



In the same year, a more marked departure from the phase space expectation was found in the analysis of pictures taken with the 20 in. bubble chamber at the AGS [125]. A beam of negative kaons with energies of 2.24 and 2.5 GeV was directed into the hydrogen of the chamber. 37 exposures containing one of the following two reactions were analysed for resonant structures:



The very prominent peak at the beginning of the phase space (see figure 3.1) was interpreted as either a resonance (then dubbed  $K^*$ ) of mass 1020 MeV and a width of 20 MeV or an  $S$ -wave final state interaction between the kaons. This resonance was soon thereafter seen in the reaction  $\pi^- p \longrightarrow \bar{K}^0 K^0 n$  with the 72 in. bubble chamber at the Lawrence Radiation Laboratory [127].

The Lawrence Radiation Laboratory group then also studied the  $K^- p$  initial state to determine the nature of the resonance. In subsequent publications [128, 129], both the east and west coast groups confirmed the existence of a resonance, now named  $\phi^1$  as proposed

---

<sup>1</sup>In the first few publications, the  $\varphi$  character for  $phi$  was used, and only later on  $\phi$  became the standard designation. In this thesis,  $\phi$  stands for the meson, whereas  $\varphi$  stands for an azimuthal angle.

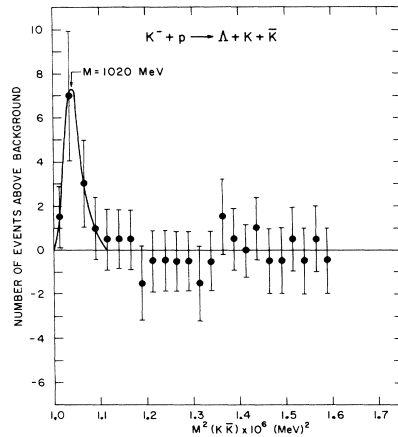


FIGURE 3.1: “The (effective mass)<sup>2</sup> distribution for  $\bar{K}K$  from the channel  $\Lambda\bar{K}K$  for those events above phase space.” From [125].

by Sakuari [130]. In the Brookhaven analysis, the mass was found to be  $1019 \pm 1$  MeV and the width was estimated to  $1_{-1}^{+2}$  MeV. From the absence of  $K_L K_L$  and  $K_S K_S$  decays it was deduced that the resonance has a parity  $P$  of  $-1$ , which in the  $\bar{K}K$  system also implies a charge conjugation quantum number  $C$  of  $-1$ . This in turn implies an odd spin  $J$ . The spin was approximately determined from the relative branching ratio to charged and neutral kaons. This branching ratio is spin dependent because of the mass difference between neutral and charged kaons and the different coulomb barrier for the decay. The measured fraction of  $45 \pm 10\%$  was found to be in better agreement with the 39% expectation for spin 1 than the 26% expectation for spin 3. The shape of the resonance was also in better agreement with the spin 1 hypothesis. Finally, the isospin was determined from the  $G$ -parity. For odd spin, it is  $G = -(-1)^I$ . If the  $G$ -parity were  $+1$ , the decay mode  $\phi \rightarrow \pi^+\pi^-$  would be allowed. Bubble chamber pictures showing the reaction  $K^-p \rightarrow \Lambda\pi^+\pi^-$  were searched for an enhancement in the  $\pi^+\pi^-$  invariant mass spectrum around 1019 MeV and none was found. Thus the relative branching fraction for the decay to pions versus the decay to kaons was constrained to be less than 20%, compared to a factor of 10 to 20 expected for positive  $G$ -parity. The negative  $G$ -parity of the  $\phi$  was confirmed by the observation of an enhancement in the  $\pi^+\pi^-\pi^0$  invariant mass spectrum for the reaction  $K^-p \rightarrow \Lambda\pi^+\pi^-\pi^0$ . With less than 40 events, the quantum numbers of the  $\phi$  were thus correctly determined to be  $I^G(J^{PC}) = 1^-(1^{--})$  and the three main decay channels had been properly identified.

## 3.2 Mass and Width of the $\phi$ Meson

The currently best measurements of the  $\phi$  meson mass and width were made at the VEPP-2M  $e^+e^-$  collider in Novosibirsk. At this machine, the Spherical Neutral Detector (SND, [131]) and the Cryogenic Magnetic Detector 2 (CMD-2, [132]) study the production and decay of  $\phi$  mesons. The CMD measurement reconstructs the  $\phi \rightarrow K_S^0 K_L^0$  decay from the  $K_S^0$  decay pions seen in the drift chamber and the  $K_L^0$  detected in the cesium iodide calorimeter [133] or alternatively the all-neutral decay into  $\phi \rightarrow \eta\gamma$  with subsequent  $\eta \rightarrow \gamma\gamma$  decay [134]. The SND measurement on the other hand is based on the three most common  $\phi$  decay modes (see also the following section), reconstructed using a drift chamber and a sodium iodide calorimeter [135]. The  $\phi$  mass and width are determined from event rates at different

Decay mode	Branching ratio
$K^+K^-$	$(49.2 \pm 0.6)\%$
$K_L^0K_S^0$	$(34.0 \pm 0.5)\%$
$\pi^+\pi^-\pi^0$ , including $\rho\pi$	$(15.3 \pm 0.4)\%$
$\eta\gamma$	$(1.30 \pm 0.02)\%$
$\pi^0\gamma$	$(1.25 \pm 0.07) \times 10^{-3}$
$f_0(980)\gamma$	$(4.40 \pm 0.21) \times 10^{-4}$
$e^+e^-$	$(2.97 \pm 0.04) \times 10^{-4}$
$\mu^+\mu^-$	$(2.86 \pm 0.19) \times 10^{-4}$
$\eta e^+e^-$	$(1.15 \pm 0.10) \times 10^{-4}$
$\pi^0\pi^0\gamma$	$(1.09 \pm 0.06) \times 10^{-4}$
$\pi^0\eta\gamma$	$(8.3 \pm 0.5) \times 10^{-5}$
$a_0(980)\eta\gamma$	$(7.6 \pm 0.6) \times 10^{-5}$
$\pi^+\pi^-$	$(7.3 \pm 1.3) \times 10^{-5}$
$\eta'(958)\gamma$	$(6.2 \pm 0.7) \times 10^{-5}$
$\omega\pi^0$	$(5.2 \pm 1.3) \times 10^{-5}$
$\pi^0e^+e^-$	$(1.12 \pm 0.28) \times 10^{-5}$
$\pi^+\pi^-\gamma$	$(4.1 \pm 1.3) \times 10^{-5}$
$\mu^+\mu^-\gamma$	$(1.4 \pm 0.5) \times 10^{-5}$
$\pi^+\pi^-\pi^+\pi^-$	$(3.9 \pm 2.8) \times 10^{-6}$

 TABLE 3.1:  $\phi$  meson decay modes with a measured branching fraction, taken from [95].

beam energies, which in turn are determined from the resonant depolarisation method for certain runs and from the momenta of charged kaons seen in CMD-2 for others.

The world average of the  $\phi$  mass is  $m_\phi = 1019.460 \pm 0.019$  MeV and the world average of the width is  $\Gamma = 4.26 \pm 0.05$  MeV [95], both dominated by the aforementioned measurements in Novosibirsk.

### 3.3 $\phi$ Meson Decays

$\phi$  mesons decay strongly within less than  $1.55 \cdot 10^{-22}$ s [95]. It is thus the  $\phi$  decay products that are seen with the H1 detector. The dominant decay channels are to charged (branching

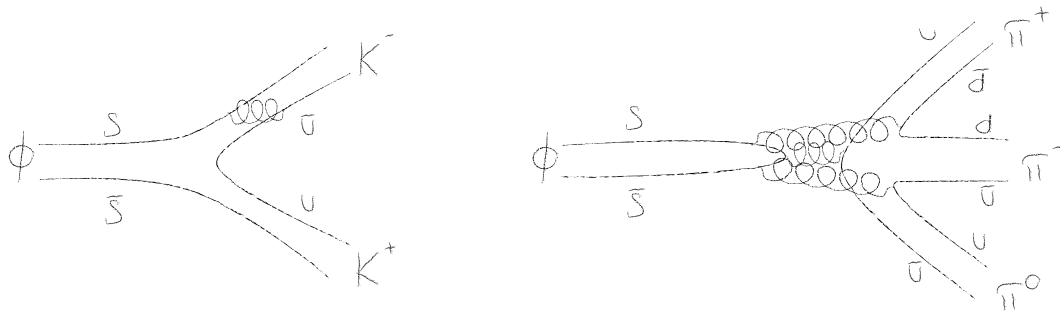


FIGURE 3.2: Illustration of the Zweig rule for the example of the  $\phi$  meson decay. The kinematically disfavoured decay to kaons has continued quark lines and involves the exchange of one gluon whilst the decay to pions has broken quark lines and requires the exchange of three gluons, leading to a suppression.

ratio 49.2%) and neutral (34.0%) kaons<sup>2</sup> (see also table 3.1). Even though the decay to kaons is kinematically disfavoured, the Zweig rule suppresses the more favourable decay to  $\pi^+\pi^-\pi^0$  (see figure 3.2). In the present thesis, the decay to charged kaons is studied, as this is the only channel with a significant branching ratio involving no neutral particles which would have to be reconstructed in the calorimeter. As the mass of the two decay kaons ( $2 \times 493.7 \text{ MeV} = 987.4 \text{ MeV}$ ) is only 32.1 MeV smaller than the  $\phi$  mass of 1019.5 MeV, the kaons have only 127 MeV momentum in the  $\phi$  rest frame.

The decay to pions is experimentally more challenging as the  $\pi^0$  has to be reconstructed from two photons measured in the calorimeter [136]. The advantage of higher momenta of the decay particles is partly obscured by the phase space constraints imposed by the fact that the  $\pi^0$  has to be isolated from the charged pions to allow for a good photon identification.

### 3.4 The $\phi$ Meson in the Quark Model

In the quark model, mesons are bound states  $q\bar{q}$  of a quark and an antiquark. Neglecting the heavier charm, beauty and top quarks, the mesons can be classified in multiplets of  $SU(3)_{flavour}$ , representing the symmetry of the strong force between up, down and strange quarks. Bound states of a quark and an antiquark can thus be classified as an octet and a singlet of mesons:

$$\mathbf{3} \otimes \bar{\mathbf{3}} = \mathbf{8} \oplus \mathbf{1}. \quad (3.6)$$

For the vector mesons ( $J^{PC} = 1^{--}$ ), the corresponding states are depicted in figure 3.3. There are three states with isospin  $I = 1$  ( $\rho$ ), four states with  $I = \frac{1}{2}$  ( $K^*$ , with non-zero strangeness  $S$ ) and two states with isospin  $I = 0$ . These isoscalars (one belonging to the octet of  $SU(3)_{flavour}$ , the other one to the singlet) can mix. The wave functions of the octet  $\psi_8$  and singlet  $\psi_1$  are respectively

$$\psi_8 = \frac{1}{\sqrt{6}}(u\bar{u} + d\bar{d} - 2s\bar{s}) \quad (3.7)$$

$$\psi_1 = \frac{1}{\sqrt{3}}(u\bar{u} + d\bar{d} + s\bar{s}). \quad (3.8)$$

The physical states are mixtures of these with a mixing angle  $\theta_V$

$$\phi = \psi_8 \cos \theta_V - \psi_1 \sin \theta_V \quad (3.9)$$

$$\omega = \psi_8 \sin \theta_V + \psi_1 \cos \theta_V. \quad (3.10)$$

The mixing angle is linked to the masses of the particles in the multiplet [137]:

$$\tan \theta_V = \frac{4m_{K^*} - m_\rho - 3m_\phi}{2\sqrt{2}(m_\rho - m_{K^*})} \quad (3.11)$$

and also

$$\tan^2 \theta_V = \frac{4m_{K^*} - m_\rho - 3m_\phi}{-4m_{K^*} + m_\rho + 3m_\phi}. \quad (3.12)$$

It turns out (inserting the measured masses) that the mixing angle  $\theta_V$  is very close to the *ideal* mixing angle of  $\theta_V = 35.3^\circ$  where  $\tan \theta_V = 1/\sqrt{2}$  and thus the  $\phi$  is a pure  $s\bar{s}$  state. This finding is confirmed by the suppression of the pionic decay mode of the  $\phi$ .

The fact that the  $\phi$  consists almost exclusively of strange quarks makes it an excellent probe for pomeron exchange in  $\gamma p$ -interactions: The valence quark contents of the proton and the  $\phi$  meson are disjoint and thus there can be no reggeon exchange [138–141].

---

<sup>2</sup>The different branching ratios for charged and neutral kaons are due to the mass difference between them - the size of the difference stems from the small available phase space in these decays.

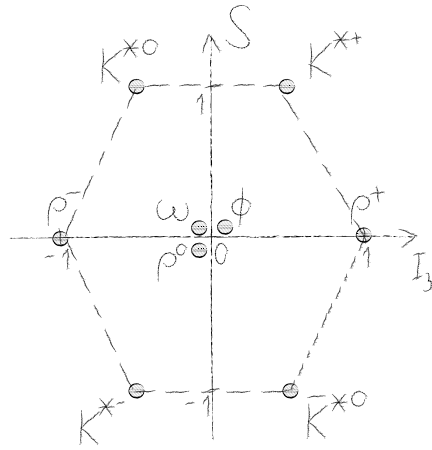


FIGURE 3.3: *The vector meson multiplet of  $SU(3)_{\text{flavour}}$ .*



## Chapter 4

# The H1 Detector at HERA

*There is no money for apparatus; we shall have to use our heads.*

ERNEST RUTHERFORD [142]

*... ich bin verwirrt, der bescheidene Arbeitstisch Otto Hahns steht mir vor Augen, auf welchem die erste Atomspaltung glückte, irgendwo sah ich ihn abgebildet, er hätte auch in Doktor Fausts Kabinett gepaßt: einige Batterien, Glühlampen, Spulen, ein Paraffinschutzring; und nun diese Ungeheuerlichkeit, die Experimentalphysik braucht nicht zu sparen, hier bastelt sie mit Zyklopenarmen und Millionenkrediten.*

FRIEDRICH DÜRRENMATT [143]

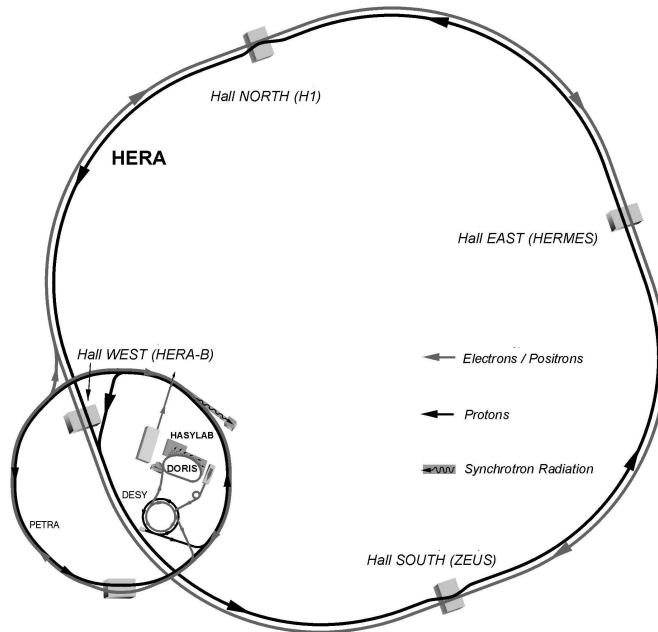
### 4.1 The HERA Accelerator at DESY

The HERA (*Hadron Elektron Ring Anlage*) collider at DESY (*Deutsches Elektronen Synchrotron*) incorporates two accelerators in a common ring tunnel of 6.3 km length (figure 4.1). One accelerates protons counterclockwise to an energy of up to 920 GeV, the other boosts electrons or positrons clockwise to an energy of 27.5 GeV. The two beams are brought into collision inside the detectors H1 and ZEUS, with a centre of mass energy  $\sqrt{s} = 318$  GeV. Also located at HERA is the spin physics experiment HERMES, which directs the polarised electron/positron beam onto a polarised hydrogen or deuterium target. The fourth experimental hall used to be occupied by the *b*-physics experiment HERA-B, which was dismantled in 2001.

Besides the centre of mass energy which defines the accessible phase space and reactions, the luminosity is the second key parameter of a high energy physics accelerator. The luminosity  $\mathcal{L}$  defines how frequent a reaction with a cross section  $\sigma$  occurs ( $\frac{dN}{dt}$  is the expected rate of interactions):

$$\frac{dN}{dt} = \sigma \mathcal{L}. \quad (4.1)$$

In the case of a colliding beam experiment with matched beam sizes, the luminosity is given by the following expression:

FIGURE 4.1: *The accelerators at DESY (adapted from [144]).*

$$\mathcal{L} = fn \frac{N_1 N_2}{4\pi\sigma_x\sigma_y}, \quad (4.2)$$

where  $f$  is the frequency of revolution for particles in the ring,  $n$  is the number of colliding bunches in each beam,  $N_1$  and  $N_2$  are the number of particles per bunch of the respective beams and  $\sigma_x$  and  $\sigma_y$  is the horizontal and vertical beam size respectively.

In the case of HERA, the electron/positron and the proton beam consist of up to 180 colliding bunches<sup>1</sup>, containing of the order of  $10^{10}$  particles each. Whilst the electron bunches are relatively short ( $\approx 8$  mm), the proton bunches extend over  $\approx 30$  cm. Every 96 ns two bunches intersect inside the detectors, defining the *HERA-Clock* with a frequency of 10.4 MHz. The revolution frequency is 50 kHz.

HERA is in operation since 1992, but has undergone an extended shutdown and upgrade [145, 146] in 2001. The addition of superconducting focussing magnets within H1 and ZEUS reduces the beam size and thus increases the luminosity seen by the experiments.

## 4.2 The H1 Detector at HERA

The H1 detector [147, 148] is located in the north of the HERA ring; the very complex apparatus was built and is maintained by a collaboration of about 400 physicists from 41 institutes located in 15 countries.

The experiment consists of three main sections, namely tracking, calorimetry and the muon system (see figure 4.2), each of which is made up of several sub-detectors. The

<sup>1</sup>In order to obtain a precise luminosity measurement and to study the contributions from beam-gas interactions, a number of so-called pilot bunches, which have no counterpart in the other beam are also part of the beam profile

HERA II	e-beam	p-beam
Energy	27.5 GeV	920 GeV
Number of bunches total/colliding	180/174	180/174
Particles per bunch	$4.2 \cdot 10^{10}$	$10 \cdot 10^{10}$
Beam current	58 mA	140 mA
Beam size $\sigma_x \times \sigma_y$	$118 \mu\text{m} \times 32 \mu\text{m}$	$118 \mu\text{m} \times 32 \mu\text{m}$
Luminosity	$7.36 \cdot 10^{31} \text{cm}^{-2} \text{s}^{-1}$	
Specific luminosity	$1.64 \cdot 10^{30} \text{cm}^{-2} \text{s}^{-1} \text{mA}^{-2}$	

TABLE 4.1: *Design parameters of HERA II (from [145]).*

*tracking* detectors are located closest to the interaction point and measure tracks of charged particles. There are precision silicon detectors to identify decay vertices from long lived particles, multiple wire proportional chambers mainly used for triggering and drift chambers for the reconstruction of tracks. The tracking detectors are surrounded by *calorimeters* which measure particle energies. In the forward<sup>2</sup> and central part a liquid argon detector with lead (electromagnetic part) and steel (hadronic part) absorber plates is used, whilst the backward spaghetti calorimeter identifies the scattered electron with a lead-scintillator-fibre detector. The tracking and calorimetry detectors are enclosed by a superconducting magnet, generating a field of 1.15 Tesla. Muons and high energy hadrons which penetrate the calorimeters are detected with limited streamer tubes installed between the iron plates of the magnet yoke and a separate *muon detector* in the forward direction.

### 4.3 The Central Tracking System of H1

The analysis presented in this thesis makes full use of the capabilities of the H1 tracking system. Its design and principles of operation are thus described in some detail. H1's central tracker (see figures 4.3 and 4.4) consists of proportional chambers, whose fast signals are mainly used for triggering, and silicon detectors and drift chambers providing precise position measurements.

The innermost tracking detectors are silicon solid-state detectors. In the 2005 running period analysed in this thesis, only the Central Silicon Tracker CST was operative, whilst the forward and backward devices (FST and BST) were being repaired. The CST [149–151] consists of two layers of double-sided silicon detectors at radii between 4 and 13 cm in an elliptical arrangement to accommodate the elliptical beam pipe.

Going from the beam pipe outward, the CST is followed by the Central Inner Proportional Chamber (CIP) which is described in some more detail in section 4.3.1. H1's main tracking detector is the Central Jet Chamber CJC, which is split into two concentric parts and described in section 4.3.2. Between the two rings there is the Central Outer Proportional Chamber COP<sup>3</sup> and the Central Outer  $z$ -Chamber COZ which delivers precise  $z$ -coordinates of tracks.

<sup>2</sup>The H1 coordinate system is based on the proton beam direction, which defines the  $z$ -axis and the “forward” or “downstream” direction (see figure 4.2).

<sup>3</sup>The COP was usually powered and read out during 2005, but its signals were not used in physics triggers or the offline reconstruction.

	Detector component	Abbreviation
1	Nominal interaction point	IP
<i>Tracking detectors</i>		
2	Central silicon tracker	CST
3	Backward silicon tracker	BST
4	Forward silicon tracker	FST
5	Central inner proportional chamber	CIP
6	Central outer proportional chamber and Central outer $z$ drift chamber	COP COZ
7	Inner central jet chamber	CJC1
8	Outer central jet chamber	CJC2
9	Forward tracking detectors	FTD
10	Backward proportional chamber	BPC
<i>Calorimeters</i>		
11	Liquid argon cryostat	
12	Liquid argon electromagnetic calorimeter	LAr elm.
13	Liquid argon hadronic calorimeter	LAr hadr.
14	Liquid argon cryogenics system	
15	Electromagnetic spaghetti calorimeter	SpaCal elm.
16	Hadronic spaghetti calorimeter	SpaCal hadr.
17	Plug calorimeter	Plug
18	Superconducting solenoid	
<i>Muon detectors</i>		
19	Instrumented iron (central muon / tail catcher)	CMD/TC
20	Forward muon detector (incl. toroid magnet)	FMD
21	New superconducting focusing magnets	GO/GG
22	Concrete shielding	

TABLE 4.2: *The main components of the H1 detector - legend to figure 4.2. Note: The forward and backward silicon trackers were not in operation and also not present in the detector during the 2005 data taking period.*

### 4.3.1 The Central Inner Proportional Chamber (CIP)

The CIP is a multi-wire proportional chamber [152], whose main purpose is to deliver fast tracking information, allowing a reconstruction of the position of an interaction along the beam line ( $z$ -vertex) on trigger level. The chamber [153] consist of 5 layers at radii between 15 and 20 cm. The chamber is segmented 16-fold in  $\varphi$ . In  $z$ , a projective geometry [154] dictates the arrangements of the 9600 readout pads. In this projective geometry, tracks originating from the same  $z_0$  along the beam line produce the same pattern in the chambers, shifted by a number of pads according to the track  $\vartheta$  (see figure 4.5).

The projective geometry of the CIP allows for a fast track recognition and vertex reconstruction in the CIP2000 trigger [154–159]. A pad in the central layer is taken as pivot element and its local neighbourhood searched for track patterns, where a four-out-of-five layer requirement is applied to compensate for inefficiencies<sup>4</sup>. Due to the projective geometry, these track patterns can be easily assigned to a specific bin along the beamline (see figure 4.6). The number of tracks pointing to a specific bin is then summed up to construct a  $z$ -vertex histogram (figure 4.7). The trigger decision is then derived from the total number

<sup>4</sup>In regions where only a reduced number of layers is available due to hardware faults, the requirement is relaxed.



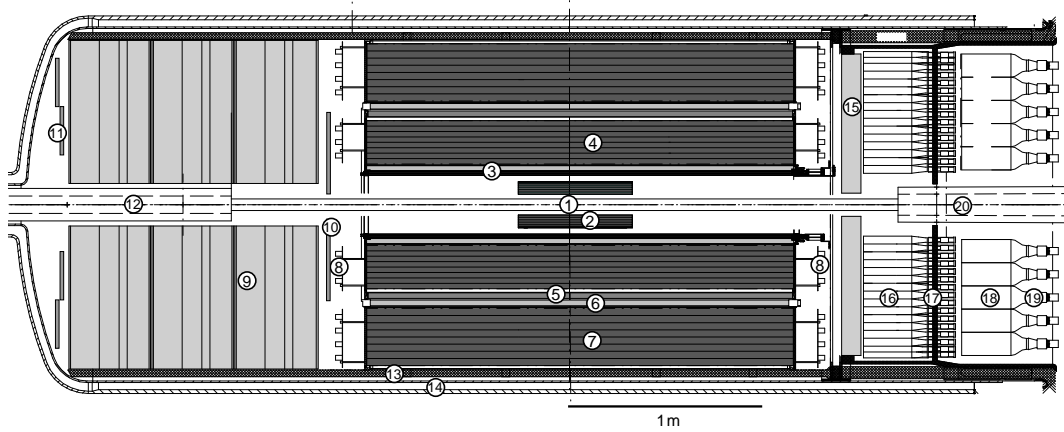
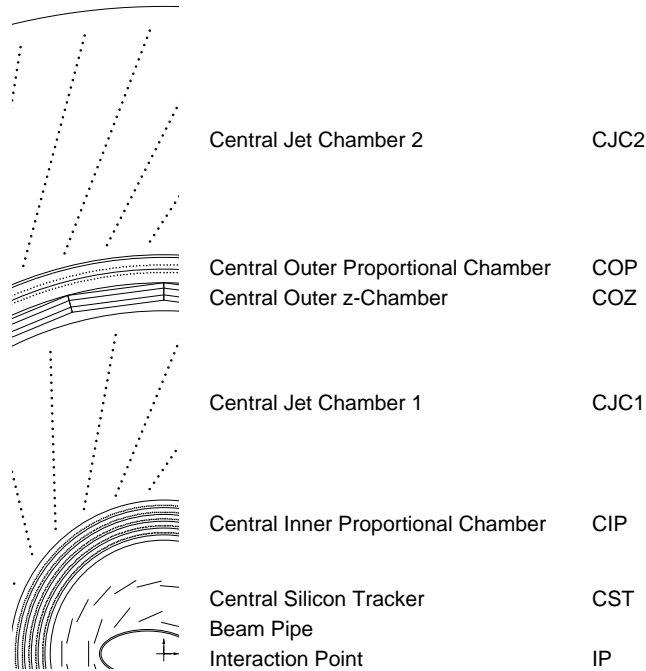


FIGURE 4.3: *The inner part of the H1 detector in the 2005 configuration. A legend to the various subsystems can be found in table 4.3.*

Detector component	Abbreviation
1 Nominal interaction point	IP
2 Central silicon tracker	CST
3 Central inner proportional chamber	CIP
4 Inner central jet chamber	CJC1
5 Central outer $z$ drift chamber	COZ
6 Central outer proportional chamber	COP
7 Outer central jet chamber	CJC2
8 CJC electronics	
9 Forward tracking detectors	FTD
10 Forward trigger scintillator 1	FTi1
11 Forward trigger scintillator 2	FTi2
12 Superconducting quadrupole magnet	GO
13 Forward Tracker cables	
14 Inner wall of LAr vacuum tank	
15 Backward proportional chamber	BPC
16 Electromagnetic Spaghetti Calorimeter	SpaCal Em
17 Photomultipliers for SpaCal Em	
18 Hadronic Spaghetti Calorimeter	SpaCal Had
19 Photomultipliers for SpaCal Had	
20 Superconducting quadrupole magnet	GG

TABLE 4.3: *The main components of the H1 tracker (and the backward calorimetry) in the 2005 configuration – legend to figure 4.3.*

FIGURE 4.4: *Radial view of the H1 central tracker.*

of entries in the histogram (*CIP Multiplicity*) and the fraction of central entries to backward entries (*CIP Significance*). The fast signals from the proportional chamber also determine the time of the interaction (*CIP  $t_0$* ).

### 4.3.2 The Central Jet Chamber (CJC)

The CJC [160] is a drift chamber [161, 162] of the jet type [163, 164]. It is split into an inner ring (CJC1) with 30 azimuthal cells and an outer ring (CJC2) with 60 cells (see table 4.4 for the complete dimensions). The cells are tilted with regard to the radial direction such that in the presence of the magnetic field, the ionisation electrons drift approximately perpendicular to high momentum (“stiff”) tracks. This tilt also ensures that stiff tracks cross the wire plane at least once per ring, allowing for a precise determination of the track timing<sup>5</sup>. The actual positions of the sense wires are staggered by  $\pm 150 \mu\text{m}$  with regard to the nominal wire plane such that adjacent wires are pulled to definite positions on opposite sides of the plane by the electric field. This staggering, together with the crossing of cell boundaries also helps to resolve the inherent left-right ambiguity of the drift chamber.

The position of the hit in the transverse plane is determined from the drift time (found from the pulse shape in a  $Qt$  analysis, see section 13.4.1) and the precise knowledge of the wire positions, drift velocity and angle in the magnetic field (“Lorentz angle”). The position along the wire is determined from the ratio of the charges read out from both wire ends (see section 13.4.1). The single hit resolution is about  $160 \mu\text{m}$  in the transverse plane and between 2 and 8 cm in  $z$ , depending on the charge of the hit.

<sup>5</sup>This helps in recognising events from cosmic ray muons, where the upper segment of the track is earlier than the lower one and the arrival times are uncorrelated to the bunch crossing times.

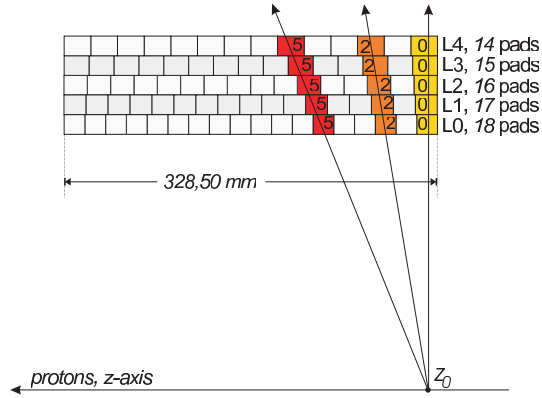


FIGURE 4.5: The projective geometry of the CIP. All tracks originating from a common  $z_0$  hit pads with the same offset on all layers. Figure from [154].

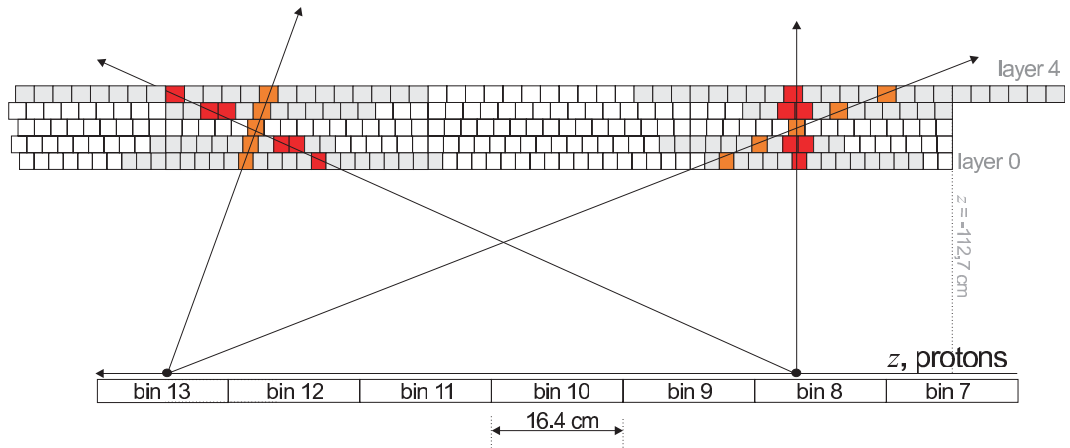


FIGURE 4.6: Principle of operation of the CIP2000 trigger. Figure adapted from [154].

	CJC1	CJC2
Active length	220 cm	
Inner radius	20.3 cm	53.0 cm
Outer radius	45.1 cm	84.4 cm
Active radial length	22.4 cm	29.6 cm
Number of cells	30	60
Sense wires per cell	24	32
Potential wires per cell	50	66
Field wires per cell	10	10
Cathode wires per cell	49	65
Sense wire distance	1.016 cm	
Maximum drift distance	44.5 mm	43.1 mm

TABLE 4.4: CJC mechanical parameters. Both chambers together have a total of 14370 wires. Numbers taken from [148].

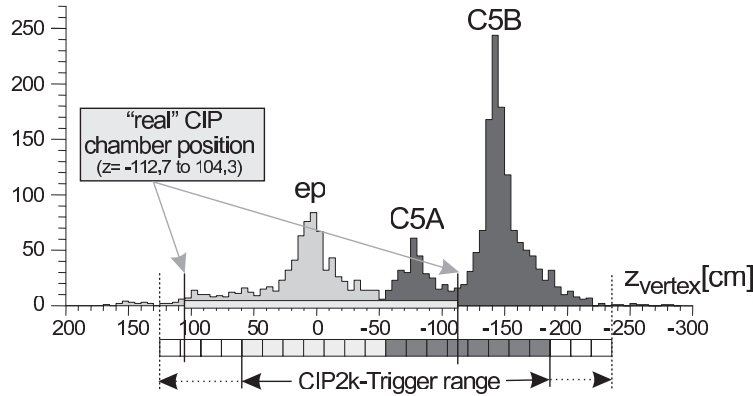


FIGURE 4.7:  $z$  vertex histogram of the CIP 2000 trigger. On top, a typical vertex distribution before trigger vetoes is shown; the peak originating from ep interactions is shadowed by the two peaks from interactions of the proton beam with the collimators designated C5A and C5B. The acceptance of the CIP trigger is shown by the squares below the histograms. Due to hardware limitations, the histogram is only evaluated for the shaded bins, where the light gray bins count as signal (central) and the dark gray bins as background (backward). Figure adapted from [154].

### 4.3.3 Track Reconstruction

#### Pattern Recognition and Track Finding

The track reconstruction starts with a list of all hits detected in the jet chamber [165–167]. First, the event timing is determined from a drift time histogram (hits close to the wire plane have the shortest drift times and thus determine the  $t_0$  [168]). The pattern recognition starts by identifying triplets of hits from adjacent or next-to-adjacent wires. These triplets are fitted with a circle through the origin in the  $r - \varphi$  plane, resulting in an approximate value for the track curvature  $\kappa$  and the track angle at the origin  $\varphi$ . Triplets belonging to the same track will cluster in the  $\kappa - \varphi$  plane (this is a generalised Hough-transform, see section 13.4.5). In an iterative procedure, triplets are merged to larger groups of hits, the fits are repeated and outliers rejected. At the end of this procedure stands a set of *non-vertex-fitted tracks*, for each of which  $\kappa$ ,  $\varphi$  and the distance of closest approach to the origin ( $dca$ ) are known. In a straight line fit in the  $s - z$  plane ( $s$  is the track length),  $\vartheta$  and the intercept with the beam line  $z_0$  are determined. If a track has a kink, e.g. due to multiple scattering in the material between CJC1 and CJC2, the pieces before and after the kink are treated separately.

#### Vertex Fit

The fact that most tracks in an event originate from a common vertex lying on the beamline is a powerful constraint used to improve the track resolution. The vertex fit proceeds as follows:

1. A provisional  $z_{vtx}$  is determined from a weighted mean of the  $z_0$  values of the non-vertex fitted tracks.
2. The beam position at this  $z_{vtx}$  is used to get a provisional  $x_{vtx}$  and  $y_{vtx}$ <sup>6</sup>.

<sup>6</sup>The beam position is calculated as an average over many events and varies slowly within a luminosity fill. As the beam is not perfectly aligned with the H1 coordinate system (“beam tilt”),  $x_{vtx}$  and  $y_{vtx}$  depend on  $z_{vtx}$ .

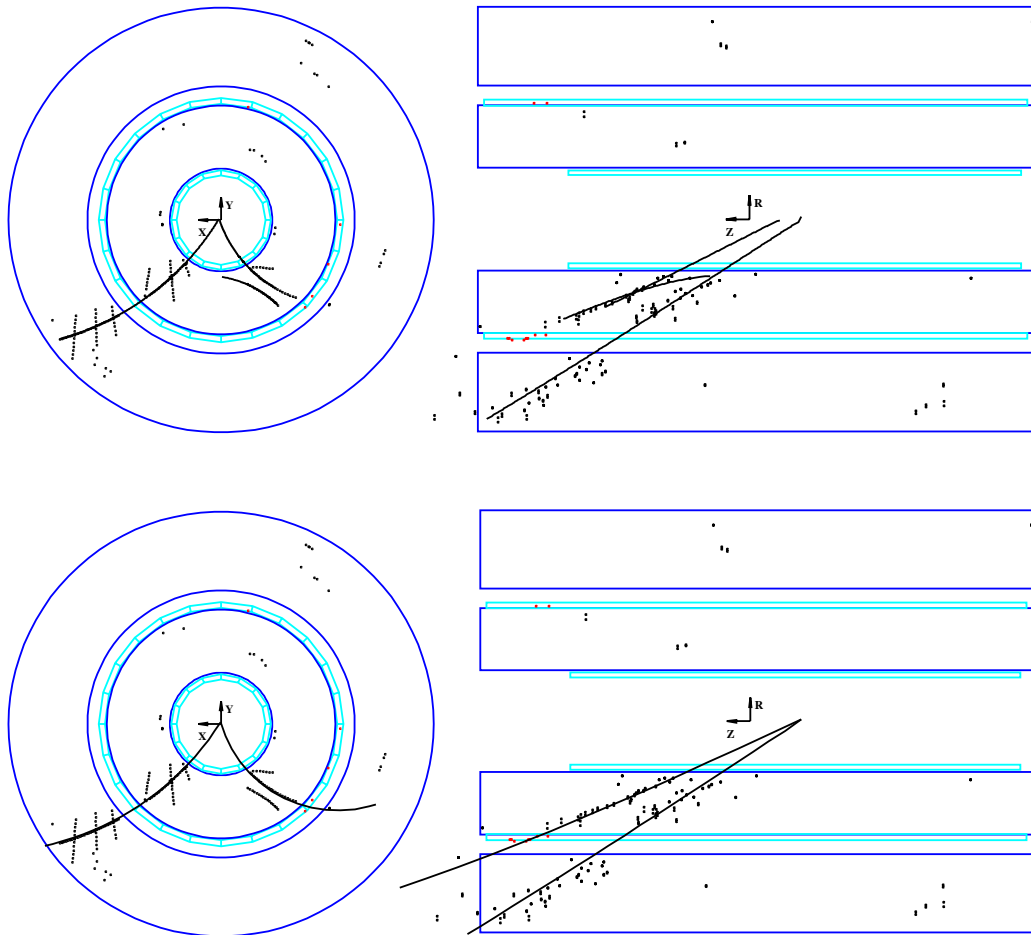


FIGURE 4.8: *Example of a vertex fit. The top views show a typical  $\phi$  event candidate in the transverse and longitudinal plane respectively with the tracks before the vertex fit. As can be seen, a group of mirror hits from a track almost parallel to the wire plane, is also identified as a track. Due to the limited resolution in  $z$  and the short length of one of the tracks, the tracks do not meet in a single vertex. The bottom views show the same event with the vertex fitted tracks.*

3. All tracks are individually refitted in the  $r - \varphi$  plane, using the vertex as a constraint.
4. The track parameters obtained in step 3 are used for a common  $z$ -fit of all tracks.
5. Steps 2 to 4 are repeated iteratively if necessary.

On their way from the interaction point to the CJC, the particles producing the tracks traverse the material of the beampipe, the CST, the CIP and the CJC inner wall. In this material they lose part of their energy, which implies that the track parameters measured in the CJC do not coincide with those at the vertex (which are of interest for the measurement). To improve the vertex fit and to obtain the best possible set of parameters at the vertex, the effects of traversing the material are corrected for, using a detailed description of the detector. The Bethe-Bloch formula (equation (7.1)) with excitation energies in the Barkas and Berger parametrisation [169] is used to describe energy loss, the energy straggling [170] is described using a Gaussian model introduced by Schorr [171]. The correction includes a full error propagation, taking into account multiple scattering [172]. As the energy loss corrections are however dependent on the speed  $\beta$  of a particle, and at this stage of the reconstruction only its momentum is known, an assumption on the particle mass has to be made. The H1 reconstruction code always assumes a pion mass, thus underestimating the energy loss corrections for heavier particles such as protons — and of relevance to the present thesis — kaons. The improvement of the energy loss corrections are described in section 6.4.1.

### **$dE/dx$ Measurement**

Whilst the mass dependence of the ionisation energy loss ( $dE/dx$ ) in the material in front of the CJC potentially spoils the track reconstruction, the mass dependence of the energy loss in the CJC allows for particle identification. To obtain a useful  $dE/dx$  measurement from the integrated charges read out from the CJC wires, a number of corrections have to be applied. First, the individual charges are corrected for double-pulses and the relative gain of each pre-amplifier. Then the charges from both wire ends are added to give the total charge collected on the wire. This charge is corrected for the  $r - \varphi$  length of the track in the drift cell concerned. The length in the  $r - z$  plane is only corrected for on analysis level, when the best possible  $\vartheta$  measurement is available.

The charges from individual hits are then averaged to obtain the mean energy loss along a reconstructed track. To enter into the averaging procedure, hits have to fulfil the following quality criteria:

- The hit has to be used in the track reconstruction (no outliers).
- There has to be a charge measurement above a threshold from both wire ends.
- The drift distance has to be in a range where near-field effects of the wire and edge effects can be ignored.
- The  $z$ -coordinate of the hit obtained by charge division has to be consistent with the  $z$  obtained from the track parameters.
- The hit has to have a minimum distance in  $r - \varphi$  to the next hit, in order to ensure that the charge collected really originates from the correct hit.

These cuts ensure a well defined charge measurement for the surviving hits but also create a bias toward larger charges and thus larger  $dE/dx$  (see section 7.3 for an ansatz to correct for this bias). The individual energy loss follows a Landau distribution [173] around the value predicted by the Bethe-Bloch equation. As the Landau distribution is asymmetrical, it is not a priori obvious which statistical estimator (mean, median, truncated mean etc. of the individual measurements) is best used to measure  $dE/dx$ . At H1, the individual hit

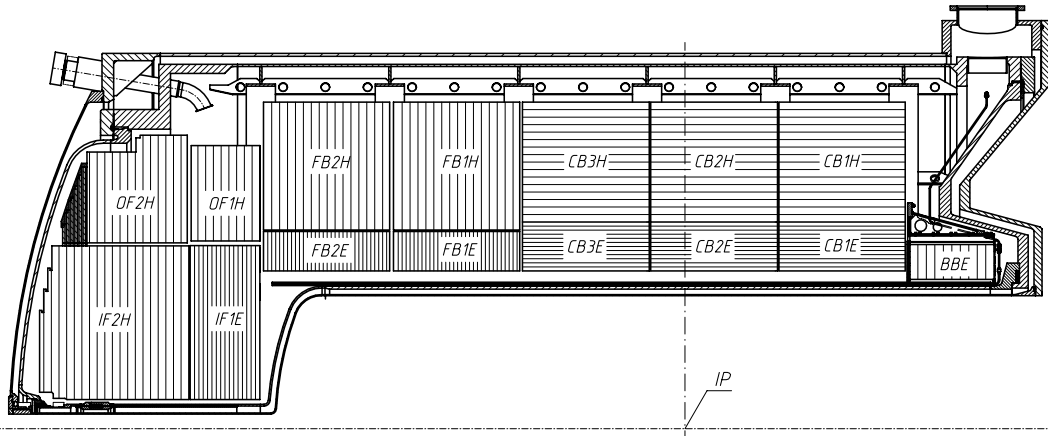


FIGURE 4.9: Longitudinal cross section through the upper half of the H1 liquid argon calorimeter. The various modules are designated by their respective abbreviations – modules with a designation ending in ‘E’ form the electromagnetic section and are equipped with lead absorbers, whereas modules ending in ‘H’ belong to the hadronic section and contain steel absorbers.

values are transformed as follows

$$\left(\frac{dE}{dx}\right)_i \longrightarrow \frac{1}{\sqrt{\left(\frac{dE}{dx}\right)_i}}, \quad (4.3)$$

which yields an approximately symmetric distribution. The mean of this distribution, transformed back, is then used as the  $dE/dx$  value to be compared with the Bethe-Bloch expectation:

$$\frac{dE}{dx} = \frac{1}{\left(\frac{1}{N_{hits}} \sum_{i=1}^{N_{hits}} \frac{1}{\sqrt{\left(\frac{dE}{dx}\right)_i}}\right)^2}. \quad (4.4)$$

The conversion factor from measured charge to  $dE/dx$  depends on the gain of the chamber, or more precisely, the individual wire. This gain in turn depends on such diverse factors as high voltage settings, space charges produced by beam related background, atmospheric pressure, temperature, gas composition etc. The gain is constantly monitored individually for both rings of the CJC using cosmic ray muons (“identified particles”) [174]. The  $dE/dx$  is corrected for these gain variations and stored in units of energy loss of minimum ionising particles (MIPs) at  $\vartheta$  of  $90^\circ$ .

## 4.4 Calorimetry at H1

### 4.4.1 The Liquid Argon Calorimeter

In the central and forward part, the H1 tracker is surrounded by a liquid argon (LAr) calorimeter [175]. The inner part of the calorimeter uses lead absorbers and detects electromagnetic showers whilst hadronic showers usually penetrate into the outer part which is equipped with steel absorbers. The LAr is equipped with a trigger system which sums energy deposits in certain regions of the calorimeter and compares them with thresholds.

### 4.4.2 The Spaghetti Calorimeter

In the backward direction, the H1 calorimetry is complemented by a lead-scintillating fibre Spaghetti Calorimeter (SpaCal, [176]) which is read out by photomultiplier tubes (PMTs). Its main purpose is the detection of the scattered electron for medium  $Q^2$  (2-100 GeV<sup>2</sup>) events.

## 4.5 Luminosity Measurement at H1

The luminosity delivered by HERA is determined by measuring the rate at which the Bethe-Heitler process ( $ep \rightarrow ep\gamma$ , [177]) occurs. This process has a well known and large cross section calculable in Quantum Electro Dynamics (QED). The photons are detected by a quartz-fibre calorimeter with tungsten absorber located at  $z = -103$  m [178]. The electron beam focusing magnets produce large amounts of synchrotron radiation, against which the photon calorimeter is shielded by two radiation lengths of beryllium. The uncertainty of the luminosity measurement is dominated by the uncertainty on the photon detector acceptance, which changes with different beam optics. The total uncertainty amounts to 1.5%.

## 4.6 Forward Instrumentation at H1

In the framework of this analysis, the detectors forward of the central tracker acceptance ( $\vartheta < 20^\circ$ ) are used to ensure the diffractive nature of the events (i.e. the existence of a rapidity gap) and to separate proton dissociative from elastic events. The forward part of the liquid argon calorimeter serves to this end both on trigger and reconstruction level down to  $\vartheta \approx 5^\circ$ . The FTi2 scintillating detector serves the same purpose in a similar angular range and is used as a veto on trigger level, whilst the plug calorimeter, the forward muon and forward tagging systems are used to tag proton dissociative events.

### 4.6.1 The FTi2 Scintillating Detector

With the HERA II luminosity upgrade, H1 was also equipped with an upgraded forward tracker. In the new setup, two rings of scintillators called FTi were supposed to replace the forward proportional chambers as a forward track trigger. The first ring (FTi1) is located between the central and forward trackers and read out by avalanche photo diodes (APDs), whilst the second ring (FTi2) is located between the forward tracker and the liquid argon inner forward calorimeter and read out by photomultipliers. Unfortunately, the FTi1 was never operational after its insertion into the detector and it has been inaccessible for repairs ever since. The use of the FTi2 as a veto for proton dissociative events was introduced into the triggers developed for [17] and this analysis. Later it was found out that a part of the technical drawings of this detector had been lost; whilst the dimensions of the 32 individual scintillator paddles are known, their precise placement is not and had to be reconstructed from photographs and using the position of clusters in the forward liquid argon calorimeter [179].

### 4.6.2 The Forward Muon Detector (FMD)

The forward muon detector consists of six double-layers of drift chambers forward of the H1 main detector. Three layers are located in front and three behind a toroid magnet, which provides the analysing power to measure the momentum of forward going muons. Both the pre- and the post-toroid sections consist of two  $\vartheta$ -chambers with the wires strung in octants



four level filter. On the first level (L1), specifically built hardware generates trigger signals from subsets of the information delivered by individual sub-detectors. On the second level (L2), the information available from L1 is combined in neural networks or using topological criteria. The third level was not yet operational in 2005; it attempts a partial event reconstruction on commercial processors. The fourth level finally runs on standard PCs, performs a full event reconstruction and selects events based on the reconstructed quantities. The Fast Track Trigger described in the second part of this thesis significantly enhances the first two trigger levels and adds an operational third trigger level.

### 4.7.2 Level 1

The first trigger level (L1, [181]) operates dead-time free, i.e. the data taking continues whilst the trigger decision is formed. During the L1 latency of  $2.3 \mu\text{s}$  (22 bunch crossings), data are written to pipelines. In parallel, algorithms implemented in hardware scan limited information from sub-detectors for interesting signals, e.g. muon tracks in the muon system, large energy deposits in the calorimeter or tracks in the central tracker. The sub-detectors derive a total of 256 *Trigger Elements* (TEs) from these signals and send them to the *Central Trigger Logic* (CTL). There, the TEs are combined via logical ANDs and ORs to up to 192 *Subtriggers* (STs). If a subtrigger condition is fulfilled, the pipelines are halted and the second level trigger starts its work.

The rates of subtriggers vary considerably with the instantaneous luminosity and the beam conditions. The L1 output rate should however remain in a narrow band to ensure that on one hand the higher trigger levels can cope with the input rate and on the other hand the available bandwidth is used to its best for physics data. This is achieved by *prescaling* subtriggers. A subtrigger with a prescale  $N$  will only trigger the event every  $N^{\text{th}}$  time it fires. A subtrigger that has its condition fulfilled is called *raw subtrigger*; if also the prescale condition is fulfilled, it is called *actual subtrigger*. With varying beam conditions, new prescales are calculated automatically according to a predefined strategy [182], giving triggers for rare processes more weight than those for processes with large cross sections, e.g. light vector meson production.

The Level 1 trigger also has to determine the bunch crossing of origin of a particular event, so the sub-detectors know, which pipeline position has to be read out. To this end, detectors with good timing resolution such as the CIP or the SpaCal generate so-called  $t_0$  trigger signals which mark the bunch crossing of origin.

### 4.7.3 Level 2

The second trigger level (L2, [183]) combines L1 information from various sub-detectors for a global decision. This is done using two different approaches, namely neural networks [184, 185] (which have been used to study  $\phi$  photoproduction in [186]) and a topological trigger, which combines signal from trackers, calorimeters and the muon system based on their origin in  $\vartheta - \varphi$ -space. The fast track trigger adds a third level 2 trigger, providing track information with a resolution comparable to that of the full offline reconstruction (see section 13.6).

The decision time available to the level 2 triggers is  $20 \mu\text{s}$ . During this time the data taking is stopped and dead-time accumulates. The trigger elements generated are again combined to subtriggers; the elaborate nature of the trigger decisions however usually leads to subtrigger conditions consisting of just one trigger element. Specific L2 subtriggers are used to validate specific L1 subtriggers; many L1 triggers do not have L2 conditions and are validated by default. If there is no positive L2 decision, the pipelines are cleared and the data taking is resumed, otherwise the detector is read out.

#### 4.7.4 Readout and Level 3

After a positive level 2 decision, the various H1 subsystems start their readout; usually a processor card reads the contents of the pipelines around  $t_0$ , performs a zero suppression and writes the data into a buffer in the H1 storage format BOS (Bank Object System, [187]). When all the data are read, the subsystem signals to the central trigger logic that it is ready again. As soon as all systems are ready, the pipelines are cleared and the data taking is resumed. The complete readout takes between 0.6 and more than 2 ms, depending on the size of the event; the average lies around 1.3 ms. This readout time is the major source of dead-time and the previous trigger levels have to ensure that it occurs with less than 50 Hz.

The third level trigger (L3) can abort the readout if its partial event reconstruction cannot validate the earlier trigger levels. This occurs about 100  $\mu\text{s}$  into the readout time and can thus reduce dead-time. The level 3 trigger was still in the commissioning phase when the data analysed in this thesis were taken, but it is fully operational since summer 2006 (see also section 13.7).

#### 4.7.5 Event-building and Level 4

After the subsystem readout is completed, all further steps happen asynchronously, i.e. decoupled from the data taking, whenever the relevant processors are available. In a first step, the subsystems write the contents of their buffers into the memory of another processor card (one per subsystem). These processors then send the subsystem event data via gigabit Ethernet [188] to the central event builder, where the complete raw data are assembled. These raw events are then sent to a farm of PCs, where the reconstruction program (*H1Rec*) is being run. Based on this full reconstruction events are filtered once more (the L4 trigger) and those containing objects of interest are stored on tape both with the full detector information (*POT*, Production Output Tape) and with reconstructed objects (tracks, clusters etc.) only (*DST*, Detector Summary Tape).

During the event reconstruction, calibration constants are extracted (e.g. the gain of the CJC) and applied to the data (e.g. to the  $dE/dx$  measurement in the CJC). The detector performance is constantly monitored, both automatically and via histograms which are available to the shift crew.

## Chapter 5

# Monte Carlo Modelling of Diffractive $\phi$ Meson Production

*Is 2 a random number?*

DONALD E. KNUTH [189]

*Probably the only non-random number in the known universe is 42 (the proof of this is left to the reader as an exercise).*

JOS VISSER [190]

The number of events observed in an experiment does not only depend on the luminosity and cross section of the relevant process, but also on the acceptance and efficiency of the detector. These quantities in turn depend on the detailed detector geometry, interactions of decay particles with the detector material, dead channels and many more details. The intricacies of the interaction of subatomic particles with a macroscopic detector elude analytical calculation and have to be computer modelled. In addition, also parts of the physics process, i.e. the hadronisation of the proton dissociative system are modelled rather than analytically determined. These models have in common that they are based on random sampling – they apply a *Monte Carlo* method.

In the context of this analysis (and most high energy physics analyses), the Monte Carlo simulation consists of three steps:

- *Generator*: The physics process under study is simulated by a dedicated program (DIF-FVM for this analysis) - the four-vectors of the stable particles produced are generated by randomly sampling the physical distributions.
- *Simulation*: The passage of particles through the material of the detector and the detector response are simulated using a program describing the detector (H1SIM) which in turn relies on a program package describing interactions with material (GEANT) which may in turn call specialised programs to simulate specific interactions (e.g. GHEISHA for nuclear interactions).
- *Reconstruction*: The detector output from the simulation is then subjected to a reconstruction which should be very nearly the same as in the data (H1REC) and produces the same output format, which is then available for analysis.

## 5.1 The DIFFVM Generator

All simulated events used for the present analysis were generated using the DIFFVM generator [44, 191]. It was written to simulate diffractive vector meson production at HERA in the framework of Regge theory and the Vector Dominance Model.

### 5.1.1 From Electrons to Photons to Vector Mesons

The program starts by generating a virtual photon according to the Weizsäcker-Williams approximation (section 2.2.5). Each photon is assigned a helicity  $\lambda$ , which is later used to determine the  $Q^2$  dependence of the cross section and the angular distribution of the vector meson decay particles. The diffractive  $ep$  cross section is calculated from the  $\gamma p$  cross section using the photon flux.

The transition from a transverse virtual photon to the vector meson is given by

$$\sigma_{\gamma^*p}^T = \sigma_{\gamma p}^\rho \left( \frac{1}{1 + \frac{Q^2}{\Lambda^2}} \right)^n, \quad (5.1)$$

with  $\Lambda = m_{VM}$ , the mass of the produced vector meson and  $\sigma_{\gamma p}^\rho$  the  $\rho^0$  photoproduction cross-section on protons.  $n$  is an adjustable parameter of the generator. The ratio of the longitudinal to the transverse cross section is parametrised as

$$\frac{\sigma_{\gamma^*p}^L}{\sigma_{\gamma^*p}^T} = R(Q^2) = \frac{\xi \frac{Q^2}{\Lambda^2}}{1 + \chi \xi \frac{Q^2}{\Lambda^2}}, \quad (5.2)$$

where  $\xi$  parametrises the  $Q^2$  dependence of  $R$  and  $\chi$  is a purely phenomenological parameter limiting  $R$  to  $1/\chi$  for  $Q^2 \gg \Lambda$ . For  $\Lambda = m_{VM}$  and  $\chi = 0$  this reduces to

$$\frac{\sigma_{\gamma^*p}^L}{\sigma_{\gamma^*p}^T} = R(Q^2) = \xi \frac{Q^2}{m_{VM}^2}. \quad (5.3)$$

### 5.1.2 Pomeron Exchange

DIFFVM simulates the interaction of the vector meson with the proton as the exchange of a pomeron. The exchange of the sub-leading meson trajectories is not simulated. The proton can either stay intact or dissociate in the interaction. The cross section is determined by the pomeron trajectory  $\alpha_{\mathbb{P}}(t) = \alpha_{\mathbb{P}}(0) + \alpha'_{\mathbb{P}}t = 1 + \epsilon + \alpha'_{\mathbb{P}}t$ :

$$\frac{d\sigma}{dt} = \left. \frac{d\sigma}{dt} \right|_{t=0, W=W_0} \cdot e^{-b|t|} \cdot \left( \frac{W}{W_0} \right)^{4\epsilon}, \quad (5.4)$$

with

$$b(W) = b(W_0) + 4\alpha'_{\mathbb{P}} \ln \left( \frac{W}{W_0} \right). \quad (5.5)$$

The values of  $\sigma(W_0) = \int_{t_{min}}^{t_{max}} \frac{d\sigma}{dt} dt$ ,  $b(W_0)$  and  $W_0$  are parameters that have to be provided by the user. The settings used are shown in table 5.1. The parameters  $n$ ,  $\chi$  and  $\xi$  were extracted by fits to DIS data, the cross section is taken from [47], which also defines the  $W_0$ . The pomeron trajectory was set to a standard intercept and no shrinkage in order to facilitate reweighting at a later stage. The values of  $b$  were chosen such as not to be statistically limited at high  $|t|$ .

Process	$\sigma_{\gamma p,0}$ [ $\mu\text{b}$ ]	$n$	$\Lambda$	$\xi$	$\chi$	$\epsilon^{gen}$	$\alpha_{\mathbb{P}}^{gen}$ [ $\text{GeV}^{-2}$ ]	$W_0^{gen}$ [ $\text{GeV}$ ]	$b^{gen}$ [ $\text{GeV}^{-2}$ ]
Elastic	0.96	2.4	$m_\phi$	0.42	1.11	0.0808	0.0	90.0	4.0
Proton dissociative	0.96	2.4	$m_\phi$	0.42	1.11	0.0808	0.0	90.0	1.5

 TABLE 5.1: DIFFVM *generator settings*.

### 5.1.3 Proton Dissociation

For diffractive dissociation of the proton, the proton remnant mass ( $M_Y$ ) spectrum is modelled according to

$$\frac{d\sigma}{dM_Y^2} \propto \frac{f(M_Y^2)}{M_Y^{2(1+\epsilon)}}, \quad (5.6)$$

where  $f(M_Y^2)$  models the cross section for low  $M_Y$ , including resonance states; For  $M_Y^2 > 3.6 \text{ GeV}^2$ ,  $f(M_Y^2) = 1$ , for lower masses  $f(M_Y^2)$  is obtained from a fit to the measured differential cross section for diffractive proton dissociation on deuterium  $pD \rightarrow XD$  at fixed  $t$  [192]. For the low mass states, the dissociative system is assumed to be one of the  $N^{*+}$  resonances  $N(1440)$ ,  $N(1520)$ ,  $N(1680)$  and  $N(1700)$ . For higher masses, it is treated as a quark-diquark system and the hadronisation is performed using the Lund string model (see e.g. [193] for a discussion of hadronisation models) as implemented in the JETSET program [194].

### 5.1.4 Helicity Distributions

The helicity angle (see section 2.2.4 for definitions of the helicity angles)  $\theta_h$  is generated according to the expectation of  $s$ -channel helicity conservation (SCHC). For  $\phi_h$  and  $\psi_h$ , flat distributions are generated.

## 5.2 Kinematical Distributions

For the present analysis, five million elastic and five million proton dissociative events were generated, simulated and reconstructed. The Monte Carlo samples were reweighted in three generated variables, namely  $m_{KK}$ ,  $t$  and  $W$ .

### 5.2.1 $\phi$ Meson Mass

The reweight in  $m_{KK}$  was necessary because DIFFVM uses a non-relativistic Breit-Wigner distribution [195]

$$BW(m_{KK}) = \frac{\Gamma_{\phi,0}^2/4}{(m_{KK} - m_\phi)^2 + \Gamma_{\phi,0}^2/4} \quad (5.7)$$

for the mass shape ( $\Gamma_{\phi,0}$  is the nominal  $\phi$  width). The actual shape is however a relativistic Breit-Wigner

$$rBW(m_{KK}) = \frac{m_{KK} m_\phi \Gamma_\phi}{\left(m_{KK}^2 - m_\phi^2\right)^2 + m_\phi^2 \Gamma_\phi^2} \quad (5.8)$$

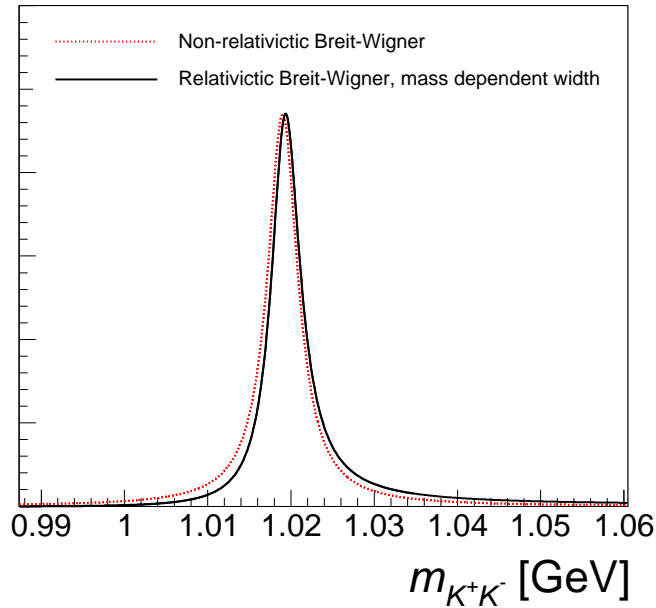


FIGURE 5.1: Comparison between a non-relativistic Breit-Wigner and a relativistic Breit-Wigner with mass dependent width.

with a mass dependent width [196]

$$\Gamma_\phi = \Gamma_{\phi,0} \left( \sqrt{\frac{m_{KK}^2 - 4m_K^2}{m_\phi^2 - 4m_K^2}} \right)^3 \left( \frac{m_\phi}{m_{KK}} \right). \quad (5.9)$$

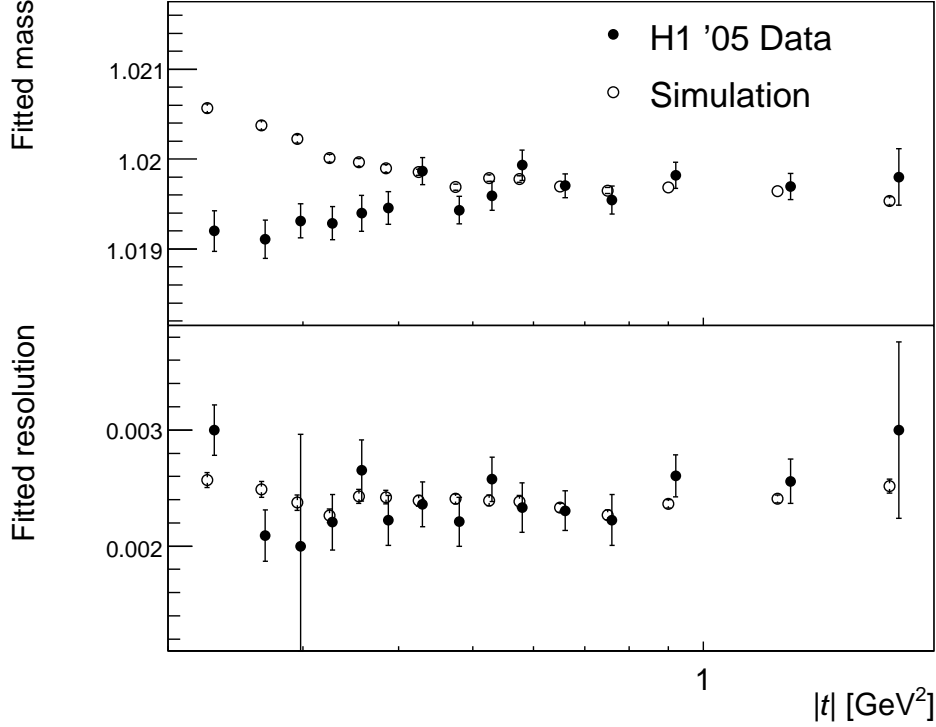
The Monte Carlo samples were correspondingly reweighted with a weight

$$w_m(m_{KK}) = \frac{rBW(m_{KK}) / \int_{2m_K}^{\infty} rBW(m_{KK})}{BW(m_{KK}) / \int_{2m_K}^{\infty} BW(m_{KK})}. \quad (5.10)$$

The relativistic Breit-Wigner distribution is skewed towards higher masses because it takes into account the phase-space available to the decay particles. In addition it naturally goes to zero at the boundary of the phase space  $m_{KK} = 2m_K$ .

### 5.2.2 Momentum Transfer at the Proton Vertex $t$ and Photon-Proton Centre of Mass Energy $W$

The  $t$ -dependence, the  $W$ -dependence and the  $W$ -dependence of the  $t$ -dependence (shrinkage) of the cross section are the main measurements of this thesis. For  $\phi$  photoproduction, they have not been measured with sufficient precision before. The Monte Carlo was thus generated with a standard  $W$  dependence (pomeron intercept  $\alpha_{\mathbb{P}}(0) = 1 + \epsilon = 1.0808$  [197]) and no shrinkage ( $\alpha_{\mathbb{P}}^{gen} = 0 \text{ GeV}^{-2}$ ). The generated  $t$  slopes were chosen smaller than the expected values in order to generate enough events at large  $|t|$  so as not to be limited by the statistical error of the Monte Carlo sample. The generated shape is a pure exponential ( $\frac{d\sigma}{dt} \propto e^{-b_0^{gen}|t|}$ ). In  $\rho^0$  photoproduction, a behaviour of the cross section according to


 FIGURE 5.2: *Fitted mass and resolution in data and simulation versus  $|t|$ .*

$\frac{d\sigma}{dt} \propto e^{-b_0|t|+b_0^2|t|^2/2a}$  is observed [17], whilst at higher  $|t|$ , the cross section follows a power law  $\frac{d\sigma}{dt} \propto |t|^{-a}$  [16]. Assuming that the  $\phi$  cross sections show the same behaviour as the  $\rho^0$  cross sections, the Monte Carlo events were reweighted to a shape

$$\frac{d\sigma}{dt} \propto e^{a \ln(1+b_0|t|/a)} \quad (5.11)$$

which interpolates smoothly between the exponential and power law regimes. The full reweight in  $W$  and  $t$  takes the form

$$w_{Wt}(W, t) = \frac{\sigma_{\gamma p,0} \cdot e^{a \ln(1+b_0|t|/a)} \cdot b_0 \cdot \left(\frac{W}{W_0}\right)^{4(\epsilon+\alpha'_p t)}}{\sigma_{\gamma p,0}^{gen} \cdot e^{b_0^{gen}} \cdot b_0^{gen} \cdot \left(\frac{W}{W_0^{gen}}\right)^{4(\epsilon^{gen}+\alpha'_p{}^{gen} t)}} \quad (5.12)$$

The exponent  $a$  was taken from a measurement of  $\rho^0$  photoproduction [21] and set to 23.0 for elastic and 6.0 for proton-dissociative  $\phi$  production, whilst the slope parameters  $b_0$  and total cross sections were taken from ZEUS measurements [47, 198] and adjusted within errors to better fit the present data. The standard Donnachie-Landshoff parameters were used for the pomeron trajectory.

### 5.3 Detector Simulation with H1SIM and GEANT

Starting from the four-vectors generated by DIFFVM, the particles emerging from the  $ep$  collision are tracked through the H1 Detector by the H1SIM program, which is based on

the GEANT 3 program [199]. Electromagnetic interactions and the detector response are simulated by GEANT routines whilst nuclear interactions are simulated by the GEISHA program. In order to obtain a good description of the track parameters measured in the CJC, the amount of material between the beamline and the tracking detectors has to be very well modelled<sup>1</sup>.

Figure 5.2 shows that there is a difference in reconstructed mass for small transverse momenta; this seems to be mainly due to missing material in the simulation, as the slope there is largest. The detector resolution (dominated by energy loss and multiple scattering) on the other hand seems to be well described.

### 5.3.1 Simulation of Nuclear Interactions with GEISHA

The GEISHA program [200] was developed in the late 1970ies to simulate the response of hadronic calorimeters. In H1SIM it is used to model interactions of hadrons with nuclei of the detector material. GEISHA uses a fragmentation mechanism at kinetic energies above 500 MeV, for both interactions on free nucleons and intra-nuclear cascades. This model has one free parameter which was fitted to the data. At low energies, an optical model is used to predict elastic and inelastic cross sections. In the intermediate region (which is the region of interest for the present work) interpolations have been developed, “...which do not necessarily fit the data on nuclear interactions, but are sufficient to predict results on calorimetry” [200]. For studies of tracking in this energy range, a good description of the energy dependence of the cross section in the range from  $\approx 100$  to 500 MeV is highly desirable. Especially the prominent resonances in the negative kaon – proton cross section need to be modelled. This problem has been tackled with a study of nuclear interactions in the material between the two rings of the central jet chamber, see section 8.3.3.

---

<sup>1</sup>Due to technical reasons, the detector model used to determine the energy loss in the simulation is not the same as the one used for energy loss corrections in the reconstruction.

# Chapter 6

## Trigger and Data Selection

*Misura ciò che è misurabile, e rendi misurabile ciò che non lo è.*

GALILEO GALILEI

### 6.1 Triggers for $\phi$ Photoproduction

The aim of this thesis is to study the elastic photoproduction of  $\phi$  mesons. The corresponding events have a very unspectacular signature in the H1 main detector: two tracks with low transverse momentum and an invariant mass close to threshold. Many of the new possibilities offered by the FTT were used to select these events online over a vast amount of background.

#### 6.1.1 A FTT Based $\phi$ Trigger for Level 1

The level 1 trigger condition (assigned the subtrigger number 12, s12 for short) for the  $\phi$  triggers in 2005 was the following:

```
CIP_TO && CIP_sig > 2 && CIP_mul < 6 && !LAr_IF &&  
FTT_mul-Ta > 1 && FTT_mul-Ta < 4 && FTT_Qtot > 2 && FTT_Qtot < 6 &&  
FTT_topo_7 && FTT_seg &&  
!SPCLh_AToF_E_1 && !SPCLh_ToF_E_2 && !VETO_BG && !BToF_BG && !SToF_BG &&  
!FTI2_G1
```

Where the individual conditions denote the following:

- CIP\_TO: The CIP (see section 4.3.1) trigger has determined the event timing (bunch crossing of origin).
- CIP\_sig > 2: The  $z$ -vertex histogram of the CIP has more than four times more entries in the central region than in the backward region. This condition suppresses proton-rest gas and proton-wall interactions upstream of the nominal interaction point.
- CIP\_mul < 6: There are less than 30 valid track patterns seen in the CIP. This condition suppresses high multiplicity events (mostly non- $ep$  interactions).
- !LAr\_IF: The energy sum of all clusters with more than 0.8 GeV in the inner forward partition of the liquid argon calorimeter is below 2 GeV. This cut suppresses non-diffractive events and proton-dissociative events with a large mass  $M_Y$  of the proton remnant.

- `FTT_mul-Ta > 1 && FTT_mul-Ta < 4`: The number of tracks with a transverse momentum above 100 MeV seen by the FTT is either 2 or 3. Only two tracks are expected, the level 1 FTT, however, occasionally double-counts tracks if momentum ambiguities cannot be resolved in the linking step.
- `FTT_Qtot > 2 && FTT_Qtot < 6`: The charges of the FTT tracks sum up to -1, 0, or +1. If there are two or three FTT tracks of the same (usually positive) charge (as is often the case in proton-nucleus interactions from beam-gas and beam-wall collisions), the event is rejected.
- `FTT_topo_7`: The FTT tracks are located within three adjacent sectors in  $\varphi$  in a tenfold segmentation. This and the following condition are discussed in more detail in the next sub-section.
- `FTT_seg`: There is at least one FTT track segment in FTT layer three or four.
- `!SPCLh_AToF_E_1 && !SPCLh_ToF_E_2 && !VETO_BG && !BToF_BG && !SToF_BG`: None of a variety of timing sensitive detectors indicates that the event is of non- $ep$  origin. The detectors are:
  - The hadronic SpaCal,
  - the large veto wall,
  - the backward ToF scintillators,
  - the SpaCal ToF scintillators.
- `!FTI2_G1`: There is no signal in the FTi2 detector (see section 4.6.1).

The  $\phi$  trigger is based largely on the  $\rho$  trigger developed in [17]. In order to reach low values of  $|t|$ , the threshold for the FTT tracks was however lowered from 160 to 100 MeV transverse momentum. The rate of  $\rho$  production is much higher<sup>1</sup> than the rate for  $\phi$  production; consequently additional conditions had to be added to enrich  $\phi$  mesons and to obtain thus a sizeable data sample within the bandwidth constraints.

### Topological FTT Conditions

The low momentum of the  $\phi$  decay kaons in the  $\phi$  rest frame produces two tracks with a narrow opening angle in the laboratory system if the  $\phi$  is slightly boosted. The topological trigger of the FTT at level 1 (see section 13.4.6) allows to use this narrow opening angle to discern  $\phi$  mesons from  $\rho$  mesons and other heavier states. The condition `FTT_topo_7` demands that the FTT tracks all lie within three adjacent sectors in a tenfold segmentation in  $\varphi_3$ . The angle  $\varphi_3$  is not measured at the vertex, but at the radius of the third FTT layer, leading to differences between in- and out-bending topologies. The sectors are located at fixed angles in  $\varphi_3$ ; the trigger condition starts to accept events from an angular difference between the two tracks at the third layer of  $108^\circ$  and becomes fully effective if the opening angle is below  $72^\circ$ .

In test runs during the setup phase of the trigger it was found that the above condition enriches  $\phi$ s, but also very low transverse momentum tracks which curl back to the beam pipe and are counted twice by the FTT (see figure 6.1 for an event display). As these events took up almost half of the available bandwidth, the additional condition `FTT_seg` was added. This trigger element was modified for this purpose and now demands that at least one segment was seen in FTT layers three or four, i.e. that at least one track reaches out to a radius of 40 cm.

<sup>1</sup>Assuming a universal pomeron, the  $\rho$  cross section is 9/2 of the  $\phi$  cross section. The difference in the visible rate of two track events is however dominated by the larger momentum of the decay pions of the  $\rho$  which produces detectable events down to  $|t| = 0 \text{ GeV}^2$ , whereas the  $\phi$  decay Kaons do not penetrate into the jet chamber for  $|t|$  below  $\approx 0.1 \text{ GeV}^2$ .

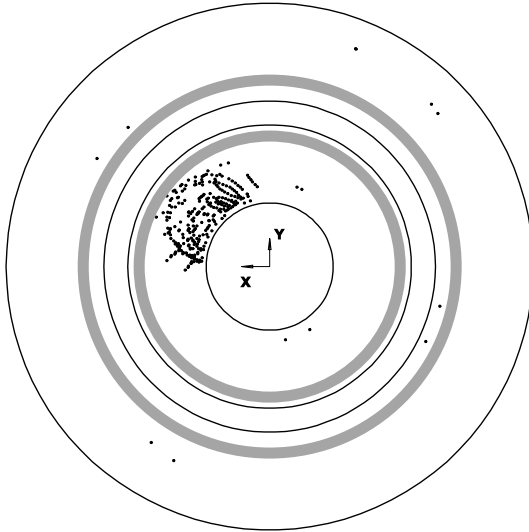


FIGURE 6.1:  $r - \phi$  view of a typical event with the hits produced by a single, very low transverse momentum curling track in the H1 central tracker. The FTT reconstructs both the outward- and the inward-going part of the curler. The topology condition enriches events of this type, as the tracks are close together in azimuthal angle. The condition of at least one segment in FTT layers three or four (shaded in grey), removes these events.

The complete trigger was in operation from H1 run 411314 (April 22<sup>nd</sup> 2005) onward. The raw rate was between  $\approx 20$  and  $\approx 100$  Hz depending on the beam currents and quality. For high luminosities, the trigger was prescaled by factors above 1000, leading to negligible output rates whereas towards the end of luminosity fills the diffractive vector meson triggers are attributed most of the free bandwidth (up to 10 Hz for the  $\phi$  trigger). The average prescale for s12 over the analysed period was 10.63.

### 6.1.2 A FTT Based $\phi$ Trigger for Level 2

During the 2005 data taking period, the level 2 FTT became fully operational. In order to test and monitor the level 2 system performance, a test trigger based on s12 was set up and assigned the subtrigger number 51. It has the same level 1 condition as s12 and in addition asks for precisely two FTT tracks on level 2. The resulting trigger proved to be very successful, as it provided a significant rate reduction (by a factor of 2 to 10, depending on background conditions) at an efficiency above 90% compared to the level 1 trigger. It has now superseded s12 as the main  $\phi$  trigger. During the data taking period considered in this thesis, both triggers were running concurrently with varying prescale strategies, resulting in an average prescale of 7.72 for s51.

For data taken after September 2006, the s51 trigger was tightened using a FTT level 2 invariant mass condition (see chapter 15).

### 6.1.3 The Level 4 $\phi$ Finders

On the H1 filter farm (level 4 trigger) two finders are used to recognise  $\phi$ s. The main finder is an algorithm designed to identify  $\rho$ s, it cuts on the following quantities:

- There is a reconstructed primary vertex.

- This vertex is located between  $z = -50$  and  $+50$  cm.
- There are exactly two vertex fitted tracks.
- The invariant mass of the two tracks under a charged pion hypothesis is smaller than 4 GeV.
- The maximum cluster energy not associated to one of the tracks is smaller than 600 MeV.

For parts of the data taking period, this finder was not applied to the  $\phi$  subtriggers and  $\phi$  events were instead saved by a dedicated  $\phi$  finder developed in [186]. The conditions applied are similar, with the exception that the  $\phi$  finder does not cut on the unassociated energy but has an upper mass limit of 1.06 GeV under a charged kaon hypothesis.

Events which fail to satisfy any of the finder criteria are saved only every  $10^{th}$  or  $60^{th}$  time and are assigned a corresponding weight, which is stored in the event data.

## 6.2 Run Selection

### 6.2.1 Run Selection for s12

The data considered in this analysis were taken in a period from August to November 2005, when HERA was operated with electrons. The beginning is marked by the introduction of the final setup of the subtrigger s12 and a switch in the threshold applied in the FTT  $Qt$ -algorithm (see section 13.4.1). At the end of the period, HERA and H1 were shut down for repairs one last time in order to prepare them for the final run from spring 2006 to summer 2007. During the data taking period, the gain of the CJC was raised twice, subdividing the run range into a *low-gain*, *medium-gain* and *high-gain* period.

Within the run range specified above (H1 runs 421402 - 436893), three periods were excluded from the analysis of s12:

- Runs 422373-426100: The FTT level 1 topological trigger was incorrectly loaded, turning it into a  $\phi$  veto.
- Runs 429944-429969: These runs were used for tests before the CJC gain was increased for the first time.
- Runs 435323-435950: The exchange of a pump led to a gas leak in the CJC, dramatically decreasing the gain due to a large oxygen content in the chamber gas.

### 6.2.2 Run Selection for s51

The s51 subtrigger data set is analysed for the run range 430500 to 436893, where two periods were excluded:

- Runs 435323-435950: The same CJC gas leak as above.
- Runs 435657-435800: A faulty firmware update decreased the FTT level 2 efficiency.

### 6.2.3 Common Run Selection

In the run ranges mentioned in the previous section, runs with more than  $0.1 \text{ nb}^{-1}$  luminosity were selected if they have all relevant detector components at nominal high voltage and read out. The detector components are: CJC, CIP, LAr, SpaCal, ToF, LUMI, FMD, FTS. In addition the FTT is required to be read-out so that monitoring information is available.

Sample	s12			s51				Total lumi [nb <sup>-1</sup> ]
	run lumi [nb <sup>-1</sup> ]	pre- scale	corrected lumi [nb <sup>-1</sup> ]	run lumi [nb <sup>-1</sup> ]	pre- scale	overlap fraction [%]	corrected lumi [nb <sup>-1</sup> ]	
Low gain	10947	13.8	795	–	–	0	–	795
Med. gain	9997	8.4	1185	10006	5.5	32	1232	2417
High gain	16254	10.7	1519	16011	10.2	20	1266	2785
<b>Total</b>	<b>37198</b>	<b>10.63</b>	<b>3500</b>	<b>26017</b>	<b>7.72</b>	<b>26</b>	<b>2498</b>	<b>5998</b>

TABLE 6.1: *Luminosities of the various subsamples.*

## 6.3 Luminosity Determination

The luminosity seen by prescaled triggers can be determined in two ways: Either the total luminosity seen by the experiment is taken and each event is assigned a weight according to the prescale or the total luminosity is divided by the average prescale. For the present analysis, the second method was chosen.

The s51 and s12 data samples are not necessarily disjoint and some care has to be taken to prevent double-counting or a wrong luminosity determination. To this end, the samples are combined with the following procedure:

- The s12 sample is taken as such, with the luminosity given by the H1 luminosity divided by the prescale.
- The fraction of events appearing in both samples is determined for each run.
- All events also triggered by s12 are removed from the s51 sample.
- The prescale corrected luminosity for s51 is reduced run wise by the overlap fraction.

The luminosities in the final sample can be found in table 6.1. In total there are 2'602'823 events entering the analysis, corresponding to a luminosity of 5998 nb<sup>-1</sup>.

## 6.4 Reconstruction of Kinematic Quantities

In diffractive  $\phi$  photoproduction, the only detected final state particles are the  $\phi$  decay kaons. All kinematic quantities have to be reconstructed from the two kaon tracks and the knowledge about the incoming beam particles. It is therefore important to get the best possible track information from the two kaons.

### 6.4.1 Energy Loss Corrections

For the vertex fit and the final determination of the track parameters at the vertex, the energy lost between the vertex and the tracking detectors has to be taken into account (see also section 4.3.3). This correction relies on a hypothesis for the mass of the particle responsible for the track. In H1, all corrections are done under a pion assumption. For kaons, especially at low momenta, the corrections are much bigger. This leads to a distortion of the reconstructed kinematic quantities; e.g. the reconstructed  $\phi$  mass depends on  $|t|$ . For the present analysis, several methods were tried to correct for this effect. In the end, an improved version of the reconstruction software became available and all the data were reprocessed using a kaon hypothesis, finally giving a momentum independent reconstructed mass and a reduced width of the  $\phi$  peak (see figure 6.2).

The correction methods tested are briefly described in the following; they are all based on the energy loss code of the reconstruction program, applied in different ways:

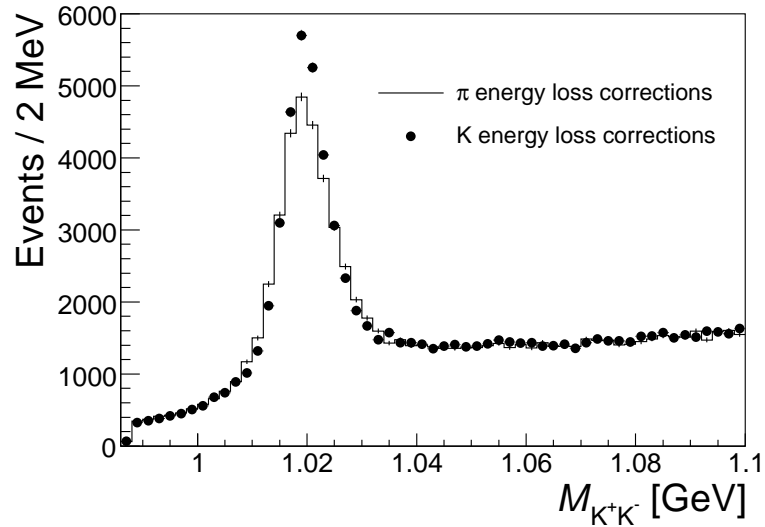


FIGURE 6.2: *Di-kaon invariant mass distribution with pion and kaon energy loss corrections.*

- *Energy loss correction on vertex fitted tracks:* For vertex fitted tracks, the uncorrected parameters were estimated in an iterative procedure starting with the pion-corrected parameters. Starting from a guess at the size of the original corrections, they were adjusted such that the pion-hypothesis correction of the uncorrected parameters yielded the corrected parameters the algorithm started with. Then kaon-hypothesis corrections were applied. This procedure tends to over-correct the energy loss. This can be understood from the fact that the vertex fit is dominated by the beam line constraint and thus forces the vertex to the “right” position, thus partially correcting the parameters.
- *Energy loss correction on non vertex fitted tracks:* In the next attempt the same algorithm was applied to non vertex-fitted tracks. This gave no improvement, as the powerful constraint of the beam line in the vertex fit is missing.
- *Energy loss correction on non vertex fitted tracks with subsequent vertex fit:* Refitting the corrected tracks in the transverse plane using a beam line constraint using the SVFIT package [201] gave good results, only a weak kinematic dependence was left.
- *Re-reconstruction using a Kaon hypothesis:* The H1REC reconstruction program was modified such that a kaon (or any other) mass hypothesis can be used for the energy loss corrections [202]. This gives excellent results, also confirming that the material description used for the corrections is very close to the actual material distribution in the detector.

The  $|t|$  dependence of the reconstructed  $\phi$  mass for the various correction methods is shown in figure 6.3.

The description of the detector material and the energy loss within it in the simulation is rather precise; fits to the reconstructed  $\phi$  peaks for data and simulation reproduce the measured mass to better than 0.5 MeV precision and the detector resolution to better than 100 KeV.

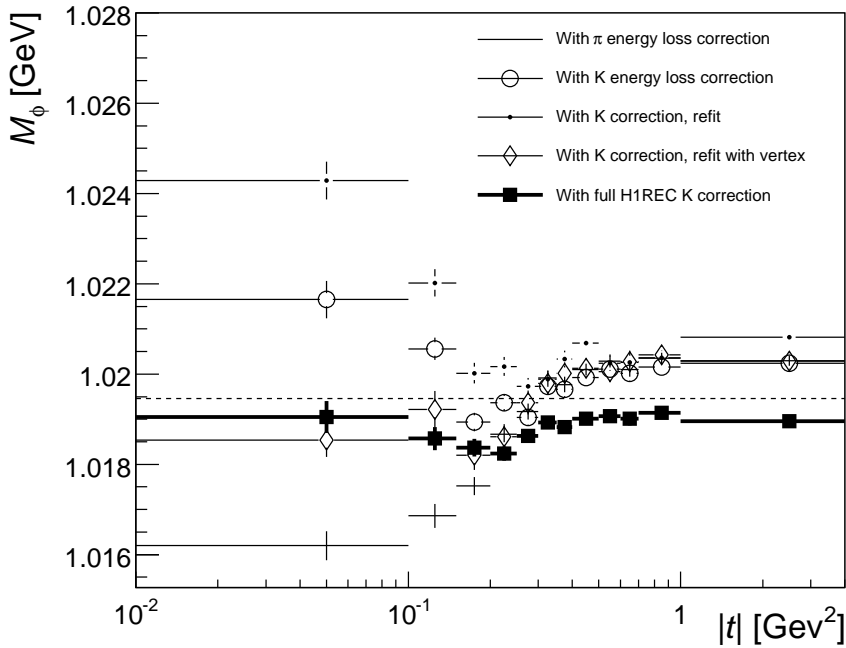


FIGURE 6.3:  $|t|$  dependence of the reconstructed  $\phi$  mass for various energy loss correction algorithms. The dashed line represents the nominal  $\phi$  mass.

## 6.4.2 Kinematic Variables and their Resolution

### Four momentum transfer at the electron vertex $Q^2$

In deep inelastic scattering events, the value of  $Q^2$  is reconstructed from the scattered electron:

$$Q^2 = 2EE'(1 + \cos \vartheta_e) \quad (6.1)$$

with  $E$  being the beam electron energy (27.6 GeV),  $E'$  the measured energy of the scattered electron and  $\vartheta_e$  its polar angle. The backward calorimeter (SpaCal) can detect electrons down to scattering angles of approximately  $4.5^\circ$  ( $\vartheta_e < 175.5^\circ$ ) corresponding to a minimum  $Q^2$  of about 2.5 GeV<sup>2</sup>. Events with smaller  $Q^2$  are considered as “photoproduction”-events whereas events with a larger  $Q^2$  are treated as background in the present analysis.

### Reconstruction of the $\phi$ four-momentum

The kinematics of the  $\phi$  mesons are reconstructed from the decay kaon momenta reconstructed in the H1 central tracker. If the momenta of the positive and negative kaon are denoted by  $p_+^{\vec{}}$  and  $p_-^{\vec{}}$ , their four-momenta are  $p_+ = (\sqrt{m_K^2 + |p_+^{\vec{}}|^2}, p_+^{\vec{}})$  and  $p_- = (\sqrt{m_K^2 + |p_-^{\vec{}}|^2}, p_-^{\vec{}})$ . The four-vector of the  $\phi$  meson is trivially reconstructed as follows:

$$p_\phi = p_+ + p_- \quad (6.2)$$

The  $\phi$  candidate mass is then

$$m_\phi = \sqrt{E_\phi^2 - |\vec{p}_\phi|^2} \quad (6.3)$$

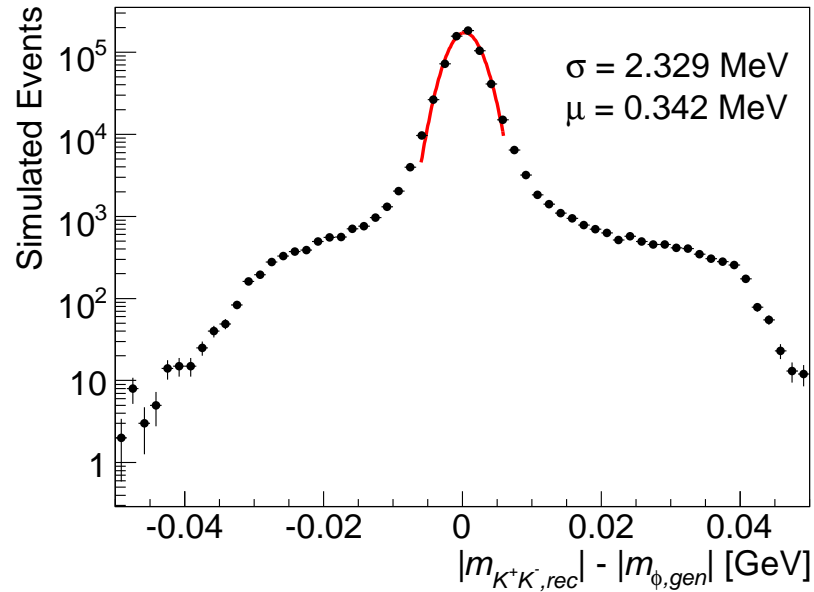


FIGURE 6.4: Difference between the reconstructed di-kaon and the generated mass for simulated events passing all selection cuts. The fit is a Gaussian, yielding the indicated width  $\sigma$  (experimental mass resolution) and mean  $\mu$ .

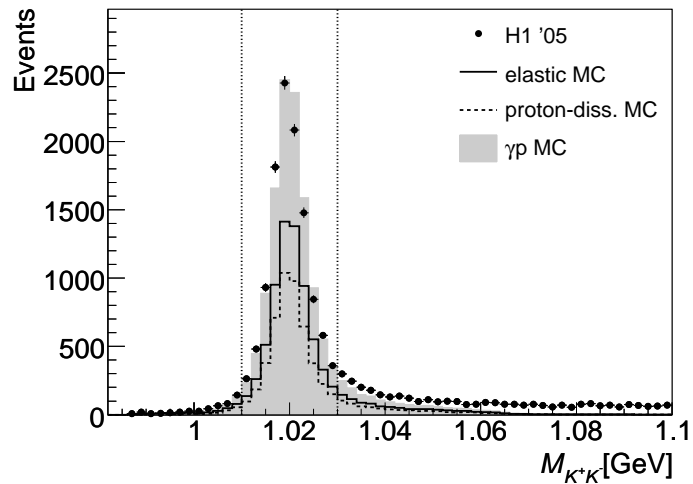


FIGURE 6.5: Invariant mass distribution for kaon pairs after applying all selection cuts. Note that the simulated peak is at a slightly higher mass than the peak in the data whilst the resolution is well described. The shaded area denoted by  $\gamma p$  is the sum of the elastic and proton-dissociative contributions indicated by the lines. The vertical dashed lines indicate the region from 1.01 to 1.03 GeV shown in the plots for the other kinematic quantities.

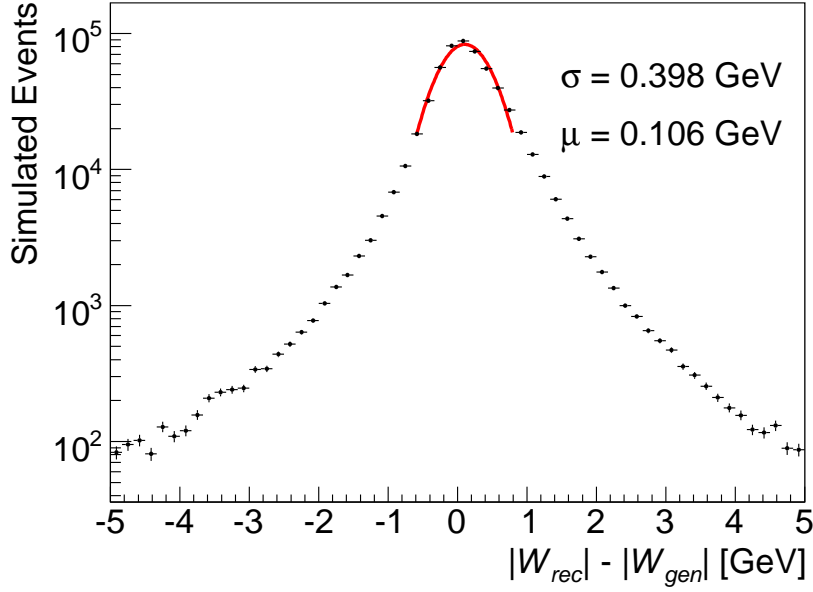


FIGURE 6.6: *Difference between the reconstructed and the generated  $W$  for events passing the  $\phi$  selection cut and having a di-kaon mass between 1.01 and 1.03 GeV. The fit is a Gaussian, yielding the indicated width  $\sigma$  (experimental mass resolution) and mean  $\mu$ .*

The mass resolution was studied using Monte Carlo events; a comparison of the generated and reconstructed mass can be seen in 6.4. The resolution determined from a fit to the difference distribution is in good agreement with the resolution obtained from fitting the  $\phi$  meson shape (see section 10.1 for details of the fit). As can be seen in figure 6.5, the peak position is shifted to higher masses by about 0.5 MeV in the simulation, compare also section 5.3.

#### $\gamma p$ centre of mass energy $W$

For low values of  $Q^2$ , the transverse momentum of the exchanged photon can be neglected; the longitudinal momentum is then  $-E_\gamma$ . Energy- and longitudinal momentum conservation can then be written as<sup>2</sup>:

$$E_\gamma + E_p = E_\phi + E_{p'} \quad (6.4)$$

$$p_{z,\gamma} + p_{z,p} = p_{z,\phi} + p_{z,p'}. \quad (6.5)$$

The beam protons have only longitudinal momentum. As they are scattered under small angles, also the outgoing protons have mainly longitudinal momentum and  $E_{z,p'} \approx p_{z,p'}$ . Combining equations (6.4) and (6.5) we obtain:

$$E_\gamma - p_{z,\gamma} = 2E_\gamma = E_\phi - p_{z,\phi}. \quad (6.6)$$

$W$  is defined as (see section 2.2.2)  $W^2 = (p_p + p_\gamma)^2$ . Using equation (6.6),  $W$  can be written as

$$W^2 \approx 4E_\gamma E_p \approx 2(E_\phi - p_{z,\phi}) E_p. \quad (6.7)$$

<sup>2</sup>Quantities indexed with  $p$  refer to the beam protons, those with  $p'$  to the scattered proton or the proton remnant  $Y$ .

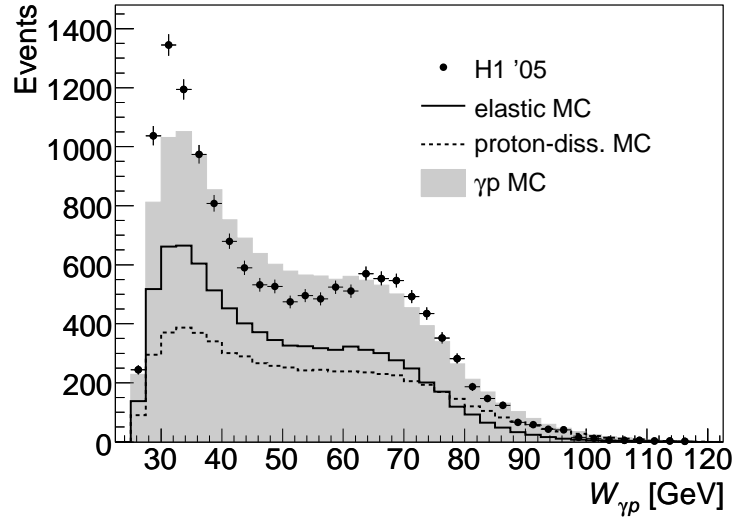


FIGURE 6.7: The photon-proton centre of mass energy  $W$  for all events fulfilling the selection cuts.

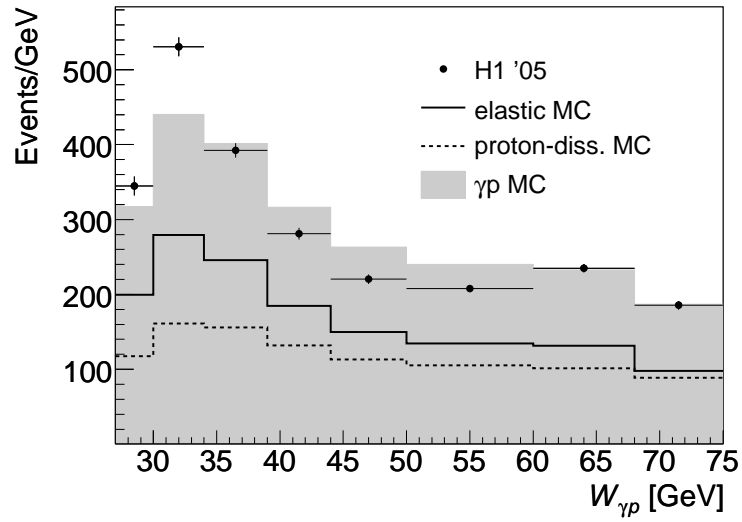


FIGURE 6.8: The number of  $\phi$  meson events in bins of the photon proton centre of mass energy  $W$ .

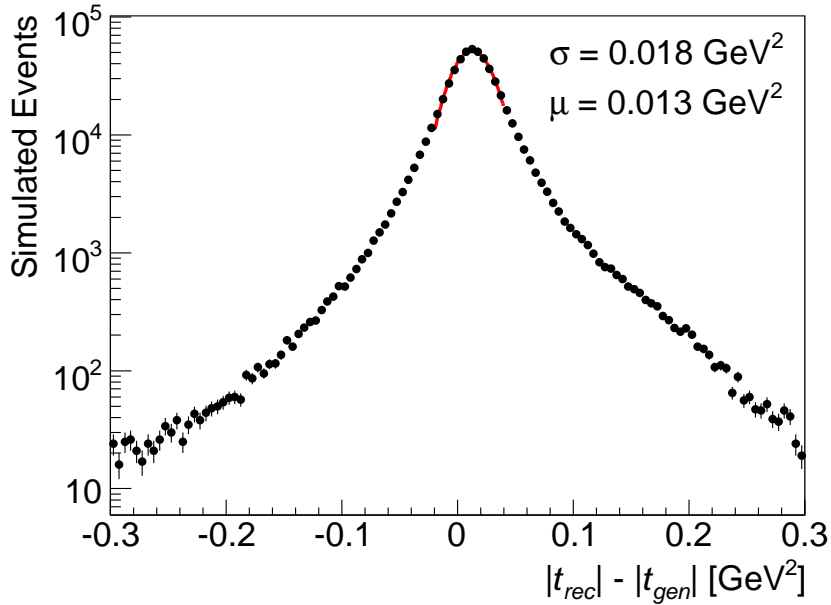


FIGURE 6.9: *Difference between the reconstructed and the generated  $|t|$  for simulated events passing the  $\phi$  selection cut and having a di-kaon mass between 1.01 and 1.03 GeV. The fit is a Gaussian, yielding the indicated width  $\sigma$  (experimental mass resolution) and mean  $\mu$ .*

The  $W$  reconstructed thus is compared to the generated value for MC events in figure 6.6. The comparison of measured and simulated  $W$  spectra (figures 6.7 and 6.8) shows an excess of data events at low  $W$  and a lack of such events at medium  $W$ , which is not fully understood.

#### Four-momentum transfer at the proton vertex $t$

The four-momentum transfer at the proton vertex  $t$  can be expressed in the  $Q^2 \approx 0$  and  $E_\gamma \approx -p_{z,\gamma}$  approximation as:

$$\begin{aligned}
 t &= -Q^2 - 2p_\gamma p_\phi + m_\phi^2 \\
 &\approx -2E_\gamma(E_\phi + p_{z,\phi} + m_\phi^2) \\
 &\approx -(E_\phi - p_{z,\phi})(E_\phi + p_{z,\phi}) \\
 &\approx -p_{T,\phi}^2.
 \end{aligned} \tag{6.8}$$

The approximation  $Q^2 = 0$  is of course not strictly true and especially for  $\phi$  mesons reconstructed at higher  $|t|$ , there can be a significant contribution to the  $\phi$  transverse momentum from a non-zero  $Q^2$ . As can be seen in figures 6.9 to 6.10, the reconstruction of  $t$  is not strongly affected by this and the contribution from events with a significant  $Q^2$  remains small even for high  $t$  (see figure 6.11). The  $Q^2$  contribution however has to be taken into account for helicity studies.

The simulated  $t$  spectra are compared to the data in figures 6.12 and 6.13, showing a good agreement.

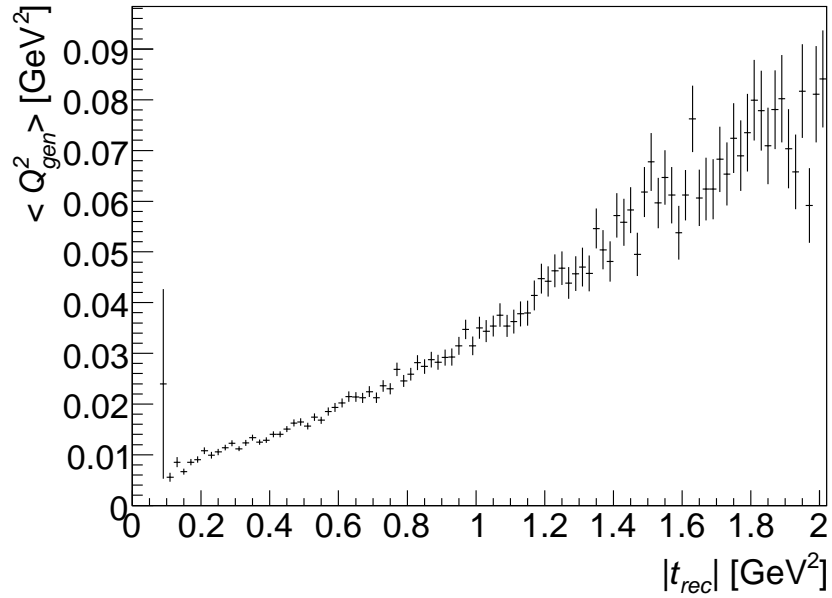


FIGURE 6.10: Average generated  $Q^2$  versus reconstructed  $|t|$  for simulated events passing the  $\phi$  selection cut and having a di-kaon mass between 1.01 and 1.03 GeV.

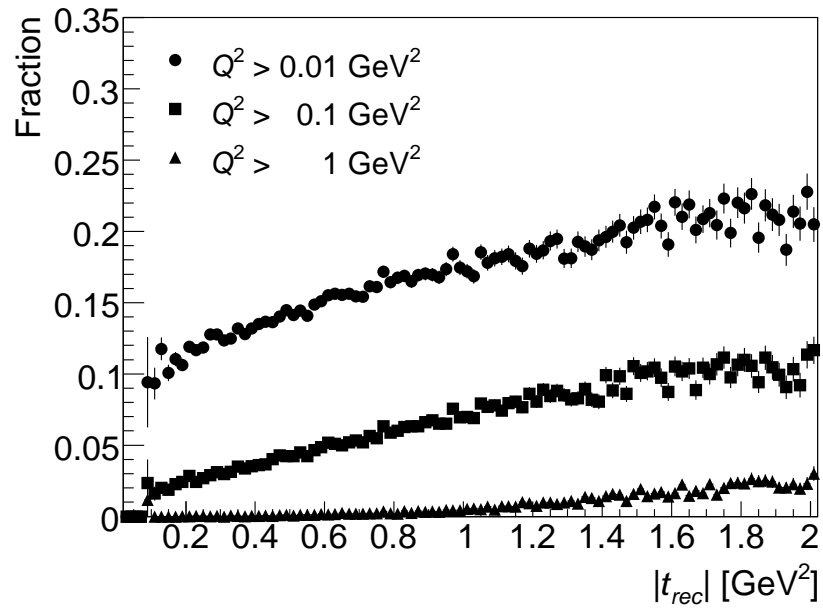


FIGURE 6.11: Fraction of events with a  $Q^2$  above 0.01, 0.1 and 1 GeV versus reconstructed  $|t|$  for simulated events passing the  $\phi$  selection cut and having a di-kaon mass between 1.01 and 1.03 GeV.

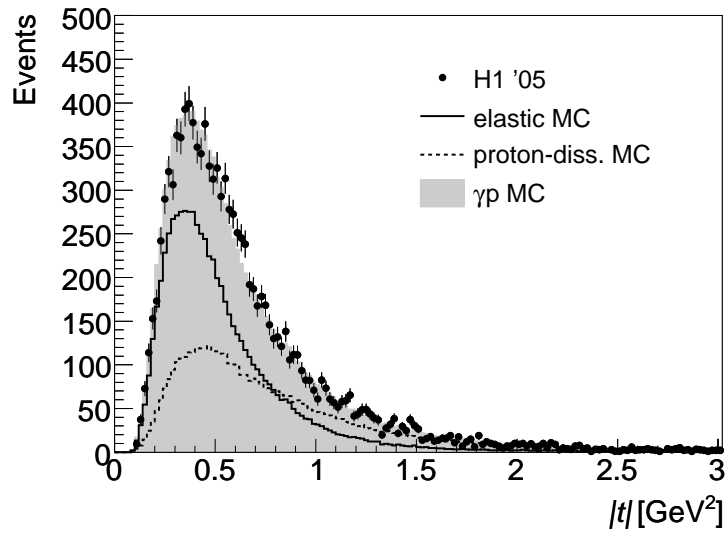


FIGURE 6.12: *The squared four momentum transfer at the proton vertex  $|t|$  for all events fulfilling the selection cuts.*

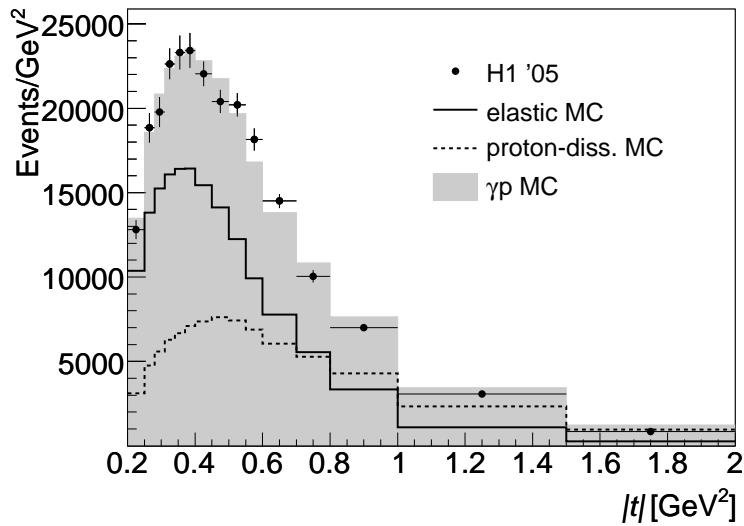


FIGURE 6.13: *The number of  $\phi$  meson events in bins of the squared four momentum transfer at the proton vertex  $|t|$ .*

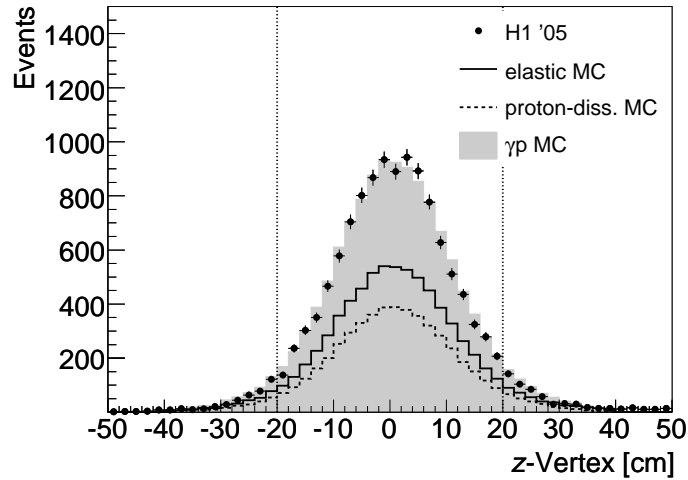


FIGURE 6.14: *Distribution of the  $z$  vertex of the selected events. The cut at  $\pm 20$  cm is indicated by the dashed lines.*

## 6.5 Event Selection

The events triggered by the subtriggers s12 and s51 within the selected run ranges were subjected to the analysis cuts described in the following in order to select diffractively photoproduced  $\phi$  mesons.

### 6.5.1 Event Properties

#### No Scattered Electron

In photoproduction, the electron is scattered under low angles and not seen in the main H1 detector. Events containing a scattered electron were thus excluded from the analysis. Due to the steep fall of the cross section with  $Q^2$ , this cut excludes only 1.3% of the recorded events.

#### $z$ -Vertex

The events are required to have a reconstructed primary vertex not more than 20 cm away from the nominal interaction point. This cut suppresses events originating from interactions of one of the beams with the rest gas in the beam pipe or the beam pipe itself. Whilst the  $z$  vertex distribution of  $ep$  interactions is centred in the nominal interaction point and has a width<sup>3</sup> of about 8 cm, beam gas interactions are spread equally along the  $z$  axis. The amount of non- $ep$  and satellite background<sup>4</sup> can be estimated by fitting the  $z$ -vertex distribution with a Gaussian and a constant term. The constant term turns out to contribute less than 1.5% to the total number of events in the selected region.

<sup>3</sup>Due to small variations in the beam timing, the centre of this distribution can be displaced from the nominal position by a few cm for a luminosity fill. Averaging over many fills yields the distribution shown in figure 6.14 with a width of 11.5 cm.

<sup>4</sup>This is the contribution from protons in so-called satellite bunches (earlier and later buckets of the accelerating radio-frequency system) with the electron beam.

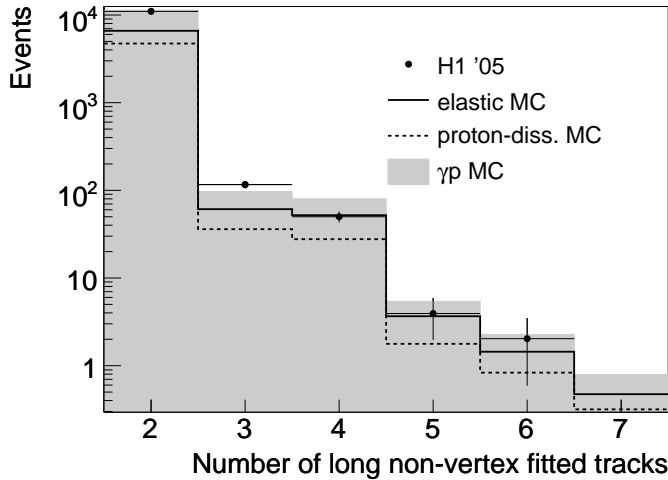


FIGURE 6.15: Number of non-vertex fitted tracks with a start radius below 25 cm and an end radius above 38 cm for all events passing the other selection criteria. Note that this number includes the two tracks that are fitted to the vertex in a later stage.

### Track Multiplicity

As the  $\phi$  decay to two charged kaons is studied, the events are required to contain exactly two primary vertex fitted tracks. As additional tracks not pointing to the vertex can be caused by nuclear interactions of the kaons in the material between CJC1 and CJC2, it is not advisable to demand an otherwise completely empty detector. Additional long tracks starting close to the inner edge of the CJC however usually appear in events where the  $\phi$  is not exclusively produced. It is thus required that there are no additional tracks with a start radius below 25 cm and an end radius above 38 cm. The number of events with additional tracks fulfilling these criteria is below 2% both in the simulation and in the data, see figure 6.15.

### Unassociated Energy

In order to suppress background from processes where additional neutral particles are produced (e.g.  $\omega \rightarrow \pi^+ \pi^- \pi^0$ ), no calorimetric cluster with an energy above 600 MeV is allowed to be present in the event. This cut also suppresses proton dissociative events with a large mass of the dissociative system, where parts of the proton remnant hit the forward part of the liquid argon calorimeter. As a similar cut is already performed on the fourth trigger level, the recorded data events tend to have less unassociated energy than the simulated ones, see figure 6.16.

## 6.5.2 Track Properties

### Track Quality

A H1 standard set of track quality criteria is applied to all track candidates:

- Central track: The track has to be reconstructed from hits in the CJC.
- Start radius less than 50 cm: The track has to originate in CJC 1.
- Radial track length larger than 10 cm (this cut is relaxed to 5 cm for  $\vartheta > 150^\circ$ ).

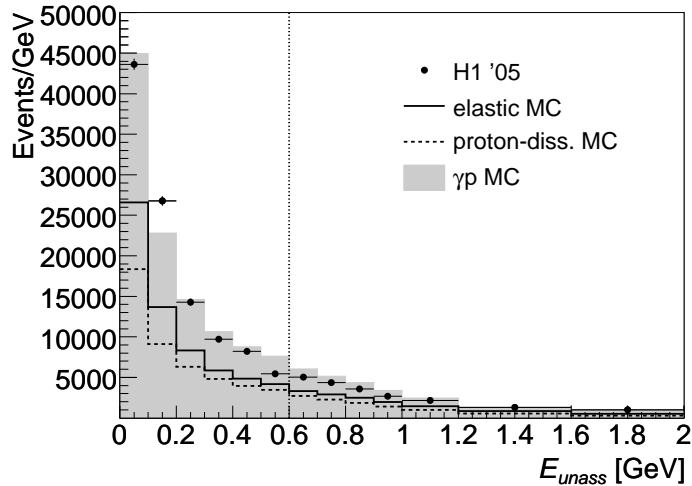


FIGURE 6.16: Number of  $\phi$  meson candidates in bins of energy of the most energetic cluster not associated to a track. The dashed line indicates the cut at 0.6 GeV.

- Distance of closest approach in the transverse plane to the event vertex less than 2 cm. In addition, the track timing has to be consistent with the timing expectation for tracks originating from  $ep$  events.

### Transverse Momentum

The track transverse momentum at the vertex is required to be above 200 MeV. This ensures that the momentum in the chamber (after the energy loss in the beam pipe) is well above the FTT threshold of 100 MeV and the track curvature is small enough for the track to reach the third FTT layer. Also, the nuclear interaction cross section is smaller at higher momenta and fewer kaons decay in flight due to their larger velocities and boosts. See figure 6.17 for the simulated and measured transverse momentum spectra.

### Track Polar Angle

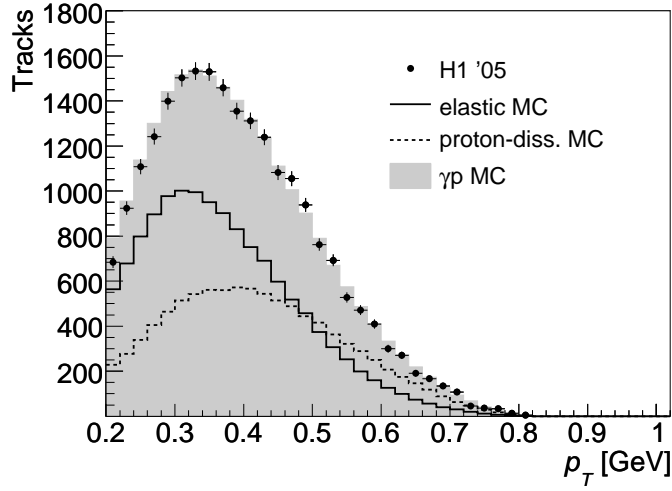
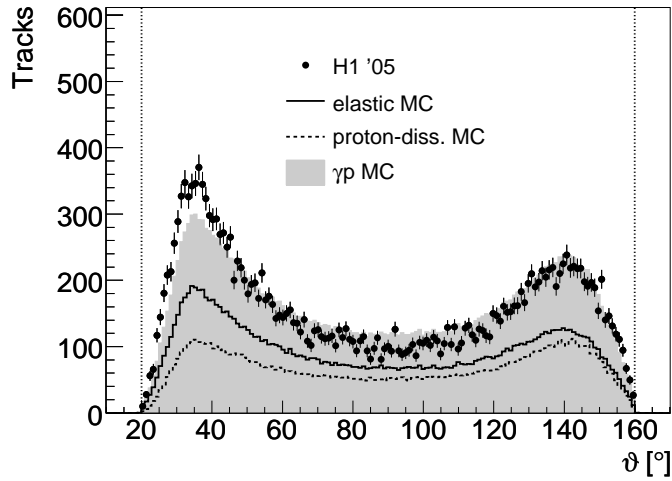
The track polar angle  $\vartheta$  is required to be in the range from  $20^\circ$  to  $160^\circ$  in order to ensure a good acceptance of the central tracker and the FTT. Figure 6.18 shows the polar angle spectrum for data and simulation.

## 6.6 Kinematic Phase Space and Binnings

The events passing all selection cuts are distributed into bins in order to measure differential cross sections. Depending on the measured quantity, different binnings and phase space restrictions are applied in order to get the largest possible kinematic coverage without being hampered by edge effects in acceptance and efficiency (see also the following chapter).

### 6.6.1 Phase Space for the Pomeron Analysis

Figure 6.19 shows that larger values of  $W$  become accessible as  $|t|$  increases. This improved lever arm in  $W$  is used for the extraction of the pomeron trajectory, where a  $t$  dependent  $W$  binning with 22 bins is used as described in table 6.2.

FIGURE 6.17: *Track transverse momentum.*FIGURE 6.18: *Track polar angle.*

$ t $ range [GeV <sup>2</sup> ]	Number of $W$ bins	$W$ bin edges [GeV]
0.2 - 0.3	3	[30,40,65]
0.3 - 0.4	4	[30,40,50,58,65]
0.4 - 0.5	4	[30,40,50,60,75]
0.5 - 0.65	4	[30,40,55,70,80]
0.65 - 0.9	5	[30,40,50,60,70,80]
0.9 - 1.5	3	[30,50,70,90]

TABLE 6.2: *Binning for the pomeron trajectory measurement.*

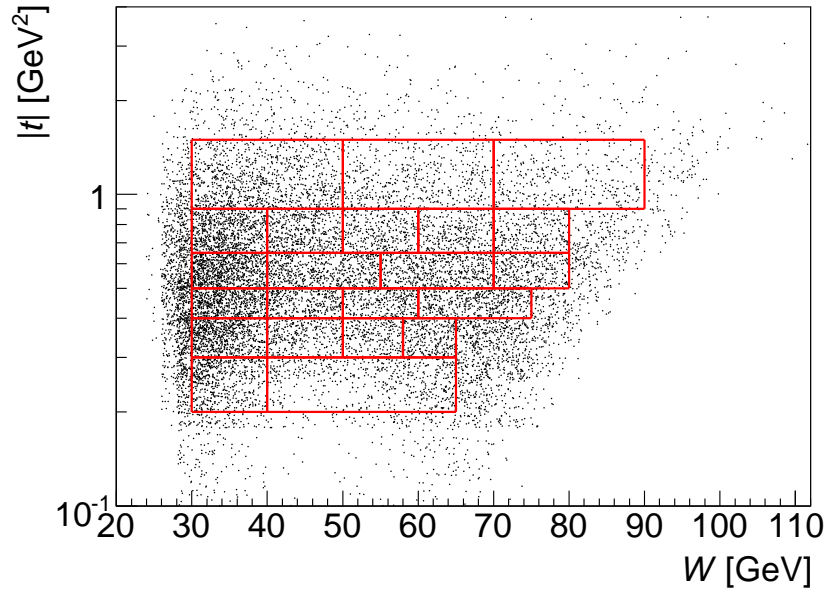


FIGURE 6.19: *Binning for the pomeron trajectory measurement overlaid over a scatter-plot of the selected events in the mass range  $1.01 < m_{K^+K^-} < 1.03$  GeV.*

Quantity	Unit	Divisions	Bin edges
$W$	GeV	4	[32, 40, 48, 58, 62]
$t$	GeV <sup>2</sup>	6	[0.2, 0.3, 0.4, 0.5, 0.65, 0.9, 1.5]

TABLE 6.3: *Binning for the  $t$  dependence measurement.*

### 6.6.2 Phase Space for the $t$ -Dependence Measurement

For the measurement of the  $W$  dependence of the cross section, the  $W - t$  plane is split into 24 bins, with four divisions in the  $W$  direction and 6 divisions in the  $t$  direction, see table 6.3 and figure 6.20.

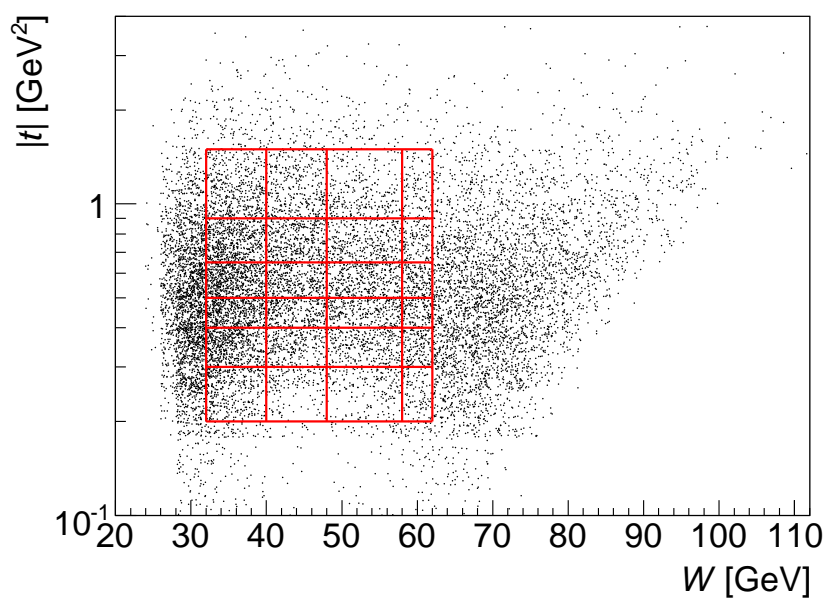


FIGURE 6.20: *Binning for the  $t$  dependence measurement, overlaid over a scatter-plot of the selected events in the mass range  $1.01 < m_{K^+K^-} < 1.03$  GeV.*



## Chapter 7

# Event Selection with Specific Energy Loss

*It is impossible to travel faster than light, and certainly not desirable, as one's hat keeps blowing off.*

WOODY ALLEN

The high specific energy loss of kaons allows for a very good separation of kaons and pions at low momenta. In the present analysis, this selection is used to suppress pions (mainly from  $\rho^0$  decays) and thus enhance the signal to background ratio for  $\phi$  mesons.

### 7.1 The Bethe-Bloch Equation

The specific energy loss of a particle traversing matter is described by the Bethe-Bloch formula [95]:

$$-\frac{dE}{dx} = \kappa z^2 \frac{Z}{A} \frac{1}{\beta^2} \left( \frac{1}{2} \ln \frac{2m_e c^2 \gamma^2 \beta^2 T_{max}}{I^2} - \beta^2 - \frac{\delta(\beta\gamma)}{2} \right), \quad (7.1)$$

where

- $\kappa = 4\pi N_A r_e^2 m_e c^2$  with
  - $N_A$ : Avogadro's number  $6.0221415 \times 10^{23} \text{ mol}^{-1}$ ,
  - $r_e$ : Classical electron radius  $e^2/4\pi\epsilon_0 m_e c^2$ ,
  - $m_e$ : Electron mass,
  - $c$ : speed of light,
  - $e$ : - electron charge,
- $z$ : charge of incident particle in units of  $e$ ,
- $Z$ : atomic number of absorber,
- $\beta = v/c$ : Speed of incident particle  $v$  in units of  $c$ ,
- $\gamma = 1/\sqrt{1-\beta^2}$ : Boost of incident particle,
- $I$ : mean excitation energy of electrons in the absorber,

- $T_{max}$ : Maximum kinetic energy which can be imparted on a free electron in a single collision by an incident particle of mass  $M$

$$T_{max} = \frac{2m_e c^2 \beta^2 \gamma^2}{1 + 2\gamma m_e/M + (m_e/M)^2}, \quad (7.2)$$

- $\delta(\beta\gamma)$ : Density effect correction (due to the polarisation of the medium, very long range interactions otherwise occurring at high  $\beta\gamma$  are suppressed). At highest energies,

$$\delta/2 \longrightarrow \ln(\hbar\omega_p) + \ln(\beta\gamma) - 1/2, \quad (7.3)$$

where  $\omega_p$  is the plasma frequency. For lower energies, the density correction is usually described using the Sternheimer parametrisation [203,204]:

$$\delta(\beta\gamma) = \begin{cases} 2(\ln 10)x - \bar{C} & \text{if } x \geq x_1; \\ 2(\ln 10)x - \bar{C} + a(x_1 - x)^k & \text{if } x_0 \geq x > x_1; \\ 0 & \text{if } x < x_0, \end{cases} \quad (7.4)$$

where  $x = \log_{10}(\beta\gamma)$ .  $\bar{C}$  is chosen such that the high energy limit matches equation 7.3 and the other parameters are fitted to the data.

The specific energy loss depends on  $\beta\gamma$ , i.e. the speed of the incident particle, whilst the tracking detector in the magnetic field measures the momentum of the particle. The comparison of the particle's momentum and its energy loss thus allows to deduce its mass. The velocity dependence of the energy loss is however not monotonous, so three different regions can be identified:

- The highly ionising region at low momenta, where the  $1/\beta^2$  term dominates, i.e. the ionisation increases strongly with decreasing momentum.
- The minimum ionising region at medium momenta.
- The relativistic rise region at high momenta, where the ionisation increases with increasing momentum (the increase is however damped by the density correction).

In the momentum range considered for this thesis, protons, kaons and deuterons are in the highly ionising region, pions and muons are minimally ionising and electrons are in the relativistic rise region. For the particle selection, a  $dE/dx$  expectation is determined and compared to the measured value corrected for detector effects. The expected resolution is determined using particles identified with specific decays and a likelihood for every particle hypothesis is calculated.

## 7.2 Detector effects influencing the $dE/dx$ measurement and their correction

### 7.2.1 Path length

The ionisation seen on a wire depends on the path length of the particle in the chamber. The dependence on the angle to the drift direction  $\beta$  is corrected during the track reconstruction. In addition, the measured  $dE/dr$  ( $r$  being the radial coordinate) has to be multiplied with the sine of  $\vartheta$  to obtain the  $dE/dx$ . The detector however sees approximately  $dE/dr$ , consequently the detector level corrections are applied to this quantity.

Bin	$\varphi_{min}$	$\varphi_{max}$
Left	$315^\circ$	$45^\circ$
Top	$45^\circ$	$135^\circ$
Right	$135^\circ$	$225^\circ$
Bottom	$225^\circ$	$315^\circ$

TABLE 7.1:  $\varphi$  bins for the  $dE/dx$  calibration.

## 7.2.2 Saturation

In a drift chamber, the gas amplification occurs in the (large) near field of the sense wires. For large ionisation, close to these wires large ion densities can develop, effectively screening the field of the wire. This *saturation* effect depends on the primary ionisation and on the length along the wire over which the charge is collected; for tracks running perpendicular to the wires, the complete charge is collected on a very short piece of wire, leading to a large saturation. For the present analysis, an empirical saturation correction [174] was applied: for  $dE/dr > 1$ :

$$\left(\frac{dE}{dr}\right)_{satcor}^{measured} = \left(\frac{dE}{dr}\right)^{measured} \frac{1 + \xi \sqrt{\left(\frac{dE}{dr}\right)_{Bethe-Bloch}^{expected} - 1}}{1 + |\cos \vartheta| \xi \sqrt{\left(\frac{dE}{dr}\right)_{Bethe-Bloch}^{expected} - 1}}, \quad (7.5)$$

where  $\xi$  is determined in the calibration procedure described in section 7.3. The saturation correction mainly affects the highly ionising regime.

## 7.2.3 Threshold effects

The determination of the average  $dE/dx$  along a track (see section 4.3.3) requires a minimum hit size. Very small hits are not detected by the  $Qt$  algorithm for the CJC. This loss of small hits leads to a bias towards larger measured values. Also here, an empirical correction [174] was applied. This correction depends on the charge deposited on the wire and thus on the gain of the chamber. The charge  $C$  expected to be seen by the wire is

$$C = \chi \left(\frac{dE}{dr}\right)_{satcor}^{expected}, \quad (7.6)$$

where  $\chi$  is a gain dependent conversion factor and the saturation correction has been applied to the expectation. The calculation of the charge dependent correction factor  $f_{thresh}$  is modelled with an error function behaviour in the inverse charge. For details see appendix A.

The correction is usually a few permille except for minimum ionising particles at low gain,

$$\left(\frac{dE}{dr}\right)_{sat,threshcor}^{measured} = f_{thresh} \left(\frac{dE}{dr}\right)_{satcor}^{measured}. \quad (7.7)$$

## 7.3 $dE/dx$ Calibration

Several parameters both in the Bethe-Bloch equation and in the correction functions have to be determined from the data. To this end, a set of identified particles was used. A high purity pion sample can be obtained from  $\rho^0$  decays [17], kaons were obtained from

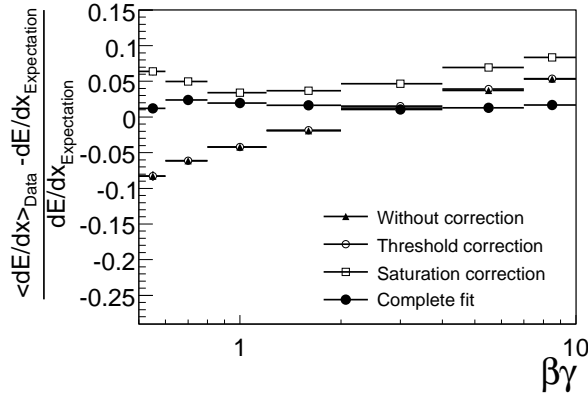


FIGURE 7.1: The average deviation of the measured  $dE/dx$  from the parametrisation for different steps in the correction procedure versus  $\beta\gamma$  for positive particles.

$\phi$  decays, where the other kaon was tagged using a likelihood derived from a preliminary  $dE/dx$  calibration [174]. The proton sample was taken from  $\Lambda$  decays [205]. The data were treated separately for the three gain periods considered in this analysis (see section 6.2). As the CJC has thicker wires in the quadrant from  $\varphi = 225^\circ$  to  $315^\circ$ , whose different gain was not compensated for in the data studied, the tracks were also distributed in four bins of  $\varphi$ , as shown in table 7.1. The two possible charges of the tracks were also treated separately, leading to a total of 24 bins. In each of these bins, a modified Bethe-Bloch parametrisation and a charge normalisation  $\chi$  valid for all three particle species and the  $\xi$  factor for every particle species were determined with a global fit. The modified Bethe-Bloch equation used is:

$$\frac{dE}{dx} = P_3 \frac{1}{\beta P_0} (P_4 + \ln(\beta^2 \gamma^2) - P_5 \beta^2 - \delta) + P_6 \quad (7.8)$$

with ( $x = \log_{10}(\beta\gamma)$ ,  $y = \sqrt{\frac{2 \ln 10}{3 P_1}}$ ):

$$\delta(x) = \begin{cases} 2(\ln 10)(x - P_2) & \text{if } x \geq P_2 - P_1 \frac{y^3}{2 \ln 10} + y; \\ 2(\ln 10)(x - P_2) + P_1 (P_2 - P_1 y^3 + y - x)^3 & \text{if } y > x - \left(P_2 - P_1 \frac{y^3}{2 \ln 10}\right) \geq 0; \\ 0 & \text{if } x < P_2 - P_1 \frac{y^3}{2 \ln 10}, \end{cases} \quad (7.9)$$

Thus the parameter  $P_0$  determines the rise for low values of  $\beta\gamma$  and is expected to be 2 if the saturation is correctly described.  $P_1$  and  $P_2$  tune the Sternheimer density correction — they are not very well determined by the data fitted, as high momentum particles are missing.  $P_3$ ,  $P_4$ ,  $P_5$  and  $P_6$  modify shape and normalisation of the Bethe-Bloch curve and thus parametrise the material properties of the chamber gas.

### 7.3.1 Fitting procedure

In a fitting procedure using the *Minuit* package [206], a function  $\Sigma$  of the form

$$\Sigma = \sum_{\text{tracks}} \left( \frac{1/\sqrt{\left(\frac{dE}{dr}\right)^{\text{expected}}} - 1/\sqrt{\left(\frac{dE}{dr}\right)^{\text{measured}}_{\text{sat,threshcor}}}}{1/\sqrt{\left(\frac{dE}{dr}\right)^{\text{expected}}}} \right)^2 \quad (7.10)$$

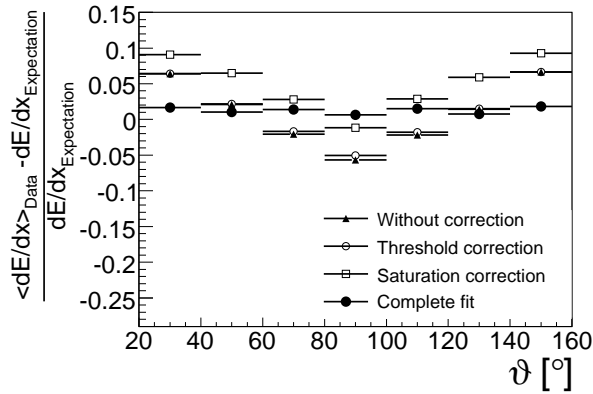


FIGURE 7.2: The average deviation of the measured  $dE/dx$  from the parametrization for different steps in the correction procedure versus  $\vartheta$  for positive particles.

was minimised with 11 free parameters  $P_0$  to  $P_6$ ,  $\chi$ ,  $\xi_h$  where  $h$  runs over pion, kaon and proton. For each bin around 8000 tracks were used. Similar to the averaging of the individual hits in the  $dE/dx$  reconstruction, a transformation to  $1/\sqrt{dE/dx}$ , yielding a symmetric distribution, is used. An example for the improvements achieved with this procedure can be seen in figures 7.1 and 7.2; the fitted parameters are shown in table A.2 in appendix A.

### 7.3.2 Resolution determination

The resolution of the  $dE/dx$  measurement depends on the number of CJC hits used and — in the framework presented here — on the particle type. It was determined as the square root of the mean squared relative deviation (RMS) of the measured and corrected  $dE/dx$  from the parametrization. The resolution ranges from 20% for protons with 15 hits down to 9% for pions with more than 45 hits. The resolutions are parametrised for each particle in each of the 24 bins of the global fit using the form

$$\frac{\delta\left(\frac{dE}{dx}\right)}{\frac{dE}{dx}} = E_0 + \frac{E_1}{\sqrt{N_{hit}}} + E_2 N_{hit}. \quad (7.11)$$

The resolution parameters thus determined can be found in table A.1 in appendix A.

## 7.4 Likelihood Determination

For the final particle identification, a likelihood is used. Under the assumption that the particle is a kaon, the  $dE/dx$  expectation is determined. Using this expectation, the measured value is corrected for saturation and threshold effects. The difference  $\Delta$  between the expectation and the corrected measurement is then calculated. With the expected resolution  $r_{exp}$  known from the number of hits, the likelihood for a particle to be a kaon is then

$$L_K = \text{prob}\left(\left(\frac{\Delta}{r_{exp}}\right)^2, 1\right) = 1 - \text{erf}\left(\frac{\Delta}{\sqrt{2}r_{exp}}\right) = 1 - \frac{2}{\sqrt{\pi}} \int_0^{\frac{\Delta}{\sqrt{2}r_{exp}}} e^{-t^2} dt \quad (7.12)$$

where  $\text{prob}(\chi^2, ndf)$  is the probability to obtain a value greater or equal to  $\chi^2$  from a  $\chi^2$ -distribution for  $ndf$  degrees of freedom.  $\text{erf}(x)$  is the error function as defined in the above equation.

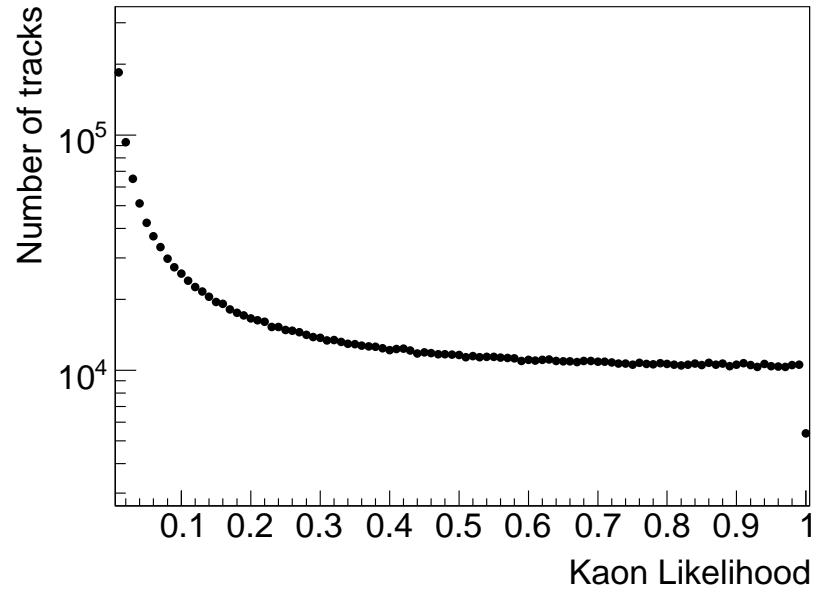


FIGURE 7.3: *Kaon likelihood for all tracks in the events triggered by the  $\phi$  triggers.*

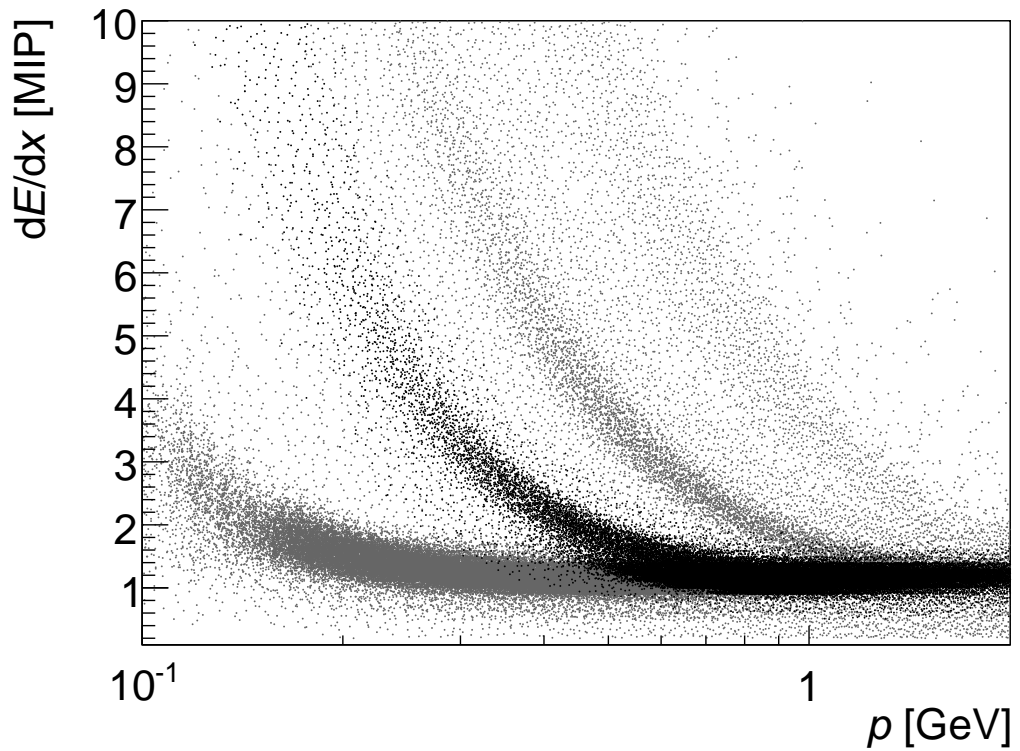


FIGURE 7.4:  *$dE/dx$  versus momentum for all tracks in the events triggered by the  $\phi$  triggers. The measured  $dE/dx$  was corrected under a kaon hypothesis. Tracks with a kaon likelihood of less than 5% are shown with grey dots. From lower left to top right the pion, kaon, proton and deuteron bands are visible.*

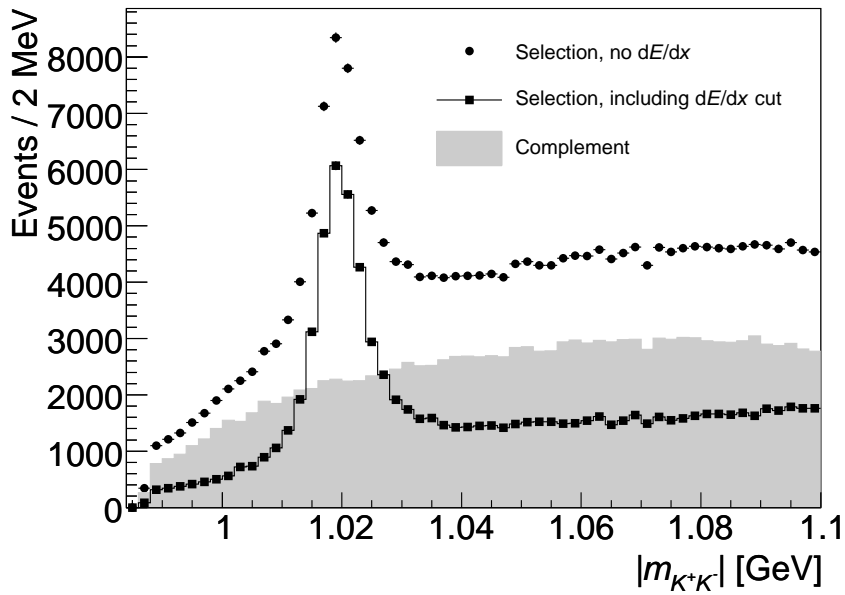


FIGURE 7.5: Effect of the loose  $dE/dx$  cut (one track with a likelihood above 5%) on the invariant mass distribution. The shaded area shows the distribution for events failing the  $dE/dx$  cut (complement).

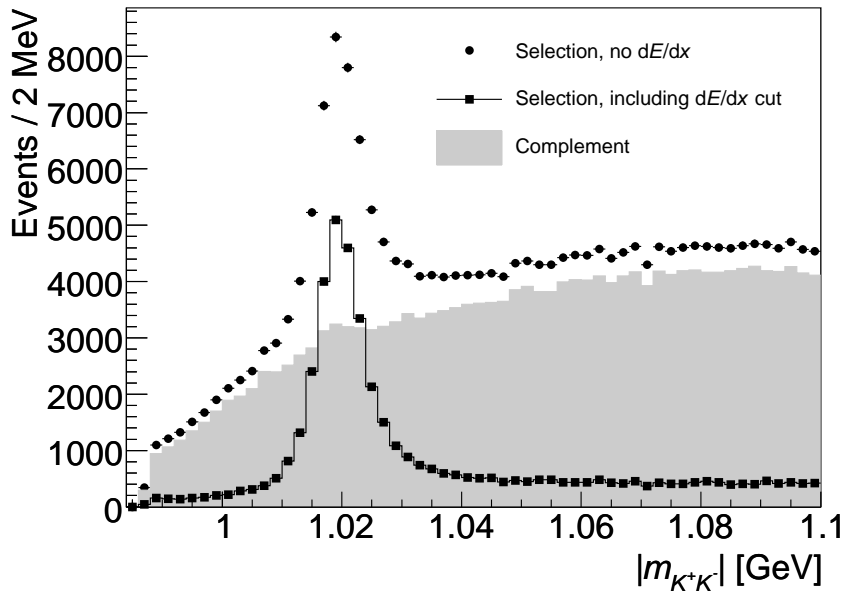


FIGURE 7.6: Effect of the tight  $dE/dx$  cut (both tracks with a likelihood above 5%) on the invariant mass distribution. The shaded area shows the distribution for events failing the  $dE/dx$  cut (complement).

The likelihood distribution seen in the  $\phi$  trigger data is shown in figure 7.3. As there are many more pions and protons than kaons in this sample, the peak for low likelihoods is expected. The region of near-overlap between the pion and kaon bands (see figure 7.4) is responsible for the slope of the likelihood all the way to 1.

For the selection of  $\phi$  mesons, a cut on one of the two tracks having a kaon likelihood above 5% or both tracks having this likelihood were considered. The first cut improves the signal-to-background ratio by a factor 5 at an expected efficiency of  $\epsilon = 1 - 0.05^2 = 99.75\%$  (figure 7.5). The second cut leads to a tenfold increase in signal-to-background ratio at an expected efficiency of  $\epsilon = 0.95^2 = 90.25\%$  (figure 7.6). In reality, the efficiencies are somewhat lower as there are also tracks without a  $dE/dx$  measurement, see section 8.4.1. The cut on both tracks leads to a larger systematic uncertainty from the inefficiency which is however more than compensated by the higher statistical accuracy and the reduced uncertainty due to the background shape. Whilst for some of the resolution- and reconstruction studies, the cut on at least one track was used, the main analysis employs the cut on both tracks.

## Chapter 8

# Acceptance and Efficiencies

*Confidence is what you have before you understand the problem.*

WOODY ALLEN

In order to obtain a cross section from the number of events passing the selection, several corrections have to be applied. First, the visible cross section definition takes care of events not originating from the phase space under study. Then the geometrical and kinematic acceptance  $a$  of the H1 detector have to be considered. Finally there is a finite efficiency  $\epsilon$  of the detector elements, the triggers and the applied cuts.

Acceptance and efficiencies were obtained using the Monte Carlo sample described in chapter 5, or using a set of monitor data with different triggers. Whenever possible, the Monte Carlo simulation was checked against the data. Many of these checks led to an improvement of the simulation, resulting in a better description of the observed event properties.

All corrections were determined individually for each bin used in the analysis (see also chapter 10), i.e. differentially in  $t$  for the measurement of the  $t$  slope, differentially in  $W$  and  $t$  for the extraction of the pomeron trajectory and determination of the  $W$  dependence and differentially in  $t$ ,  $\cos\theta_h$  and  $\phi_h$  for the helicity analysis.

### 8.1 Visible Cross Section Definition

A cross section can only be measured for a process within a well defined phase space. This analysis attempts to measure the elastic  $\phi$  photoproduction cross section  $\sigma(\gamma p \rightarrow \phi p)$  and the diffractive  $\phi$  photoproduction cross section  $\sigma(\gamma p \rightarrow \phi Y)$ . Photoproduction is operationally defined as

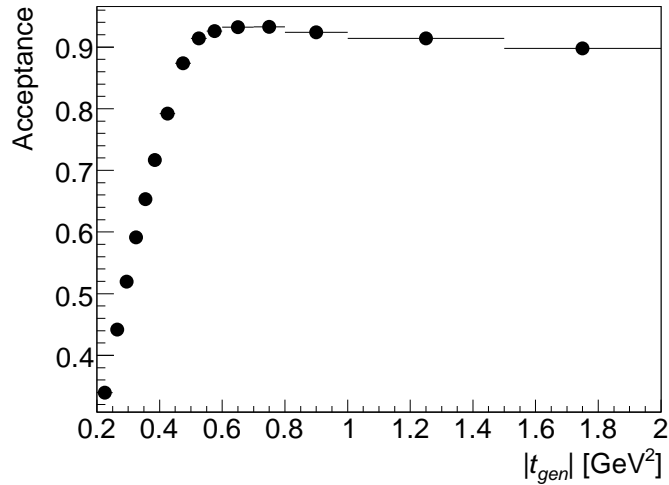
$$Q^2 < 2.5 \text{ GeV}^2. \quad (8.1)$$

In the proton dissociative case, the diffractive nature of the process is ensured by requiring [207]

$$M_Y < 5 \text{ GeV}. \quad (8.2)$$

In addition, a minimum momentum transfer at the proton vertex  $|t|$  is required:

$$|t| > 0.2 \text{ GeV}^2. \quad (8.3)$$

FIGURE 8.1: *Acceptance versus  $|t|$ .*

Events from outside this phase space are also simulated and treated as background in the analysis, if they enter the analysis phase space because of resolution effects.

## 8.2 Acceptance

Since the H1 detector does not offer a full  $4\pi$  coverage, there are regions where the final state is not or only partially detected. For the present analysis, the geometrical and kinematical acceptance of the central tracker is decisive. It is demanded that the four-vectors of the generated decay kaons fulfil the following two criteria:

$$20^\circ < \vartheta < 160^\circ \quad (8.4)$$

$$p_T > 200 \text{ MeV}. \quad (8.5)$$

As these criteria are independent of the detailed detector description, they are well described by the simulation. Events where both four-vectors fulfil the cuts fall into the detector acceptance and are counted in  $N_{acc}$ . The acceptance is defined as

$$a = \frac{N_{acc}}{N_{sig}}, \quad (8.6)$$

where  $N_{sig}$  is the number of simulated events fulfilling the signal definition given in the previous section. The acceptance versus  $t$  and  $W$  is shown in figures 8.1 and 8.2. Figure 8.3 shows the acceptance for the bins used to extract the pomeron trajectory. The drop towards low  $t$  is caused by the transverse momentum cut, as the decay kaons have very little momentum in the  $\phi$  rest system and a transverse kick ( $\propto \sqrt{|t|}$ ) is required to pass the cut. The acceptance drop for high and low  $W$  values are caused by the restriction on  $\vartheta$  – for low  $W$  values, one or both decay kaons are boosted too much into the forward region to be seen, for high values of  $W$  the same applies to the backward direction.

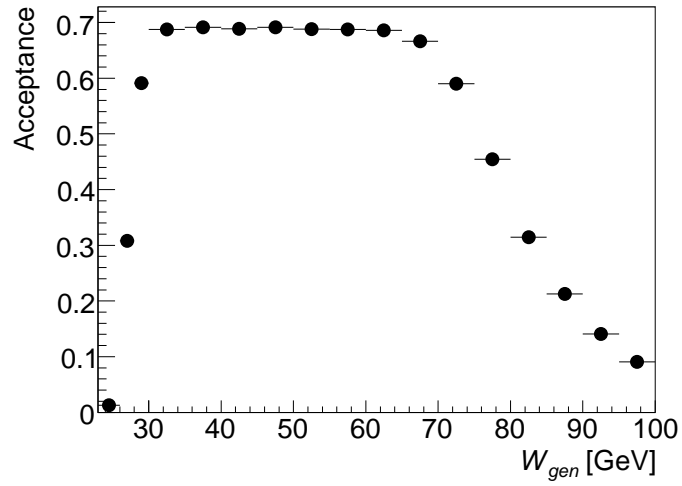


FIGURE 8.2: *Acceptance versus  $|W|$  for events with  $|t| > 0.3 \text{ GeV}^2$ .*

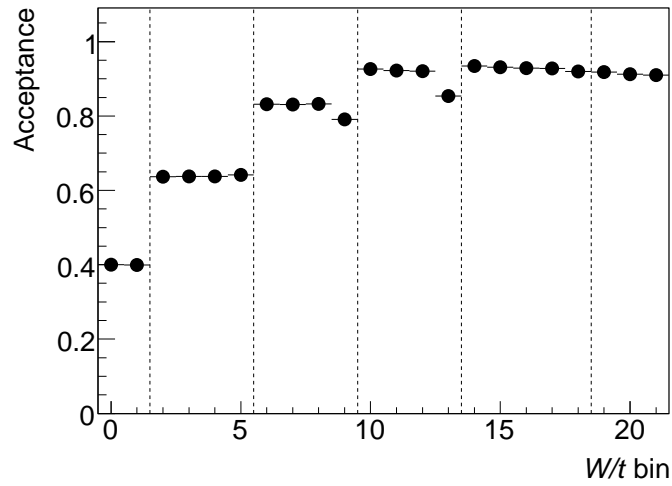


FIGURE 8.3: *Acceptance for the  $W/t$  bins used to extract the pomeron trajectory. A series of bins delimited by a dashed line constitutes the  $W$  bins for a specific range in  $t$ .*

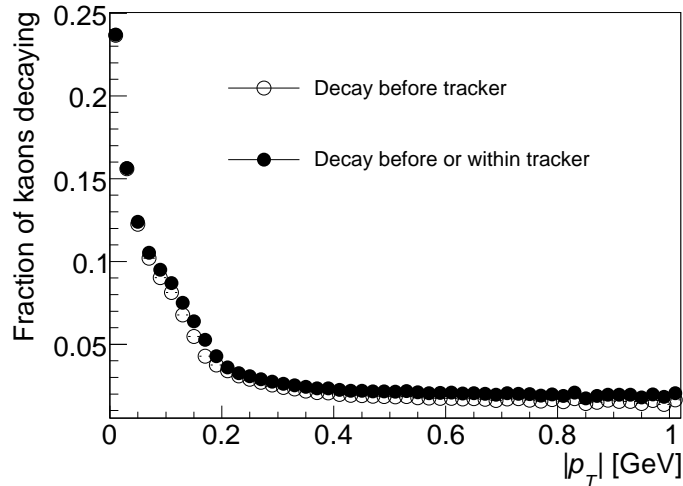


FIGURE 8.4: *Fraction of kaons decaying before reaching the start and end radius of the CJC respectively versus the kaon transverse momentum.*

### 8.3 Reconstruction Efficiency

An event will only enter the analysis if two oppositely charged tracks are found in the central tracker and are fitted to the primary vertex. There are three main reasons why a charged kaon should not lead to a vertex fitted track in the reconstruction:

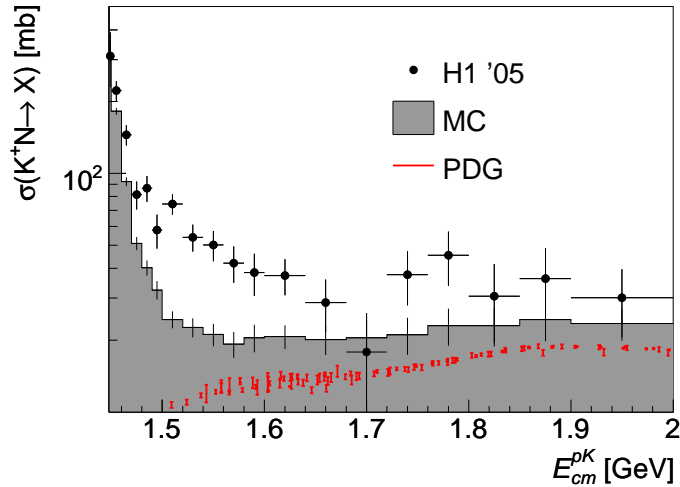
- The kaon does not reach the sensitive volume of the tracker due to energy loss, multiple scattering and nuclear interactions in the material between the beamline and the tracker.
- The kaon decays before leaving a long enough track.
- The kaon traverses the tracker, but the reconstruction fails to recognise the resulting hit pattern as a track.
- The track is found but not fitted to the primary vertex.

#### 8.3.1 Energy Loss

The loss of tracks due to energy loss (and eventual stopping) in the material and due to multiple scattering is large for low momenta. If however the description of the material in the simulation is adequate to describe the real detector (which is corroborated by the mass shift and resolution studies in section 6.4.1), GEANT describes these losses well.

#### 8.3.2 In-Flight Decays of Kaons

Charged kaons have a lifetime  $\tau$  of  $(1.2385 \pm 0.0024) \cdot 10^{-8}$ s [95]. This leads to a significant amount of kaon decays on the way through the detector, especially at low momenta (low speed  $\beta$  and boost  $\gamma$ ), see figure 8.4. If the decay happens before the kaon has left a long enough trace in the jet chamber to pass the reconstruction cuts and set off the trigger, no  $\phi$  can be reconstructed. Decays in the outer ring of the chamber on the other hand will not affect the  $\phi$  reconstruction but may lead to calorimetric energy deposits not associated to the primary vertex tracks. These effects are however well simulated and corresponding corrections can be derived.

FIGURE 8.5:  $K^+$ -Nucleon cross section measured with the COP/COZ.

### 8.3.3 Nuclear Interactions

The situation is more difficult for the case of nuclear interactions. As mentioned in section 5.3.1, the GHEISHA modelling of the kaon-nucleon cross section at kinetic energies below 500 MeV will not necessarily describe the data.

The nuclear interaction cross section was determined from the fraction of events interacting in the material between the two CJC rings. For identified kaons found in CJC1, the survival probability in CJC2 was studied by searching for matching tracks. The resulting loss fraction was corrected for in-flight decays of kaons using the simulation. The amount of material between the chambers can be determined from the momentum dependence of the range of kaons and turns out to be about 1.2 g/cm<sup>2</sup> in accordance with a measurement using photon conversions [208]<sup>1</sup>. The COP and COZ chambers are built from ROHACELL and G10 plastics, having an effective atomic number  $Z$  of 7.2 and an effective atomic weight  $A_{eff}$  of 14.6. The target can thus be treated as isoscalar to good approximation. The kaon-nucleon cross section can then be calculated as

$$\sigma_{Kn \rightarrow X} = - \frac{\ln \left( 1 - \frac{N_{K,int}}{N_K} \right) \frac{A_{eff}}{A_{eff}^{0.77}}}{\langle M \rangle \frac{N_A}{A_{eff}}}, \quad (8.7)$$

where  $N_K$  is the number of kaons produced,  $N_{K,int}$  is the number of kaons interacting and  $\langle M \rangle$  is the average amount of material seen by the kaons (in grammes per millibarn). The fraction  $\frac{A_{eff}}{A_{eff}^{0.77}}$  corrects for nuclear shadowing and  $N_A$  is Avogadro's number.

This cross section measurement is beset with very large uncertainties; on one hand, the amount of material between the two CJC rings is known to 30% accuracy at best, its detailed distribution is even less well known<sup>2</sup>. On the other hand, over 95% of the losses are due to kaon decays and not due to nuclear interactions; this large subtraction also has a considerable uncertainty, as the decay length depends on the kaon's velocity, which is in turn influenced by the amount of material.

<sup>1</sup>In the energy loss correction routines used in H1, about half that amount of material is assumed.

<sup>2</sup>Here the dismantling of H1 in summer 2007 offers the opportunity for a precise measurement. In principle also the atomic composition of the material could be determined by controlled burning of the chambers and subsequent mass spectroscopy.

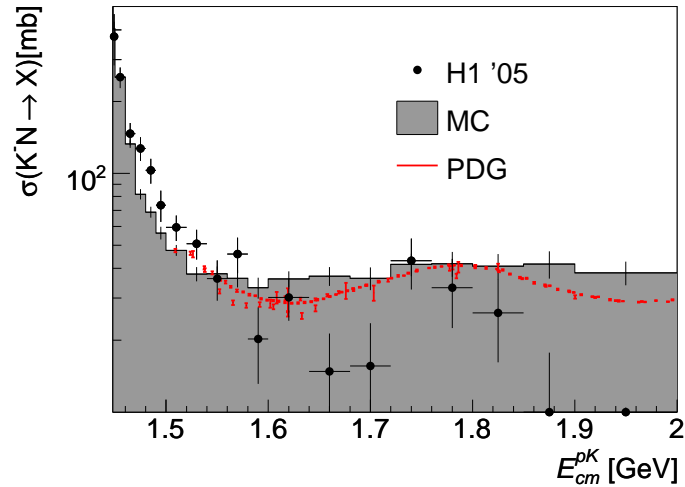


FIGURE 8.6:  $K^-$ –Nucleon cross section measured with the COP/COZ.

The simulated cross section was found to agree at least in order of magnitude with the data and also a compilation of cross sections for an isoscalar target [95] for nucleon-kaon centre-of-mass energies. For the positive kaons, there seems to be an additional loss mechanism not described by the simulation (see figure 8.5). For the negative kaons, the cross section is approximately described above 1.6 GeV centre of mass energy, at lower energies however, the data cross section lies markedly above the simulation and no previous measurements are available. In a pragmatic approach, the Monte Carlo events were reweighted such that the cross section is in agreement with the measured cross section; the corresponding weight is everywhere below 10%, giving an upper limit for the corresponding uncertainty.

### 8.3.4 Track Finding Efficiency

The central jet chamber has a total of 56 layers – if a charged particle traverses the chamber (without decaying or getting stuck), the corresponding track is found in almost all the cases, especially for low multiplicity events. The remaining inefficiency is believed to be at the percent level and described by the simulation. During the data period under consideration the online reconstruction was however encumbered with an error in a correction routine. The parametrisation of field distortions sometimes gave improper results for wires at the edges of CJC rings. As these corrections were performed after the outlier rejection, the wrongly corrected hits were included in the final track fit, leading to a bad  $\chi^2$  and a subsequent discarding of the track, affecting about 3% of all tracks. For these events, the level 4 trigger saw only one track and thus the  $\phi$  meson finders failed. This effect is not present in the Monte Carlo simulation, as the field distortions are neither simulated nor corrected for there.

In order to correct for this effect,  $\phi$  meson candidate events triggered by the SpaCal and containing an electron were studied. These events are saved by the level 4 trigger irrespective of tracking conditions. They were reprocessed with a reconstruction software with a fixed distortion correction. For all  $\phi$  meson candidates in the reprocessed sample it was checked whether at least two tracks were found by the old reconstruction software. The simulation was then corrected for the resulting loss. As the affected layers have a low hit efficiency, the effect is more pronounced for large ionisation and thus small kaon momenta, see figure 8.7.

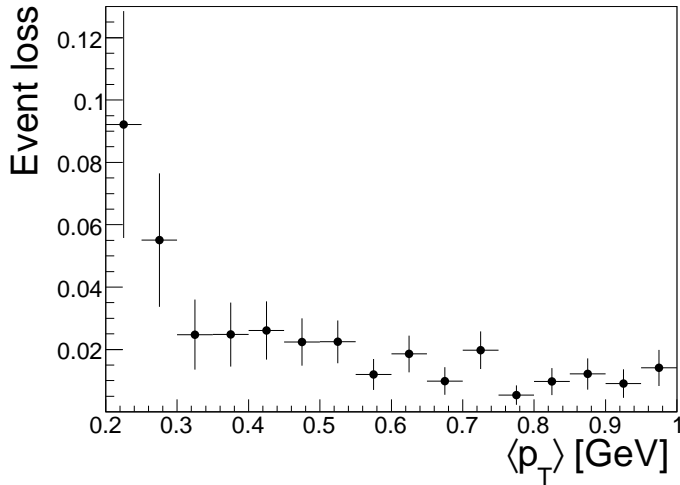


FIGURE 8.7: Loss of events from missing tracks due to the wrong field distortion corrections versus the average transverse momentum of the tracks.

Parameter	Value for positive tracks	Value for negative tracks
$D_1$	0.92	2.41
$D_2$	-1.53	-0.523
$D_3$	0.0	-0.02
$D_4$	0.90	0.96
$D_5$	$4.44 \cdot 10^{-5}$	$-2.10 \cdot 10^{-5}$
$D_6$	$-6.30 \cdot 10^{-9}$	$5.06 \cdot 10^{-9}$

TABLE 8.1:  $dE/dx$  efficiency parametrisation.

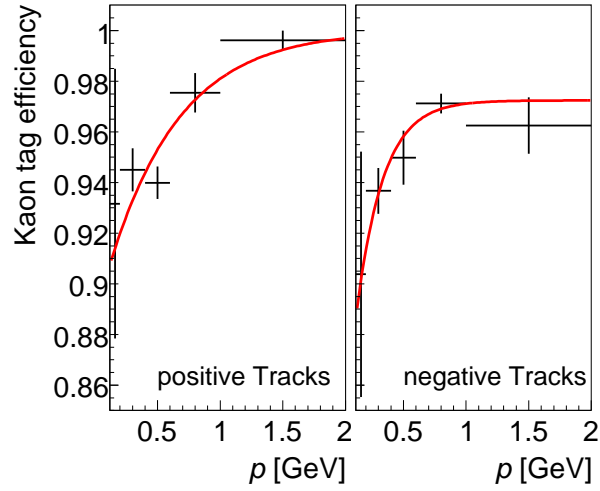
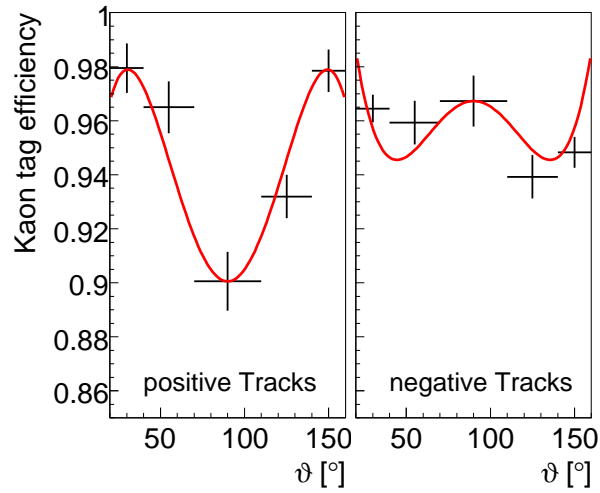
### 8.3.5 Vertex Fitting Efficiency

For tracks with a high specific energy loss, the main source of reconstruction inefficiency is a failure of the primary vertex fit. Due to the selection criteria applied on the fourth trigger level, only events where both kaon tracks can be fitted to the primary vertex both with pion energy loss corrections and kaon energy loss corrections will end up in the selected sample. The inefficiency due to this is corrected for using the simulation, where the events are first reconstructed with pion energy loss corrections and then with kaon energy loss corrections; only if both reconstructions yield two primary vertex fitted tracks, the event is selected.

## 8.4 Selection Efficiency

### 8.4.1 Efficiency of the $dE/dx$ Selection

The description of the specific energy loss  $dE/dx$  in the simulation does not include the sizeable saturation effect and likelihoods have to be determined with a different parametrisation than for data. Efficiencies determined from simulated events will thus not necessarily match the efficiencies in data. The efficiency of the  $dE/dx$  selection was thus determined using data. In a two track sample, a rather clean kaon sample was obtained by requiring a kaon likelihood above 5% for one of the tracks. The efficiency for also tagging the second track was then determined by extracting the number of  $\phi$  candidates (see chapter 10 for the fitting

FIGURE 8.8: *Efficiency of the  $dE/dx$  tag versus track momentum.*FIGURE 8.9: *Efficiency of the  $dE/dx$  tag versus track polar angle.*

	$A_0$	$A_1 \cdot 10^3$	$A_2 \cdot 10^9$	$A_3 \cdot 10^{10}$	$A_4 \cdot 10^{16}$	$A_5$
Data	$0.965 \pm 0.009$	$42 \pm 3$	$5.7 \pm 1.4$	$3.9 \pm 2.9$	$3.2 \pm 0.6$	91.2
MC	$0.9943 \pm 0.0002$	$4.59 \pm 0.16$	$1.80 \pm 0.08$	$4.3 \pm 0.3$	$3.62 \pm 0.04$	90.8

TABLE 8.2: *Parameters used for reweighting the FTT efficiency for simulated tracks, see equation (8.10) for the meaning of the parameters.*

procedure) with and without the tag on the second track. The correlation between the two tracks was studied by comparing samples where either the positive, the negative or any track was used for the tag. Within the statistical uncertainty of the sample, no correlation was observed.

As shown in figures 8.8 and 8.9, the efficiency for the tag  $\epsilon_{dE/dx}^{\pm}$  for a track with a specified charge is everywhere above 90%. As the  $dE/dx$  efficiency is not taken from the simulation, the dependence of the inefficiency on the momentum was parametrised with

$$\epsilon_{dE/dx}^{\pm}(p) = \tanh(D_1(p - D_2)) D_3, \quad (8.8)$$

and the three parameters  $D_1$ ,  $D_2$  and  $D_3$  determined from a fit to the data, see figure 8.8. Correspondingly, the  $\vartheta$  dependence was parametrised with a polynomial

$$\epsilon_{dE/dx}^{\pm}(\vartheta) = D_4 + D_5(\vartheta - 90^\circ)^2 + D_6(\vartheta - 90^\circ)^4 \quad (8.9)$$

and again the parameters were determined by a fit to the data, see figure 8.9. The fit parameters are shown in table 8.1. For the analysis, the Monte Carlo events are weighted with the  $dE/dx$  efficiency, calculated from the parametrisation depending on  $p$  and  $\vartheta$  of the two tracks, where the  $\theta$  reweight is scaled to give an average efficiency of one, thus preventing a double counting of the inefficiency.

## 8.5 Trigger Efficiency

In order to tune the description of the level 1  $\phi$  trigger in the simulation, a set of independently triggered data is needed. For the present analysis, this *monitor sample* consists of  $\phi$  mesons produced in deep inelastic scattering (DIS), where the scattered electron in the backward calorimeter (SpaCal) serves as a trigger. The corresponding subtriggers are `s0` and `s3`, based solely on the SpaCal, with different energy thresholds.

The events triggered such are then subject to the same selection as the photoproduction events, allowing for the additional energy deposited by the electron. As the  $\phi$  mesons produced in DIS have a harder transverse momentum spectrum than the photoproduction events, the track transverse momentum spectrum is reweighted to that expected from photoproduction for the subsequent studies.

### 8.5.1 Single Track Efficiency of the FTT

The FTT is read out to provide information on the tracks found by the trigger. The efficiency (for a given multiplicity) can thus be determined track wise as a function of track  $p_T$ ,  $\vartheta$  and  $\varphi$ . The comparison of the monitor data with the simulation shows that the FTT efficiency is underestimated for large track inclinations and overestimated for small track inclinations (see figure 8.10). In order to correct for this, the two-dimensional efficiency distributions in  $\vartheta$  and  $p_T$  for data and simulation are fitted with a function of the form

$$\epsilon_{FTT}(\vartheta, p_T) = A_0 + A_1\sqrt{p_T} + (A_2 + A_3\sqrt{p_T}) \cdot (\vartheta - A_5)^4 - A_4 \cdot (\vartheta - A_5)^8. \quad (8.10)$$

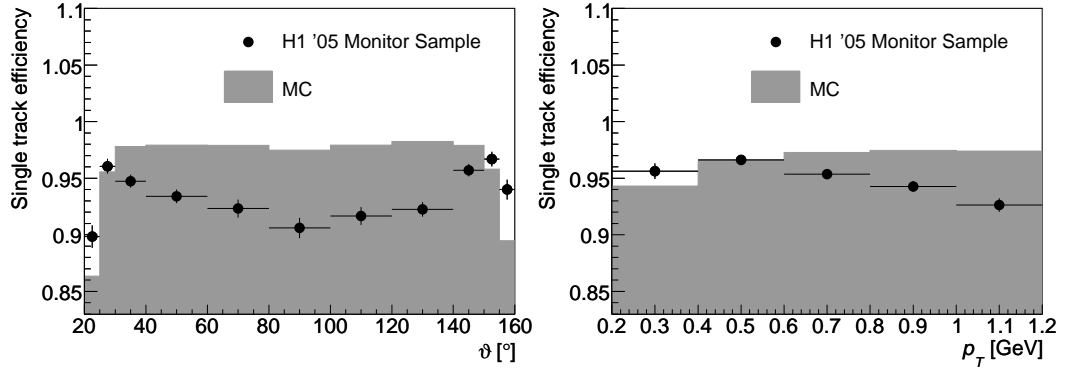


FIGURE 8.10: *Single track efficiency of the FTT versus track polar angle (left) and track transverse momentum (right).*

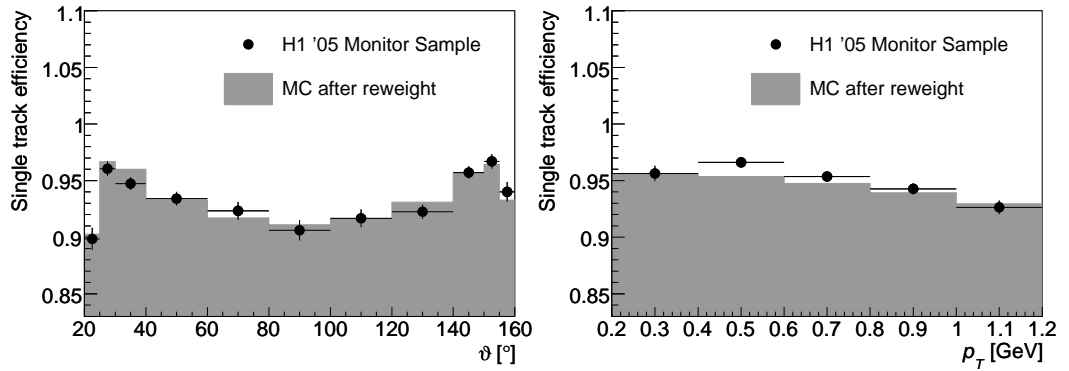


FIGURE 8.11: *Single track efficiency of the FTT after reweighting the simulation versus track polar angle (left) and track transverse momentum (right).*

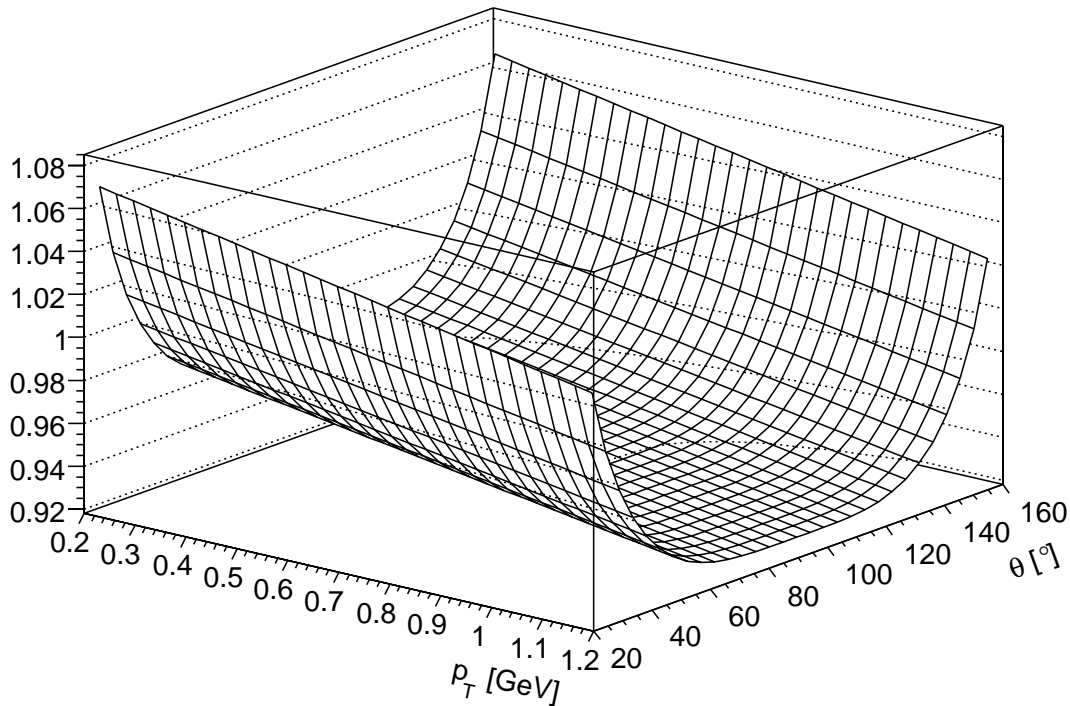


FIGURE 8.12: *Reweight of the simulation for the FTT single track efficiency.*

The six parameters  $A_k$  can be interpreted as follows:

- $A_0$ : overall normalisation of the efficiency,
- $A_1$ :  $p_T$  dependence,
- $A_2$ : depth of the dip for intermediate  $\vartheta$ ,
- $A_3$ :  $p_T$  dependence of the depth of the dip,
- $A_4$ : falloff for large inclination,
- $A_5$ : position of the dip.

The parameters obtained from the fits are shown in table 8.2 and the resulting weight applied to the simulated events is shown in figure 8.12. The efficiency distribution in the simulation after reweighting is compared to the monitor data in figure 8.10.

The level 1 FTT has a tendency to double count tracks. This double counting is due to ambiguities in the linking step and is simulated well; however, as the overall track efficiency is overestimated in the simulation, so is the frequency of double counting; if the FTT counts more than three tracks, the event is rejected by the  $\phi$  trigger. This inefficiency due to this veto is overestimated in the simulation (see figure 8.13.) and thus the simulation is reweighted differentially in transverse momentum and polar angle, using fits of fourth-order polynomials to the measured and the simulated efficiency distributions (see figure 8.14 for the efficiency distributions after weighting).

### 8.5.2 Efficiency of the Global FTT Trigger Elements

The efficiencies of the global FTT trigger elements (segment in layers 3 or 4) and the topology condition are slightly overestimated in the simulation (partly due to the discrepancy between the actual and simulated amount of material in the COP and COZ which lie between the

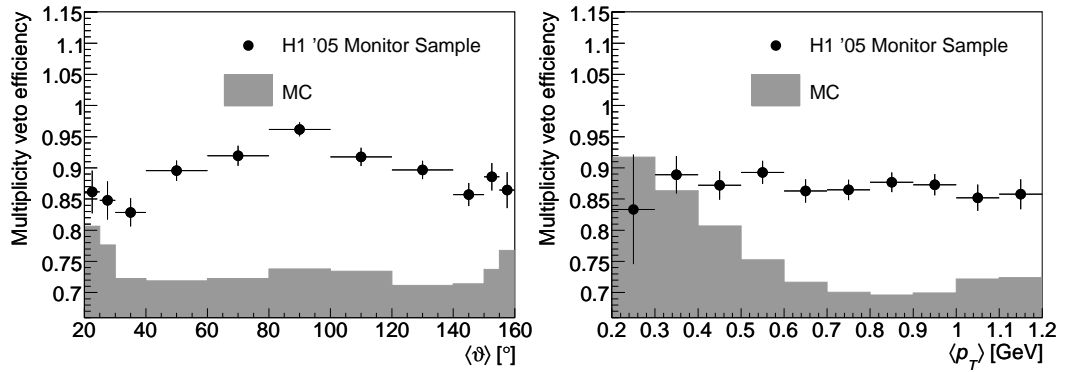


FIGURE 8.13: Efficiency of the FTT multiplicity condition (less than 4 FTT level 1 tracks) versus the average polar angle (left) and transverse momentum (right) of the two tracks.

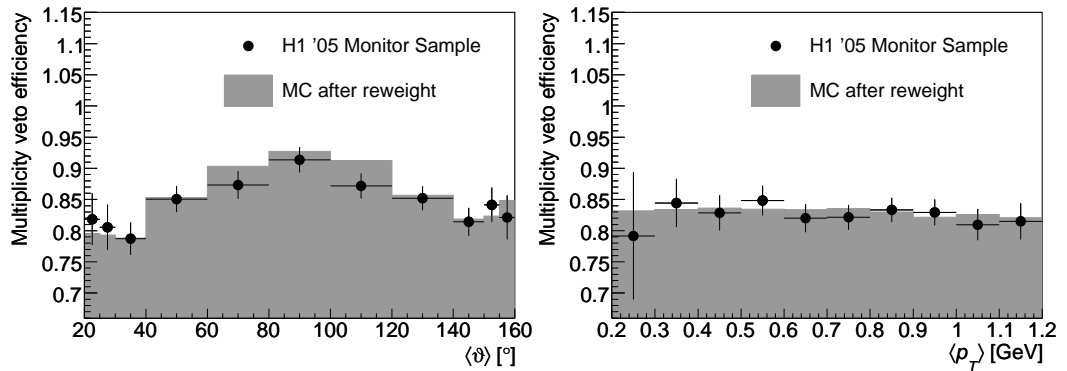


FIGURE 8.14: Efficiency of the FTT multiplicity condition (less than 4 FTT level 1 tracks) versus the average polar angle (left) and transverse momentum (right) of the two tracks after reweighting.

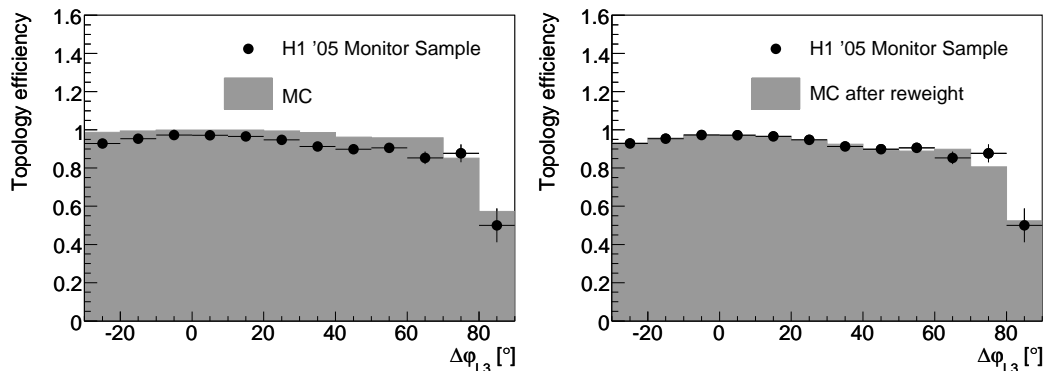


FIGURE 8.15: Efficiency of the FTT topology condition versus the track opening angle at the third trigger layer before (left) and after reweighting (right).

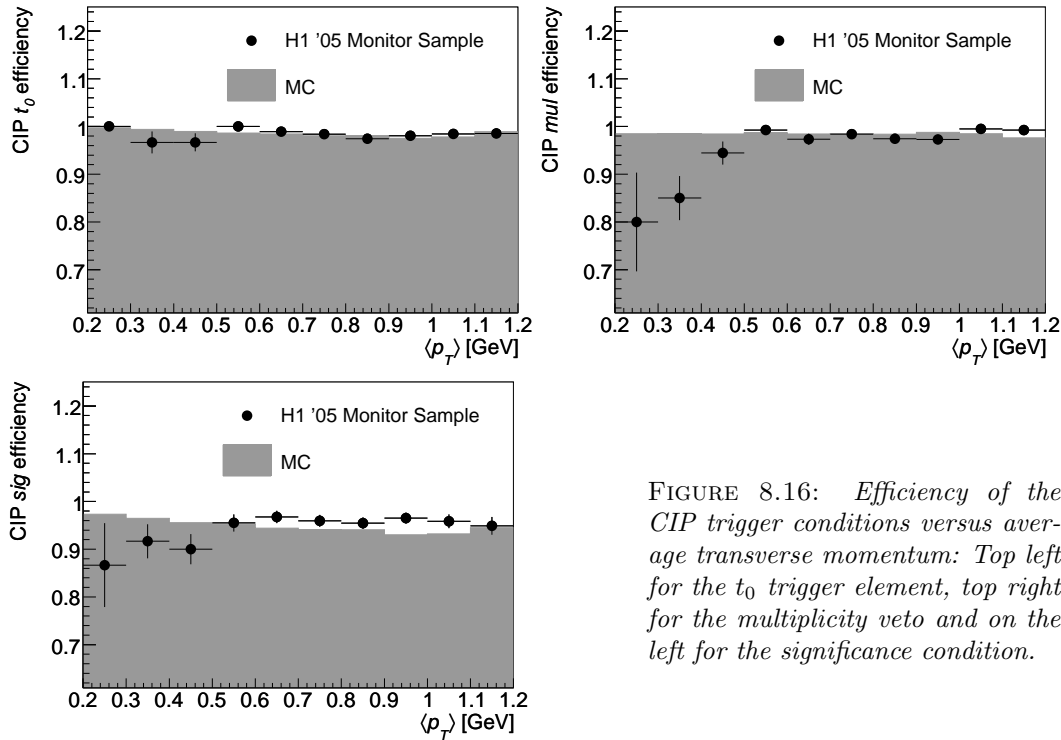


FIGURE 8.16: *Efficiency of the CIP trigger conditions versus average transverse momentum: Top left for the  $t_0$  trigger element, top right for the multiplicity veto and on the left for the significance condition.*

third and fourth layer). The segment efficiency is found to be globally underestimated by about 4%.

The topology condition has a slightly larger acceptance in the signed angular opening (as measured from the positive track) at the radius of the third trigger layer ( $\Delta\phi_{L3}$ ) in the simulation than in the data (see figure 8.15). This is corrected for by fitting a fourth-order polynomial to the efficiency shape in the simulation and the data and then reweighting the simulation by the ratio.

### 8.5.3 CIP Efficiency

The CIP multi-wire proportional chamber has a very high single hit efficiency. The CIP  $t_0$  signal is generated if at least one track is seen by the CIP trigger. The efficiency for this  $t_0$  trigger signal was determined from monitor data with a SpaCal  $t_0$  and found to be 98.3%, almost independent of the event kinematics (see figure 8.16).

The CIP multiplicity and significance vetoes employed for the FTT on the other hand induce larger inefficiencies (see also figure 8.16); especially at low transverse momenta the kaons from the  $\phi$  meson decay traverse the CIP at large angles to the radial direction, which can set off multiple pads in the same layer. The simulation tends to underestimate the number of CIP pads set off by a track [209], a problem which becomes more prominent for large ionisation and large angles to the radial direction. The additional pads can form additional track patterns in the trigger, leading to a higher reconstructed multiplicity and possibly a wrongly reconstructed  $z$ -vertex. The inefficiency due to this was corrected for by reweighting the simulated events.

The behaviour of this effect on the average transverse momentum of the tracks  $\langle p_T \rangle$  is

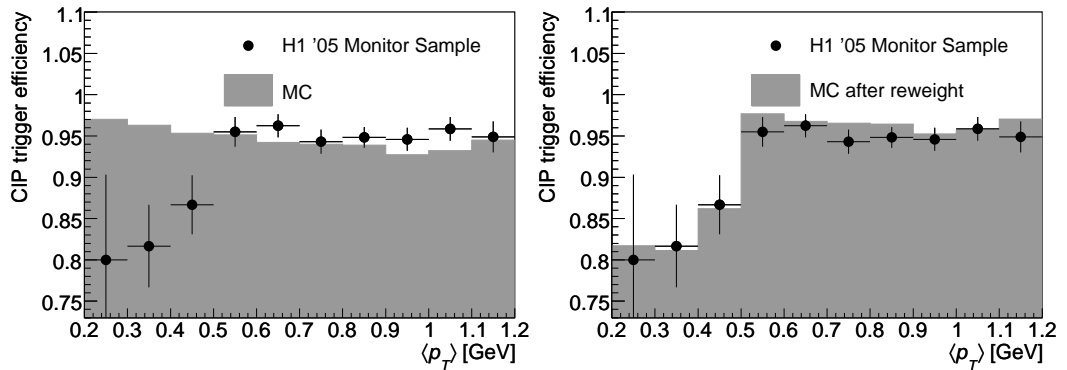


FIGURE 8.17: Overall CIP trigger efficiency versus average track transverse momentum before (left) and after (right) reweighting.

modelled using the following form:

$$\epsilon_{CIP}(\langle p_T \rangle) = C_0 + C_1 \cdot \text{erf}(C_2 \cdot \langle p_T \rangle + C_3), \quad (8.11)$$

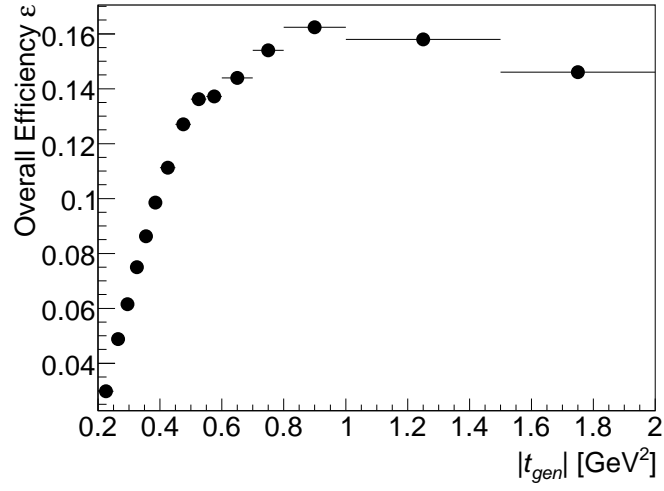
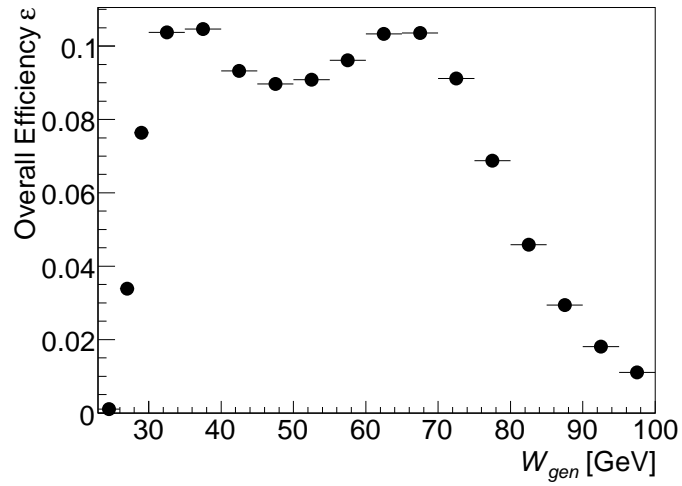
whereas the behaviour in the simulation can be modelled with a straight line. The overall CIP trigger efficiency before and after reweighting is shown in figure 8.17.

#### 8.5.4 Veto Efficiencies

The inefficiency of the vetoes derived from the time-of-flight (ToF) systems due to noise and coincidences with cosmic ray and beam halo particle initiated events can be determined from randomly triggered events and amounts to less than 3 permille. The rejection of events due to particles produced in the  $ep$  interactions crossing the scintillators outside of the allowed timing windows is harder to estimate. From special runs without veto conditions it is known that the rejection of DIS events with an electron detected in the SpaCal is less than 3%. This can serve as an upper bound for  $\phi$  photoproduction events which have a much lower multiplicity of charged particles produced.

### 8.6 Overall Efficiency

The overall efficiency (including acceptance, reconstruction- and trigger efficiency, with all weights applied) lies between 4 and 15%. The lowest values are found at low  $|t|$  (see figure 8.18). In  $W$ , all the measurement bins are inside the plateau region (see figures 8.19). The overall efficiency is not dominated by a single cut; the largest loss is due to the limited detector acceptance (see table 8.3 for an overview of efficiencies).

FIGURE 8.18: *Total efficiency versus  $|t|$ .*FIGURE 8.19: *Total efficiency versus  $W$ .*

Cut	Events	Elastic $\phi$		Proton diss. $\phi$		All $\phi$	
		Eff.	Eff. cum.	Eff.	Eff. cum.	Eff.	Eff. cum.
Signal	61440	100.0%	100.0%	100.0%	100.0%	100.0%	100.0%
Acceptance	38789	63.1%	63.1%	78.3%	78.3%	70.2%	70.2%
+ at least two tracks	27151	70.0%	44.2%	80.7%	63.2%	75.5%	53.0%
+ track selection	25251	93.0%	41.1%	94.0%	59.4%	93.6%	49.6%
+ exactly two tracks	19982	79.1%	32.5%	64.3%	38.2%	70.9%	35.2%
+ pion vertex fit	19686	98.5%	32.0%	98.7%	37.7%	98.6%	34.7%
Reconstructed events	28508	144.8%	46.4%	119.1%	44.9%	131.8%	45.7%
+ Opposite charge	28210	99.0%	45.9%	99.3%	44.6%	99.1%	45.3%
+ $\phi$ mass window	23294	82.6%	37.9%	83.8%	37.4%	83.1%	37.7%
+ $p_T$ cut	20200	86.7%	32.9%	92.3%	34.5%	89.3%	33.6%
+ $dE/dx$ cut	18186	90.0%	29.6%	90.5%	31.2%	90.3%	30.4%
+ $z$ -vertex cut	16406	90.2%	26.7%	91.3%	28.5%	90.7%	27.5%
+ unassociated energy cut	11997	73.1%	19.5%	59.4%	16.9%	66.5%	18.3%
+ at least two FTT tracks	11274	94.0%	18.4%	93.4%	15.8%	93.7%	17.2%
+ max. three FTT tracks	10431	92.5%	17.0%	92.2%	14.6%	92.4%	15.9%
+ No LAr IF activity	10337	99.1%	16.8%	98.9%	14.4%	99.0%	15.7%
+ CIP trigger	9007	87.1%	14.7%	88.4%	12.7%	87.7%	13.8%
+ Scintillator vetoes	8997	99.9%	14.6%	98.3%	12.5%	99.2%	13.7%

TABLE 8.3: *Simulated efficiencies of the various cuts applied for the pomeron trajectory measurement phase space. Note that the lines above “Reconstructed Events” quote efficiencies for events with generated kinematical quantities within the analysis bin grid, whilst the lines below do this with regards to the reconstructed kinematic quantities; efficiencies above 100% are thus caused by migrations into the analysis bins.*

## Chapter 9

# Separation of Elastic and Proton Dissociative Events

*Not to be absolutely certain is, I think, one of the essential things in rationality.*

BERTRAND RUSSELL [210]

In order to separate elastic events from events where the proton dissociates into a low mass state  $Y$ , detectors in the forward region of H1 (see section 4.6 for details) are used to identify particles belonging to  $Y$ . These detectors are the plug calorimeter, the forward muon detector FMD and the forward tagging system FTS with scintillators at  $z = 26$  m and  $z = 28$  m.

Whilst there is much more response from these detectors for dissociative events than for elastic events, there is a sizeable fraction of inelastic events not causing any response due to inefficiencies and acceptance limitations. In addition, part of the elastic events will cause a response of the forward detectors, either because the scattered proton hits the beam pipe (more frequent for large  $|t|$ ) or because of beam induced background or electronic noise. The extraction of the number of elastic and inelastic events thus has to be done by an unfolding procedure from the numbers of tagged and untagged events. The unfolding relies on the Monte Carlo simulation of the forward region. The forward simulation is, especially for the detectors far downstream, beset with large uncertainties due to the large amounts of material (HERA magnets) and the changing magnetic fields (beam optics). In addition, electronic noise and beam induced background (subsumed under the term “noise”) are not included in the simulation and have to be treated separately, see the following section.

Unfortunately, also the acceptance and efficiency of the forward detectors, especially the forward muon detector, are badly described in the simulation and have to be tuned to the data by discarding hits.

In order to obtain a high tagging efficiency combined with a low sensitivity to noise, an OR-combination of the following four criteria is used:

- At least one scintillator hit in the FTS 26 m station.
- At least one scintillator hit in the FTS 28 m station.
- At least two hit pairs in the forward muon detector.
- At least 5 GeV of reconstructed energy in the plug calorimeter.

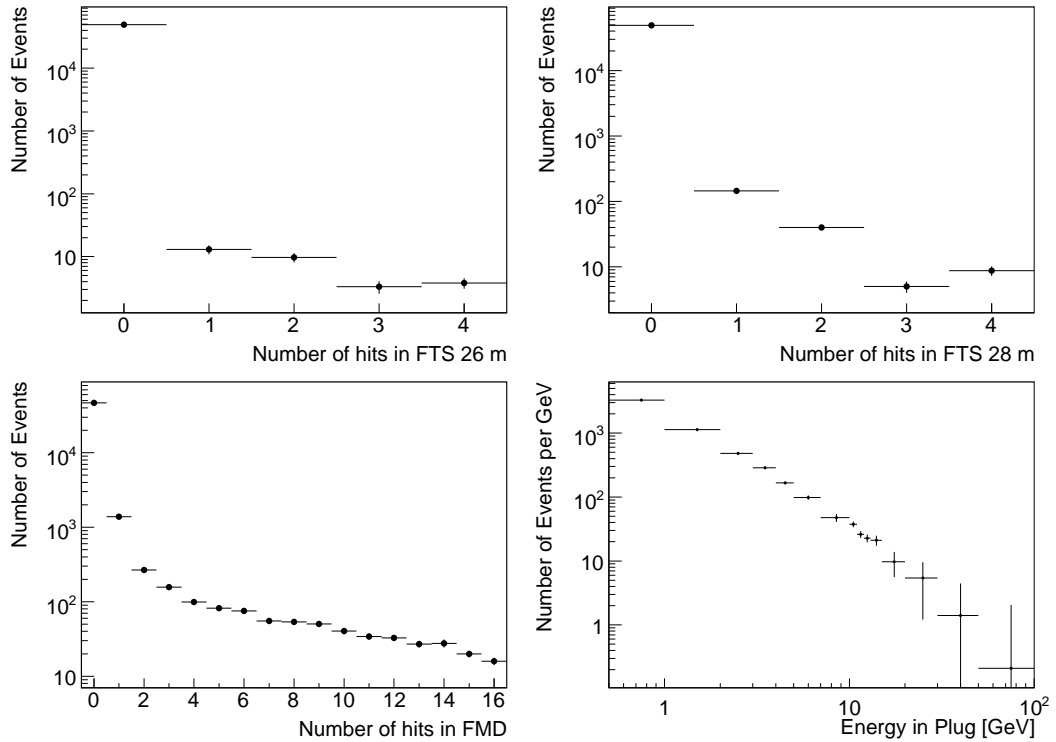


FIGURE 9.1: *Noise distributions for the forward detectors extracted from random triggered events, weighted with the inverse  $\phi$  trigger prescales. The top distributions show the number of hits in the FTS stations at 26 and 28 m. The bottom left distribution shows the number of hits in the forward muon system, whereas the bottom right panel shows the energy deposit in the plug calorimeter. In the plug histograms, events with no measured energy are not shown.*

## 9.1 Treatment of Detector Noise

Detector signals can be caused by the final state particles of an  $ep$  interaction, interactions of beam particles with material along the beamline and by electronic noise within the detector and its readout chain. Whilst the first case is covered by the simulation, the latter two are usually not. For the forward detectors, noise and beam induced contributions are not simulated, but occur in a significant fraction of the events. For the  $\rho^0$  analysis [17] and the present work, a framework to estimate these effects using randomly triggered events was developed.

The following procedure is applied: Randomly triggered events from the runs used in the analysis are selected if they do not fire any of the vetoes applied in the  $\phi$  triggers. For these events, the response of the forward detectors is histogrammed, weighted with the inverse sum of the prescales of the  $\phi$  triggers<sup>1</sup> (see figure 9.1). In addition, a histogram of the inter-correlation of the tags is produced, see figure 9.2.

The addition of the noise to the simulated events proceeds as follows:

- A combination of tags is diced according to the correlation distribution.

<sup>1</sup>This weighting is essential because random trigger events are recorded at a constant rate, while the  $\phi$  trigger is most active towards the end of a luminosity fill, where background conditions are on average more favourable.

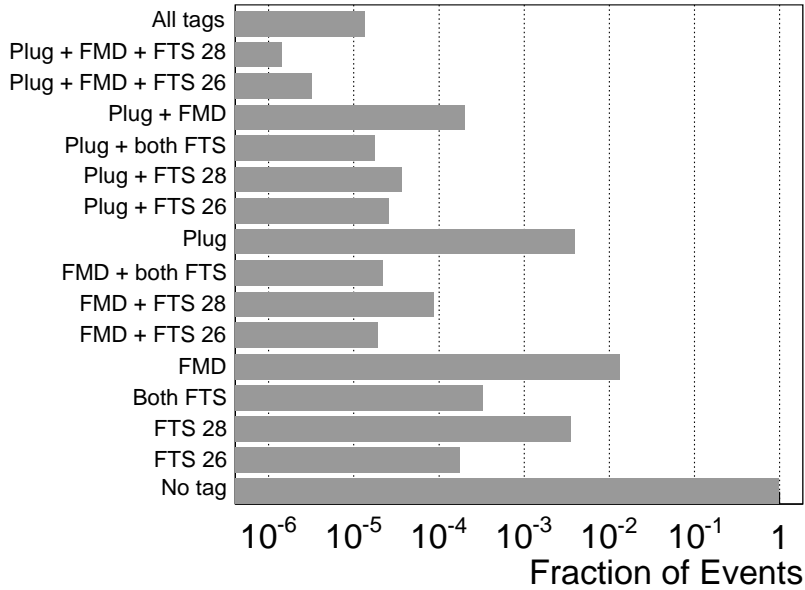


FIGURE 9.2: Correlation of noise in the forward detectors for all combinations of forward tags. Note that “noise” also includes beam induced background and overlay events and that here, tags are exclusive, i.e. “FTS 26” stands for FTS 26 m station and nothing else is on.

- For every sub-detector, the noise histogram is split at the value required for a tag, e.g. between one and two hits for the forward muon detector.
- Depending on whether the detector under consideration was specified as tagged or not in the first step, a number of hits/energy is diced either from the no-tag or the tag part of the noise histogram.
- The diced value is added to the simulated number of hits/energy.

## 9.2 Simulation of Forward Detectors

### 9.2.1 The Forward Muon Detector

The simulation of the forward muon detector is relatively coarse and neglects several sources of inefficiencies. In order to describe the hit multiplicity spectra, about 10% of the simulated hits have to be thrown away; this still does not lead to a good description of the multiplicity, but to a tagging efficiency in broad agreement with the data (see figure 9.3).

### 9.2.2 The Forward Tagging System

The simulation of the FTS is beset with large uncertainties; even though the HERA magnets are simulated in detail, most of the other material between the detector and the scintillators 26 and 28 m downstream are not. It therefore does not come as a surprise that the hit multiplicities in the forward tagger are badly described. The tagging efficiency on the other hand is in accordance with the data to better than 20% for each station. The 28 m station efficiency is over- and the 26 m station efficiency is underestimated, the overall FTS tagging efficiency ends up being in agreement with the data, see figure 9.4.

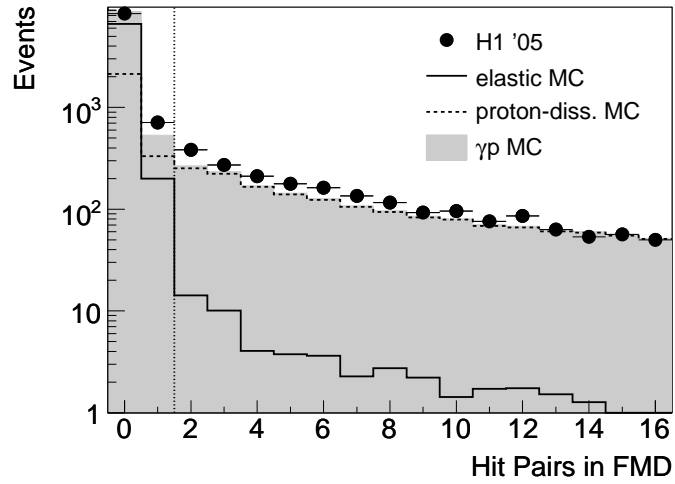


FIGURE 9.3: Number of hit pairs in the FMD after applying the  $\phi$  selection and the addition of noise from random triggered events and the removal of 10% of the non-noise hits.

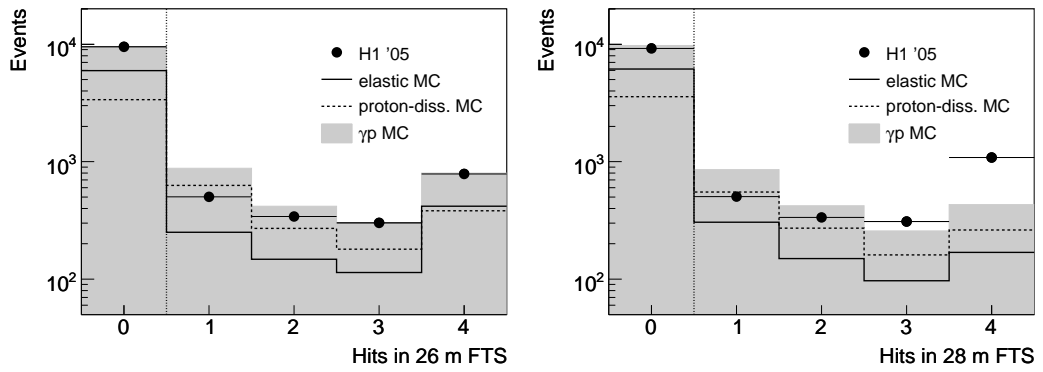


FIGURE 9.4: Hit multiplicity distributions for the 26 m (left) and 28 m (right) FTS stations after the addition of noise from random trigger events.

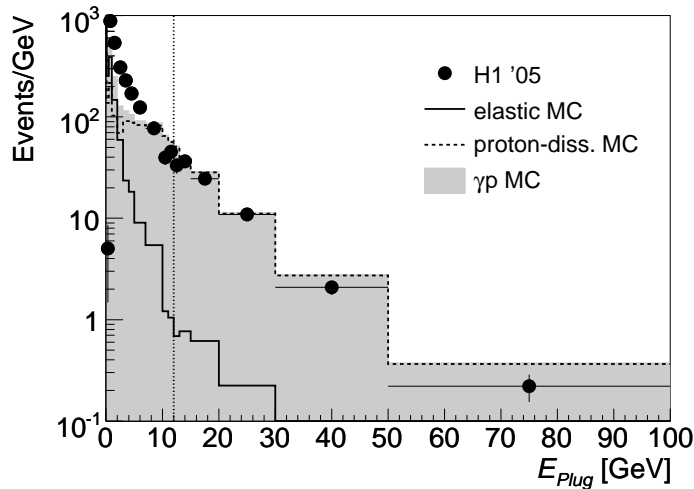


FIGURE 9.5: *Energy measured in the plug calorimeter after the addition of noise from random triggered events and degrading the simulated energies to 75% of their simulated values.*

### 9.2.3 The Plug Calorimeter

The plug calorimeter simulation tends to overestimate the amount of energy deposited; the simulated energy has to be reduced to 75% in order to match the data. Noise is not simulated and has to be added from random trigger events. It appears however that the noise is induced in part by activity in other parts of the detector and the random trigger sample thus underestimates the plug noise, see figure 9.5. Correspondingly a high cut of 12 GeV is chosen for the plug tag.

## 9.3 Tagging Efficiencies

The efficiency of the forward tags depends on  $t$ , the transverse deflection of the proton remnant and on its mass,  $M_Y$ . Whilst the “near” detectors plug and FMD require large  $M_Y$  and  $|t|$ , the FTS sensitivity is more uniform and thus less dependent on the badly known  $M_Y$  spectrum (see figure 9.6). The tagging efficiencies versus  $|t|$  and the corresponding mis-tagging efficiencies for elastic events are shown in figure 9.7. The measured and simulated  $t$  spectra with the three different tags are shown in figure 9.8. The corresponding spectra for events with- and without a tag are displayed in figure 9.9. The overall tagging efficiencies and the fraction of tagged events in the data is shown in figure 9.10.

## 9.4 Unfolding Procedure

The numbers of elastic  $N_{elas}$  and proton-dissociative events  $N_{pdis}$  are derived from the number of events with a forward tag  $N_{tag}$  and those without  $N_{untag}$  using the tagging efficiencies for elastic  $\epsilon_{elas}$  and proton dissociative  $\epsilon_{pdis}$ . The numbers of tagged and untagged events are

$$N_{tag} = \epsilon_{elas} \cdot N_{elas} + \epsilon_{pdis} \cdot N_{pdis} \quad (9.1)$$

$$N_{untag} = (1 - \epsilon_{elas}) \cdot N_{elas} + (1 - \epsilon_{pdis}) \cdot N_{pdis}. \quad (9.2)$$

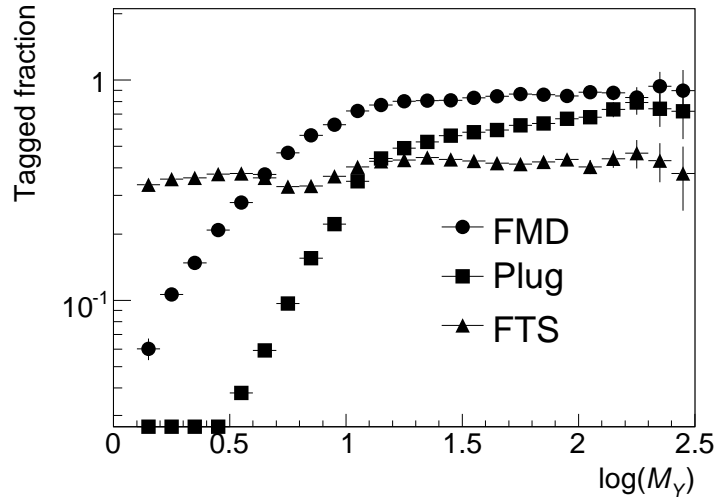


FIGURE 9.6: *Tagging efficiencies versus  $\log(M_\gamma)$ , taken from the simulation.*

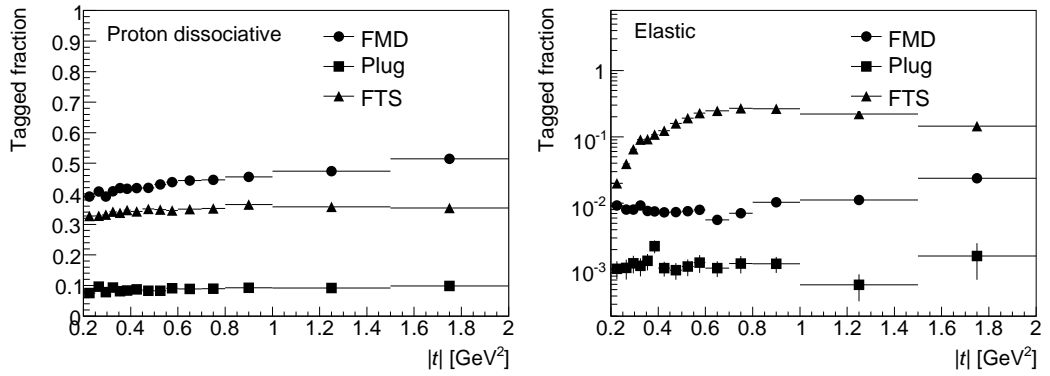


FIGURE 9.7: *Fraction of events tagged versus  $|t|$  for proton dissociative events (left) and elastic events (right).*

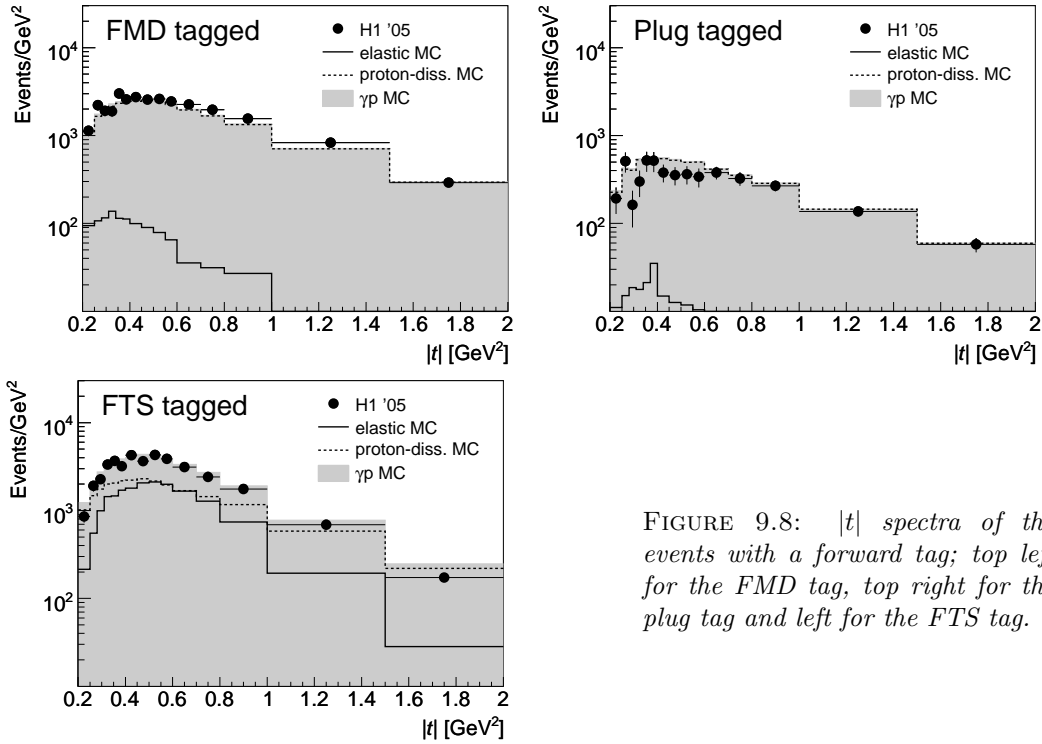


FIGURE 9.8:  $|t|$  spectra of the events with a forward tag; top left for the FMD tag, top right for the plug tag and left for the FTS tag.

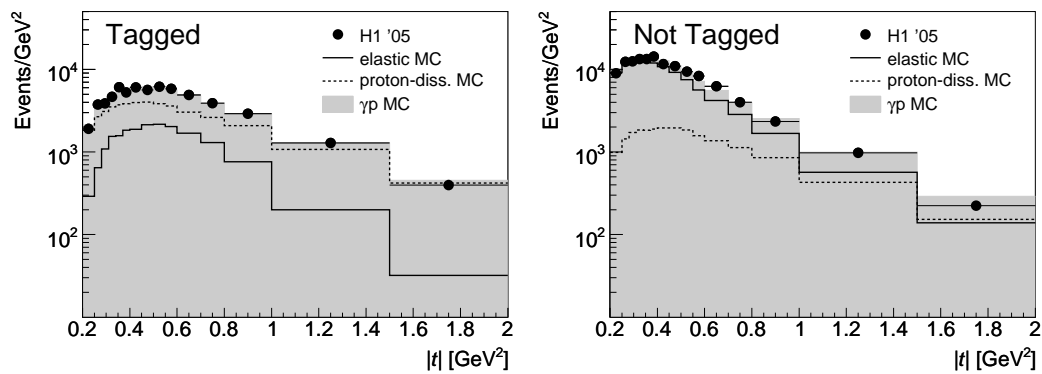
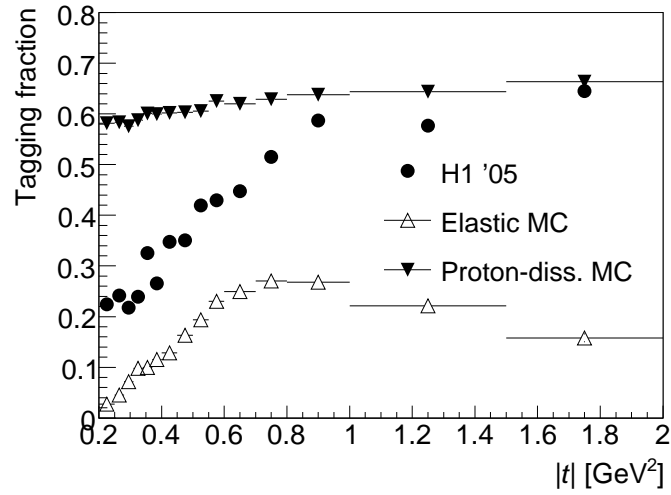


FIGURE 9.9:  $|t|$  spectra of events with any (left) and without a forward tag (right)


 FIGURE 9.10: *Fraction of tagged events versus  $|t|$  in the simulation and in data.*

Solving for  $N_{elas}$  yields

$$N_{elas} = \frac{N_{untag} + N_{tag} \cdot \left(1 - \frac{1}{\epsilon_{pdis}}\right)}{1 - \frac{\epsilon_{elas}}{\epsilon_{pdis}}} = N_{obs} \cdot \frac{\epsilon_{pdis} - f_{tag}}{\epsilon_{pdis} - \epsilon_{elas}}, \quad (9.3)$$

where a fraction  $f_{tag}$  of the total number of observed events  $N_{obs}$  has a forward tag. For the proton dissociative events, we obtain

$$N_{pdis} = N_{obs} \cdot \frac{f_{tag} - \epsilon_{elas}}{\epsilon_{elas} - \epsilon_{pdis}}. \quad (9.4)$$

The tagging efficiencies are determined for each analysis bin separately. The event numbers obtained by the unfolding then enter the cross section determination.

# Chapter 10

## Cross Section Determination

*With four parameters I can fit an elephant, and with five I can make him wiggle his trunk.*

ATTRIBUTED TO JOHN VON NEUMANN BY ENRICO FERMI [211]

### 10.1 Fitting the $\phi$ Shape

The  $\phi$  resonance shape (see also section 5.2.1) is expected to follow a relativistic Breit-Wigner distribution [195]

$$rBW(m_{KK}) = \frac{m_{KK}m_\phi\Gamma_\phi}{\left(m_{KK}^2 - m_\phi^2\right)^2 + m_\phi^2\Gamma_\phi^2} \quad (10.1)$$

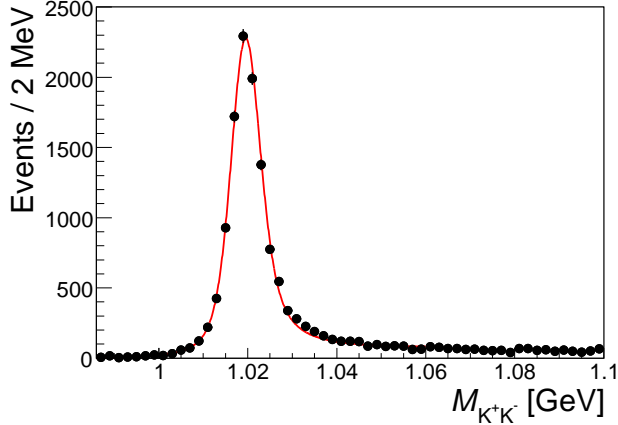
with a mass dependent width [196]

$$\Gamma_\phi = \Gamma_{\phi,0} \left( \sqrt{\frac{m_{KK}^2 - 4m_K^2}{m_\phi^2 - 4m_K^2}} \right)^3 \left( \frac{m_\phi}{m_{KK}} \right). \quad (10.2)$$

The invariant mass distribution in the data is wider because of the finite detector resolution, the resonance shape observed is thus the above shape convoluted with a Gaussian centred at 0

$$R(m_{KK}) = N \int_{-\infty}^{+\infty} rBW(\tau) \frac{1}{\sigma\sqrt{2\pi}} e^{-\frac{(\tau - m_{KK})^2}{2\sigma^2}} d\tau, \quad (10.3)$$

where  $N$  is the normalisation and  $\tau$  the integration variable. This integral has no closed analytical solution. For the purpose of fitting the  $\phi$  mass shape it was approximated numerically by replacing the integral by a sum running from twice the kaon mass to 1.1 GeV, where the value of the relativistic Breit-Wigner distribution drops to less than 0.5% of its maximum value. Tests have shown that sampling the convolution at fifty equidistant points within this interval results in a sufficient precision for the fit. The Gaussian and Breit-Wigner contributions to the width of the resonance shape cannot really be distinguished in the fit – the nominal  $\phi$  meson width was thus set to the world average value of  $\Gamma_{\phi,0} = 4.26$  MeV [95] and the experimental resolution  $\sigma$  left as a free parameter.

FIGURE 10.1: *Fitted  $\phi$  peak.*

Besides the resonant contribution, there is some background from non-resonant di-kaon production, but mainly from misidentified pions from  $\rho^0$  decays. The shape of this background distribution is found to be well described by the form

$$BG(m_{KK}) = B_1 + B_2 \frac{m_{KK} - 2m_K}{m_\phi - 2m_K} + B_3 \sqrt{\frac{m_{KK} - 2m_K}{m_\phi - 2m_K}} \quad (10.4)$$

with three free parameters  $B_1$ ,  $B_2$  and  $B_3$ .

The complete event sample used in this analysis is shown with the fit in figure 10.1 while figure 10.2 shows the fitted invariant mass distributions in the 24 bins used to measure the  $t$  dependence of the cross section versus  $W$ .

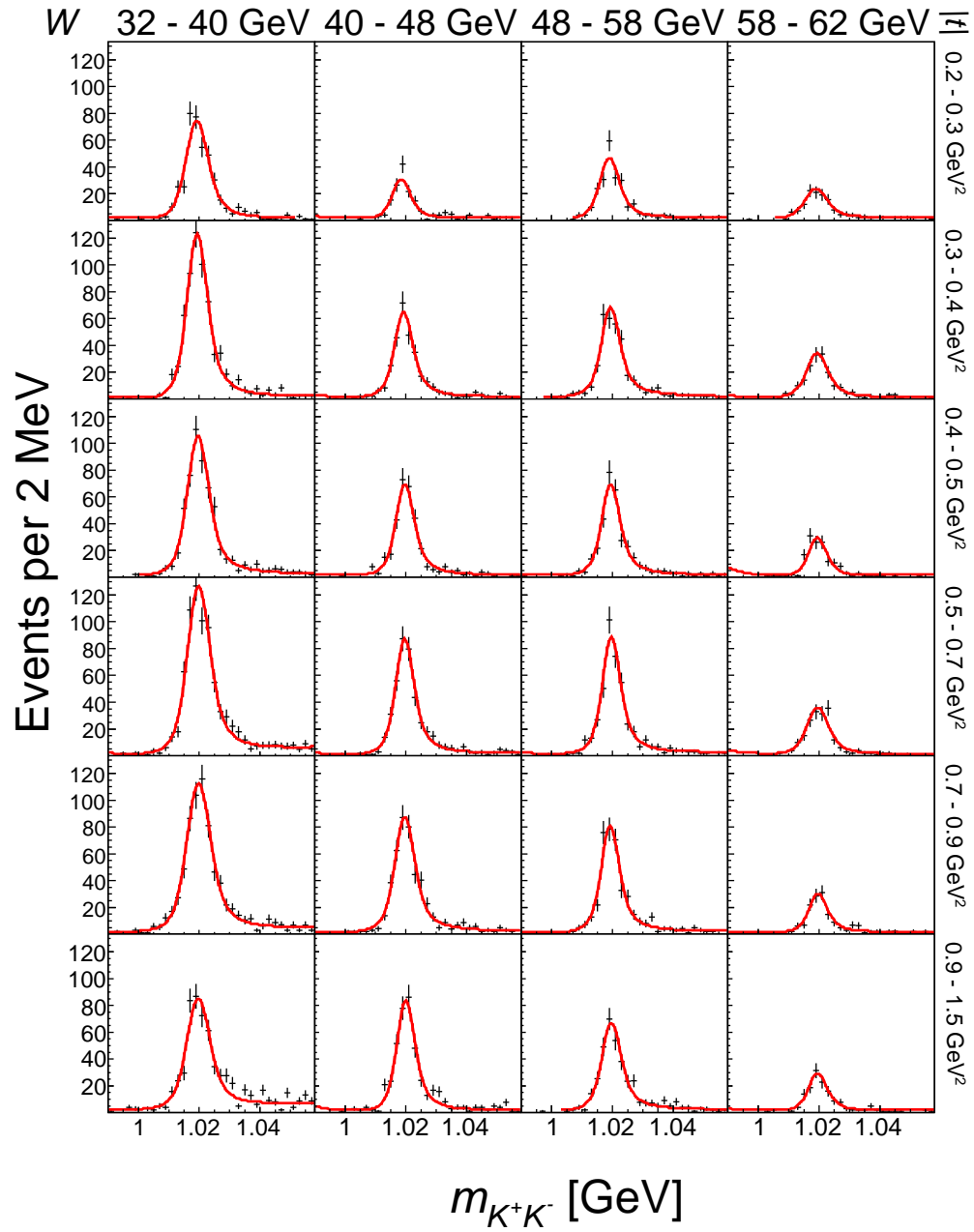
The number of  $\phi$ -meson events is obtained by integrating the signal shape between 1.01 and 1.03 GeV di-kaon mass; the error is taken from the relative normalisation error of the fit. An alternative signal extraction used to estimate systematic effects counts the number of events in the same range and then subtracts the integral of the background function; here the error is taken to be the square root of the number of signal events and the square root of the number of background events added in quadrature.

## 10.2 Cross Section Calculation

### 10.2.1 Cross Section Differential in $t$

The differential photon-proton cross section in  $t$ ,  $d\sigma_{\gamma p}/dt$ , is obtained from the number of  $\phi$  events  $N_\phi$  obtained from the fit by dividing by the luminosity  $\mathcal{L}$ , the total efficiency  $\epsilon$ , the branching fraction to charged kaons  $\mathcal{B}$ , the photon flux  $\Phi_W$  in the  $W$  range under consideration and the bin width in  $t$ ,  $\Delta t$ :

$$\frac{d\sigma_{\gamma p}}{dt} = \frac{N_\phi}{\mathcal{L} \cdot \epsilon \cdot \mathcal{B} \cdot \Phi_W \cdot \Delta t}. \quad (10.5)$$

FIGURE 10.2: Invariant mass distributions binned in  $W$  and  $t$  shown together with the fits.

### 10.2.2 $W$ Dependence of Cross Section

In order to obtain the  $W$  dependence of the cross section, an integration over  $t$  is performed in bins of  $W$ :

$$\sigma_{\gamma p} = \int_{t_{min}}^{t_{max}} \frac{d\sigma_{\gamma p}}{dt} dt, \quad (10.6)$$

where  $t_{min}$  and  $t_{max}$  are the minimum and maximum  $t$  values kinematically possible. In practice, the integral is run from  $-\infty$  to 0, as  $t_{max}$  is very close to 0 and the cross section falls off very quickly towards large negative  $t$  values. For the elastic events, the cross section is well described by an exponential:

$$\frac{d\sigma_{\gamma p}}{dt} = \left. \frac{d\sigma_{\gamma p}}{dt} \right|_{t=0} \cdot e^{bt}, \quad (10.7)$$

which can be integrated to give

$$\sigma_{\gamma p} = \frac{\left. \frac{d\sigma_{\gamma p}}{dt} \right|_{t=0}}{b}. \quad (10.8)$$

The parameters  $\left. \frac{d\sigma_{\gamma p}}{dt} \right|_{t=0}$  and  $b$  are obtained from a fit to the  $t$  dependence of the cross section, the error is obtained by standard error propagation, taking into account the correlation between the fit parameters. The ZEUS experiment [47] adopted a different convention, integrating the cross section from 0 to 0.5 GeV<sup>2</sup> which takes into account that for large  $|t|$ , a departure from exponential behaviour is seen. Extrapolating the ZEUS measurement to the full  $t$  range using their measured  $t$  slope incurs a 3% change in the total cross section.

## 10.3 Systematic Uncertainties

Besides the statistical error, the results are also affected by systematic uncertainties. These uncertainties were estimated by varying corrections and then repeating the full analysis chain. 30 variations in ten classes were considered, namely:

A: Statistical uncertainty of the correction derived from the simulation:

- A.1 the bin wise corrections are varied simultaneously by  $1\sigma$  of the Monte Carlo statistical error upward;
- A.2 the bin wise corrections are varied simultaneously by  $1\sigma$  of the Monte Carlo statistical error downward.

B: Variations in the  $W$  and  $t$  dependence of the Monte Carlo:

- B.1 increase the pomeron intercept  $\alpha(0)$  by 0.04;
- B.2 decrease the pomeron intercept  $\alpha(0)$  by 0.04;
- B.3 increase the pomeron slope  $\alpha'$  by 0.25 GeV<sup>-2</sup>;
- B.4 decrease the pomeron slope  $\alpha'$  by 0.25 GeV<sup>-2</sup>;
- B.5 increase the  $t$  slope parameter  $b_0$  by 10%;
- B.6 decrease the  $t$  slope parameter  $b_0$  by 10%.

C: Variations in the FTT efficiency (see figure 10.3 for the effects on the reweights and figure 10.4 for the corresponding efficiency distributions):

- C.1 decrease the  $p_T$  dependence by setting the reweight parameter  $A_1$  to -0.015;
- C.2 increase the  $p_T$  dependence by setting the reweight parameter  $A_1$  to 0.025;
- C.3 decrease the magnitude of the dip at  $\vartheta = 90^\circ$  by setting  $A_2$  to 0;

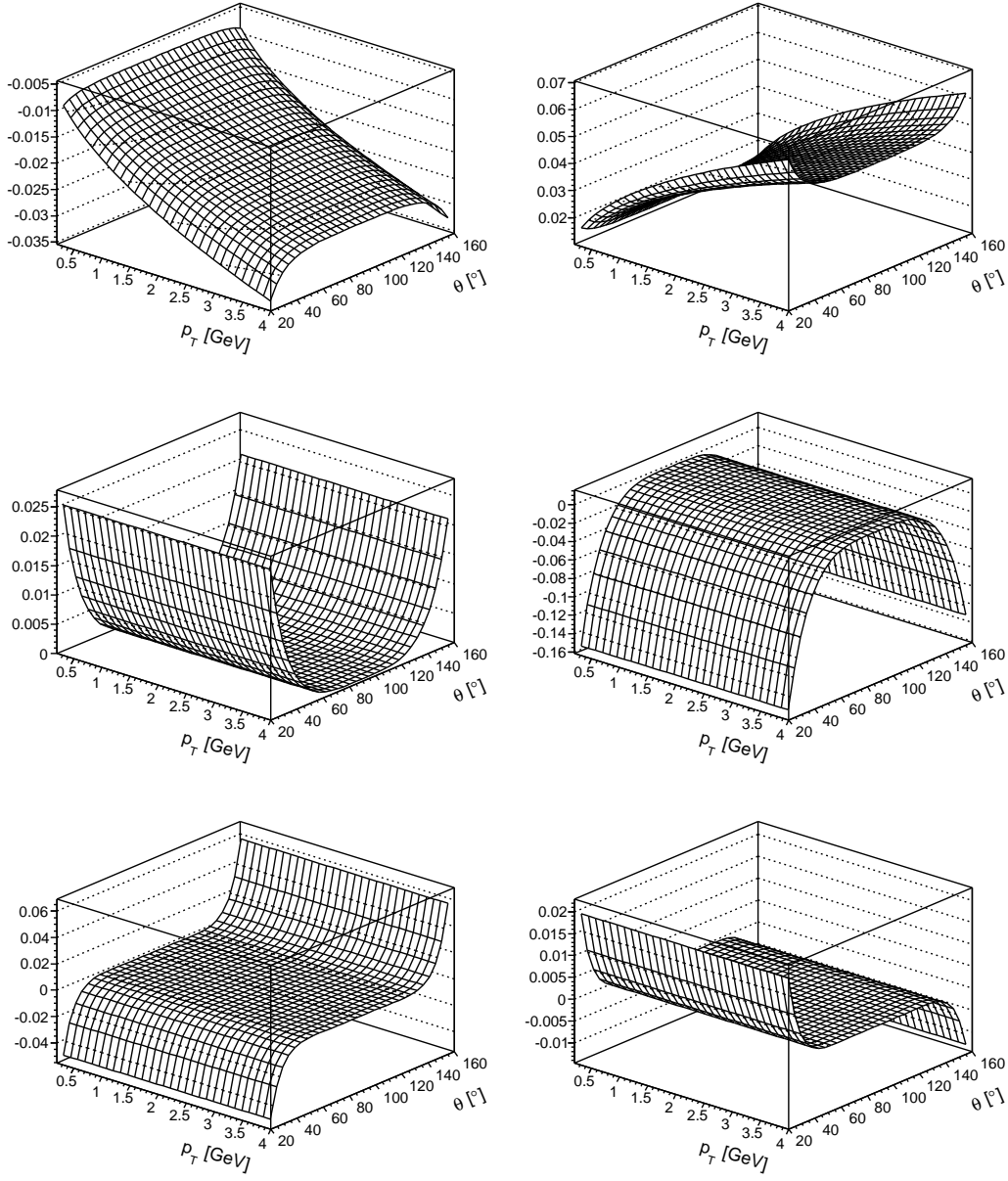


FIGURE 10.3: Changes of the MC reweight used for the study of systematic effects from the FTT trigger efficiency.

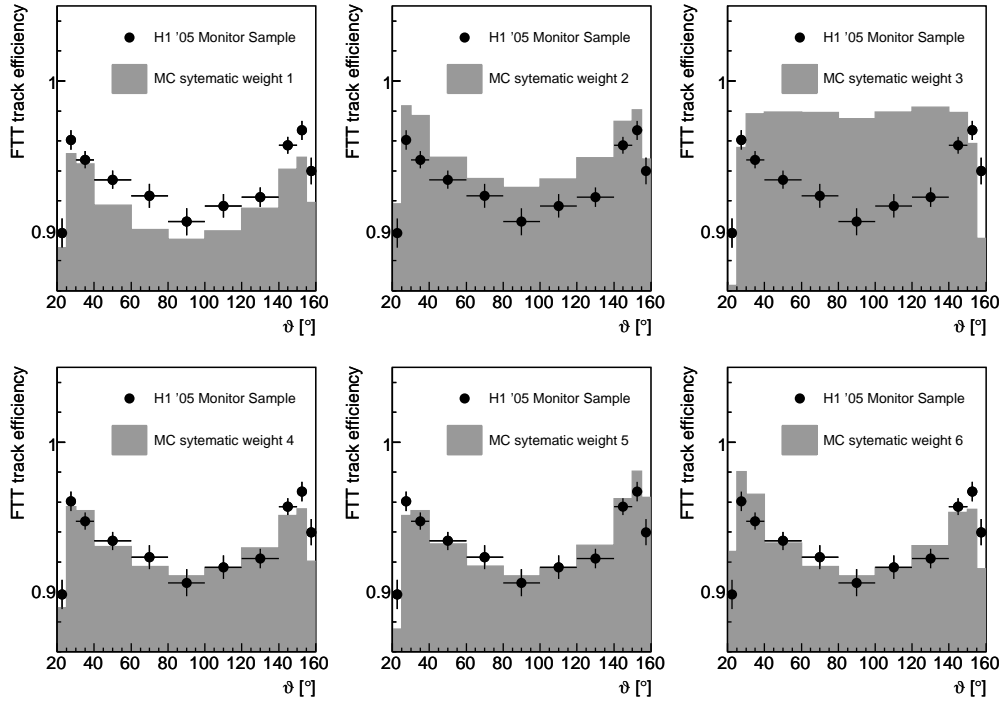


FIGURE 10.4: The result of the six systematic variations of the FTT MC reweight on the  $\vartheta$  dependence of the efficiency is compared to the efficiency obtained from the monitor sample.

- C.4 increase the magnitude of the dip at  $\vartheta = 90^\circ$  by setting  $A_2$  to  $3 \cdot 10^{-9}$ ;
- C.5 change the forward-backward asymmetry forwards by expanding around  $\vartheta = 88.5^\circ$ ;
- C.6 change the forward-backward asymmetry forwards by expanding around  $\vartheta = 92.5^\circ$ ;
- C.7 increase the reweight for the multiplicity veto and the topology condition by 20%;
- C.8 decrease the reweight for the multiplicity veto and the topology condition by 20%;
- D: Variations in the CIP efficiency:
  - D.1 increase the CIP reweight by 20%;
  - D.2 decrease the CIP reweight by 20%.
- E: Variations in the  $dE/dx$  efficiency:
  - E.1 increase the measured inefficiency of the  $dE/dx$  cut by 50%;
  - E.2 decrease the measured inefficiency of the  $dE/dx$  cut by 25%.
- F: Nuclear interactions not simulated in the Monte Carlo:
  - F.1 double the amount of additional nuclear interactions;
  - F.2 half the amount of additional nuclear interactions.
- G: Variations in the efficiency of the forward tagging:
  - G.1 induce no additional inefficiency to the FMD (default 10%);
  - G.2 induce 30% additional inefficiency to the FMD;
  - G.3 increase the FTS efficiency for tagging dissociative events by 20%;
  - G.4 decrease the FTS efficiency for tagging dissociative events by 20%;
  - G.5 tag at plug energies above 13 GeV in the simulation (12 GeV in data);

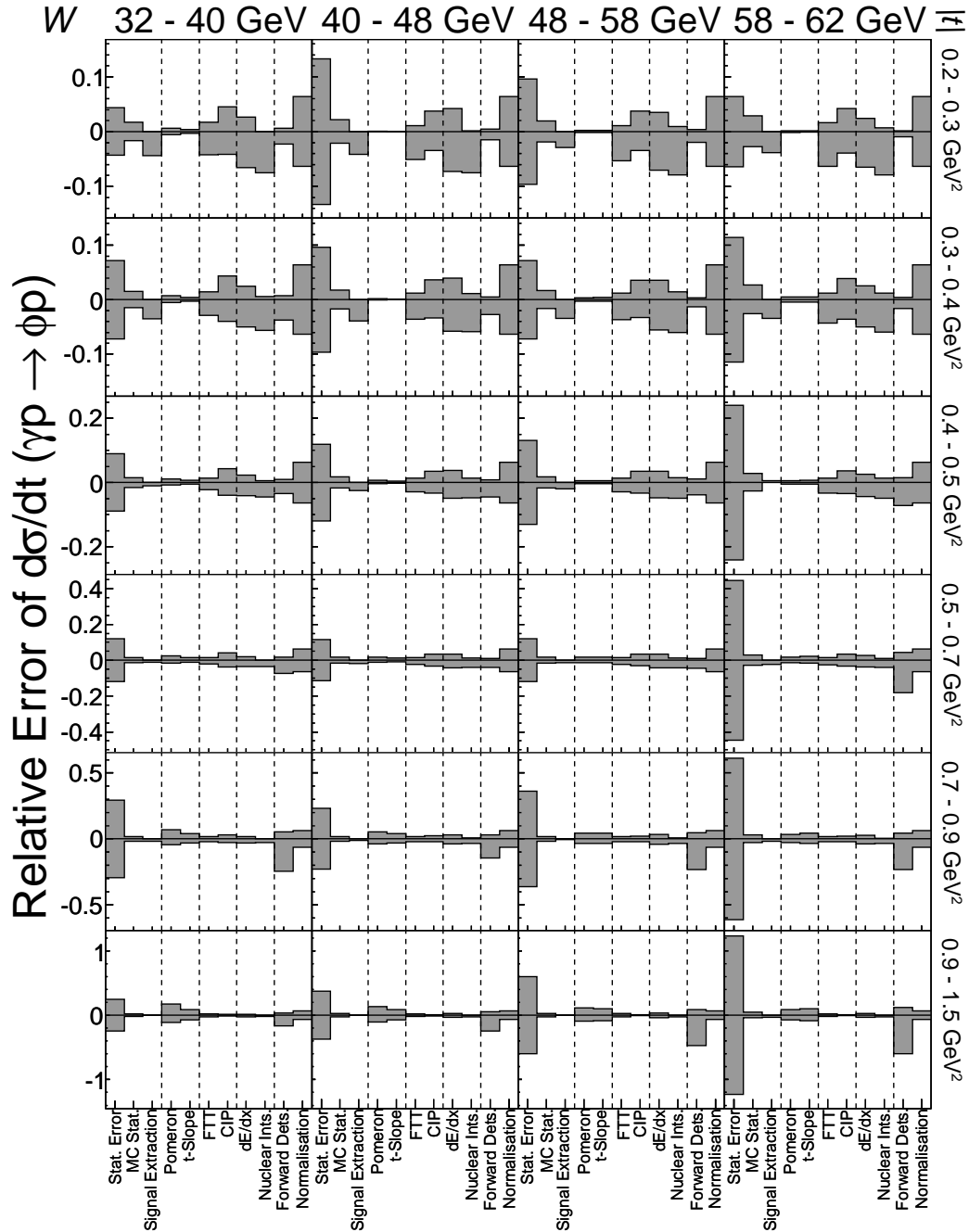


FIGURE 10.5: Relative errors on the elastic cross sections in 24 bins in  $W$  and  $t$ . The first bin in each histogram shows the statistical error, the following bins depict the systematic errors studied. The bin labelled "forward detectors" contains both contributions from efficiency variations and variations of the  $M_Y$  spectrum.

G.6 tag at plug energies above 11 GeV in the simulation.

H: Variations in the proton dissociative mass ( $M_Y$ ) spectrum. The  $M_Y$  spectrum is modelled by DIFFVM according to a  $1/M_Y^{2(1+\epsilon)}$  behaviour. This spectrum is altered according to

$$f_{M_Y}(M_Y) = \left( \frac{M_Y^2}{M_{Y,0}^2} \right)^\delta \quad (10.9)$$

with a scaling factor of  $M_{Y,0} = 5$  GeV and  $\delta$  the slope of the alteration [17, 212]:

H.1 set the slope to  $\delta = +0.15$ ;

H.2 set the slope to  $\delta = -0.15$ .

I: Global normalisation uncertainties (values commonly used in H1):

I.1 the luminosity measurement is accurate to 1.5%;

I.2 the tracking efficiency is uncertain to 2.5% per track, giving an uncertainty of 5%;

I.3 the overall FTT efficiency has an uncertainty of 3%;

I.4 the inefficiencies from the ToF system are known to 0.5%;

I.5 the inefficiency of the liquid argon calorimeter vetoes is estimated at 2%.

Adding these contributions in quadrature results in a global normalisation uncertainty of 6.4%.

The relative magnitude of the systematic errors in different areas of the phase space under study are shown in figure 10.5.

# Chapter 11

## Helicity Analysis

*What is a 'twist angle', and what is it good for?  
It's one fast and easy way to measure the twist in  
a singles yarn—whether yarn you're spinning right  
now, or yarn that's been sitting around for a while.*

HOLLY SHALTZ [213]

### 11.1 Helicity Angles and their Reconstruction

If the four-momenta of the incoming photon and the outgoing vector meson are denoted with  $v$  and  $q$  respectively, the corresponding three-vectors  $\vec{v}$  and  $\vec{q}$  can be used to define a right-handed coordinate system [214]:

$$\hat{z} = \frac{\vec{v}}{|\vec{v}|} \quad \hat{y} = \frac{\vec{v} \times \vec{q}}{|\vec{v} \times \vec{q}|} \quad \hat{x} = \frac{(\vec{v} \times \vec{q}) \times \vec{v}}{|(\vec{v} \times \vec{q}) \times \vec{v}|}. \quad (11.1)$$

If the three-momentum vector of the decay  $K^+$  in the rest frame of the  $\phi$ -meson is denoted with  $\vec{k}$ , the helicity angles  $\theta_h$  and  $\phi_h$  can be calculated:

$$\cos \theta_h = \frac{\vec{k} \cdot \vec{z}}{|\vec{k} \cdot \vec{z}|} \quad (11.2)$$

$$\cos \phi_h = \frac{\vec{y} \cdot (\vec{z} \times \vec{k})}{|\vec{z} \times \vec{k}|} \quad (11.3)$$

$$\sin \phi_h = \frac{\vec{x} \cdot (\vec{z} \times \vec{k})}{|\vec{x} \times \vec{k}|}. \quad (11.4)$$

The distributions in  $\cos \theta_h$  and  $\phi_h$  are shown in figures 11.1 to 11.4. The asymmetry between the negative and positive part of the  $\phi_h$  distribution stems from the different trigger- and reconstruction efficiencies for in- and out-bending topologies (see figure 11.5 for an illustration). Negative  $\phi_h$  correspond to the out-bending topology which is suppressed by the opening angle cut in the  $\phi$  meson trigger.

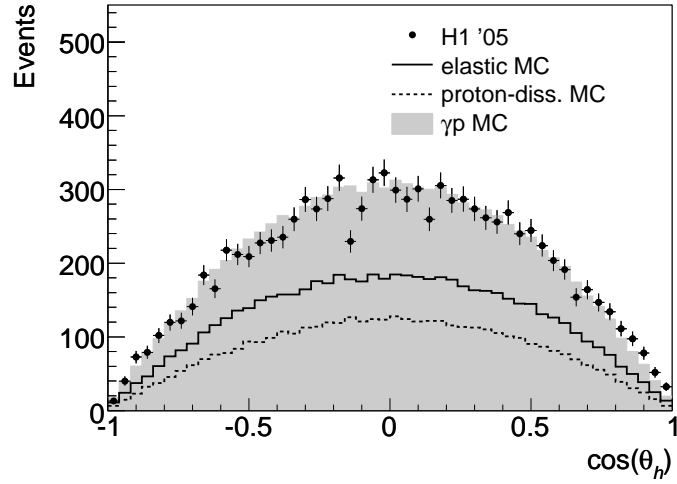


FIGURE 11.1:  $\cos \theta_h$  for the events passing the  $\phi$  selection cuts.

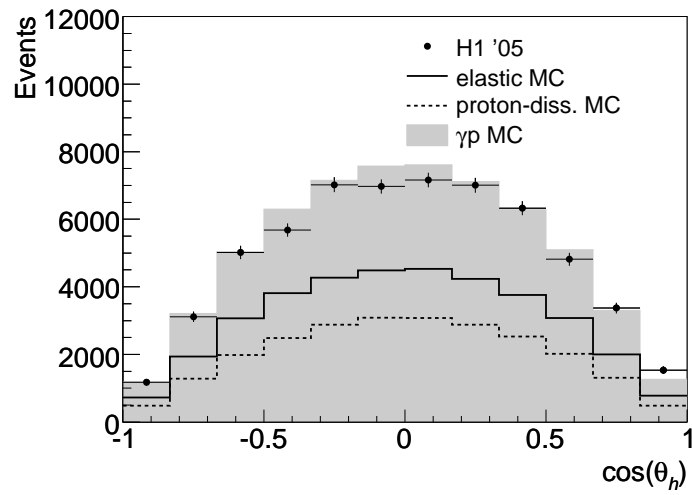
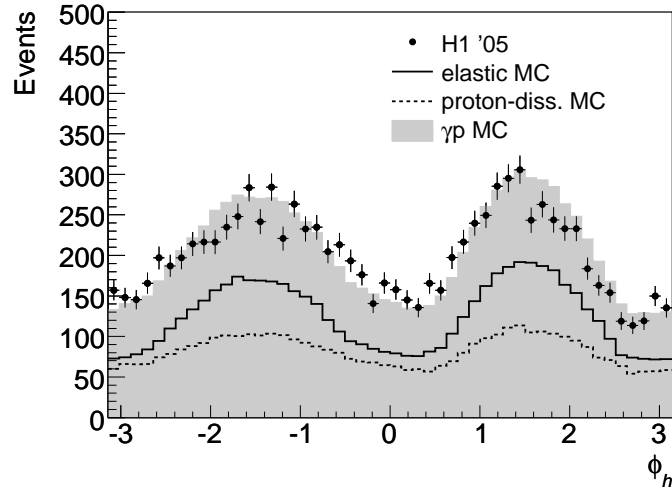
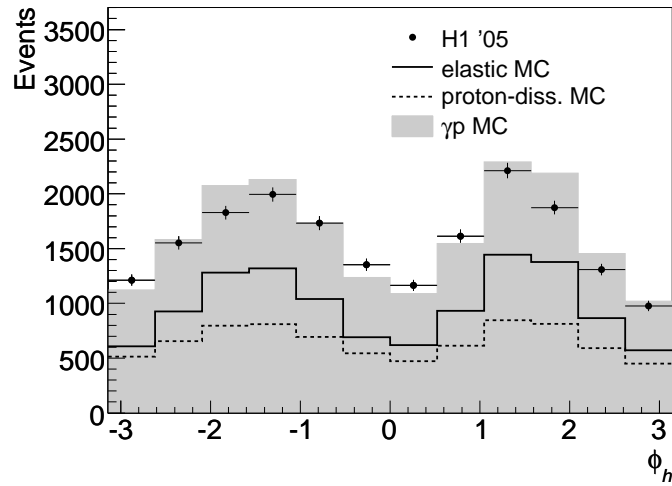


FIGURE 11.2: Number of  $\phi$  mesons in bins of  $\cos \theta_h$ .


 FIGURE 11.3:  $\phi_h$  for the events passing the  $\phi$  selection cuts.

 FIGURE 11.4: Number of  $\phi$  mesons in bins of  $\phi_h$ .

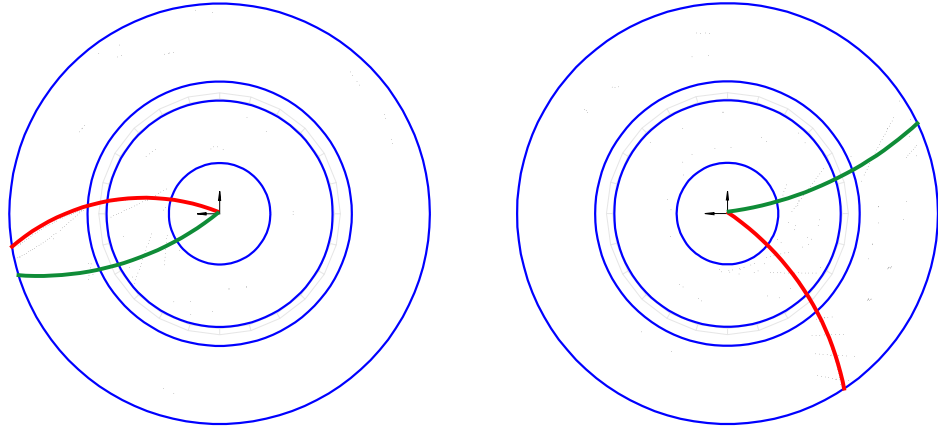


FIGURE 11.5: Displays of  $\phi$  candidate events, showing the in-bending “cowboy” (left) and the out-bending “sea-gull” (right) topologies of two oppositely charged tracks in a magnetic field.

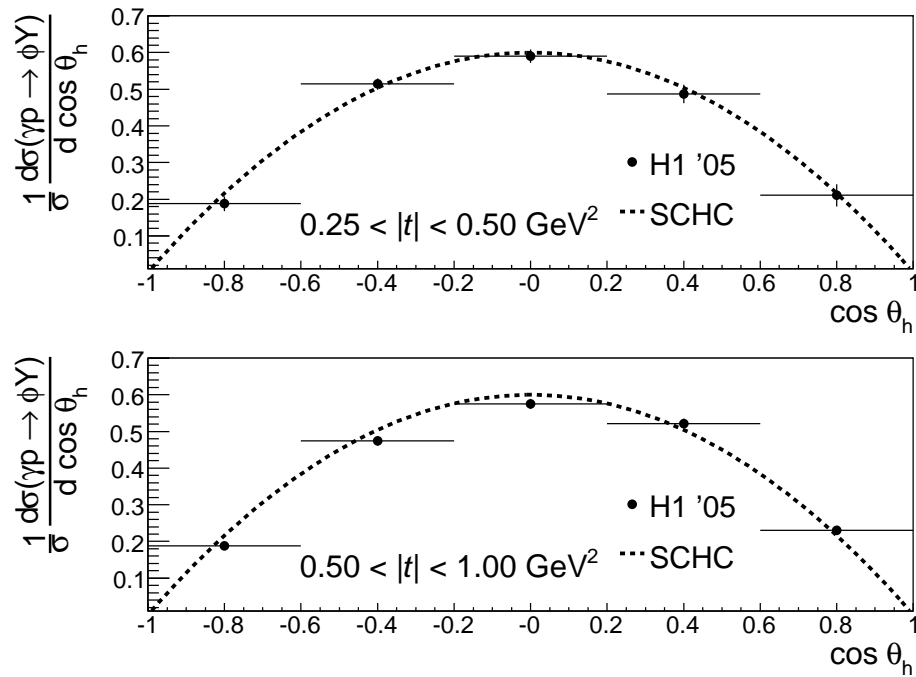


FIGURE 11.6: Inclusive cross section differential in  $\cos \theta_h$ . The dashed line shows the expectation from  $s$ -channel helicity conservation. Only statistical errors are shown.

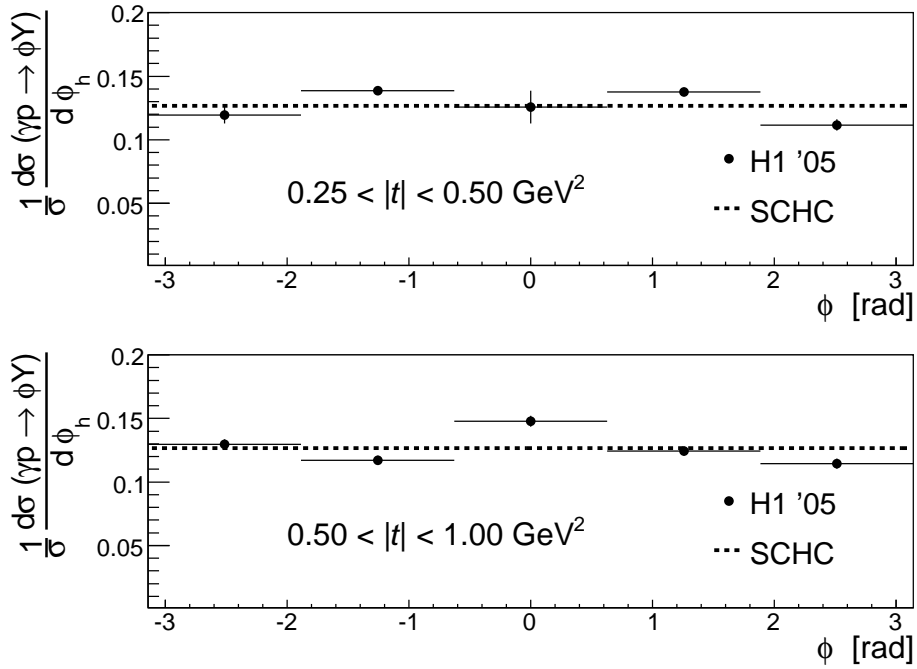


FIGURE 11.7: *Inclusive cross section differential in  $\phi_h$ . The dashed line shows the expectation from s-channel helicity conservation. Only statistical errors are shown.*

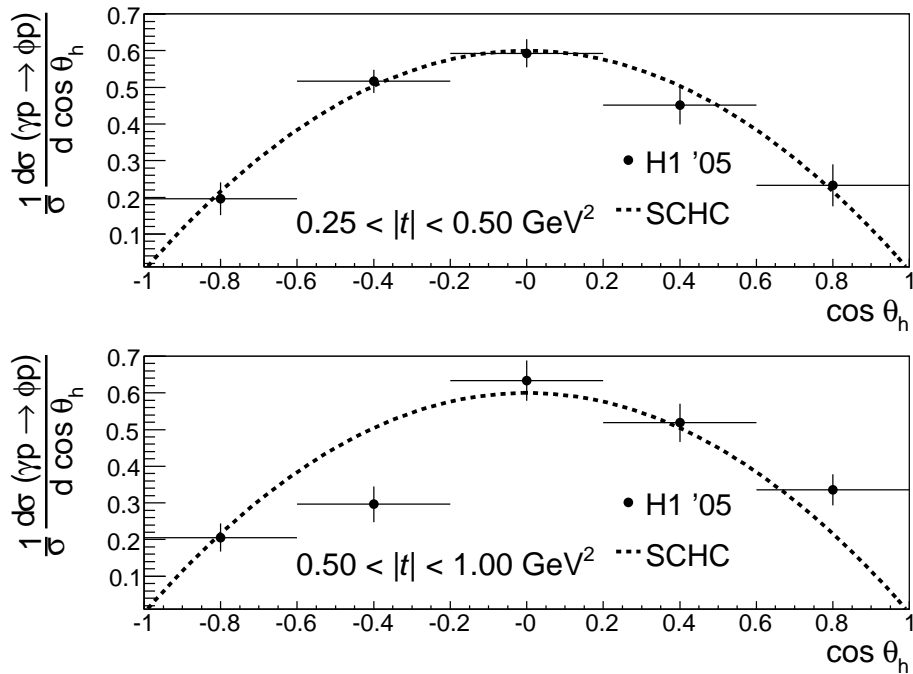


FIGURE 11.8: *Elastic cross section differential in  $\cos \theta_h$ . The dashed line shows the expectation from s-channel helicity conservation. Only statistical errors are shown.*

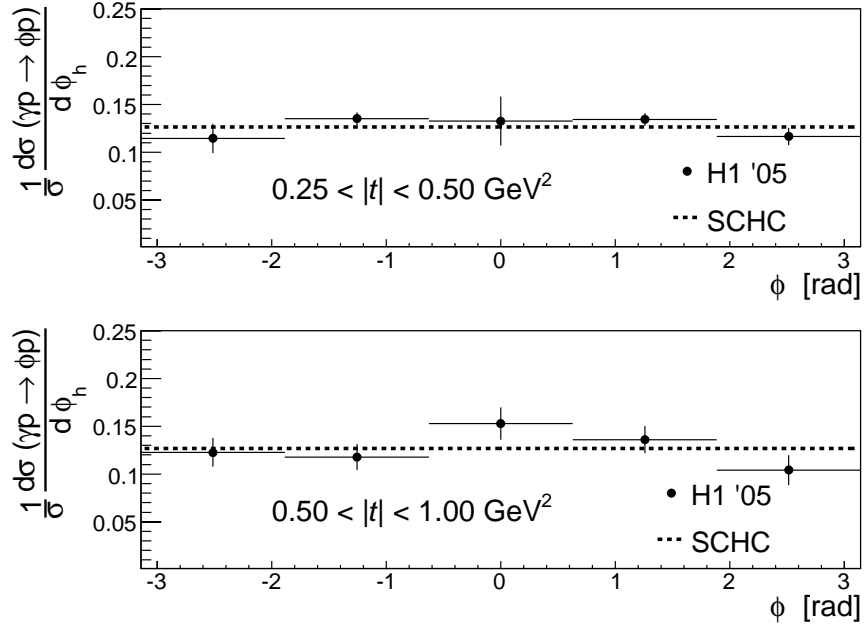


FIGURE 11.9: Elastic cross section differential in  $\phi_h$ . The dashed line shows the expectation from  $s$ -channel helicity conservation. Only statistical errors are shown.

## 11.2 Angular Dependence of Cross Sections

The angular dependence of the cross section is measured by binning the  $\phi$  meson candidates into two bins in  $t$ , each of which is subdivided into  $5 \times 5$  bins in  $\cos\theta_h$  and  $\phi_h$ . The total of 50 bins stretches the statistical power of the available sample to its edge. In every bin, the total numbers of events as well as the number of elastic and inelastic events are extracted as described in the preceding chapters. In the inelastic case the available sample is too small to make any statistical conclusion. The two-dimensional distributions obtained thus (see figures 11.6 to 11.9 for projections onto the  $\cos\theta_h$  and  $\phi_h$  axes and figures 11.10 to 11.17 for the full two-dimensional distributions in both projections including the fit) are fitted with equation 2.25, yielding the three spin density matrix elements  $r_{00}^{04}$ ,  $\text{Re}(r_{00}^{04})$  and  $r_{1-1}^{04}$ . In interpreting the results, especially for  $r_{00}^{04}$ , some care has to be taken;  $s$ -channel helicity conservation (SCHC) predicts  $r_{00}^{04}$  to be zero only for a purely transverse photon beam. As however the outgoing electron is not detected, events with values of  $Q^2$  up to  $4 \text{ GeV}^2$  pass the selection cuts. The flux of longitudinal photons is thus non-negligible and will contribute to the measured  $r_{00}^{04}$ . In the vector dominance model with SCHC,  $r_{00}^{04}$  is

$$r_{00}^{04} = \frac{Q^2}{M_\phi^2} \cdot \frac{\epsilon}{1 + \epsilon \frac{Q^2}{M_\phi^2}}, \quad (11.5)$$

where  $\epsilon$  is the ratio of the longitudinal to the transverse photon flux, which is approximately 1 in the kinematical range under study [47].  $r_{00}^{04}$  is thus expected to be  $\approx \frac{Q^2}{M_\phi^2}$  for  $Q^2 \ll M_\phi^2$ .

## 11.2 ANGULAR DEPENDENCE OF CROSS SECTIONS

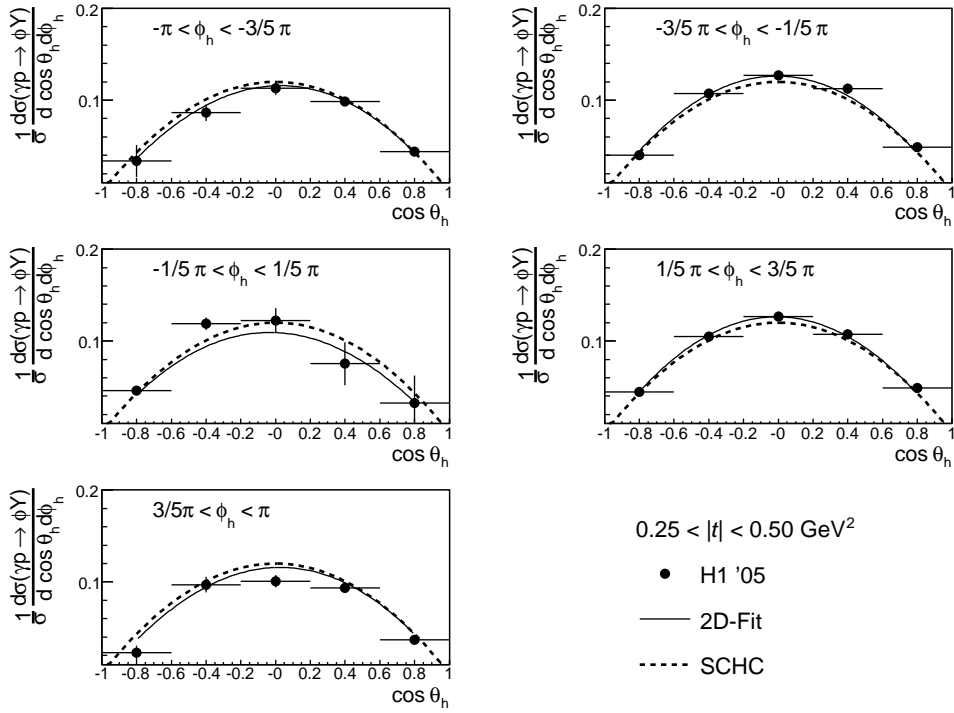


FIGURE 11.10: *The inclusive angular distribution for  $0.25 < |t| < 0.5 \text{ GeV}^2$  in slices along  $\cos \theta_h$ .*

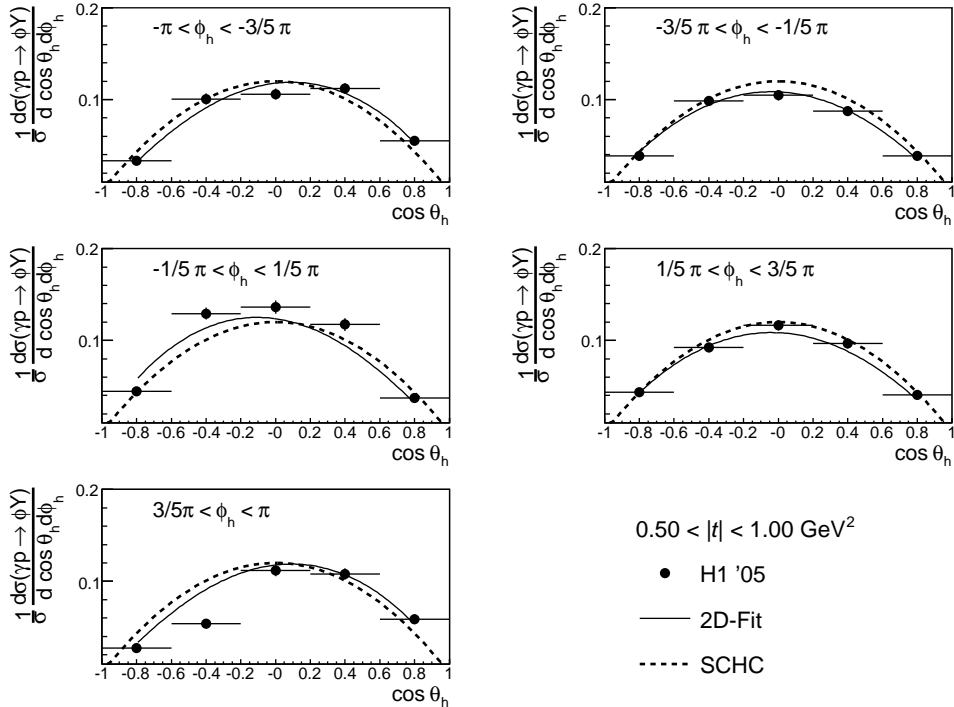


FIGURE 11.11: *The inclusive angular distribution for  $0.5 < |t| < 1.0 \text{ GeV}^2$  in slices along  $\cos \theta_h$ .*

## 11. HELICITY ANALYSIS

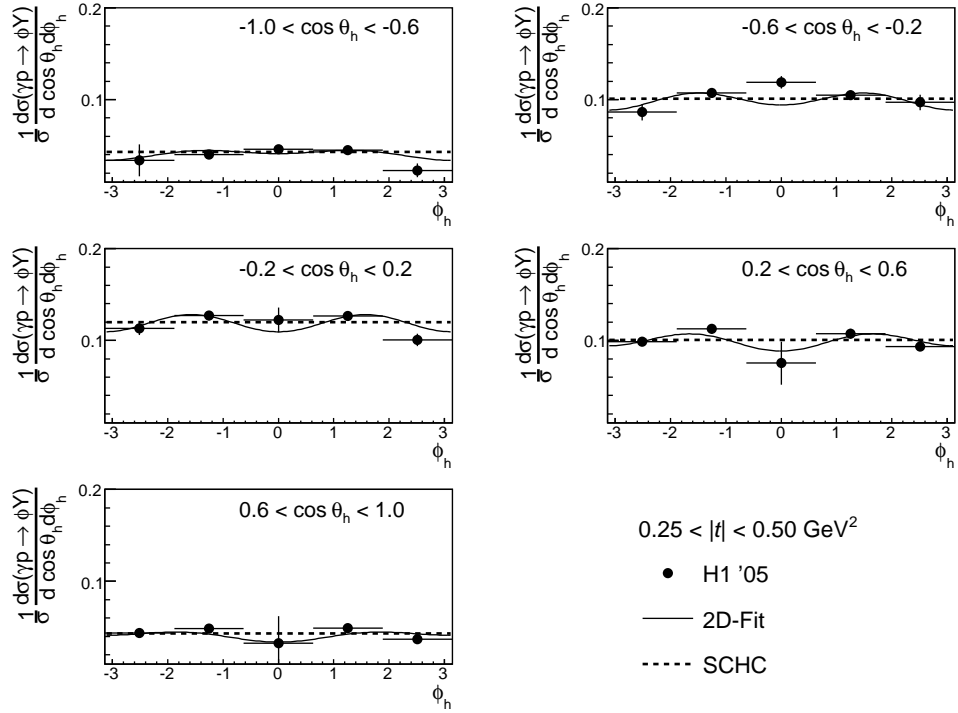


FIGURE 11.12: *The inclusive angular distribution for  $0.25 < |t| < 0.50 \text{ GeV}^2$  in slices along  $\phi_h$ .*

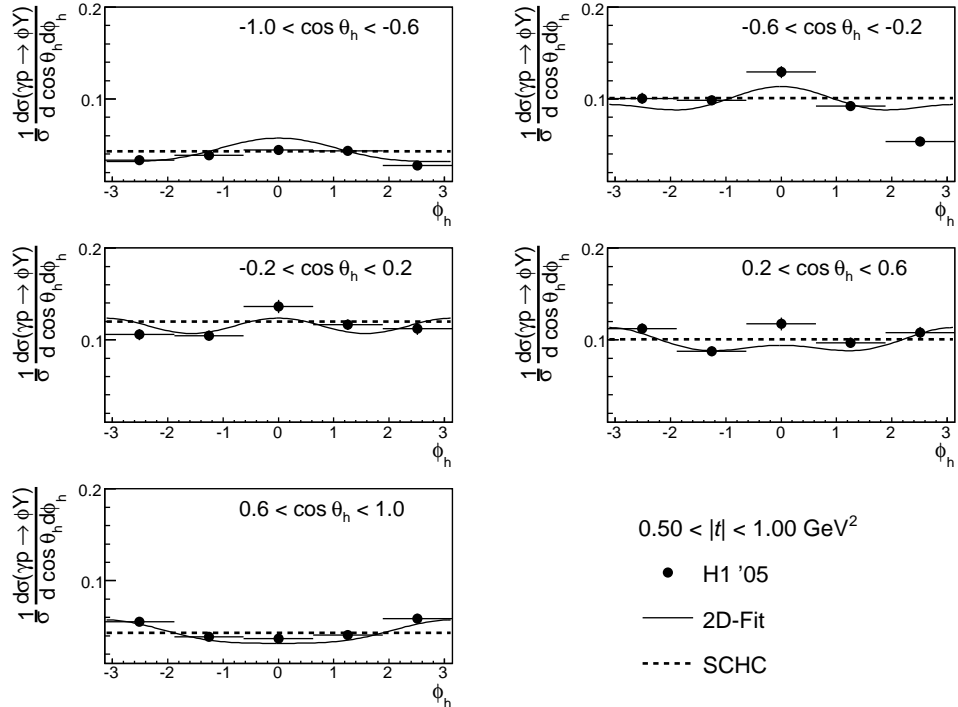
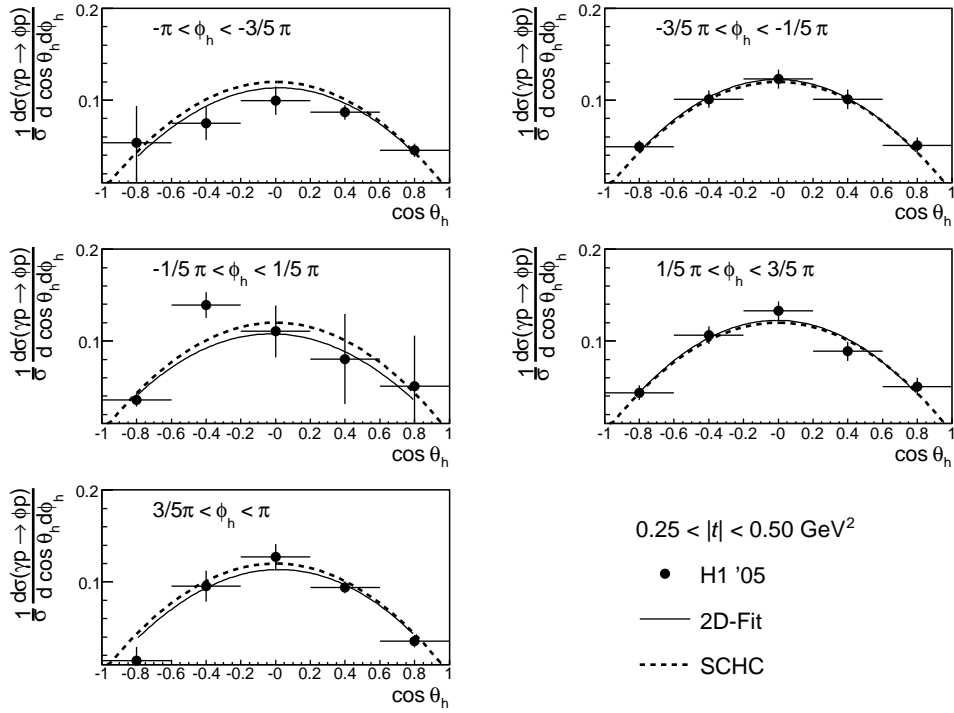
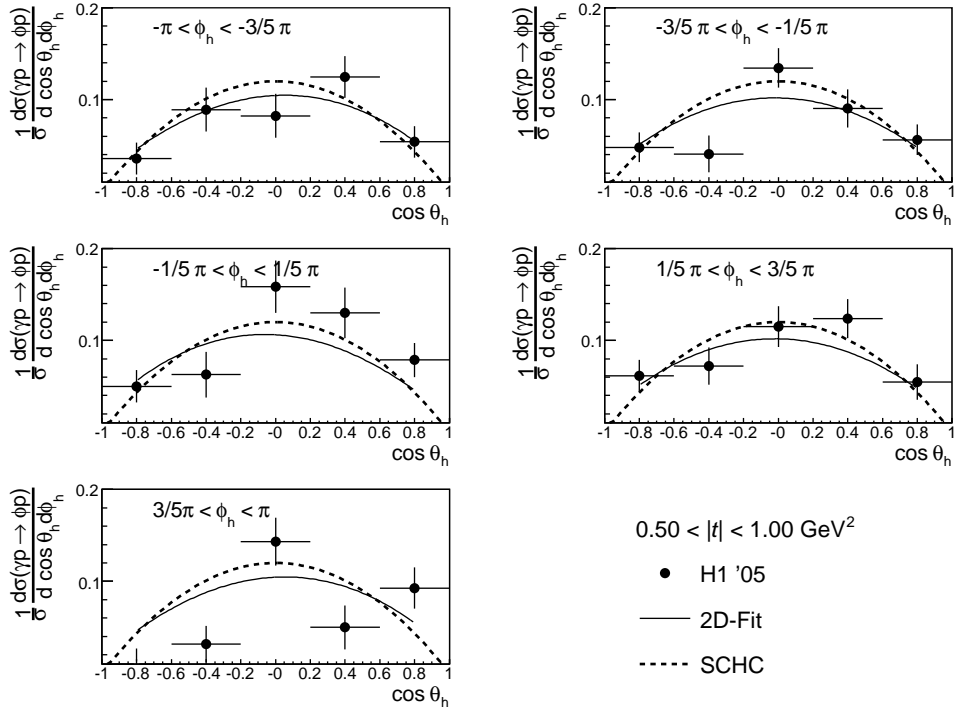


FIGURE 11.13: *The inclusive angular distribution for  $0.50 < |t| < 1.00 \text{ GeV}^2$  in slices along  $\phi_h$ .*

## 11.2 ANGULAR DEPENDENCE OF CROSS SECTIONS


 FIGURE 11.14: The elastic angular distribution for  $0.25 < |t| < 0.50 \text{ GeV}^2$  in slices along  $\cos \theta_h$ .

 FIGURE 11.15: The elastic angular distribution for  $0.50 < |t| < 1.00 \text{ GeV}^2$  in slices along  $\cos \theta_h$ .

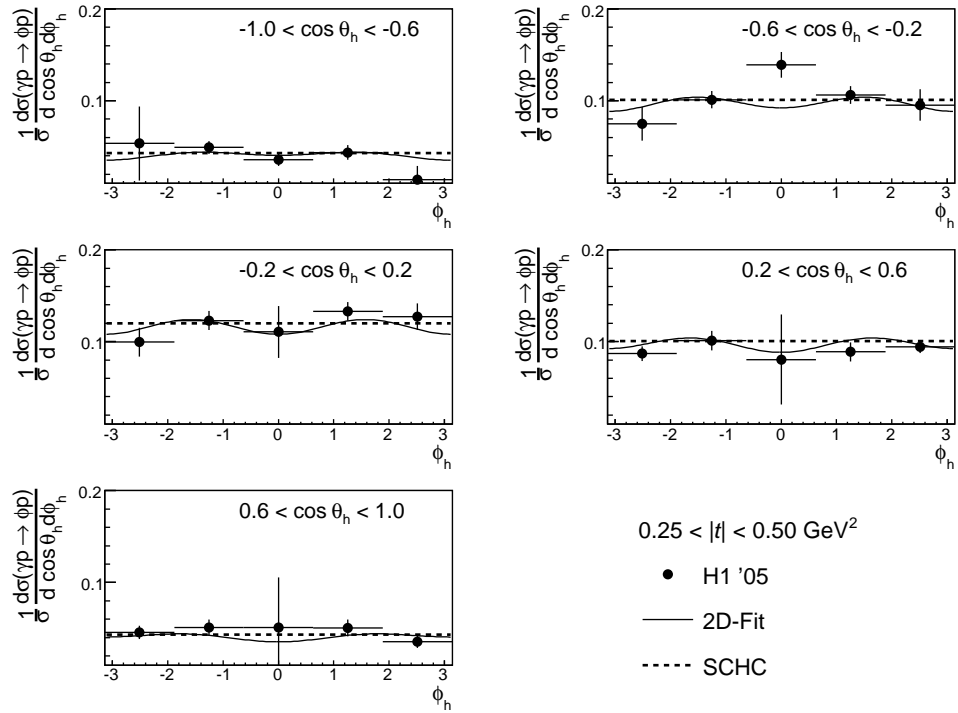


FIGURE 11.16: *The elastic angular distribution for  $0.25 < |t| < 0.5 \text{ GeV}^2$  in slices along  $\phi_h$ .*

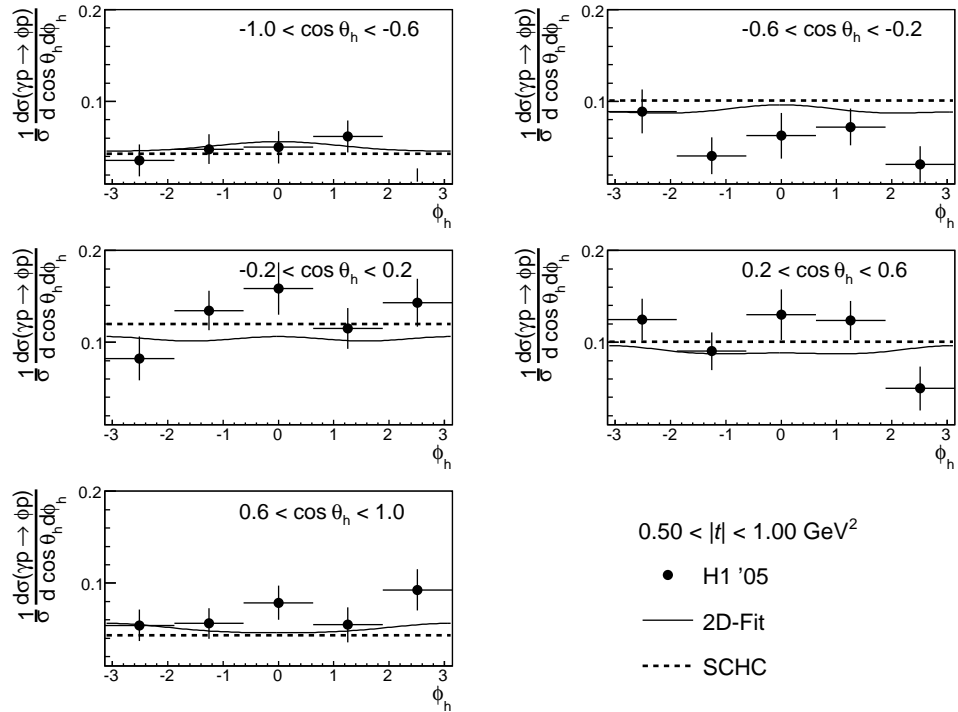
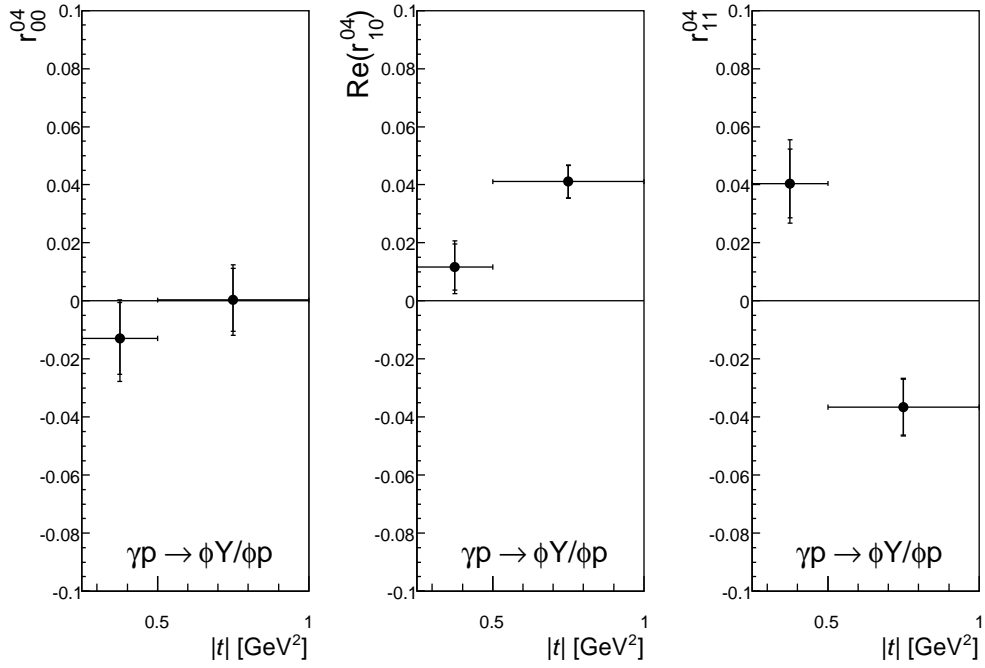
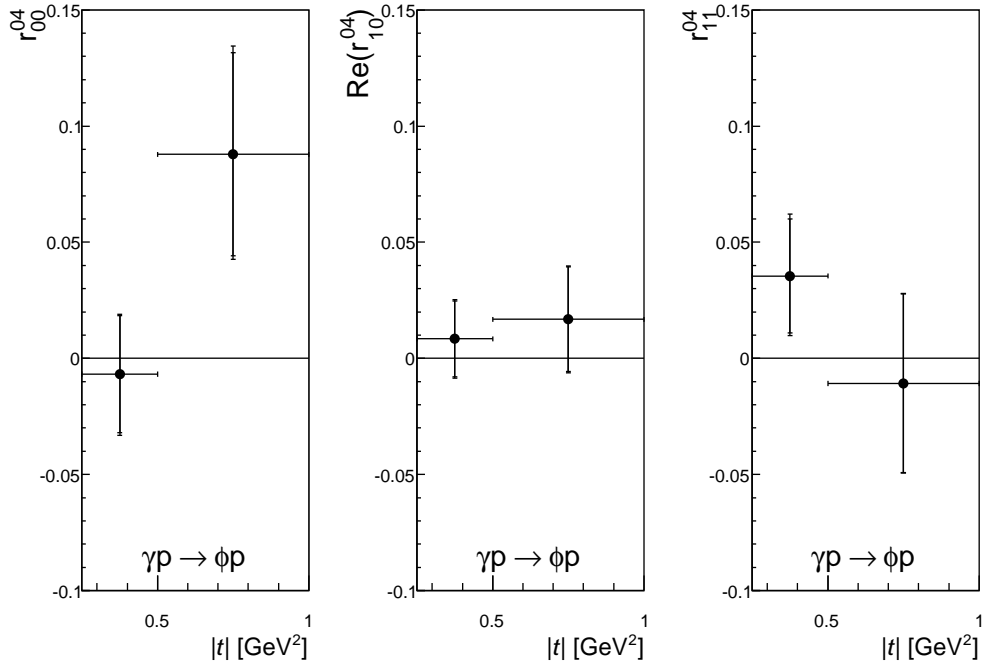


FIGURE 11.17: *The elastic angular distribution for  $0.5 < |t| < 1.0 \text{ GeV}^2$  in slices along  $\phi_h$ .*


 FIGURE 11.18: Spin density matrix elements for diffractive  $\phi$  photoproduction.

 FIGURE 11.19: Spin density matrix elements for elastic  $\phi$  photoproduction.

### 11.3 Spin Density Matrix Elements

The spin density matrix elements from the two-dimensional fit of equation 2.25 to the data as described in the previous section are shown in figure 11.18 for diffractive and 11.19 for elastic  $\phi$  meson photoproduction. For the lower of the two  $t$  bins, they are compatible with 0 within  $1\sigma$ , as expected from  $s$ -channel helicity conservation. For larger reconstructed  $t$ , the increased fraction of events with non-negligible  $Q^2$  leads to the expected departure from 0.

# Chapter 12

## Results and Discussion

*And that, my liege, is how we now know the Earth  
to be banana-shaped*

SIR BELVEDERE IN [215]

*Das Vergleichen ist das Ende des Glücks und  
der Anfang der Unzufriedenheit.*

SØREN KIERKEGAARD

### 12.1 Double-Differential Cross Sections

The differential photoproduction cross section for elastic  $\phi$  meson photoproduction  $\gamma p \rightarrow \phi p$  is measured in the kinematic range  $M_Y < 5$  GeV and  $Q^2 < 2.5$  GeV<sup>2</sup> using a data sample collected by the H1 experiment in 2005. The diffractive  $\phi$  meson photoproduction cross section shown in figure 12.1 is determined for 6  $t$  values between  $t = -0.2$  GeV<sup>2</sup> and  $t = 1.5$  GeV<sup>2</sup> over a  $W$  range of 30 – 65 GeV for the first to 30 – 90 GeV for the last  $t$  bin. The corresponding numerical values are to be found in table B.1.

The elastic  $\phi$  meson photoproduction cross section is determined by using the plug calorimeter, the forward muon system and the forward tagging system to recognise proton dissociative events. In figure 12.2 the cross sections are shown in the same bins as for the diffractive case. The numerical values are tabulated in table B.1.

The cross sections within one  $t$  bin are fitted to the form:

$$\frac{d\sigma_{\gamma p}(W)}{dt} = \frac{d\sigma_{\gamma p}(W_0)}{dt} \left( \frac{W}{W_0} \right)^{4(\alpha(t)-1)} \quad (12.1)$$

with  $W_0 = 37$  GeV. In the elastic case, the fit parameter  $\alpha(t)$  corresponds to the value of the pomeron trajectory at this  $t$ .

### 12.2 Pomeron Trajectory

The values of  $\alpha(t)$  determined in using equation (12.1) are plotted against  $t$  in figure 12.3. For the elastic case, the corresponding plot is shown in figure 12.4, where a linear fit

$$\alpha(t) = \alpha_0 + \alpha' \cdot t \quad (12.2)$$

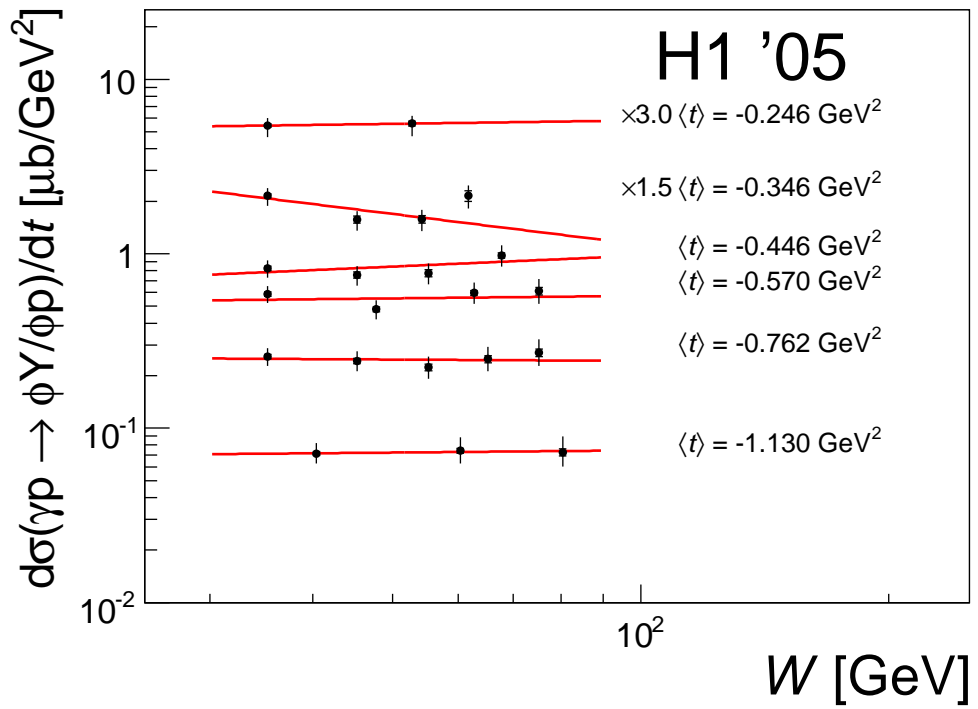


FIGURE 12.1: *Diffractive differential cross section for  $\phi$  meson photoproduction. The inner error bars denote the statistical error and the outer error bars the statistical and systematic errors (including the overall normalisation) added in quadrature.*

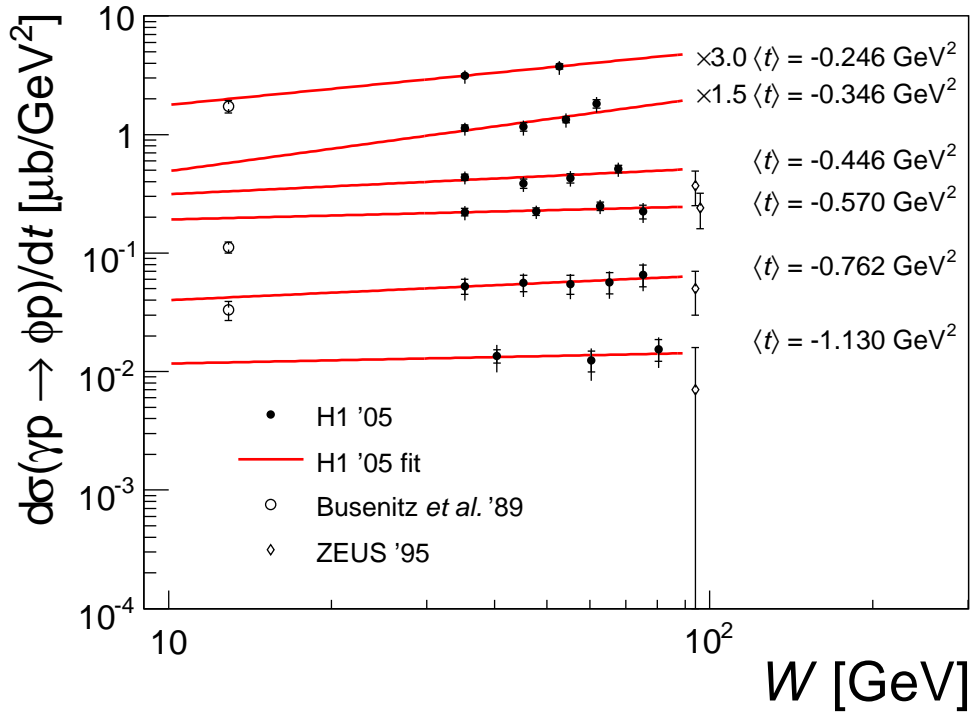


FIGURE 12.2: Elastic differential cross section for  $\phi$  meson photoproduction. For the H1 points, the inner error bars denote the statistical error and the outer error bars the statistical and systematic errors (including the overall normalisation) added in quadrature. For the measurements by Busenitz et al. with the E401 spectrometer [216] and the ZEUS measurements [198], the error bars denote statistical and systematic uncertainty added in quadrature. These measurements were corrected to the  $t$  bin centres of the present analysis using the slopes measured by the respective experiments. The ZEUS point for  $\langle t \rangle = -0.570 \text{ GeV}^2$  was shifted towards higher  $W$  by 2 GeV for clarity.

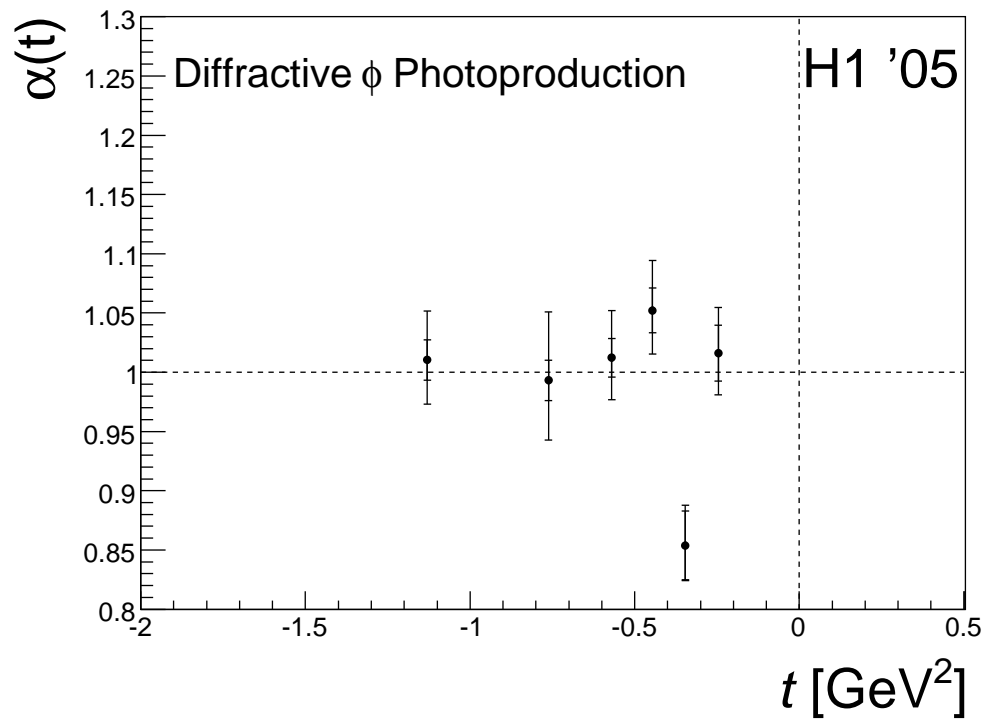


FIGURE 12.3:  $\alpha$  versus  $t$  for diffractive  $\phi$  photoproduction. The inner error bars denote the statistical error and the outer error bars the statistical and systematic errors added in quadrature.

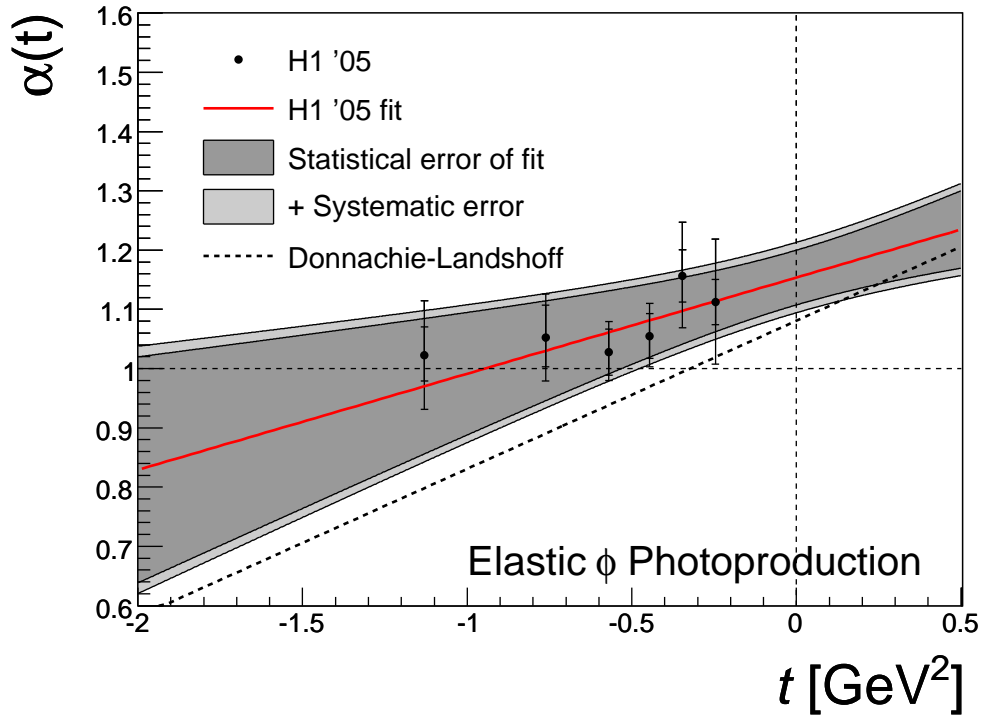


FIGURE 12.4:  $\alpha$  versus  $t$  for elastic  $\phi$  photoproduction. The solid line shows the result of a linear Pomeron trajectory fit, the dark shaded area denotes the statistical uncertainty of the fit whilst the light shaded area denotes the statistical and systematic errors of the fit added in quadrature. The “canonical” trajectory by Donnachie and Landshoff,  $\alpha(t) = 1.0808 + t \cdot 0.25 \text{ GeV}^{-2}$  is superimposed as a dashed line.

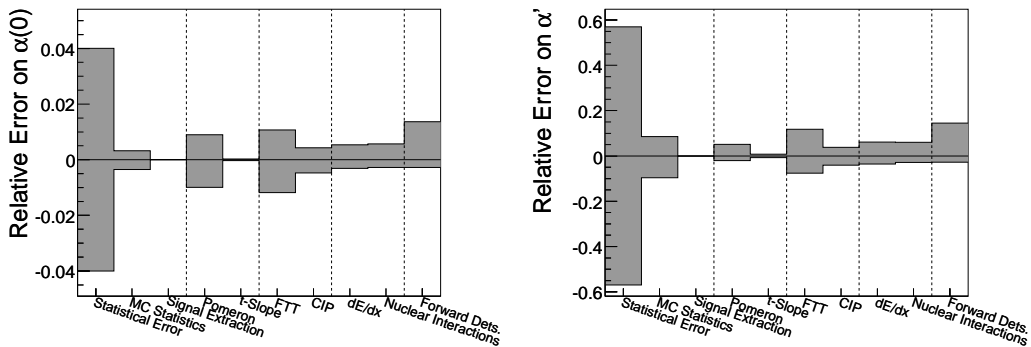


FIGURE 12.5: Error contributions to the pomeron trajectory.

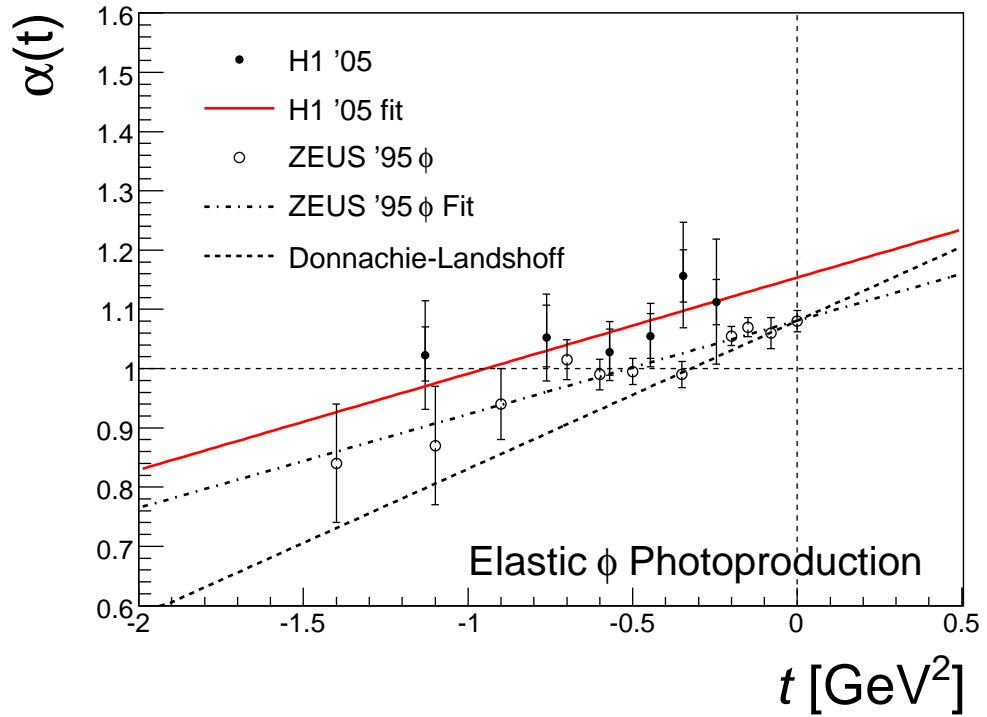


FIGURE 12.6: *The present measurement of the pomeron trajectory in  $\phi$  photoproduction compared to a measurement by the ZEUS collaboration combining ZEUS data [47, 198] with results obtained at lower energies [216–221]. Note that for the ZEUS points the relative normalisation errors between experiments were treated as uncorrelated and the point at  $t = 0$  was obtained from an extrapolation from higher  $|t|$  values.*

was performed. Statistical and systematic uncertainties of the fit results are shown in figure 12.5. The pomeron trajectory as determined from elastic  $\phi$  meson photoproduction is found to be:

$$\alpha(t) = 1.15 \pm 0.05(stat.)_{-0.03}^{+0.04}(syst.) + t \cdot (0.16 \pm 0.09(stat.)_{-0.02}^{+0.04}(syst.))\text{GeV}^{-2}. \quad (12.3)$$

This is to be compared with the “canonical” trajectory extracted from fits to total hadronic cross sections by Donnachie and Landshoff [13, 101],

$$\alpha(t) = 1.0808 + t \cdot 0.25\text{GeV}^{-2} \quad (12.4)$$

on one hand and a fit to low-energy and HERA measurements by the ZEUS collaboration [198], which yielded for the  $\phi$ :

$$\alpha(t) = 1.081 \pm 0.010 + t \cdot (0.158 \pm 0.028)\text{GeV}^{-2}. \quad (12.5)$$

The trajectory determined in this analysis has an intercept about  $1\sigma$  above the one obtained by earlier measurements, whilst the slope is smaller than the Donnachie and Landshoff slope but consistent with slopes obtained by ZEUS for  $\rho^0$  and  $\phi$  production [198] and by H1 for  $\rho^0$  [17] and  $J/\psi$  [28] production, see figure 12.9.

### 12.2.1 Note on the Errors of the ZEUS Measurement

The trajectory measurement by the ZEUS collaboration [198] combines ZEUS data points at a  $W$  of 94 GeV [198] and 70 GeV [47] with measurements by fixed target experiments at values of  $W$  of 2.64-3.60 GeV [218], 2.8 GeV [217], 2.81-4.28 GeV [219], 3.59-4.21 GeV [220], 4.73-5.85 GeV [221] and 12.89 GeV [216]. The measurements were performed at different values of  $t$  and interpolated to the ZEUS  $t$  values using an unspecified method. The much larger lever arm in  $W$  leads to a better constraint of the slopes and thus smaller (statistical) errors than for the present measurement.

The treatment of systematic errors and correlations between data points is not discussed in the ZEUS publication. The systematic errors (which are mostly normalisation errors affecting all data points) were added in quadrature to the statistical errors of the individual points and treated as uncorrelated in the subsequent fits. In addition, in the case of the ZEUS measurement and a DESY fixed-target experiment [218], results of an exponential fit to the data were used to obtain a value at  $t = 0$  and the result is then used as an additional, uncorrelated data point.

## 12.3 An Alternative Trajectory Fit

### 12.3.1 Cross Section Model

The trajectory determinations presented so far have the advantage that they do not rely on assumptions on the shape of the  $t$ -dependence of the cross section<sup>1</sup>. If we however introduce a model of the  $t$ -dependence, it becomes possible to combine measurements at all  $W$  and  $t$  and also take into account the correlation between data points due to common normalisation errors.

The cross section was modelled as<sup>2</sup>:

$$\frac{d\sigma}{dt} = \sigma_0 \left( \frac{W}{W_0} \right)^{4(\alpha_0-1)} \cdot e^{-\left(b_0+2\alpha' \log\left(\frac{W}{W_0}\right)^2\right)t-ct^2}, \quad (12.6)$$

---

<sup>1</sup>This is not strictly true, as some model is used for bin centre corrections and in the case of the ZEUS measurement also for transporting measurements of other experiments to the ZEUS  $t$  bins.

<sup>2</sup>A simple exponential fails to describe all data.

Data set	Reference	Points	$W$ [GeV]	$t$ [GeV <sup>2</sup> ]	Norm.
H1 '05	This thesis	22	35.25 - 80.4	0.246 - 1.130	6%
ZEUS '94	[47]	4	70	0.142 - 0.442	14.3%
ZEUS '95	[198]	4	94	0.462 - 1.217	15%
E401 '89	[216]	7	12.89	0.01 - 0.81	8%
LAMP2 '81	[217]	40	2.66 - 2.99	0.025 - 1.45	10%
DESY '78	[218]	110	2.64 - 3.60	0.03 - 0.39	5%
LBL-SLAC '73	[219]	10	2.81 - 4.28	0.11 - 1.2	10%
Cornell '71	[220]	3	3.59 - 4.21	0	12%
SLAC '70	[221]	31	4.73 - 5.85	0.3 - 1.4	10%

TABLE 12.1: *Data sets used for the global fit. "Norm." denotes the normalisation uncertainty.*

with five free parameters  $\sigma_0$ ,  $b_0$ ,  $c$ ,  $\alpha_0$  and  $\alpha'$ .  $W_0$  on the other hand is fixed to 5 GeV for the fit; the trajectory parameters should not depend on it.

### 12.3.2 Data Sets and Treatment of Errors

In total nine data sets were used, see table 12.1. For each measured point, statistical and systematic error were added in quadrature, where the systematic error was reduced by the global normalisation uncertainty of the respective experiment (if this had been included). If asymmetric errors were given in the publication, they were also used in the fit. For every additional data set, a free parameter for the total normalisation with a  $\chi^2$  penalty according to the respective error was introduced to the fit.

For the ZEUS '94 and SLAC '70 datasets, the numerical values of the cross sections were not available in electronic or tabulated form and had to be reconstructed from the respective figures in the publications. The normalisation uncertainties of the two ZEUS results were treated as uncorrelated as they stem mainly from the calorimeter trigger for the '94 data and mainly from the electron tagger efficiency for the '95 data.

### 12.3.3 Fit Results

Fitting the 22 cross sections obtained in this thesis yields the trajectory

$$\alpha(t) = 1.15_{-0.08}^{+0.06} + t \cdot (0.13_{-0.15}^{+0.10}) \text{ GeV}^{-2}, \quad (12.7)$$

with a rather mediocre goodness of fit with a  $\chi^2$  of 29.9 for 17 degrees of freedom (probability 2.7%). Adding the two ZEUS data sets results in the trajectory

$$\alpha(t) = 1.14_{-0.07}^{+0.05} + t \cdot (0.16_{-0.14}^{+0.08}) \text{ GeV}^{-2}, \quad (12.8)$$

at a  $\chi^2$  of 39.0 for 23 degrees of freedom. Finally, after the inclusion of all low energy data, the fit result is

$$\alpha(t) = 1.122 \pm 0.008 + t \cdot (0.150 \pm 0.017) \text{ GeV}^{-2}, \quad (12.9)$$

with a  $\chi^2$  of 337.6 for 219 degrees of freedom.  $b_0$  is fitted as  $6.06 \pm 0.18 \text{ GeV}^{-2}$ ,  $c$  is  $1.6 \pm 0.2 \text{ GeV}^{-4}$  and  $\sigma_0$  is  $2.51 \pm 0.11 \mu\text{b}$ . The largest contribution to the  $\chi^2$  is from the LAMP2 points at medium and high  $|t|$ , which seem to indicate a contribution of inelastic

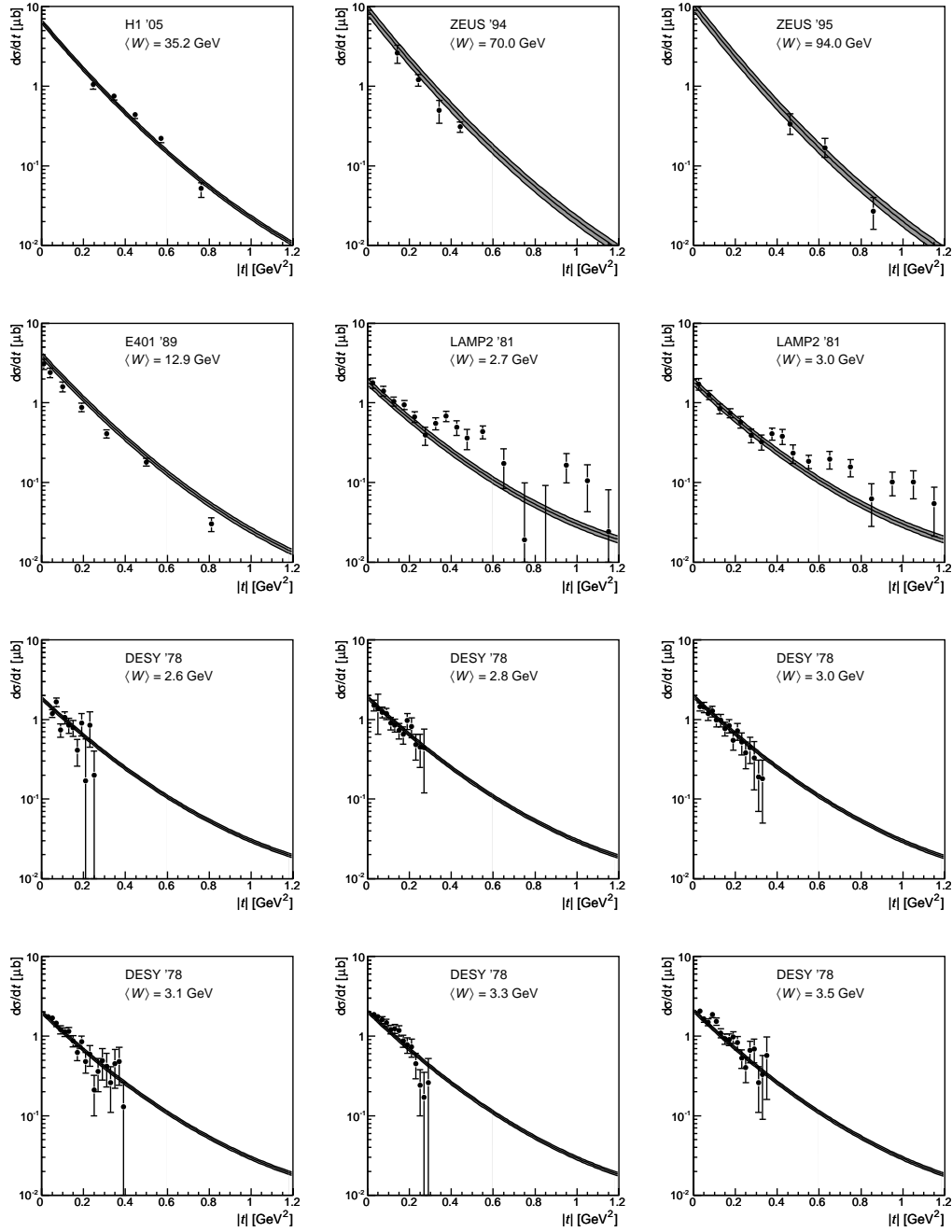


FIGURE 12.7: Data points used in the global fit are shown together with the fit results. The errors of the points represent statistical and systematic errors added in quadrature, whilst the band around the fit result represents the normalisation error of the respective measurement. For the H1 measurement, only 5 points with a common  $W$  are shown.

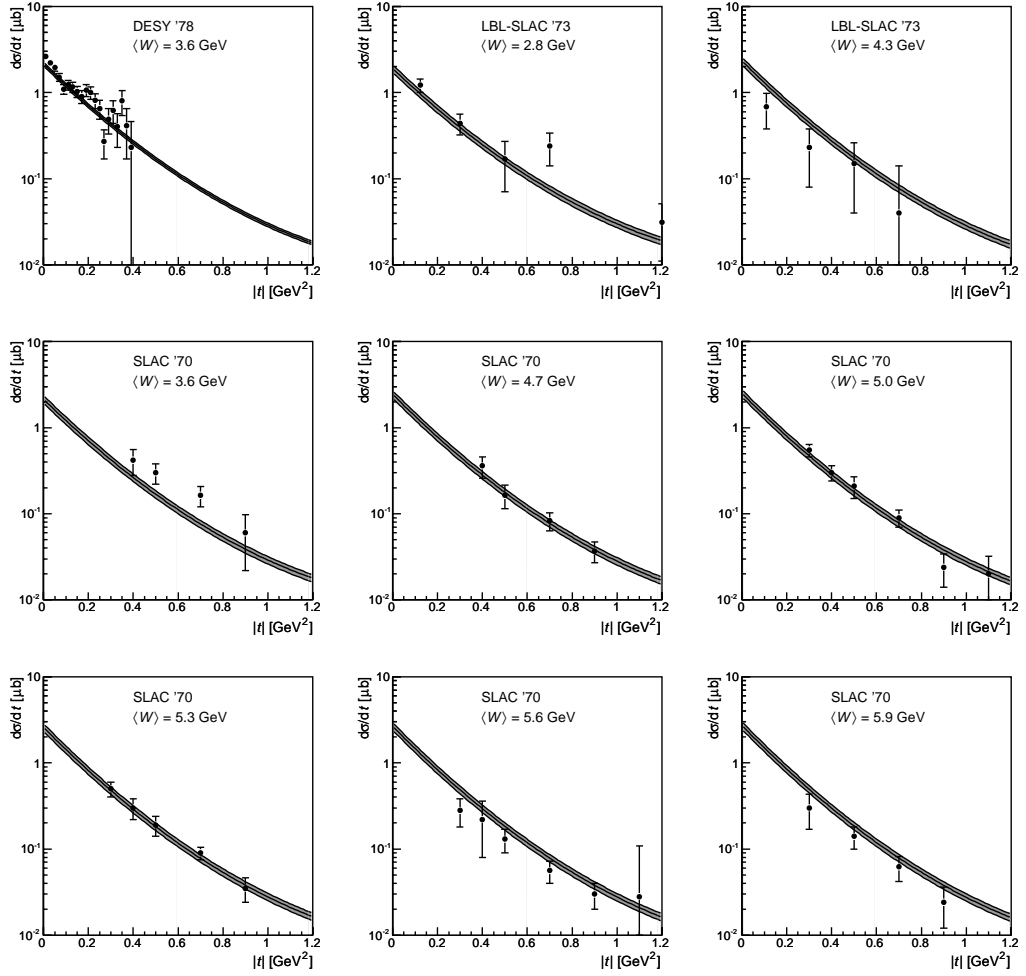


FIGURE 12.8: Data points used in the global fit are shown together with the fit results, continued from figure 12.7.

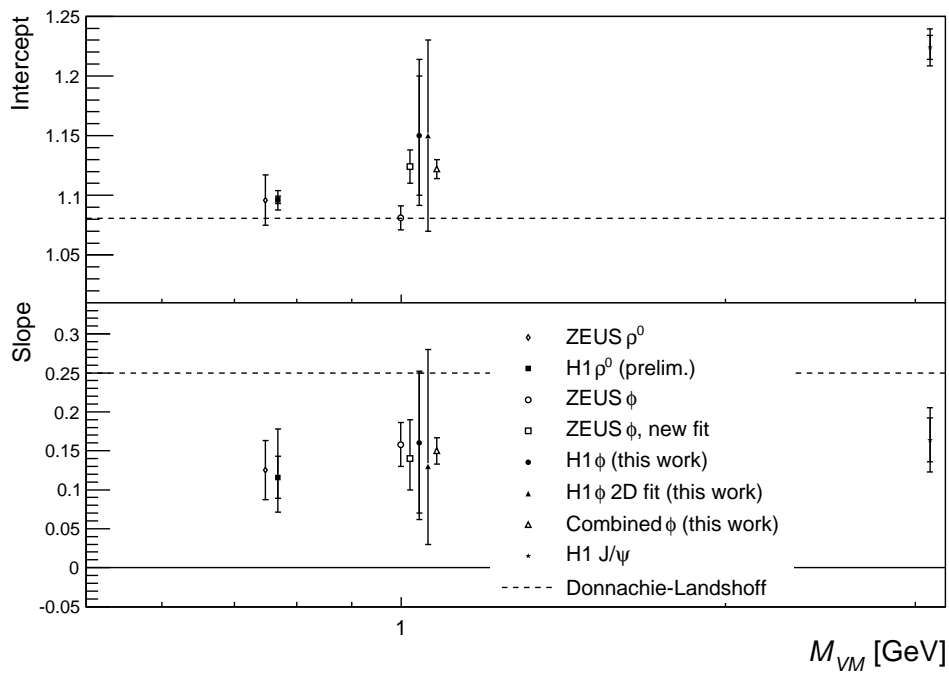


FIGURE 12.9: Comparison of pomeron trajectory measurements. The data points have been shifted in steps of 20 MeV in vector meson mass for clarity. For the H1 results ( $\rho^0$  in [17] and  $J/\psi$  in [28]), the inner error bars show the statistical errors only, whilst the outer error bars depict the statistical and systematic errors added in quadrature.

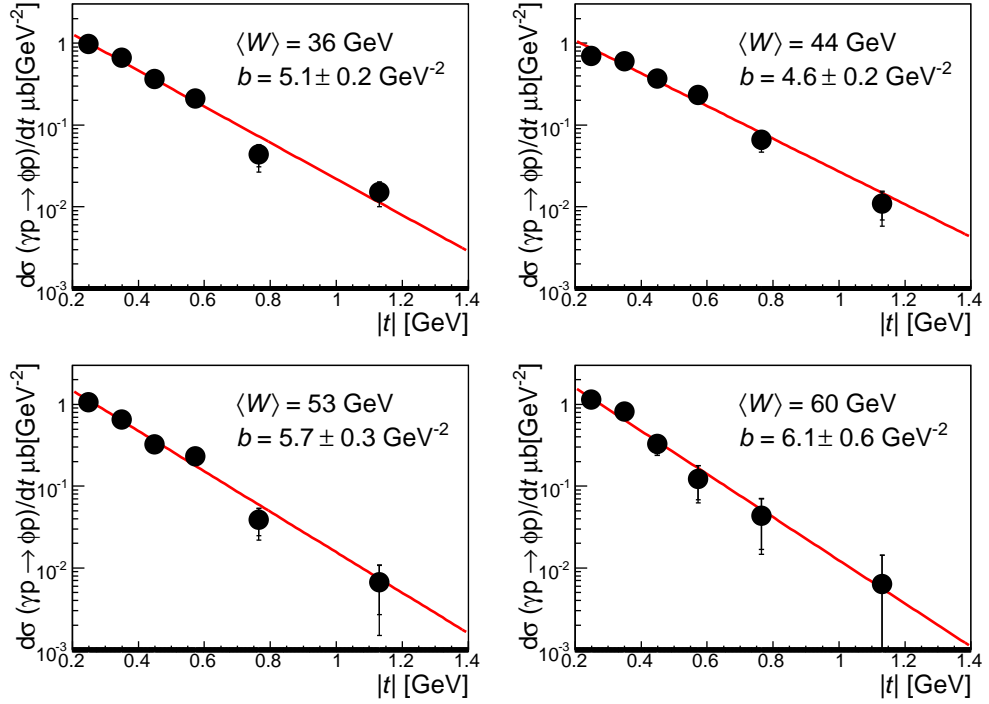


FIGURE 12.10:  $t$  dependence of the elastic  $\phi$  photoproduction cross section in bins of  $W$ . The inner error bars denote the statistical error and the outer error bars the statistical and systematic errors added in quadrature.

events not properly accounted for. A selection of data points together with the fit results is shown in figures 12.7 and 12.8. A fit without the LAMP2 points yields

$$\alpha(t) = 1.113 \pm 0.009 + t \cdot (0.10 \pm 0.02) \text{ GeV}^{-2}, \quad (12.10)$$

with a  $\chi^2$  of 241.4 for 180 degrees of freedom.  $b_0$  is fitted as  $6.35 \pm 0.21 \text{ GeV}^{-2}$ ,  $c$  is  $1.5 \pm 0.2 \text{ GeV}^{-4}$  and  $\sigma_0$  is  $2.61 \pm 0.12 \mu\text{b}$ .

The fit without the H1 data is only marginally consistent with the published ZEUS fit result, yielding

$$\alpha(t) = 1.124 \pm 0.014 + t \cdot (0.23_{-0.03}^{+0.04}) \text{ GeV}^{-2}. \quad (12.11)$$

An overview of the results is shown in figure 12.9.

## 12.4 Cross Section Differential in $W$

The differential cross section for elastic  $\phi$  meson photoproduction in four bins of  $W$  against  $t$  is shown in figure 12.10. The cross sections are fitted with an exponential as described in section 10.2.2. The slope parameter  $b$  is shown against  $W$  in figure 12.11, together with a fit of the form

$$b(t) = b_0 + 4 \cdot \alpha' \ln \left( \frac{W}{W_0} \right), \quad (12.12)$$

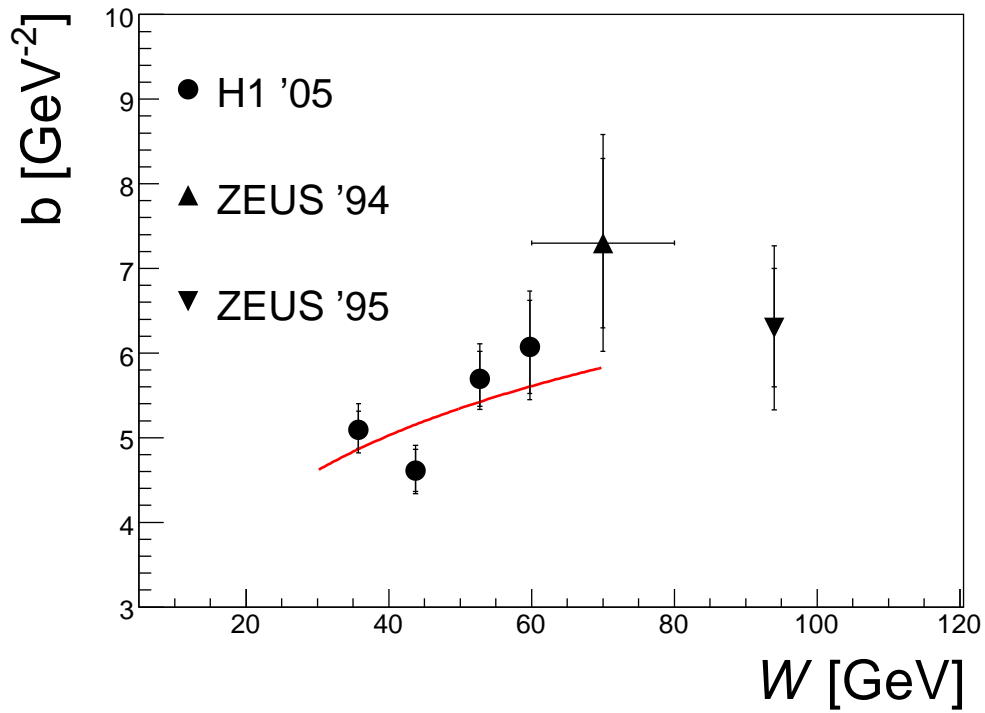


FIGURE 12.11:  $W$  dependence of the  $t$  slope parameter  $b$  for elastic  $\phi$  meson photoproduction. The inner error bars denote the statistical error only, while the outer error bars stand for the statistical and systematic errors added in quadrature. The line is a fit to the H1 data points of the form  $b(W) = b_0 + 4 \cdot \alpha' \ln\left(\frac{W}{W_0}\right)$ . The ZEUS points are from [47] and [198].

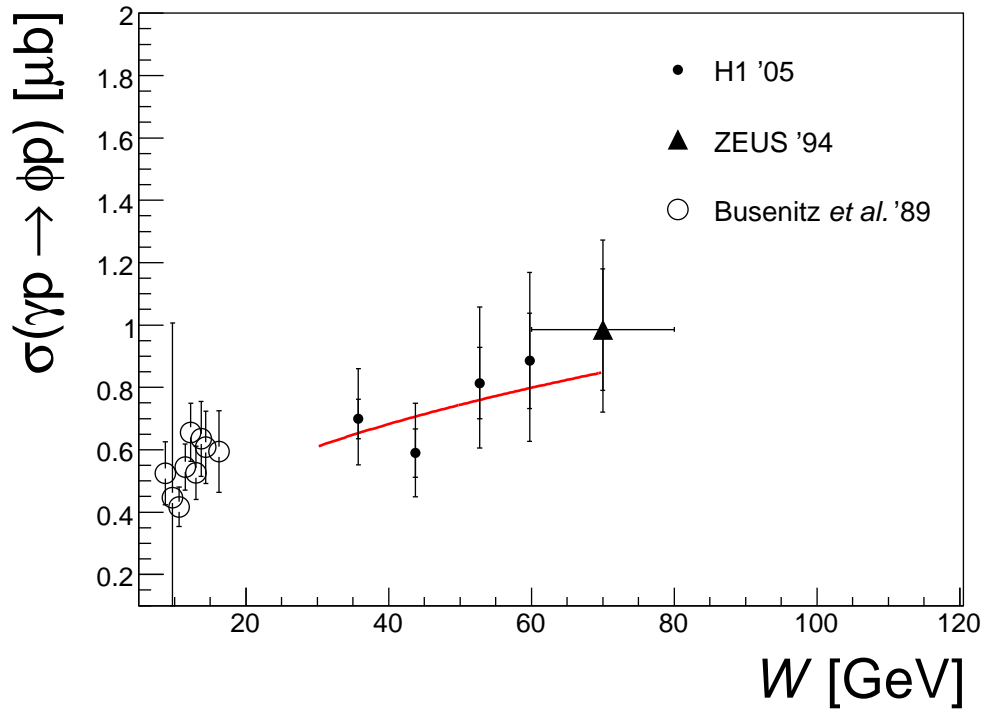


FIGURE 12.12: *Elastic  $\phi$  photoproduction cross section versus  $W$ . The inner error bars denote the statistical error and the outer error bars the statistical and systematic errors added in quadrature.*

where  $W_0$  was chosen as 50 GeV and  $b_0$  left as a free parameter of the fit. The slope parameter  $\alpha'$  is determined to be

$$\alpha' = 0.36 \pm 0.21(\text{stat.})_{-0.03}^{+0.04}(\text{syst.}). \quad (12.13)$$

Integrating the cross section over the whole  $t$  range yields the cross section as a function of  $W$ , shown in figure 12.12. The ZEUS result in the same plot has been corrected to the full  $t$  range using the  $t$  slope measured by ZEUS.

Fitting the  $W$  dependence with a function of the form

$$\sigma_{\gamma p}(W) \propto W^\delta \quad (12.14)$$

yields for the parameter  $\delta$

$$\delta = 0.39 \pm 0.36(\text{stat.})_{-0.13}^{+0.16}(\text{syst.}) \quad (12.15)$$

which compares with values of  $\delta = 0.22$  for  $\rho^0$  mesons and  $\delta = 0.75 \pm 0.03(\text{stat.}) \pm 0.03(\text{syst.})$  for  $J/\psi$  mesons [28], see figure 12.13.

## 12.5 Conclusion and Outlook

The measurements presented in this thesis show a broad agreement with the expectations of the Regge theory based approach to soft diffractive phenomena. Earlier findings that

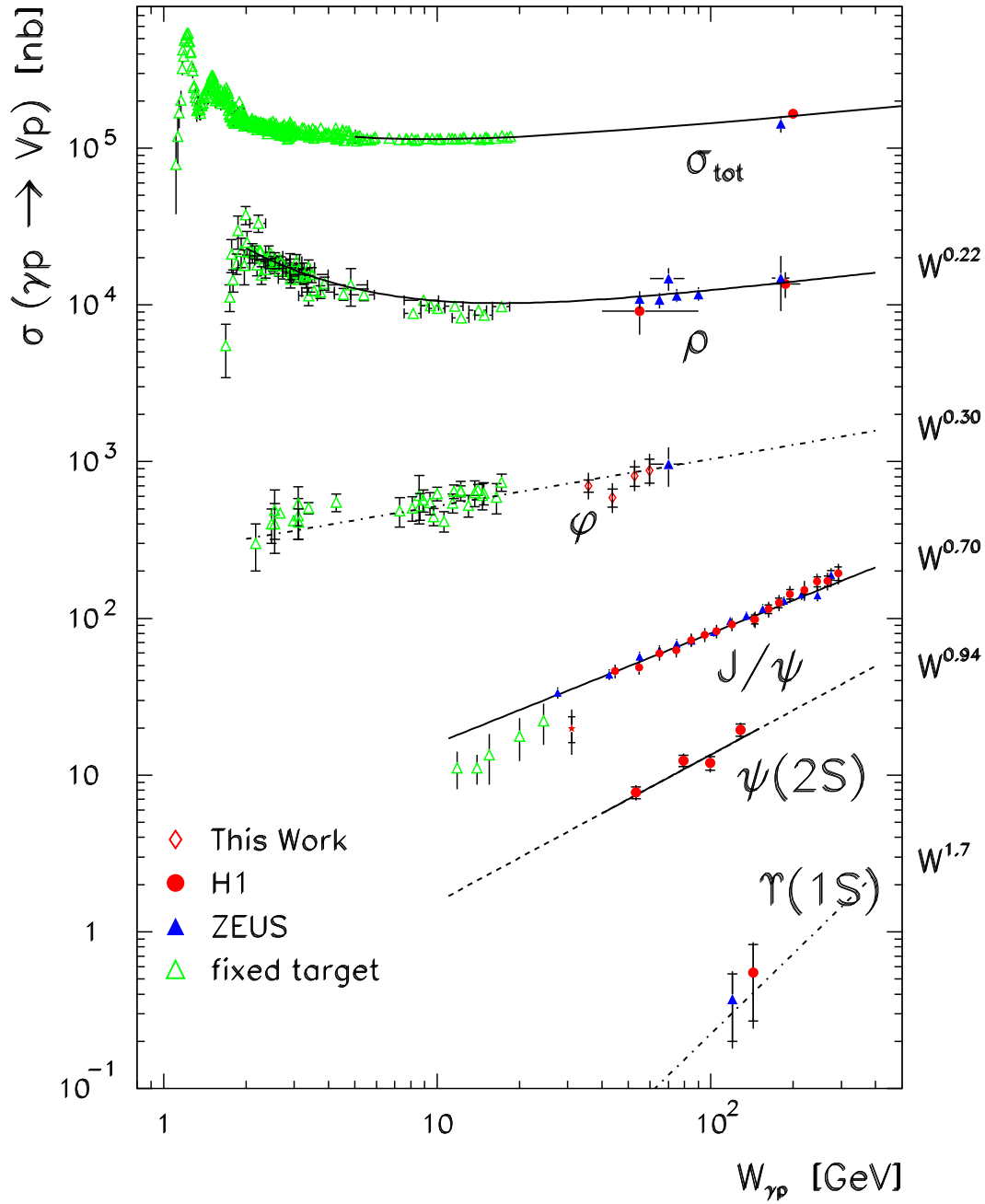


FIGURE 12.13: A compilation of vector meson photoproduction cross sections versus the photon-proton centre of mass energy  $W$ , including the measurements from this thesis.

the shrinkage as determined from vector meson measurements is about half the “canonical” value of  $0.25 \text{ GeV}^{-2}$  are confirmed, see figure 12.9. The rise of the intercept towards higher vector meson masses is already visible when comparing the  $\phi$  meson trajectory to  $\rho^0$  based measurements.

Whilst the cross section measurement is dominated by the systematic normalisation uncertainty, the shape measurements are still statistically dominated. The large  $\phi$  meson sample taken during the 2006 running period (with the help of the invariant mass trigger described in section 15) could lead to a significant improvement in precision without the need of including data from other experiments. This in turn would be helped by recent improvements in the simulation of the fast track trigger and in the track reconstruction software. The run at a lower proton energy of 460 GeV planned for the summer 2007 allows to access lower values of  $W$  and thus increases the lever arm for slope measurements. Lower values of  $|t|$  could be accessed via other decay channels (e.g.  $\phi \rightarrow \mu^+\mu^-$ ). With the end of HERA in summer 2007, a unique window of opportunity for the study of vector meson photoproduction closes. The wealth of data taken up to that time however promises interesting new results from this area for the years to come.

# List of Symbols

*Egli è scritto in lingua mathematica, e i caratteri son triangoli, cerchi, ed altre figure geometriche (...)*

GALILEO GALILEI [222]

$A$	Scattering Amplitude	$h$	Planck's constant
$a$	Acceptance	$H_{int}$	Interaction Hamiltonian
$\alpha(t)$	Regge Trajectory	$I$	Isospin
$\alpha_{em}$	Electromagnetic coupling constant	$I_3$	3-component of isospin
$\alpha'$	Slope of trajectory	$J$	Spin
$\alpha_s$	Strong coupling constant	$k$	Wave number
$\alpha(0)$	Intercept of trajectory	$\vec{k}$	Momentum vector of $K^+$
$b$	beauty (or bottom) quark	$\ell$	Angular momentum
$\beta$	Speed in units of $c$	$\mathcal{L}$	Luminosity
$\beta_{\mathbb{P}}$	Fraction of the $\mathbb{P}$ momentum interacting with the photon	$\lambda$	Wavelength
$C$	Charge conjugation	$\lambda_i$	Helicity of particle $i$
$c$	Speed of light	$m$	Mass
$\chi$	Charge conversion factor	$M_{++}$	Helicity conserving amplitude
$d$	down quark	$M_{+0}$	Single flip amplitude
$\delta$	Density correction	$M_{+-}$	Double flip amplitude
$\Delta\varphi_{L3}$	Opening angle at the third trigger layer	$M_X$	Mass of the "photon remnant"
dII	Phase space	$M_Y$	Mass of the "proton remnant"
$E$	Energy	$N_A$	Avogadro's number
$e$	Unit charge	$\omega_p$	Plasma frequency
$\epsilon$	Efficiency	$\mathbb{P}$	Pomeron
$\mathcal{F}_\gamma$	Photon flux	$\vec{p}$	3-Momentum
$G$	$G$ -Parity	$P$	Parity
$\Gamma$	Width of a resonance	$p$	4-Momentum
$\gamma$	Boost ( $1/\sqrt{1-\beta^2}$ )	$\Phi$	Flux of incoming particles
$\Gamma_\phi$	Mass dependent width of the $\phi$ resonance	$\varphi$	Azimuthal angle
$\Gamma_{\phi,0}$	Nominal width of the $\phi$ resonance	$\Phi_h$	Angle between the lepton scattering and the meson production plane in the proton rest frame
$\hbar$	Dirac's constant, $h/2\pi$	$\phi_h$	Angle between the decay and production plane in the vector meson rest frame
		$\psi$	wave function
		$\psi_h$	$\phi_h - \Phi_h$
		$q$	quark
		$\bar{q}$	anti-quark

$Q^2$	Virtuality of the exchanged boson
$\vec{q}$	Momentum vector of $\phi$
$\mathbb{R}$	Reggeon
$r_{ij}^{04}$	Spin density matrix element
$r_e$	Classical electron radius
$S$	Scattering ( $S$ ) matrix
$S$	Strangeness quantum number
$s$	Centre of mass energy squared
$s$	strange quark
$\sigma$	Cross section
$\sigma_{el}$	Elastic cross section
$\sigma_{tot}$	Total cross section
$\sigma_x$	Horizontal beam size
$\sigma_y$	Vertical beam size
$\sqrt{s}$	Centre of mass energy
$\mathcal{T}()$	Time-ordered product
$T$	Kinetic energy
$T$	Transition Matrix
$t$	Squared momentum transfer at the proton vertex
$\vartheta$	Polar angle
$\theta_h$	Polar angle of decay particle to the outgoing proton direction in the vector meson rest frame
$\theta_V$	Vector meson singlet/octet mixing angle
$U$	Quantum mechanical time evolution operator
$u$	up quark
$\vec{v}$	Momentum vector of $\gamma$
$W$	Photon-proton centre of mass energy
$x$	Fraction of the proton momentum carried by the struck quark
$\xi$	Strength of saturation correction
$x_{\mathbb{P}}$	Fraction of the proton momentum carried by $\mathbb{P}$
$y$	Inelasticity
$Z$	Atomic number

## Part II

# A Fast Track Trigger for the H1 Experiment



## Chapter 13

# Overview of the Fast Track Trigger

*Als Trigger bezeichnet man den kleinen Haken unterhalb des Rollenhalters. Den nimmt man zwischen Zeige- und Mittelfinger damit sich die Rute nicht um die Längsachse dreht. Bei der Rute mit der Stationärrolle übernimmt das der Rollenstiel.*

UDO MUNDT [223]

*So don't you fool around  
I'm gonna pull it, pull it, pull the trigger*

ACDC [224]

The commissioning of the H1 Fast Track Trigger (FTT) was at the core of this thesis work. This chapter sets out to motivate the construction of this trigger, lays out its overall design and describes in some detail the hardware implementation. Chapters 14 and 15 present two algorithms and their implementation performed for this thesis, namely the level 2  $z$ -vertex finder and the invariant mass calculation. The following chapter is then concerned with the physics performance of the FTT. The final chapter of this part describes the FTT graphical user interface developed during this thesis work.

### 13.1 Triggers for HERA II physics

The HERA II upgrade [146] has brought higher luminosities for the two collider experiments H1 and ZEUS. This allows for searches for very rare processes as well as for precision measurements with high statistical accuracy [145]. To make the best use of this potential whilst circumventing the replacement of the complete data acquisition electronics, H1 had decided to upgrade the existing trigger system (see section 4.7) with new subtriggers providing higher selectivity. With this strategy the event yield for processes of interest can be increased without raising the overall event rate and thus the demands on the data acquisition electronics. The main upgrade projects in this area are the *CIP2000* proportional chamber trigger [155–158], which mainly suppresses background from proton-gas and proton-wall interactions, the liquid argon calorimeter based *jet trigger* designed to recognise local energy

depositions and the *Fast Track Trigger* (FTT). The purpose of the fast track trigger is to reconstruct final states from tracks on trigger level and thus select events of interest (such as those involving charmed or beauty mesons - *heavy flavour physics*) from “normal” *ep* events.

## 13.2 Conceiving the Fast Track Trigger<sup>1</sup>

One of the main goals of the HERA II physics programme at H1 was the study of heavy flavour physics in the photoproduction domain. This is challenging as the event rates are higher but the heavy flavour content is lower in this kinematical domain than at high  $Q^2$ . These events deposit only moderate amounts of energy in the calorimeter, where noise problems unfortunately necessitate relatively high trigger thresholds. Triggering thus has to be based on tracks – and not just the presence of such, but on their precise properties. These arguments led to the insight that only a precise track reconstruction on trigger level could provide the necessary selectivity. The only H1 sub-detector providing the necessary precision, allowing a standalone track reconstruction and providing signals during the trigger latency is the *Central Jet Chamber* (CJC).

Track reconstruction (see [225] for an overview of the state of this field) from CJC signals requires first a digitisation and hit finding step. The CJC has a total of 2440 signal wires, read out at both ends – it is however possible to build a trigger with sufficient accuracy and redundancy using only a subset of these channels, thus reducing the input bandwidth and ultimately the cost of the project. Some pattern recognition algorithm has to construct tracks from the collection of the hits. Either a constructive algorithm such as a *Kalman Filter* [226] dynamically links hits to tracks or “correct” hit patterns are precalculated and then identified via a matching technique. In the early development phase for the FTT it has been shown that the first approach is not feasible for low level trigger purposes as the necessary input bandwidth surpasses that of available processors by several orders of magnitude [227]. A global pattern match suffers from the same problem and would require a very large number of precalculated patterns to supply the necessary accuracy<sup>2</sup>. The natural solution thus is a local pattern match followed by linking the local patterns to global tracks. To achieve high precision with a limited number of patterns, a fit can improve the resolution.

The rough outline of the trigger algorithm was thus given by the nature of the input signals, demands on the output precision and bandwidth and cost constraints. The numerical design parameters were then determined using simulations and taking into account the capabilities of the hardware available at the time (1999). The original design foresaw a level 2 FTT providing precise 3-dimensional track parameters and a level 3 FTT reconstructing final states from these parameters [228, 229]. It was however recognised that the capabilities of this trigger could only be fully exploited if a corresponding level 1 trigger would preselect the interesting events. The initial design was consequently upgraded to include a first level track trigger (without which the  $\phi$ -meson analysis described in the first part of this work would not have been possible) [230, 231]. The first level provides coarse track parameters in the transverse plane.

---

<sup>1</sup>As the major design decisions for the FTT were taken long before this thesis was started, this section tries to reconstruct the corresponding trains of thought from many conversations with the people involved. The goal is not so much to be historically faithful, but to show that the physics goals of the FTT and limitations of computational power determine its design – if the FTT were to be designed again, it would not end up fundamentally different.

<sup>2</sup>Such a global pattern match is however used in the level 1 fibre tracker trigger of the  $D\phi$  experiment at the Fermilab Tevatron. The very high efficiency of the fibres combined with high transverse momentum thresholds (and thus a very limited number of valid patterns) permit a “16 fibres out of 16 fibre layers”-condition implemented in the largest FPGAs available at the time of its construction (2003).

In the early HERA II running period, background from proton-gas and proton-wall interactions proved to be a larger problem than expected and thermal problems prevented parts of the CIP front end from running. As a fallback solution and also to provide a cross-check, the feasibility of a FTT-based  $z$ -vertex trigger was studied [232]. Consequently the interfaces for this trigger were defined and included in the existing design. Also as a response to the background problems in the early HERA II phase, an online hit counting device, called *Synchrotron Radiation Monitor* (SRM)<sup>3</sup> [233, 234] was designed and implemented.

In the next section, some of the key technologies of the Fast Track Trigger are presented. Following this, the algorithms implemented in and the data flow through the three levels of the FTT are described in some detail, intertwined by presentations of the electronics boards used.

## 13.3 Key Technologies for the Fast Track Trigger

The H1 Fast Track Trigger has been made possible by the development of high speed, highly integrated circuits. The high throughput and flexibility is provided by Field Programmable Gate Arrays (FPGAs) with (for 1999 standards) a large number of logic cells and input/output pins. A key technology for fast pattern matching is the use of FPGA-embedded Content Addressable Memories (CAMs). The floating point operations required for the track fits are performed efficiently by Digital Signal Processors (DSPs). Finally, the high bandwidth communication between the different boards of the FTT is done via Low Voltage Differential Signaling (LVDS) links.

### 13.3.1 Field Programmable Gate Arrays

Field Programmable Gate Arrays are configurable integrated circuits. They are built up of so-called *Logic Elements* (LEs), which in turn consist of a *Look-Up Table* (LUT) and a register and memory cells called *Embedded System Blocks* (ESBs). These elements are linked by configurable interconnect lines. The FPGAs used for the FTT are based on Static Random Access Memory (SRAM), where one RAM cell (consisting of six transistors) switches one interconnect or one entry in a lookup table. A hardware description language (VHDL<sup>4</sup> [235–237]) is used to describe the logic and data flow within the chip. A synthesising tool is used to generate a netlist from this description. The netlist essentially contains the logic in the LUTs and the structure of the interconnects between logic elements. This netlist is then used by a fitting tool (Altera Quartus II [238]) to map the generated logic and interconnects to physical locations on the chip. This step also takes into account the frequency at which the design should finally operate and translates this into constraints to the signal propagation time. The result of the fit is a configuration file, which can be loaded into the actual chip.

### 13.3.2 Content Addressable Memories

Content addressable memories (also called associative memories) [239, 240] invert the principle of operation of the ubiquitous Random Access Memory (RAM) by looking up the address of a pattern at the input (see figure 13.1). This allows for very fast searching and pattern

<sup>3</sup>SRM can also be read as *Spike Research Monitor* as it provides enough time resolution to study the structure of sudden short bursts of increased background (spikes) which impede smooth data taking. Studying their structure and relation to beam orbit frequencies may hint at their origin. The first results from these studies led to the introduction of new high voltage control electronics for the CJsCs, in turn leading to a higher high voltage efficiency.

<sup>4</sup>VHSIC Hardware Description Language where VHSIC stands for Very High Speed Integrated Circuit.

matching operations. CAMs are widely used in network and communication devices, e.g. as routing lookup tables. The FTT makes use of so called ternary CAMs, integrated into the FPGAs ESBs [241], where two storage cells (SRAM cells) are used per bit in order to allow not only for a 0 or 1 but also for a “don’t care” (X) entry.

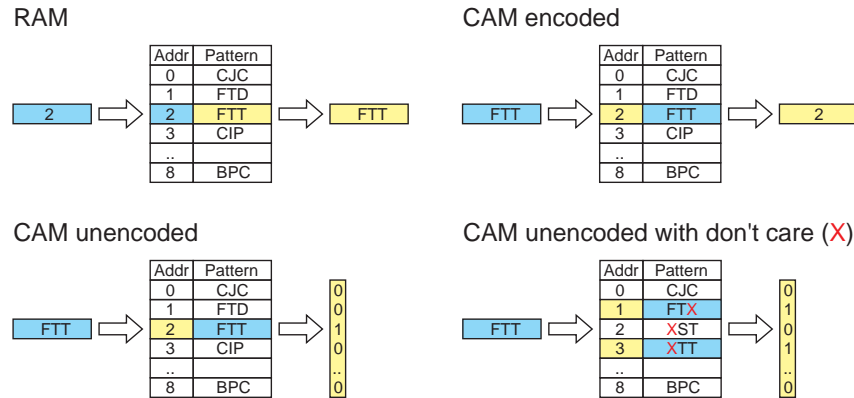


FIGURE 13.1: *Memory operation modes. Whilst a RAM returns the pattern stored at the desired address, CAMs return the address, at which a particular pattern is stored. The address can be returned encoded (bit representation of the corresponding number) or unencoded (bits are set on if the corresponding pattern matches). If the patterns contain don’t cares or if the same pattern is stored multiple times, several matches are possible.*

### 13.3.3 Digital Signal Processors

Digital signal processors (DSPs) are processors optimised for real-time processing of signals. They are widely used in communication and audio devices, where they mainly run filter algorithms. As opposed to micro-processors used in personal computers, DSPs directly include memory and bus interfaces. The FTT makes use of DSPs for the level 2 fit algorithm. The DSPs receive their data from a FPGA using their external memory interface. The FPGA also steers the DSP algorithms via interrupts, thus guaranteeing response times. The DSPs used for the FTT [242] provide 32 registers and 8 functional units operating on them - they can thus perform up to 8 operations (up to 6 of them floating point operations) in parallel.

### 13.3.4 5 Gbit/s Low Voltage Differential Signaling Links

The high bandwidth between the different components of the FTT is provided by 5 Gbit/s low voltage differential signaling (LVDS) links (dubbed “channel links”) [243]. These links were developed for digital display control, where the colour values of millions of pixels have to be updated every few milliseconds. The display origin explains also the bandwidth of 48 bits, corresponding to 3 times 16 bits for the three basic colours. The link consists of a sender chip, a transmission line and a receiver chip. The transmission line contains only 9 pairs of signal cables, one for a clock synchronising the transfer and 6 data bits. The 48 bits at the input are serialised and sent at the 8-fold input frequency (840 MHz). A DC balancing algorithm in the transmitters inverts the signals if needed to ensure that no net current flows across the cable.

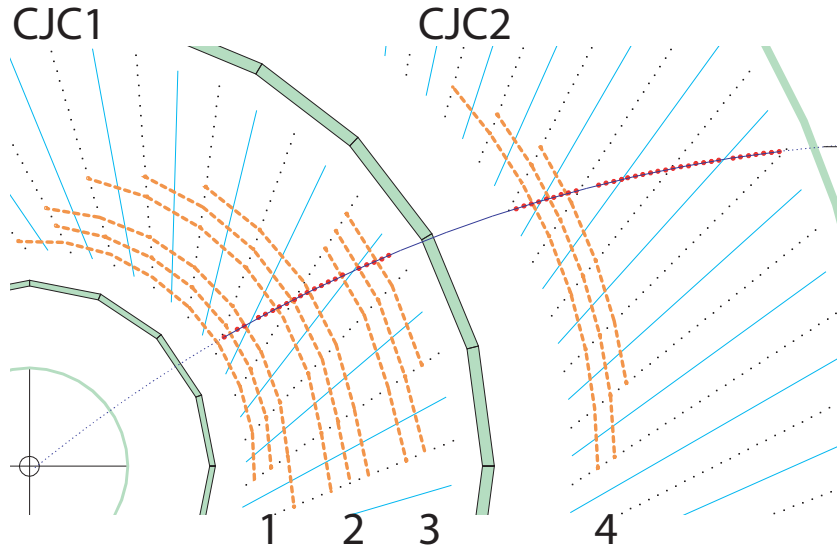


FIGURE 13.2: A radial slice of the H1 central tracker. The CJC wire layers used by the FTT are indicated with the dashed lines.

## 13.4 The Level 1 Fast Track Trigger

### 13.4.1 Digitisation and Hit Finding

The first two levels of the FTT rely solely on information from the Central Jet Chamber of H1 (see 4.3.2). The signals from four layers of three wires each (see figure 13.2) are captured off the standard (non-trigger) drift-chamber readout. 150 passive buffer cards (one for each group of three wires) then forward these data to both the FTT and its predecessor, the Drift Chamber  $r - \varphi$  ( $DCr\varphi$ ) trigger. 150 custom made cables with a total length of 0.72 km then guide the analogue signals to a total of thirty Front End Modules (FEMs, see section 13.4.3). Each FEM processes the signals of five trigger groups, i.e. both ends of fifteen wires corresponding to 30 channels. These signals are digitised by dual 10 bit Analogue to Digital Converters (ADCs) running at a frequency of 80 MHz, thus producing an input data rate of 720 Gbit/s for the complete FTT. The signals of one group are then fed into a FPGA where a so-called  $Qt$ -algorithm identifies hits and measures their charge.

#### $Qt$ -Algorithm

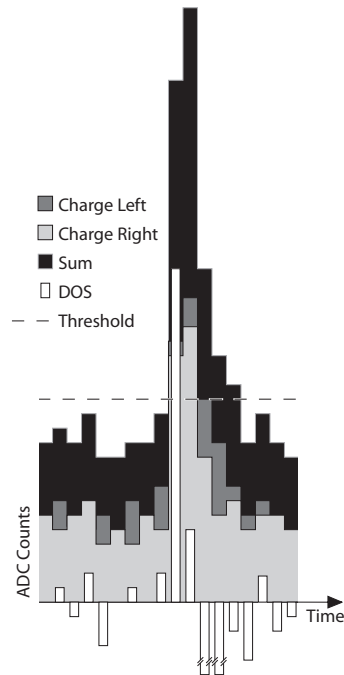
The  $Qt$ -algorithm has to fulfill three main requirements:

1. Identification of hits with the highest possible efficiency whilst maintaining a high purity.
2. Determination of the hit timing with a resolution equivalent to or better than the bin width used (12.5 ns).
3. Measurement of the charge deposited with high accuracy and uncorrelated to other factors.

The hit timing is determined using a difference of samples (DOS) technique (see also figure 13.3). The digitised values from both wire ends ( $v_n^L$  and  $v_n^R$ ) are added to give the sample  $s$  at time step  $n$

$$s_n = v_n^L + v_n^R. \quad (13.1)$$

FIGURE 13.3: An example hit, illustrating the difference of samples technique. The ADC outputs for the left and right ends of the wires are summed. The difference of samples (DOS) is the difference of the sum between time slices. If it lies above an adjustable threshold and has a maximum, the Qt algorithm signals this as a hit.



The difference to the previous sample is then calculated

$$\delta_n = s_n - s_{n-1}. \quad (13.2)$$

If this difference is above a threshold  $t$ , i.e. the slope of the rising edge of the hit surpasses a minimum value (which also implies a minimum total size for the hit) and is also larger than the difference for the next time slice ( $\delta_{n+1}$ ), the corresponding time slice  $n$  is signaled to contain a hit [244]. This implementation has the advantage that the result is available 3 clock steps (37.5 ns) after the arrival of the signal and segment finding can proceed, as it is based only on the  $r - \varphi$  coordinates of the hit derived from the hit time using the (known) wire position, drift direction and drift speed. The charge integration and charge division needed for the  $z$  coordinate (which is used by level 2 and the level 1  $z$  vertex trigger) take more time (16 clock cycles in total), which makes the implementation of the level 1  $z$  vertex trigger (see section 13.5) a very challenging endeavour. The hit finding is locked for three cycles after a hit is found, in order to avoid flagging fluctuations in large hits as double hits and to ensure that only one hit can be found per 20 MHz shift register bin (see the following subsection).

### Charge division

The  $z$  coordinate of a hit is determined from the ratio of the charges seen by the two wire ends. The charge integration starts, as soon as the difference of samples is above the threshold<sup>5</sup>. The charge values are added up for six clock cycles. A pedestal subtraction is then performed. The pedestal value is also taken from the ADC stream; six bins starting eight

<sup>5</sup>Detailed studies on data and comparisons to the standard CJC readout revealed that waiting for the maximum DOS for the charge integration introduces a systematic dependence of the charge on both the exact hit timing within the 80 MHz bin and the  $z$  coordinate. This can be understood from the fact that both the timing shift and the different times needed by the signals to reach the wire ends affect the shape of the rising hit edge as seen after the 80 MHz digitisation.

cycles<sup>6</sup> before the integration range are added up and then subtracted from the integrated charge. If there was a hit in a 20 bin wide window before the hit under consideration, an earlier pedestal is used (see also figure 13.4).

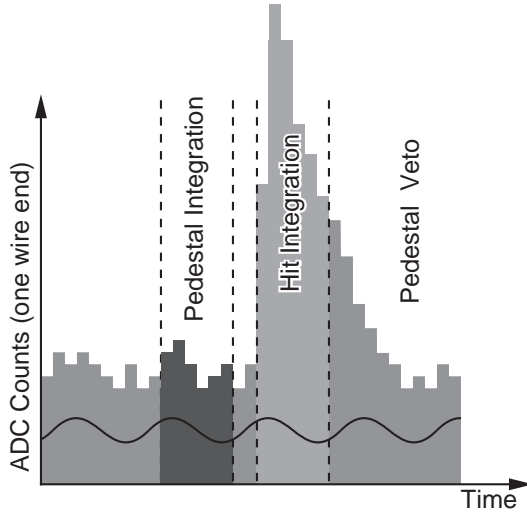


FIGURE 13.4: Schematic representation of the charge integration performed by the FTT. As soon as the difference of samples determined from both wire ends surpasses the threshold, the charge is integrated over 6 clock cycles separately for both wire ends. In phase with the HERA clock (the main source of correlated noise in H1 - represented by the sine curve), the pedestal is determined from six earlier clock cycles. For twenty clock cycles after a hit, no pedestals are taken.

The extracted charge values for both wire ends ( $q_L$  and  $q_R$ ) then enter the charge division algorithm to extract the  $z$  coordinate of the hit.

$$z = L_{eff} \frac{q_L - q_R}{q_L + q_R}, \quad (13.3)$$

where  $L_{eff}$  is the effective wire length, determined not only by the length of the physical wire but also taking into account electronics at the end of the wire (see figure 13.5).

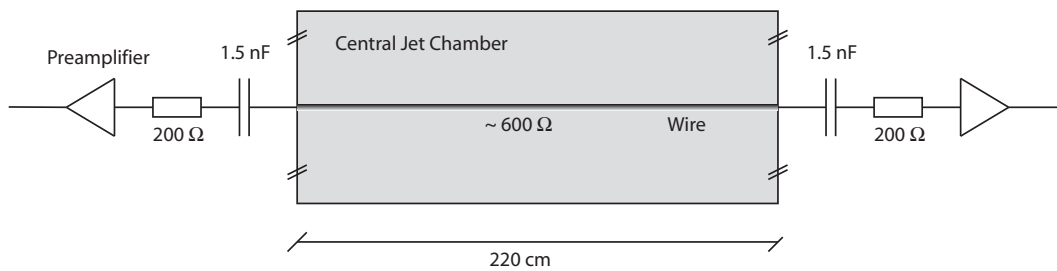


FIGURE 13.5: A CJC wire with its front end electronics giving rise to an effective wire length larger than the physical wire length.

<sup>6</sup>This offset was chosen to combat coherent noise stemming from pickup of the 10.4 MHz HERA-clock signal. With an offset of 8 cycles (96 ns), both hit and pedestal integration extend over the same phase range of the HERA-clock.

## 13.4.2 Track Segment Finding

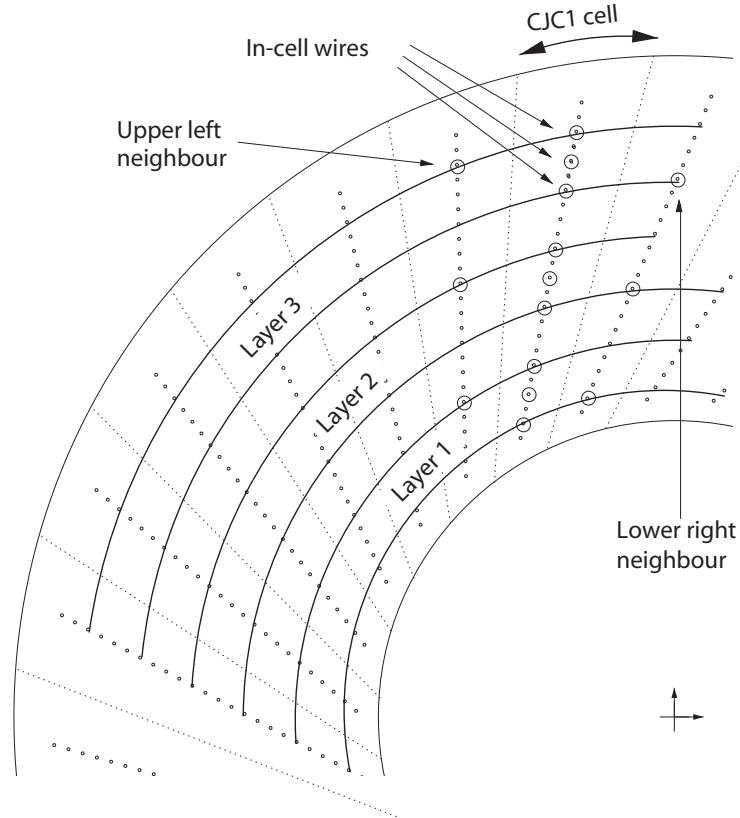


FIGURE 13.6: *The geometry of cells (including neighbour wires) for the inner ring of the central jet chamber.*

Hits identified by the  $Qt$ -algorithm are filled into shift registers clocked at a frequency of 20 MHz. The full hit information (timing with 80 MHz resolution (2 bit) and  $z$  (6 bit)) are stored in a parallel memory. For every cell there are five shift registers (three for the wires in the cell and two for the neighbours, see figure 13.6 for the geometry) with a depth of 24 bins to account for the maximum drift time of  $1.1 \mu\text{s}$  in the third layer.

For every bunch crossing hypothesis, the patterns in the shift registers are matched to up to 3072 masks per cell [245]. These masks are generated in advance on a standard PC by producing hit patterns with a time resolution of 320 MHz<sup>7</sup>, then eliminating all patterns incompatible with the assumption of a track from the vertex. To determine this compatibility, a circle-fit is performed using the best available knowledge of the chamber geometry and time-space transformation calibration. These fine-grained masks are then collected in 80 MHz masks, thereby assigning a weight corresponding to the number of valid 320 MHz masks to the 80 MHz masks. This step is repeated going from 80 MHz granularity to 20 MHz granularity. This procedure is repeated for all 150 trigger groups in order to take into account the fact that some wires are slightly misaligned. All 20 MHz masks of one layer are then collected into an ensemble. For every mask the segment curvature ( $\kappa$ )

<sup>7</sup>As there are  $\mathcal{O}(10^{10})$  of these patterns, only a subset corresponding to generously (very open  $\chi^2$  cut) validated 20 MHz masks is actually generated.

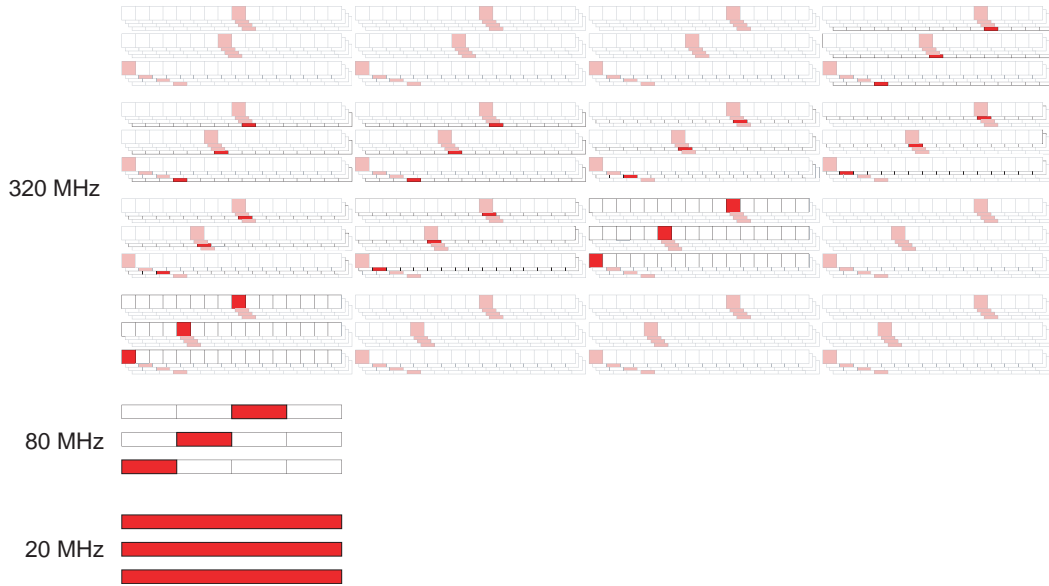


FIGURE 13.7: *Mask generation example.* For one 80 MHz mask, the corresponding 320 MHz masks are shown. For illustration, all masks fitting exactly to a straight line are declared valid (not grayed out). As there are 9 such 320 MHz masks, the 80 MHz mask would get a weight of 9. The weight of the 20 MHz mask is then the sum of the weights of 64 corresponding 80 MHz masks.

and azimuthal angle at a radius of 22 cm ( $\tilde{\varphi}$ ) is averaged over all cells. If there are more than 3072 masks<sup>8</sup>, the ones with the lowest weight summed over all cells of the layer are discarded. The remaining masks are then grouped into in-cell, left neighbour and right neighbour masks. These masks are subdivided into groups depending on which bins of the shift registers are on. The actual pattern match in the hardware thus only operates on 15 bit subsets of the full patterns [246, 247].

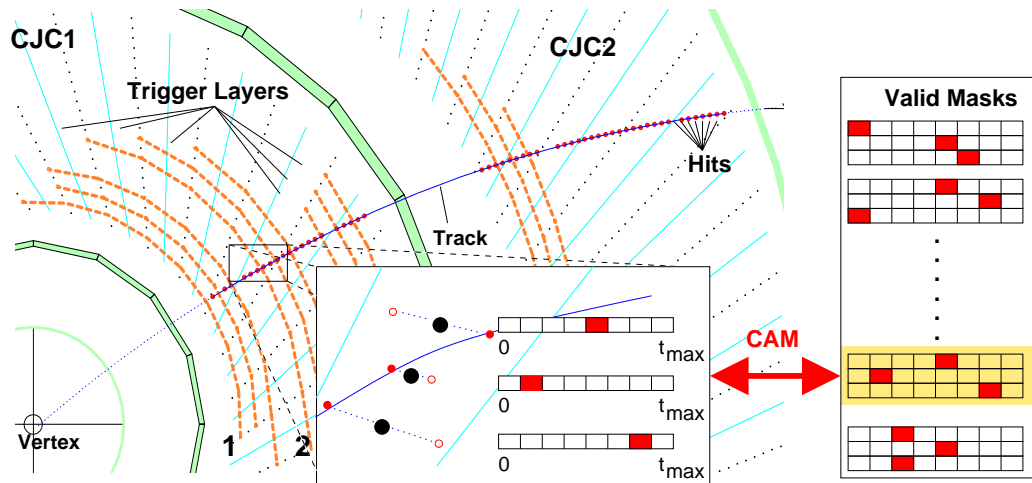
The pattern match is highly parallel<sup>9</sup>. The output is an unencoded 16 bit representation of the  $\kappa$  (track curvature,  $\propto 1/p_T$ ) values of the found segments. For the level 1 trigger, the granularity in  $\varphi$  is given by the cell size.

### 13.4.3 The Front End Module

Digitisation, hit finding and segment finding are performed on one of 30 Front End Modules (FEMs, figure 13.9) which were built by Rutherford Appleton Laboratory in the United Kingdom. Each of these 16 layer Printed Circuit Boards (PCBs) digitises the analogue signals of 5 trigger groups, i.e. 2 ends of 15 wires. To this end, it is equipped with 15 dual 10 bit Analogue to Digital Converters (ADCs) of type AD9218-80 [248] running at 80 MHz. The analogue signals of three wires are then collected on one of five so-called front FPGAs (Altera APEX20K400E [249]). These FPGAs are cross-linked with their neighbours (the link runs over the crate backplane for the first and last FPGA on a FEM) to exchange neighbour-wire hit information. The five front FPGAs are connected via a 40 bit bus each

<sup>8</sup>This is usually the case for the third layer, where the drift space is largest.

<sup>9</sup>In the complete FTT system, 18'000 bits (10'800 bits without double-counting the neighbours) of shift register information are compared to 6.912 Mbits of mask data for every bunch crossing. The total rate is  $4.8 \cdot 10^{12}$  pattern comparisons per second.

FIGURE 13.8: *Illustration of the shift registers and pattern match.*

to the so called back FPGA, another APEX20K400 chip, which has access to 4 MB of Zero Bus Turnaround (ZBT) memory for the level 2 validation and lookup. The back FPGA also controls two LVDS channel links. The FEM is in addition equipped with an ALTERA FLEX FPGA which provides an (A24/D16) VME interface for configuration and readout.

#### 13.4.4 Track Segment Merging

The track segments from 30 FEMs have to be finally collected on a single FPGA in order to link them to tracks. Due to physical limitations on the number of inputs per PCB, the number of pins of an FPGA and the available bandwidth, the segments are collected into groups using the *Merger* system [250]. It consists of 5 Multipurpose Processing Boards (MPBs - see section 13.6.3), each collecting the signals from 6 FEMs (one trigger layer in CJC1, half a layer in CJC2). Besides the six input channel links, each MPB has two output links, one to the level 1 Linker and one to the  $z$ -vertex trigger, which also forwards data to the level 2 system after a positive L1 trigger decision.

Due to bandwidth limitations, no control signals can be sent besides the data words on the links to the L1 Linker. This requires a perfect synchronisation of the data on the Merger. Unfortunately, the LVDS receiver chips used do not properly synchronise on every power-up, which then leads to transmission errors or occasional dropped data words [251]. If the synchronisation is fine, however, the link can be operated for days without transmission errors. Tests developed in [251] can be carried out after power cycles using the graphical user interface to the FTT and the data validity is continuously checked using statistical methods<sup>10</sup>. If a channel is found to be faulty, the receiver chip is powered down by software for 50 ms and then powered up again. The synchronisation is checked again and the procedure repeated if necessary. Thus, erroneous transmissions and data losses can be reduced to a sub-permille level.

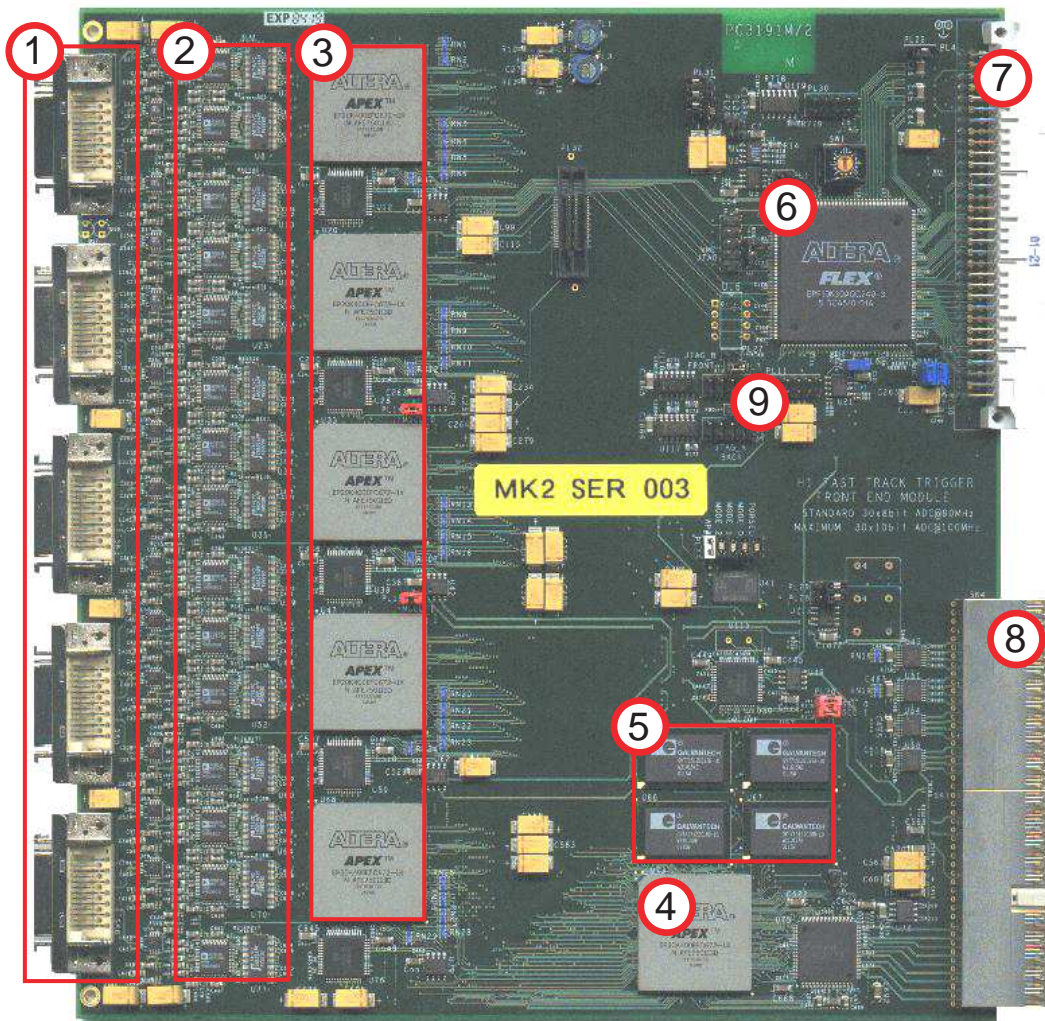


FIGURE 13.9: *Picture of a front end module. The most important components are labeled: 1: Connector for analogue signal cables 2: ADCs 3: Front FPGAs 4: Back FPGA 5: ZBT RAM 6: VME Interface FPGA 7: VME Connector J1 8: Custom backplane connector 9: JTAG Connectors.*

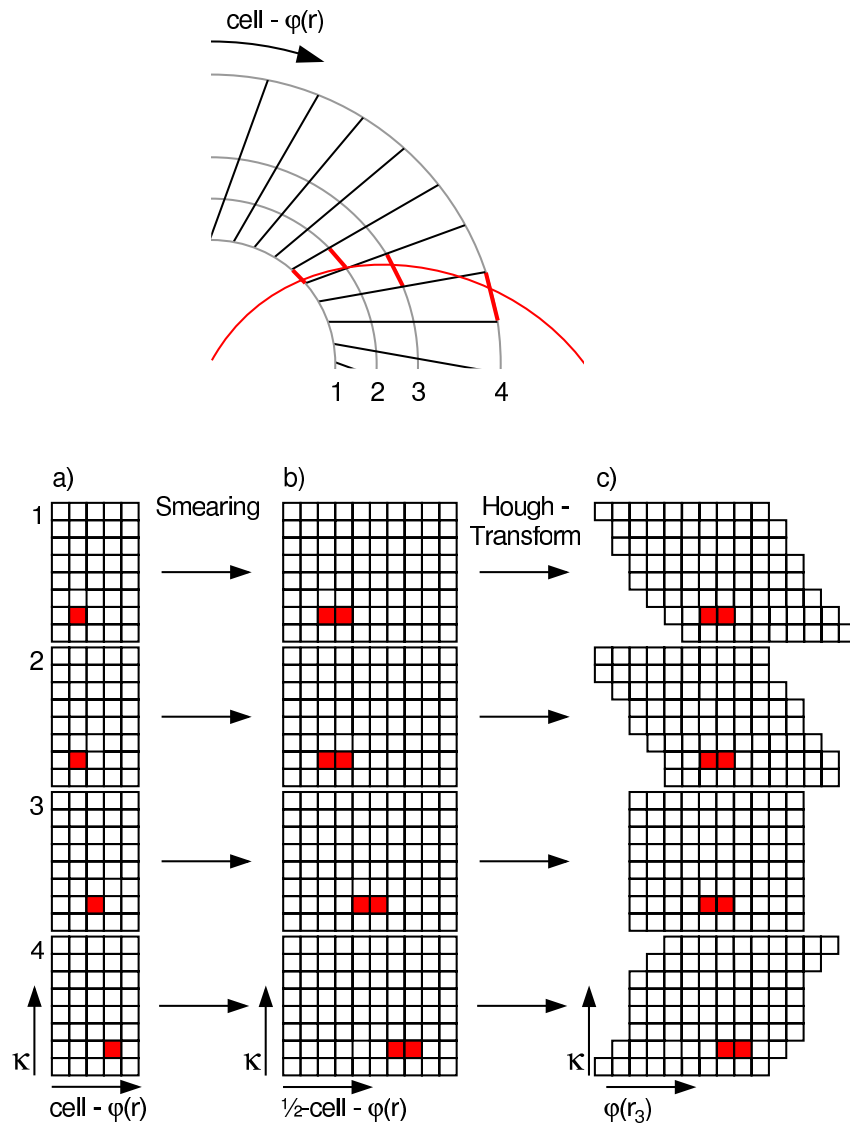


FIGURE 13.10: Schematic representation of the generalised Hough transform performed by the L1 Linker. On top, a  $r - \varphi$  view of the CJC with a track is shown. In a) parts of the four histograms for the four trigger layers are shown before the transform - each horizontal bin corresponds to a CJC cell. In b) the histograms are shown after the doubling ("smearing"). After the Hough-transform c), which also takes into account the cell tilt, the horizontal histogram axis corresponds to  $\varphi$  measured on the third layer. Entries belonging to the same track now occupy the same position in the histogram. The vertical histogram axis corresponding to the track curvature  $\kappa$  is shown here with 8 bins for clarity (the original has 16 bins).

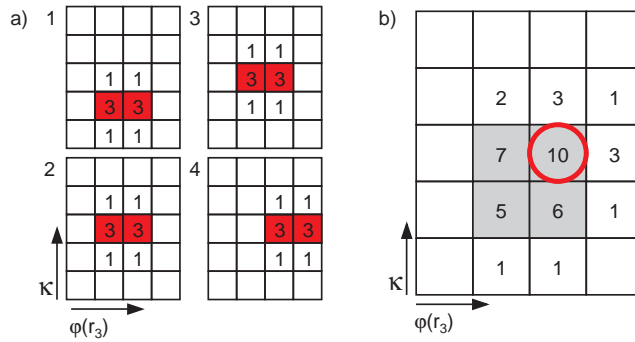


FIGURE 13.11: Schematic of the L1 Linker algorithm. a) The parts of the four histograms for the four trigger layers after smearing and Hough-transform. Hits are shaded, the numbers correspond to the weights of the bins. b) shows the “linked” histogram, i.e. after summing the weights of all four layers. Shaded bins reach the linking threshold of four and are thus track candidates. The peak search identifies the bin with the circle as a track and vetoes the three other candidates.

### 13.4.5 Track Segment Linking

On the level 1 Linker ([252,253], also an MPB), the track segments have to be combined to track candidates. The input is an array of bits, stating for which curvature  $\kappa$  and which cell (which azimuth  $\varphi$ ), track segments were seen on a particular layer. After synchronisation and sorting of the input, a generalised Hough transform [254,255] is performed, which maps all layers to the  $\kappa - \varphi$  space of the third trigger layer (see figure 13.10). This produces four histograms with  $16 \times 60$  bins in  $\kappa - \varphi$ ; the granularity of the input is only 30 bins in  $\varphi$ , but the Hough transform uses the higher resolution and the input is smeared to compensate for edge effects<sup>11</sup>. Track candidates are coincidences of at least two track segments from different layers in the same  $\varphi$  bin and the same or adjacent  $\kappa$  bins (see figure 13.11). Only local maxima (“peaks”) are considered in order to avoid double counting.

The linking algorithm is pipelined and highly parallel. Every clock cycle (corresponding to a 10<sup>th</sup> of a bunch crossing), one 10<sup>th</sup> of the total histogram is processed – only one clock cycle after receiving the last histogram section, the linked histogram is available for further processing.

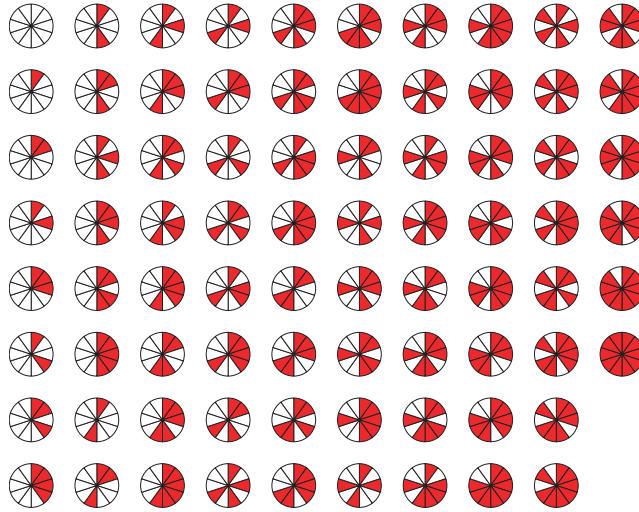
### 13.4.6 Level 1 Trigger Decision

The tracks found in the linking step are then used to derive a set of 16 trigger elements (TEs). The number of tracks is counted for eight different transverse momentum thresholds (six of which are sent to the central trigger logic) and the total charge of the tracks in the event is determined.

The arrangement of tracks in the  $r - \varphi$  plane is used to trigger on event topologies (see chapter 6 for an application example). To this aim, the  $\varphi$ -axis is divided into ten sectors. If a sector contains tracks, the corresponding bit in a 10 bit number is set, otherwise it remains zero. The resulting number is used to look up the TEs to be set in a memory. This

<sup>10</sup>At HERA, most of the bunch crossings contain no tracks, thus no track segments should be seen - the transmitted bits should be mainly zeros. By inverting specific bits (and reverting them in the end), a check of the synchronisation on a statistical basis becomes possible.

<sup>11</sup>This smearing is successful in the  $\varphi$  direction, but occasionally track links are lost due to edges in the transformations and entries in neighbouring  $\kappa$  bins.

FIGURE 13.12: *The 78 distinct topologies for a tenfold division in  $\varphi$ .*

has the advantage of being very fast and fully reconfigurable by overwriting the memory. The tenfold division in  $\varphi$  leads to a total of 1024 different possible patterns, of which 78 are distinct under rotations and reflections. These patterns are shown in figure 13.12. The last available TE, the so-called *segment bit*, indicates whether a segment was seen in some programmable subset of all cells and layers; this TE has been instrumental in designing the  $\phi$  trigger presented in chapter 6.

The level 1 FTT uses the 22 bunch crossings available as level 1 latency almost completely. Most of the time is spent waiting for long drift times and transmitting and receiving data. The actual trigger algorithms use less than 350 ns (36 clock cycles). See table 13.1 for a detailed overview of the time used.

## 13.5 The Level 1 $z$ -Vertex Trigger

The feasibility of a CJC based  $z$ -vertex trigger on level 1 was studied in [232]. In the early days of HERA II it appeared highly desirable to have a second trigger as a cross-check and fallback solution for the CIP2000  $z$ -vertex trigger. The front end module firmware and the Merger system were consequently modified to accommodate such a system. The segment finding algorithms were implemented on the back FPGAs of the first three trigger layers and an additional  $z$  Linker board hosts the vertex finding algorithm [256].

### 13.5.1 Finding Track Segments in $r$ - $z$

During the charge division in the front FPGA, the  $z$  value of a hit is determined twice; once in a range from 1 to 62 for the level two system and once in the range from 1 to 40 for the level 1  $z$  vertex trigger. On the back FPGA, 40 three-bit counters are implemented for each wire in order to buffer hits for a large part of the allowed drift times. If a hit with a  $z$  value  $z_i$  is measured, the corresponding counter is set to its maximal value. With every rising HERA clock (10 MHz), the counter is reduced by one. The pattern of all non-zero counters corresponds to the pattern of hits with a valid drift time. The counters use only about 20% of the resources that would be needed to implement a full pipeline.

Delay	Time per step		Cumulated time	
	BC	ns	BC	ns
Ionisation and drift	11.000	1056.00	11.000	1056.00
Analogue cable delay	1.875	180.00	12.875	1236.00
FEM: FADCs	0.625	60.00	13.500	1296.00
FEM: Hit finding	0.375	36.00	13.875	1332.00
FEM: Segment finding	1.000	96.00	14.875	1428.00
FEM: Collection of segments	0.900	86.40	15.775	1514.40
Channel Link: FEM → Merger	0.730	70.08	16.505	1584.48
Merger: Merging	0.900	86.40	17.405	1670.88
Channel Link: Merger → L1 Linker	0.625	60.00	18.030	1730.88
L1 Linker: Receiving and sorting input	0.800	76.80	18.830	1807.68
L1 Linker: Linking	0.500	48.00	19.330	1855.68
L1 Linker: Pipelining	1.000	96.00	20.330	1951.68
L1 Linker: Trigger decision and driver	0.700	67.20	21.030	2018.88
Transmission of trigger elements to CTL	0.500	48.00	21.530	2066.88
Time available (L1 latency)	22.000	2112.00	22.000	2112.00
Time used by analogue signals	13.500	1296.00		
Time used by digital signal transmission	4.455	427.68		
Time used by actual trigger algorithms	3.575	343.20		
Spare	0.470	45.12	0.470	45.12

TABLE 13.1: *Timing of the level 1 FTT. “BC” stands for bunch crossings.*

In the  $r - z$  plane, track segments are identified by requiring two out of three hits within one trigger group forming a valid pattern. These patterns shown in figure 13.13 are stored in CAMs and a quick lookup can be performed. The found segments set bits in an unencoded 40 bit word. The words from neighbouring drift cells are merged to ten overlapping sectors in  $\varphi$  (see figure 13.14 for the geometry of a sector) by combining the unencoded words in a logical OR. This sector information is then sent via the Merger system to the  $z$ -Linker.

### 13.5.2 Linking $z$ Segments and Trigger Decision

For all ten sectors in  $\varphi$ , all possible combinations of two segments from different layers are connected, as illustrated in figure 13.15. The intercept of the connecting line with the beam line is entered into a histogram<sup>12</sup>. The ten histograms from the  $\varphi$  sectors are then summed and a peak is searched in the resulting  $z$ -intercept distribution. Trigger elements are then derived from the peak position and the height of the peak relative to the total histogram contents.

## 13.6 The Level 2 Fast Track Trigger

### 13.6.1 Track Segment Verification and Track Parameter Lookup

After a positive level 1 trigger decision the pipelines in H1 are stopped and the level 2 decision phase begins. As the level 1 accept signal arrives a fixed time after the bunch

<sup>12</sup>This part of the algorithm was implemented using a meta-code in C, generating low-level VHDL code consisting of all possible statements of the form `if(bita AND bitb) histogrambin(intercepta,b)++`.

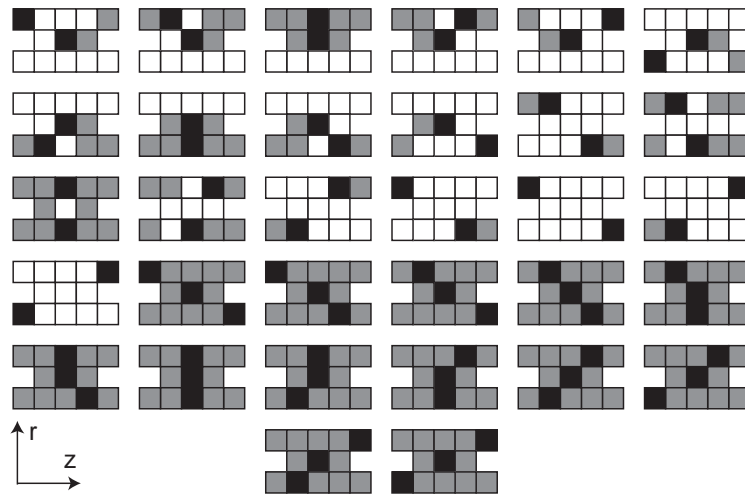


FIGURE 13.13: *Hit patterns constituting  $z$  segments. The three rows in each pattern represent the three wires of a trigger group and the five bins on the outer and the three bins on the inner wire constitute a local search neighbourhood. Black bins require a hit, white bins require no hit and grey bins are don't care bins. The patterns are chosen to be mutually exclusive and patterns with more hits and less track inclination are favoured.*

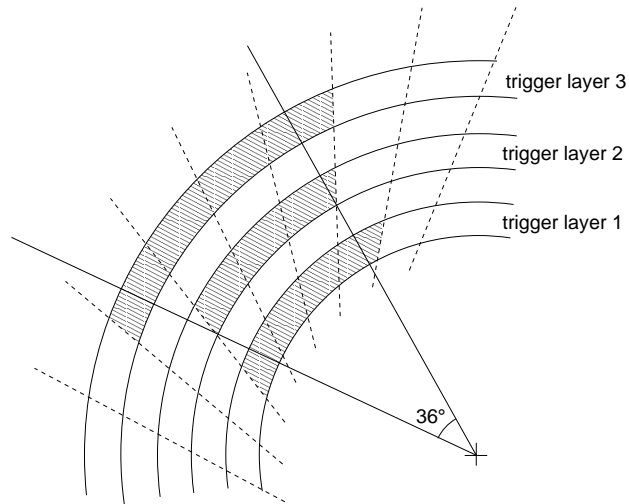
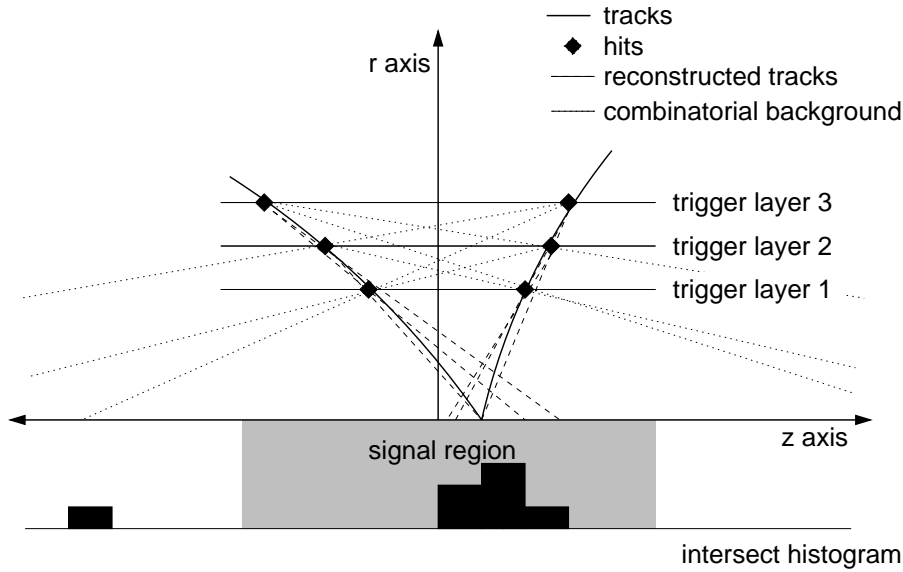


FIGURE 13.14: *Geometry of one  $\phi$  sector of the level 1  $z$ -vertex trigger.*

FIGURE 13.15: *Linking segments in the  $r - z$ -plane.*

crossing under consideration, the corresponding patterns have moved by a fixed amount in the shift registers. The CAM pattern match on the front FPGA is repeated with these shifted patterns. Using a Read-Only Memory (ROM), the hits belonging to the found patterns are identified and the higher granularity (80 MHz) time information as well as the  $z$  position retrieved from the shift registers. An *unvalidated L2 segment* is formed from the CAM pattern number, the 80 MHz information and the three  $z$  positions. A *priority encoder* serialises these segments, prioritising segments with higher transverse momenta [245]. The segments are sent to the back FPGA. The back FPGA is connected to a *validation* and a *lookup* memory. The CAM pattern number plus the 80 MHz information determine the address for the validation RAM. If the corresponding hit pattern is indeed valid, the memory contains an address in the lookup RAM, else zero. For the valid patterns, the lookup RAM contains the information specified in table 13.2.

Information for the L2 Linker			Information for the track fit		BFPGA information
L2 Linker CAM Number	$\kappa$	$\varphi$	Cell	Drift distance	Second hypothesis
5 bit	3 bit	7 bit	5 bit	10 bit	1 bit

TABLE 13.2: *Data stored in the lookup ROM. If the second hypothesis bit is on, other track parameters can be attributed to the same segment and a further lookup is performed.*

In parallel to the validation and lookup, the three  $z$  hits are checked for consistency and outliers are rejected<sup>13</sup>. There are three possible cases for the outlier rejection [257]:

- If there is a single valid hit, it is kept.
- If there are two hits, their distance in  $z$  is calculated and if it is below a limit, both are kept. Otherwise both are rejected.
- If there are three hits, the central one in  $z$  is determined. Then the distance of the other two to the central hit is calculated. If the distance is above a limit, the hit is discarded.

<sup>13</sup>The  $z$  measurement by charge division is less reliable than the time measurement, as e.g. several hits on the same wire or noise can distort the charge ratio.

If both distances are above the limit, the complete triplet is discarded.

The cleaned up  $z$  hits and the lookup information are packed into a message and sent via the merger system to the level 2 Linker.

### 13.6.2 Track Segment Linking

The L2 Linker algorithm [251] is conceptually similar to the L1 Linker, but works with a much increased granularity. This becomes possible as more time is available and the linking can proceed sequentially. The Hough-transform for the level 2 linker is performed offline and the lookup RAM on the back FPGA thus already delivers the coordinates in  $\kappa - \varphi$  space. This space is segmented into 40 times 640 bins in  $\kappa - \varphi$  – as the number of segments per layer is limited to 128, the maximum filling factor of these 25'600 bins is just 0.5 %. The four histograms corresponding to the four layers are implemented in 4 times 25 CAMs, forming a local search neighbourhood.

In a first step, all the received segments are written to a CAM, whereby the local position (within a 5 times 5 bin window) determines the CAM number and the position of the window the CAM content. In parallel, the segments are written to a seed RAM and a segment RAM. After all segments are received, the linking algorithm starts. Every segment is used as a search seed. For every seed, the global position and the position within the local window is used to determine the search pattern. This pattern is then presented to all CAMs. A weighting and priority algorithm then ensures that only links of a minimum quality are flagged as valid and that every segment is only linked once.

For the linked segments, the drift distance and  $z$  information is retrieved from the segment RAM and sent to the fitter DSPs.

### 13.6.3 The Multipurpose Processing Board

The level 1 and 2 Linker, the merger system, the fitter cards and the level 2 decider card are all implemented using different FPGA programmes on a Multi Purpose Processing Board (MPB [258]).

The MPB is a 14 layer printed circuit board. Each MPB (figure 13.16) can be equipped with up to four so-called *Piggy Back* cards, providing two 5 Gbit/s channel links each. The buses from and to the Piggy Back cards are collected at the *Data Controller* FPGA, which is either an Altera APEX20KC600E (Linker boards) or an Altera APEX20K400E (merger and fitter boards) [249]. This FPGA hosts the linking,  $z$ -vertex and decision algorithms and forwards data to the *DSP Controller* FPGA (Altera APEX20K200E) which in turn controls the external memory interfaces and interrupts of four floating point DSPs (Texas Instruments TMS320C6701, [242]) which run the track fit algorithms. Each DSP also has an external memory of 512 KB and all the DSPs are connected via a switch to a dual ported memory which is write- and readable via VME and is thus used to provide the DSPs with boot images and configuration data. Both FPGAs and the DPRAM are connected to a local bus, which is in turn interfaced to the VME backplane by a smaller FPGA (Altera FLEX EPF10K30A).

The Piggy Back cards come in two flavours, namely equipped with two LVDS inputs (II) or one input<sup>14</sup> and one output<sup>15</sup> (IO). The data flow from and to the channel links is controlled by an Altera APEX20K60E FPGA.

Both the MPB and the Piggy Back cards were designed and built by Supercomputing Systems (SCS) in close collaboration with the FTT group.

---

<sup>14</sup>National DS90C388

<sup>15</sup>National DS90C387

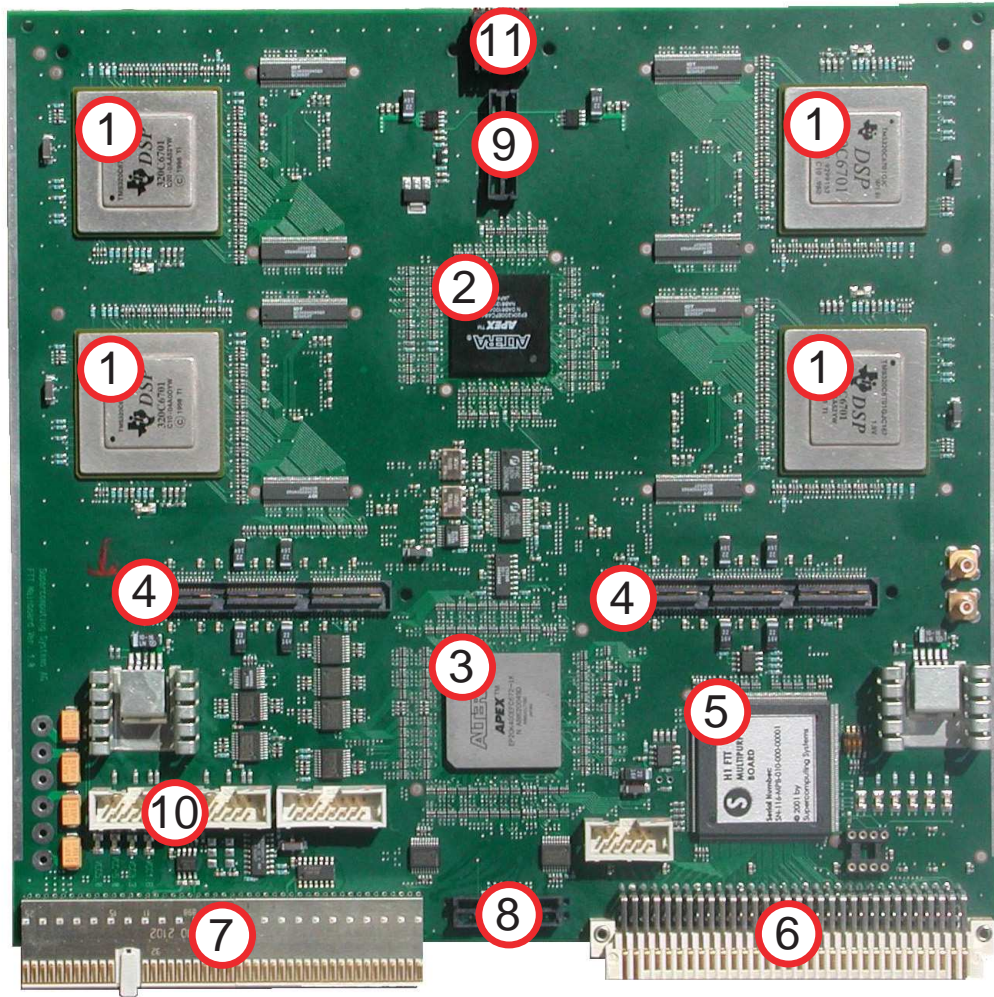


FIGURE 13.16: *Picture of a Multipurpose Processing Board. The most important components are numbered: 1: DSPs 2: DSP Controller FPGA 3: Data Controller FPGA 4: Piggy Back connectors 5: VME Interface FPGA 6: VME Connector J1 7: Custom backplane connector 8: Logic analyser connector for Data Controller FPGA 9: Logic analyser connector for DSP Controller FPGA 10: JTAG connectors 11: Status LEDs. On the back side, two more Piggy Back connectors, a dual-ported RAM and an associated DPRAM Controller FPGA are mounted.*

### 13.6.4 Data Transmission in the Level 2 System

The level 2 system consists of the L2 Linker card, 6 fitter cards and the L2 decider card. Communication between the components of these cards occurs via a message system [259]. 48 bit messages are forwarded from one component to the next one using a configurable routing table. The top 10 byte of each message contain one of 512 channel numbers plus its parity. Every FPGA has a routing table, indicating to which of its neighbouring devices it has to forward messages with a particular channel. The DSP Controller FPGA in addition provides VME-accessible First-In First-Out memories (FIFOs) as sources and destinations, which makes it possible to feed messages into the system and read them out.

The advantages of this system are the economic use of bandwidth (only data needed by a certain component is sent to that component) and its high flexibility (if different data is needed in different places, only the routing has to be changed whilst the firmware remains untouched). It is however essential that the routing information is complete (i.e. every device on a route knows the correct destination) and minimal (messages are not sent to places where they are not needed – and, crucial for the proper working of the system – there are no loops within routes, which would lead to indefinite message propagation). As the dynamic routing involves 100 channels on 20 FPGAs, some degree of automation in generation, configuration and verification is needed. The original routing algorithm was provided by SCS [259] and was based on Microsoft Excel macros. During the course of this thesis work it was realised that a more transparent system, running on the readout PowerPC (see section 13.8) was needed. Consequently, a routing algorithm was written in plain C. In addition to automatic configuration routines it provides a set of tools to reconstitute and test any generated routing on a standard PC.

### 13.6.5 Vertex Determination

The linked track segments are subject to a 3-dimensional primary vertex constrained fit (see the following section). The beam spot position in the transverse plane is determined on the H1 filter farm from the average of several thousand vertex fits using the full H1 reconstruction. As this position changes very slowly with time, the average from the previous run constitutes an excellent guess for the current vertex position. The FTT thus uses the average vertex from the previous run as an input to the fit [260]. The FTT graphical user interface provides tools to monitor the vertex position and load it into hardware.

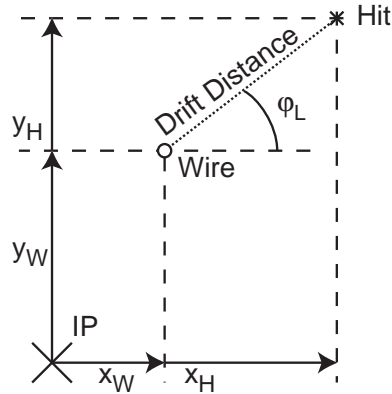
The vertex position in  $z$  (along the beamline) varies by several centimeters between events. It thus has to be determined by the FTT on an event-by-event basis. The corresponding algorithms were developed in [232] and implemented during this thesis work. Details on the implementation and performance can be found in chapter 14.

### 13.6.6 Track Segment Fitting

#### Data Transmission to the DSPs

The linked segments and the vertex position are transmitted to the digital signal processors using Direct Memory Access (DMA) controlled by the DspCtrl FPGA. At the same time, the DSP constantly polls the memory contents and as soon as it detects valid information, starts to decode them. This communication scheme ensures the fastest possible data transmission to the DSP but puts very stringent constraints on the timing and sequence control on the FPGA side. The commissioning of this vital communication link was part of the scope of this thesis. This involved a redesign in order to incorporate the vertex information and improve the reliability and fidelity of the data transmission.

FIGURE 13.17: The transverse coordinates  $(x_H, y_H)$  of a hit relative to the interaction point (IP) are determined from the known wire position  $(x_W, y_W)$ , the drift distance (which is the product of the drift time and the drift velocity) and the Lorentz angle  $\varphi_L$ .



### Drift time calibration

The linked segments message contains the segment position in the chamber (layer and segment) and the drift distance. The DSP in turn is configured with a table containing the position of the central wire of each cell and the corresponding drift angle (Lorentz angle). From this information, the position of the original hit in the transverse plane is reconstructed in cartesian coordinates (see figure 13.17).

### Track fit in the transverse plane

The segment coordinates in the transverse plane are then fitted to a circle passing through the primary vertex. This is done using the non-iterative method of Karimäki [261], adapted to running on a DSP. Mathematical functions not directly provided by the DSP floating-point execution units, such as square roots and trigonometric functions are approximated using Taylor polynomials. This in combination with a detailed optimisation of the assembler code to ensure maximum use of the DSP resources make it possible to perform a fit to four track segments in only 300 clock cycles ( $2.25 \mu\text{s}$ ) [262]. The results of the fit are the inverse transverse momentum  $1/p_T$  and a function of the azimuthal angle  $\varphi$ <sup>16</sup>.

### Track fit in the longitudinal plane

Each segment comes with up to three  $z$ -measurements. These measurements are combined with the  $z$ -vertex determined by the FTT to fit a straight line in the  $z-s$  plane<sup>17</sup>. Also this fit is highly optimised and thus requires only 150 clock cycles ( $1.12 \mu\text{s}$ ) [262]. The result of this fit is the cotangent of the polar angle  $\vartheta$ .

The fit results are standard 32-bit floating point numbers. These numbers are packed into messages and sent to the decision unit from where on they are forwarded to the level 3 system. For quick, FPGA-based calculations as implemented on the decider FPGA the three determined track parameters are also packed into a compact bit pattern, containing 38 bit of track information: 16 bit  $\varphi$ , 12 bit  $1/p_T$  and 10 bit  $\theta$ .

The level 2 latency of the H1 trigger of  $22 \mu\text{s}$  is sufficient to allow for two track fits per DSP. It is thus possible to fit up to 48 tracks per event with the 24 DSPs available.

<sup>16</sup>The projection of a circle to an octagon with unit sides is used to represent the angle as a number between zero and eight. This representation has the advantage of being a monotonous function of the angle and containing either the sine or the cosine of the angle, depending on the octant - see [262] for details.

<sup>17</sup> $s$  is the arc length along the circle fitted in the transverse plane.

Simulation studies have shown that less than 0.5 % of the events of interest have more tracks; this finding was confirmed by the data taken with the FTT.

### 13.6.7 Invariant Mass Determination

The track parameters determined by the track fits serve as inputs to a FPGA based invariant mass reconstruction algorithm, able to recognise two-body decays (e.g. vector mesons). The development and commissioning of this algorithm was a core part of this thesis. It is thus described in detail in chapter 15.

### 13.6.8 Level 2 Trigger Decision

The fitted track quantities are used to derive a set of a total of 64 FTT internal trigger elements [263]. These trigger elements verify and refine the level 1 decision by:

- Counting track multiplicities above various thresholds, making use of the better resolution of level 2 by accessing higher transverse momenta;
- Studying the track topology in the transverse plane with a 16-fold segmentation<sup>18</sup>, using the azimuthal angle at the vertex as an input;
- Determining the total charge in the event.

The level 2 trigger also expands on the possibilities of level 1 by providing kinematic quantities such as the scalar and vectorial sum of the transverse momentum ( $E_T$  and  $p_T$ ), the amount of momentum parallel and antiparallel to the direction of missing momentum ( $V_p$  and  $V_{ap}$ ) and the invariant mass of two track combinations.

In addition the  $z$ -vertex determined by the FTT and its quality can be used for trigger conditions.

To make the best use of the detailed information available from the FTT and the limited bandwidth and logic capabilities of the level 2 central trigger logic, the FTT combines its 64 internal trigger elements to 24 physics triggers, tailored to select events originating from a specific process such as diffractive  $\phi$ -meson production or  $D^*$  production.

## 13.7 The Level 3 Fast Track Trigger

The level 3 fast track trigger combines the high resolution tracks from level 2 with trigger information from other subsystems on a commercial processor [264]. This allows for a partial event reconstruction and thus the selection of specific final states involving more than two particles.

### 13.7.1 Data Transmission and Distribution

After a positive level 2 trigger decision (L2\_KEEP), the level 2 track information is sent to the *L3 receiver card* [265]. The level 2 system also collects information from other trigger subsystems (namely the muon system and the jet trigger) which is broadcast via the *Parallel Quickbus Zero-suppressed Processor* (PQZP) system, which is also forwarded to the receiver card. This is a custom built board equipped with an ALTERA APEX400K FPGA, an interface to a LVDS Piggy Back card and a further connection to a Front Panel Data Port (FPDP, [266]) interface. Via the FPDP bus, the data are transmitted in parallel to up to 12 PowerPCs, each equipped with a *Digital Parallel Input/Output* (DPIO) card receiving the

---

<sup>18</sup>The 16-fold segmentation gives 65'536 possible topologies, 2250 of which are distinct after removing rotations and reflections.

data. Via a *Direct Memory Access* (DMA) the data are transferred into the RAM of the PowerPC.

At the end of the data transfer, an interrupt starts the data preparation algorithms on the PowerPCs. They unpack the information from L2 and fill it into structures where they can be conveniently used in selection algorithms.

### 13.7.2 Physics Algorithms

The benchmark process for the level 3 FTT trigger is photoproduction of  $D^*$  mesons, where the  $D^*$  decays via the so-called "golden channel":

$$D^* \longrightarrow D^0 \pi_s \quad (13.4)$$

$$\hookrightarrow K \pi \quad (13.5)$$

where  $\pi_s$  stands for the slow (low momentum) pion from the  $D^*$  decay. In the level 3  $D^*$  finder algorithm, all combinations of two oppositely charged tracks are searched for  $D^0$  candidates. To these candidates, a third track is added and the small mass difference between  $D^*$  and  $D^0$  is then used to select  $D^*$  candidates [264].

Other algorithms include the search for elastic and inelastic vector meson candidates in deep inelastic scattering [267], where electron trigger information from the SpaCal is used or the search for leptonic decays of  $B$ -mesons using the liquid argon calorimeter [268].

## 13.8 Data Acquisition and Slow Control

In order to monitor the performance of the FTT and to use its results in physics analyses, parts of the digital information is read out and written to the H1 data stream. To this aim, most electronics boards are equipped with an interface to a VME16 (VME32 in the case of level 3) bus [269]. A PowerPC in each crate reads the appropriate registers on the FPGAs via VME. This information is then converted to the Bank Object System (BOS [187]) format. The data from the various FTT crates are collected on the STC (Subsystem Trigger Control) crate via an Ethernet [188] and TCP/IP [270,271] based data acquisition (DAQ) [272]. This system is also responsible for the initialisation and synchronisation of the various parts of the FTT. For monitoring and control purposes, it works closely together with the graphical user interface described in chapter 17. From the STC crate, the data read from the FTT are written to another VME PC, which then forwards them to the H1 event builder (see also sections 4.7.4 to 4.7.5).

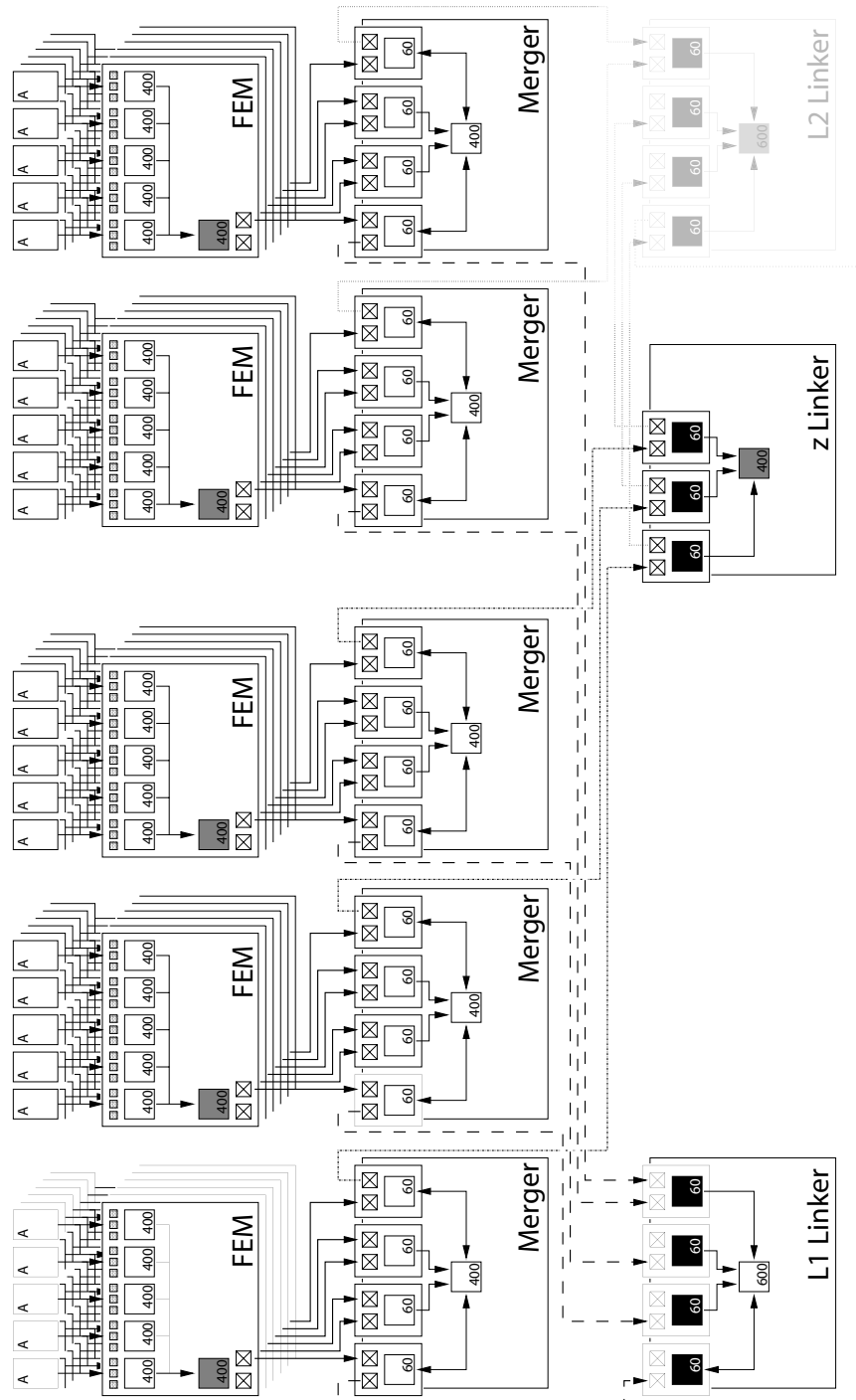


FIGURE 13.18: Flow diagram of trigger data in the FTT system (I). Level 1 part.

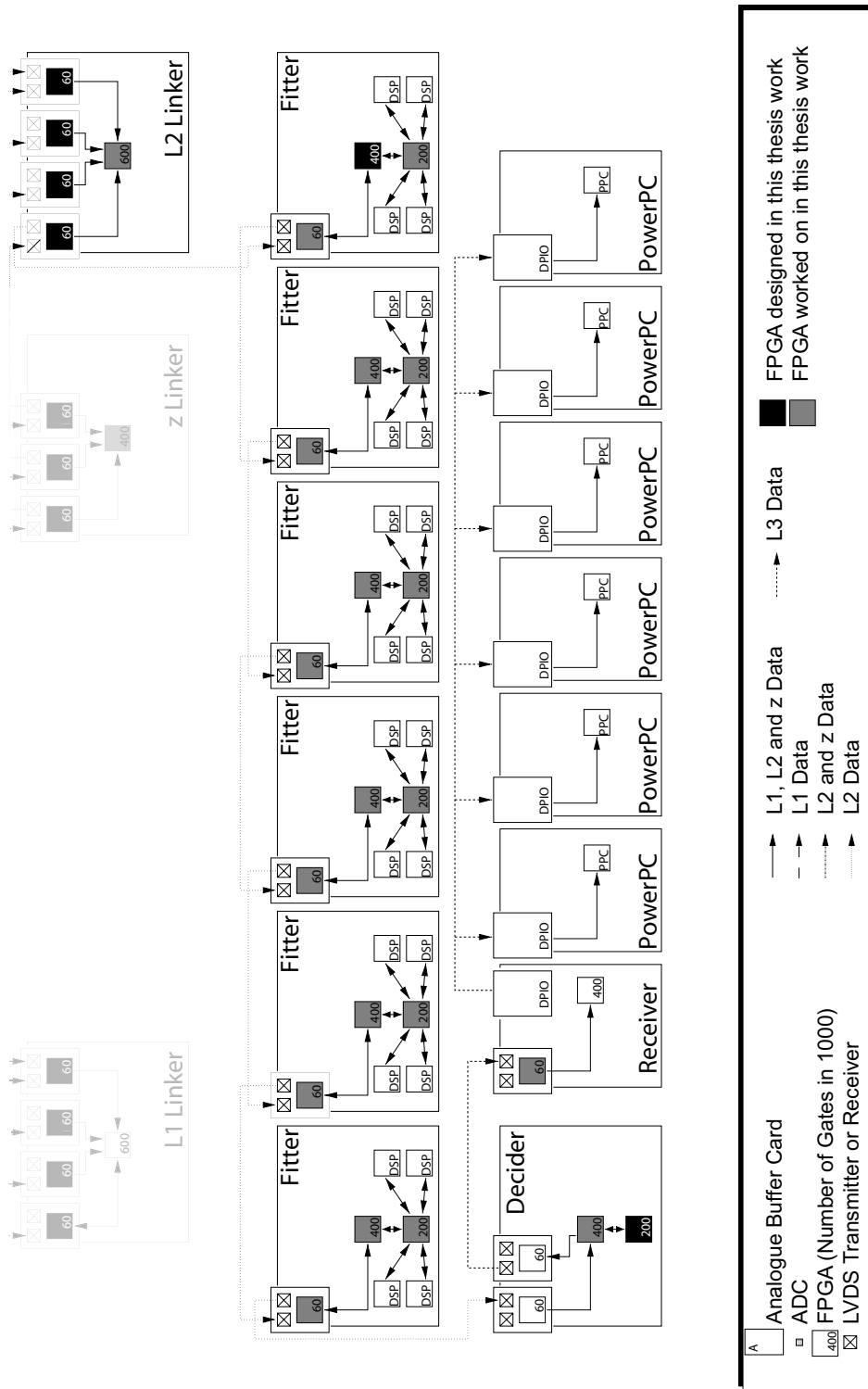


FIGURE 13.19: Flow diagram of trigger data in the FTT system (II). Level 2 and 3 parts.



## Chapter 14

# A Fast and Accurate $z$ Vertex Determination for the Level 2 FTT

*Some times it all comes together – sometimes you are gonna loosing it all.*

MARK KNOPFLER

### 14.1 Drift Chamber Based $z$ Vertex Determination

The determination of the polar angle  $\vartheta$  by the level 2 FTT track fit relies on knowledge of the position of the  $z$  vertex. The original FTT design foresaw to use the  $z$  vertex determined by the CIP-COP  $z$ -vertex trigger. This system was however only partially operational in 2005 and is now completely switched off. In [232] it was shown that the FTT can determine the  $z$  vertex with good precision from CJC information alone. This algorithm was implemented on an Altera APEX20K400E FPGA. Whilst the simulations in [232] had predicted a resolution below 2.5 cm, the measured resolution was around 12 cm and thus not better than the a priori knowledge of the bunch length.

The algorithm in [232] uses the linked L2 tracks. Within one segment, the  $z$  values of the three hits are averaged and then a fast linear pseudo-fit to all segments of a track in the  $r - z$  plane is performed. The intercepts are then averaged with weights according to the number of segments and the lever arm of a track.

The source of the bad resolution was traced to two main sources. On one hand, wires with dead preamplifiers at one end were not correctly masked. As these problems always affect a whole trigger group, the complete segment was shifted to one end of the chamber and then spoiled the intercept result of the complete track. The second problem not foreseen by the simulation was the fact that the resolution of hits is not uncorrelated between wires. In the simulation, an average single hit resolution  $\sigma_z^{hit}$  of 6 cm was assumed. The segment resolution (three hits) was determined as

$$\sigma_z^{seg} = \frac{\sigma_z^{hit}}{\sqrt{3}} \approx 3.5 \text{ cm.} \quad (14.1)$$

Tuning of the  $Qt$  algorithm of the FTT and gain increases in the CJC led to a measured  $\sigma_z^{hit}$  of around 5 cm. The source of the smearing of  $z^{hit}$  is however mostly coherent noise seen on all wires. The segment resolution  $\sigma_z^{seg}$  is consequently only marginally better than the single hit resolution, because the hits are shifted coherently into the same direction. Thus resolution and bin size in the algorithm were ill matched and for low and medium multiplicity events a single badly measured track could determine the final result.

Once these problems were identified, a correct masking of the preamplifiers was applied and a more robust algorithm developed, which also takes into account the a priori knowledge about the vertex distribution. Many of the well-tested building blocks of the old algorithm were re-used allowing for a very short development cycle.

## 14.2 A Robust $z$ Vertex Finder

### 14.2.1 Overview of the Algorithm

The new level 2  $z$  vertex finder algorithm tries to take into account all the available information and estimates of its accuracy. Figure 14.1 shows a schematic representation of the algorithm. For the first 24 linked tracks, every segment is combined with every other and the corresponding intercepts are computed. Depending on the lever arm of the segment combination, a weight corresponding to the expected resolution is assigned to each intercept. The intercept is then entered into a seven bin histogram using a gaussian smearing profile. After all tracks are processed, the peak of the histogram is identified and a weighted mean of all intercepts contributing to the peak bin is calculated with 10 bit accuracy. This mean is then sent to the DSPs as an input for the track fits.

### 14.2.2 Track Segment Preparation

The whole level 2  $z$  vertex finder algorithm works fully pipelined, i.e. it is capable of processing one track segment per 100 MHz clock-cycle. Every segment can have between zero and three valid  $z$  hits. Segments without  $z$  hits are discarded, for all other segments a mean  $z$  value is calculated. The segments with valid  $z$  measurements are filled into an array and all valid combinations of two segments each are extrapolated to the beam pipe.

### 14.2.3 Extrapolation

The extrapolation to the beam pipe can be performed with a subtraction, a single multiplication with a constant and an addition (three clock cycles in total). This is due to the fact that the radii of the trigger layers are fixed. The intercept with the beamline  $z_{int}$  for two segments with  $z$  values  $z_1$  and  $z_2$  and radii  $r_1$  and  $r_2$  is thus

$$z_{int} = z_1 + (z_1 - z_2) \frac{r_2}{r_2 - r_1}, \quad (14.2)$$

where the fraction can be pre-calculated. The fraction, denoting the extrapolation length divided by the lever arm of the two-segment combination is also a measure of the accuracy of the combination. The inverse fraction is thus used as a weight for the result.

### 14.2.4 Histogramming and Vertex Determination

A precise knowledge of the vertex position is only desirable for  $ep$  events; the determination is consequently only done in a range from -66 to +66 cm in  $z$  around the centre of the CJC

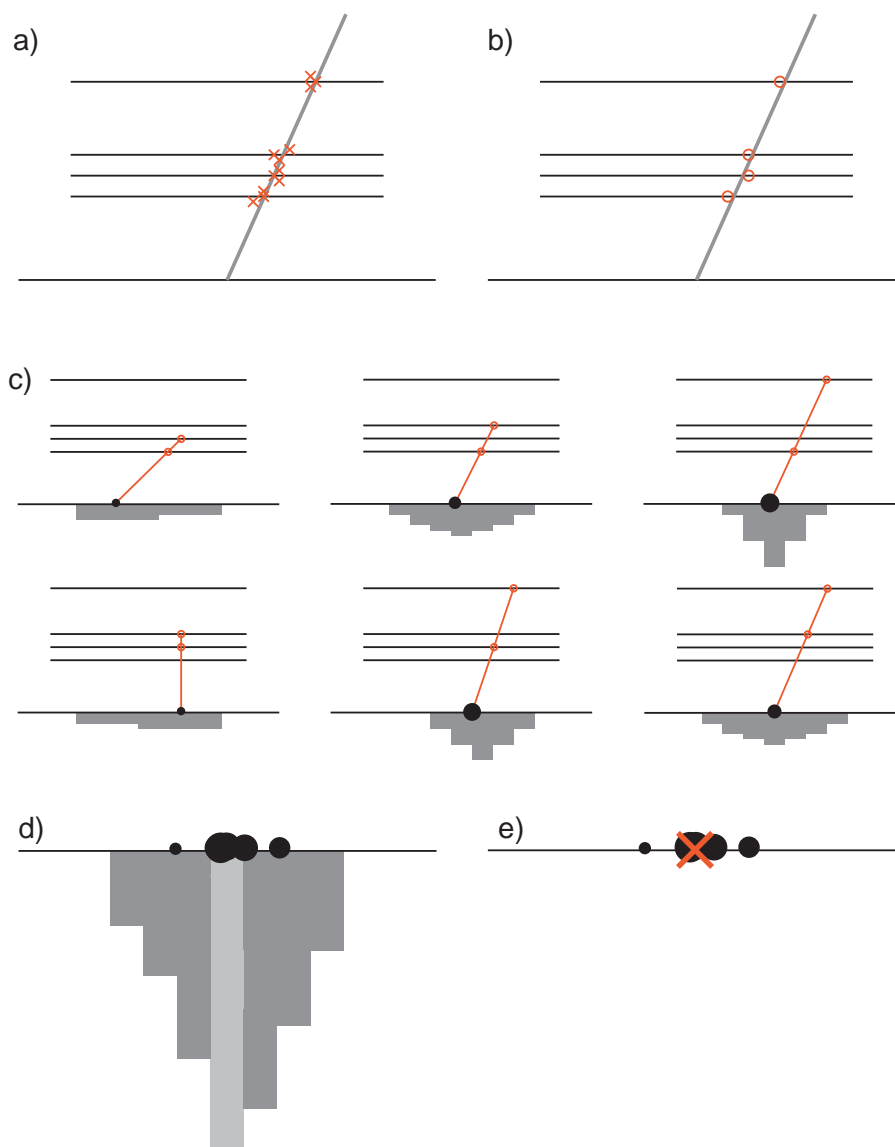


FIGURE 14.1: Schematic representation of the L2z algorithm for a single track with four linked segments. a) shows the track in the  $r - z$  projection, the horizontal lines indicate the beamline and the four FTT layers. The hits associated with the track (crosses) show a typical spread due to binning and resolution effects. In a first step, the mean  $z$  value for each segment is determined (open circles in b)). c) For all six combinations of two segments, the intercept of the connecting straight line with the beamline is calculated (filled circles). These intercepts are weighted according to the lever arm of the hit combination (size of the circles) and a gaussian profile according with the expected resolution is entered into a histogram (shown in gray below the beamline). d) the histograms are then summed (if more tracks were present, they would enter here) and a peak is identified (light gray bin in the histogram). e) A weighted average of the intercepts contributing to the peak bin is calculated – this is the estimated vertex position (large cross).

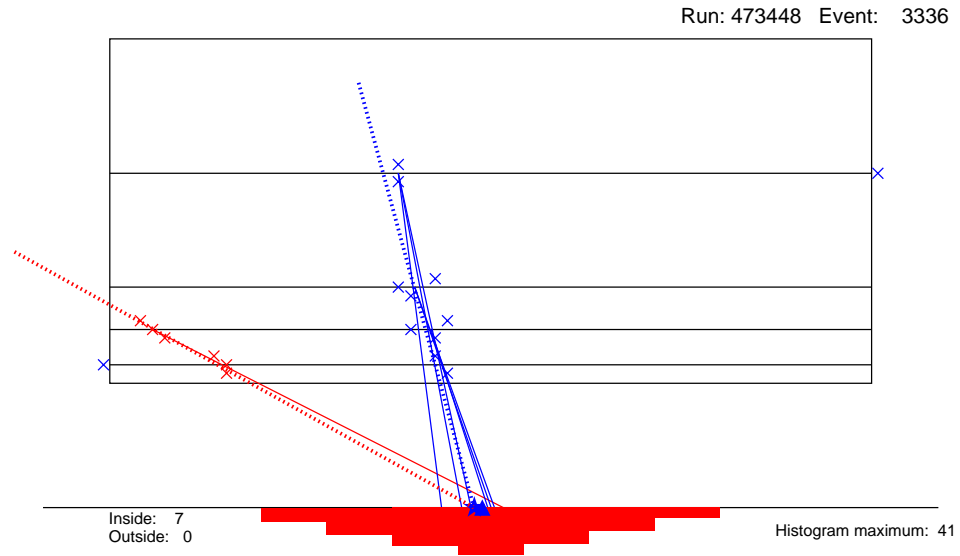


FIGURE 14.2: *Event display illustrating the L2z algorithm. An event with two FTT tracks is shown in the  $r - z$  projection. The tracker volume and the FTT layers are indicated with the boxes. The linked hits are shown as crosses, crosses outside the sensitive volume represent hits with a bad or no  $z$  measurement. The lines linking the crosses are the extrapolations which build up the histogram shown below the  $z$  axis. The FTT L2 vertex is shown as a star, the offline vertex as a triangle, partially obscuring each other. The dotted lines are the results of the  $r - z$  fit on the DSP.*

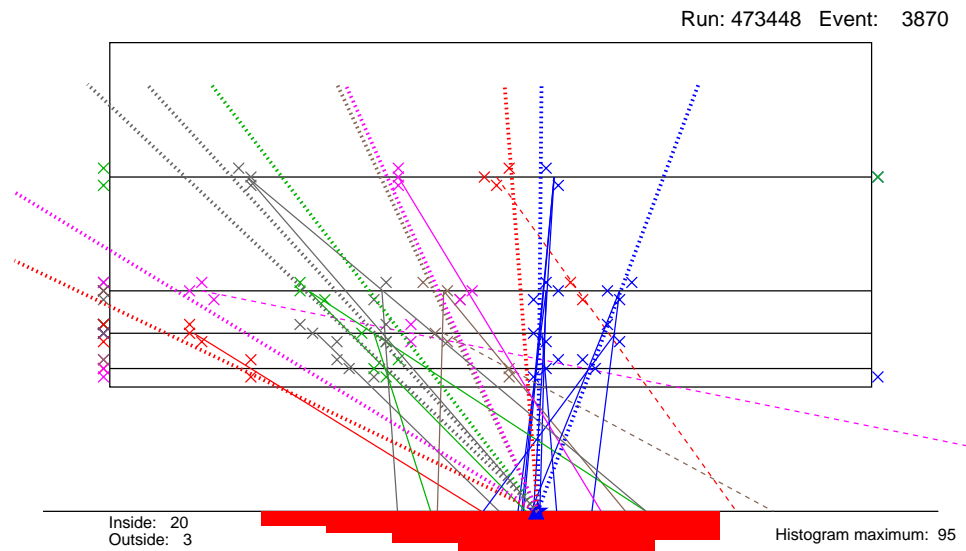


FIGURE 14.3: *Another L2z event display showing a higher multiplicity event, using the same symbols as in figure 14.2. Extrapolations not pointing into the main histogram are shown as dashed lines.*

(which is at  $z = -2.5$  cm with regards to the H1 coordinate system). This range is in turn divided into seven bins. For every extrapolation, a gaussian weight profile corresponding to the expected resolution is entered into this seven bin histogram. After all combinations have been processed, the peak of this histogram is determined. All extrapolations contributing to the peak then enter a weighted average to determine the  $z$ -vertex position. The weight of every extrapolation in the average thereby is the weight with which it contributes to the peak.

The output message sent to the DSPs and the decision unit not only contains the estimated  $z$  vertex position, but also the number of tracks and segments used in the algorithm (giving a quality estimate) and the number of extrapolations pointing into and out of the histogram (allowing for the rejection of non  $ep$  events). Figures 14.2 and 14.3 show a low and a high multiplicity data event in the event display developed during the commissioning of the algorithm.



## Chapter 15

# A FPGA Based Invariant Mass Determination

### 15.1 Triggering on Reconstructed Final States

A trigger is at its optimum when it selects all events required for the offline analysis but not others. An important part of most analyses (including the one presented in the first part of this thesis) is the reconstruction of resonances by their invariant mass. The level 3 FTT system is able to perform this selection step already on trigger level and thus gives access to processes such as  $D^*$  meson photoproduction, which would otherwise be buried in tremendous amounts of background. The input rate to the level 3 system is however restricted to a few hundred Hertz. For processes with even less distinctive signatures, such as diffractive vector-meson photoproduction, it is desirable to move the cut on the invariant mass to earlier trigger levels.

The track fitting in two rounds and the resulting early availability of the first few tracks leave several milliseconds to implement advanced algorithms on a subset of tracks already on the second trigger level. Available logic on both FPGAs of the level 2 decider board make it possible to perform an invariant mass determination. The focus here is on neutral resonances decaying to two charged particles such as  $\phi \rightarrow K^+K^-$ ,  $\rho \rightarrow \pi^+\pi^-$ ,  $J/\psi \rightarrow \ell^+\ell^-$  and  $\Upsilon \rightarrow \ell^+\ell^-$  where  $\ell$  stands for either an electron or a muon. The time and resources available allow for a search for these resonances also in events with more than two tracks; up to eight positive and negative tracks are searched for at the input.

### 15.2 Strategies for an Invariant Mass Cut

The input data for the invariant mass algorithm are the results of the track fits performed on the DSPs. The track parameters are  $1/p_T$ ,  $\phi^*$  and  $\cot \vartheta$ , where  $\phi^*$  is a representation of the azimuthal angle in a projection of a circle to an octagon, which corresponds to either the sine or the cosine of the angle depending on the octant [262]. These three variables are available both in a single so-called *compact word*, where they are bit-packet into 32 bit and as three IEEE standard single precision floating point numbers [273] (32 bit).

As the actual calculation of an invariant mass in floating-point arithmetic is something that FPGAs are not particularly well suited to do, the first idea was to solve the problem with the help of a large look-up table. In order to obtain the required precision to e.g. separate  $\phi$ s from  $\rho$ s, a result that is correct at the percent level is required. This in turn implies

	Single precision float	FTT float
Number of bits	32	23
Bits for sign	1	1
Bits for exponent	8	6
Bits for mantissa	23	16
Largest positive number	$1.7 \cdot 10^{38}$	$4.3 \cdot 10^9$
Smallest positive number	$2.8 \cdot 10^{-45}$	$9.3 \cdot 10^{-10}$

TABLE 15.1: *The FTT floating point format compared to the standard single precision floating point format.*

the use of at least 7 bit ( $1/128 \approx 1\%$ ) per track parameter, resulting in a 42 bit address lookup table (4 TB), surpassing the available memory size on the boards by several orders of magnitude. Using the  $\varphi$  symmetry of the problem, the  $\varphi$  difference between the tracks could be used to bring down the size of the address space to 35 bit (32 GB), still far out of reach with the available hardware.

As a consequence of the above considerations, it was found that the actual calculation has to be performed on the FPGA in some way. The straightforward calculation of a two particle (indexed 1 and 2) invariant mass from momentum vectors  $\vec{p}_i$  and an equal decay particle mass  $m_d$  involves at least two square roots:

$$m_{resonance} = \sqrt{(E_1 + E_2)^2 - (\vec{p}_1 + \vec{p}_2)^2} \quad (15.1)$$

$$= \sqrt{2m_d^2 + 2E_1E_2 - 2\vec{p}_1\vec{p}_2} \quad (15.2)$$

$$= \sqrt{2m_d^2 + 2\sqrt{(p_1^2 + m_d^2)(p_2^2 + m_d^2)} - 2\vec{p}_1\vec{p}_2}. \quad (15.3)$$

As these square roots are slow to calculate on a conventional processor and very time- and logic-consuming on a FPGA, a formalism without square roots is very desirable. Such a formalism had been developed for the FTT level 3 system in [264], where fourth powers of the input quantities are used to determine whether the invariant mass lies within a prescribed range. The use of fourth powers makes it very difficult to use a fixed point scheme for the FPGA based mass calculation, as the large dynamic range in the input quantities (especially transverse momentum going over two orders of magnitude) has to be followed with a correspondingly large dynamic range in the intermediate steps of the calculation. These large dynamic ranges imply a large number of bits and are thus very costly in terms of storage and calculation logic. As a consequence it was decided to implement the invariant mass algorithm using floating point numbers (*floats*).

### 15.3 Floating Point Operations on a FPGA

Timing, resource and precision considerations led to the decision of using a reduced floating point format, based on the standard IEEE single precision floating point numbers [273], but using less bits. The standard and FTT floating point formats are compared to each other in table 15.1. The range of the format is able to cover the expected values in invariant mass calculations of interest and at the same time uses manageable amounts of resources.

The *fttmassfloat* library of VHDL entities provides the following functionalities for the reduced float format:

- *Conversion* from single precision floats to reduced floats,
- *Addition* of reduced floats,

- *Multiplication* of reduced floats,
- *Inversion* of reduced floats,
- *Comparison* between reduced floats.

In addition, there is an entity based on a lookup table which returns the sine and cosine of the azimuthal angle  $\varphi$  which is received in a 12 bit representation of the FTT internal angle representation  $\varphi^*$ .

## 15.4 Steps of the Calculation

The calculation is both logically and physically split into two parts; all the quantities that are related to a single track are calculated on the *DataCtrl* FPGA of the level 2 Decider card. Tracks are then paired and sent to the *DspCtrl* FPGA, where they are combined, the energy and momentum terms are calculated and the comparison with the precalculated limits is performed. The result of the comparison is a yes/no decision, which is returned to the *DataCtrl* FPGA and enters the L2 trigger decision.

### 15.4.1 Track Parameter Determination

On the *DataCtrl* FPGA, the fit results arriving from the DSPs are stored in a memory for later processing and readout. As soon as all track parameters of a track are received, the following information is sent to the track parameter calculation entity:

- $1/p_T$  as a 32 bit float,
- $\cot \vartheta$  as a 32 bit float,
- The twelve highest bits of  $\varphi^*$  - three bits encoding the octant and 9 bits the position in the projection onto an octagon.

In a first step, the two 32 bit floats are reduced to the FTT float format. At the same time, the sine and cosine of the azimuthal angle are looked up. As soon as the reduced float representing  $1/p_T$  is available, it is stripped of its sign and sent to an inverter. During the inversion, the cotangent of  $\vartheta$  is multiplied with itself;

$$\cot^2 \vartheta = \cot \vartheta \cdot \cot \vartheta. \quad (15.4)$$

In the subsequent three cycles, the same multiplier entity is used to calculate the momentum components and the squared transverse momentum

$$p_x = |p_T| \cdot \cos \varphi \quad (15.5)$$

$$p_y = |p_T| \cdot \sin \varphi \quad (15.6)$$

$$p_z = |p_T| \cdot \cot \vartheta \quad (15.7)$$

$$p_T^2 = |p_T| \cdot |p_T|. \quad (15.8)$$

At this point (six 100 MHz cycles after receiving the parameters), the algorithm is ready to receive the next set of track parameters. The three momentum components are forwarded to the track dispatching unit and the calculation proceeds with the determination of the track energy. In an earlier cycle, the square of the cotangent became available and 1 was added to it. So as soon as the calculation of  $p_T^2$  is finished, the squared momentum  $p^2$  can be calculated:

$$p^2 = p_T^2 (1 + \cot^2 \vartheta). \quad (15.9)$$

This multiplication uses the same multiplication unit as the one used for the squares and the momentum components and thus blocks the availability of the pipeline for new tracks

Control word	Floating point numbers (one for each track)
0	invalid
1	$p_x$
2	$p_y$
3	$p_z$
n+3	$E_{i(n)}^2$
30	track number
31	Clear

TABLE 15.2: Protocol for the bus to the invariant mass calculation DSPCtrl. The track number is not sent as a floating point number but as an integer; the Clear signal resets the DSPCtrl memories.  $E_{i(n)}$  is the energy calculated under the mass hypothesis  $i(n)$  of the  $n^{\text{th}}$  search channel.

for one additional cycle. The squared track energy  $E_i^2$  under a particle hypothesis  $i$  is then determined for four particle hypotheses;  $i = e, \mu, \pi, K$ . The squared particle masses  $m_i^2$  are programmed into the FPGA as constants;

$$E_i^2 = p^2 + m_i^2. \quad (15.10)$$

### 15.4.2 Track Dispatching

The track dispatching entity collects the quantities calculated by the track parameter determination and stores them in one of two memories, depending on the track charge. As soon as the seven floats  $p_x, p_y, p_z, E_e^2, E_\mu^2, E_\pi^2$  and  $E_K^2$  have arrived, a track is flagged as ready. If two tracks of opposite charge are ready, the parameters are sent to the DSPCtrl FPGA. The sent combination is marked as done and combinations not yet sent are searched for, prioritising those containing early tracks. The algorithm stores up to eight positive and eight negative tracks and forms the corresponding 64 combinations.

The bus to the DSPCtrl is split into three parts, namely a 5 bit control word and two floats (23 bit each). The bus protocol is shown in table 15.2. Up to 26 search channels can be implemented in the FTT L2 invariant mass finder; for each active channel, the energies under a particular particle hypothesis are sent to the DSPCtrl followed by a cycle containing the track numbers of the sent tracks.

### 15.4.3 Invariant Mass Calculation

The calculation on the DSPCtrl follows the algorithm developed for the level 3 system in [264]. It determines an energy term  $\hat{E}^2$  and two momentum terms,  $\hat{p}_{low}^2$  and  $\hat{p}_{high}^2$ , incorporating the lower and upper cuts for the selection respectively. The calculation proceeds

through the following steps (the indices 1 and 2 refer to the two tracks):

$$\hat{p}_x = p_{x,1} \cdot p_{x,2} \quad (15.11)$$

$$\hat{p}_y = p_{y,1} \cdot p_{y,2} \quad (15.12)$$

$$\hat{p}_z = p_{z,1} \cdot p_{z,2} \quad (15.13)$$

$$\hat{E}^2 = E_1^2 \cdot E_2^2 \quad (15.14)$$

$$\hat{p}_{xy} = \hat{p}_x + \hat{p}_y \quad (15.15)$$

$$\hat{p}_{z,low} = \hat{p}_z + C_{low} \quad (15.16)$$

$$\hat{p}_{z,high} = \hat{p}_z + C_{high} \quad (15.17)$$

$$\hat{p}_{low} = \hat{p}_{xy} + \hat{p}_{z,low} \quad (15.18)$$

$$\hat{p}_{high} = \hat{p}_{xy} + \hat{p}_{z,high} \quad (15.19)$$

$$\hat{p}_{low}^2 = \hat{p}_{low} \cdot \hat{p}_{low} \quad (15.20)$$

$$\hat{p}_{high}^2 = \hat{p}_{high} \cdot \hat{p}_{high}. \quad (15.21)$$

If the energy term  $\hat{E}^2$  lies between  $\hat{p}_{low}^2$  and  $\hat{p}_{high}^2$ , the invariant mass criterion is fulfilled and a trigger signal for the respective channel is sent to the *DataCtrl* FPGA. The cuts  $C_{low}$  and  $C_{high}$  for each channel are precalculated and saved in a memory;

$$C_{low} = \frac{1}{2} \left( (M - \Delta_M^+)^2 - 2m_i^2 \right) \quad (15.22)$$

$$C_{high} = \frac{1}{2} \left( (M + \Delta_M^-)^2 - 2m_i^2 \right) \quad (15.23)$$

where  $m_i$  is the particle hypothesis, under which the energy term was calculated and  $M$  is the mass of the resonance searched.  $\Delta_M^+$  and  $\Delta_M^-$  finally denote the size of the trigger window in the up- and downward direction respectively. The algorithm is pipelined - the result appears after 35 100 MHz clock cycles. For the first search channel, five 100 MHz clock cycles are blocked, for every additional search channel, two more cycles are needed. With 26 active search channels, this leads to a hypothetical mass calculation rate of 47 million channels  $\times$  track pairs per second.

## 15.5 Implementation Details

### 15.5.1 Sine and Cosine Lookup

The calculation of a trigonometric function surpasses the capabilities of the FPGAs used for the FTT. The calculation is thus circumvented by using a lookup table. As the sine and cosine curves for the full period of  $2\pi$  can be obtained by translating and reflecting one of the curves for a single quadrant (e.g. the sine for  $0 - \pi/2$ ), it is sufficient to store only one quadrant in the lookup table. This is implemented with 10 bit accuracy, i.e. 1024 float values corresponding to steps in angle of 1.5 milliradians are stored. The horizontal reflection is implemented by performing two lookups, one at address  $a$  and one at address  $1023 - a$ , if  $a$  runs from 0 to 1023. The assignment of the lookup to the sine or the cosine and the corresponding signs are determined from the quadrant in which the angle is to be found (see figure 15.1).

### 15.5.2 Inversion

The inversion of a floating point number can be split into the inversion of the exponent (which consists of subtracting it from the maximal exponent) and the inversion of the mantissa. This

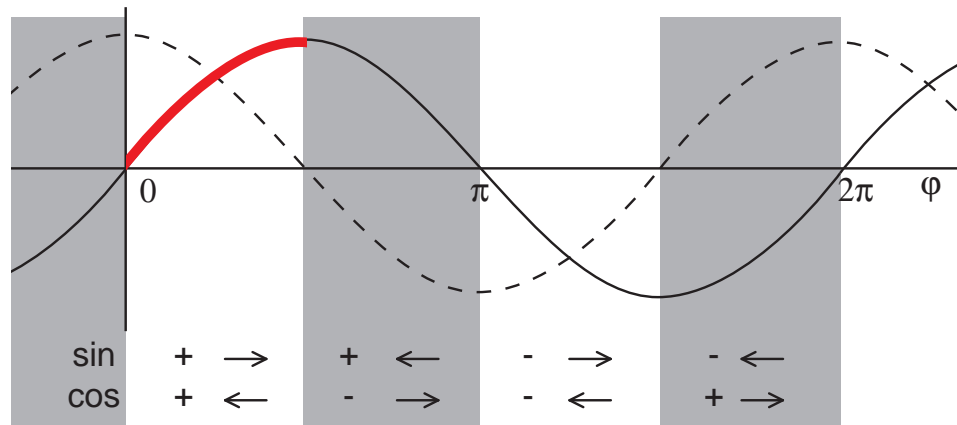


FIGURE 15.1: *Illustration of the trigonometric function lookup. The sine curve is shown as a full line, the cosine as a dashed line. The quadrant stored in the lookup ROM is highlighted. The symbols below the graph indicate the reading direction in the lookup table and the sign used to obtain sine and cosine respectively.*

inversion in turn is performed via a lookup with interpolation. In a first step, the 8 upper bits of the mantissa are used to look up a 16 bit mantissa base value and a 8 bit interpolation factor. This interpolation factor is then multiplied with the lower 8 bits of the mantissa and added to the mantissa base value. The procedure corresponds to approximating  $1/x$  with 256 linear pieces in the interval from 0 to 2.

### 15.5.3 Control of the Data Flow

The invariant mass calculation on the *DSPCtrl* FPGA is based on two multiplication and two addition units and one comparator unit. These units are fed by the results of other units or the contents of registers and write their results to registers. The whole setup is not unlike the setup of a processor. The flow of data is steered by the control signals received from the *DataCtrl* FPGA. These signals are fed into a pipeline and depending on the control word found at a specific pipeline location, the in- and output registers of every unit are chosen. The fixed sequence of control signals dispatched by the *DataCtrl* lead to an almost fixed program sequence with one “branch point” where the calculation either checks the next channel for the same track pair or proceeds to the next combination of tracks.

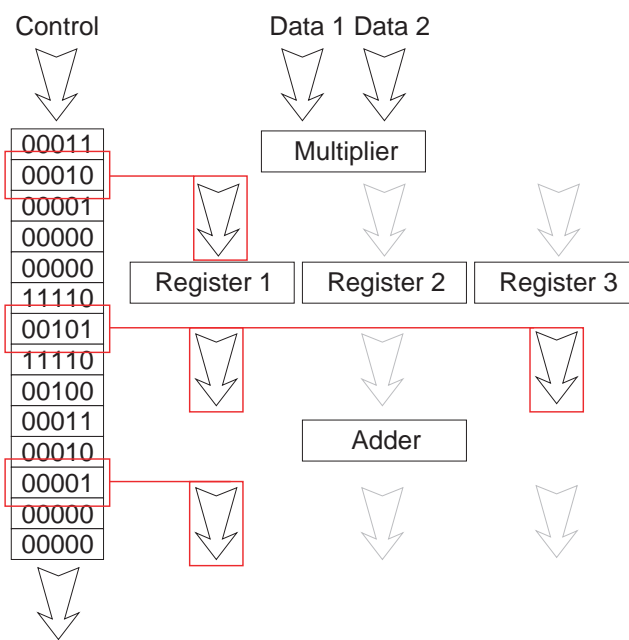


FIGURE 15.2: *Illustration of the Control mechanism of the invariant mass calculation. Control signals are fed into a pipeline (shown on the left). The values at particular places in the pipeline control the in- and outputs of arithmetic units (here an adder and a multiplier are shown).*



## Chapter 16

# Performance of the Fast Track Trigger

*I love it when a plan comes together*  
JOHN “HANNIBAL” SMITH [274]

### 16.1 Performance of the Level 1 FTT

The performance of the level 1 Fast Track Trigger has been studied intensively in the first few analyses making use of the FTT and in a dedicated diploma thesis [244]. First results and suggestions for improvements came from an analysis of diffractive  $\rho^0$  photo-production [17], an analysis of  $D^*$  meson production in deep inelastic scattering [272,275] and the  $\phi$  analysis presented in the first part of this thesis.

#### 16.1.1 Hit, Segment and Track Finding Efficiencies

The hit finding efficiency of the FTT depends mainly on three parameters: The amount of ionisation created in the chamber, the gain of the chamber and the threshold used in the  $Qt$  algorithm.

The parameter most easily varied is the  $Qt$  threshold applied during hit finding; a lower threshold leads to a higher single hit efficiency, but will also pick up more fake hits from random (noise) fluctuations in the pedestal. During a so called *cosmic run* (a period with no beams in HERA, where special triggers respond to muons from cosmic radiation) in spring 2005, a threshold scan was performed. The hit efficiency was then determined by the *triplet method*: If the outer two wires of a trigger group have seen a hit, the efficiency is defined as the probability of the middle wire also seeing a hit. The amount of noise can be estimated similarly by checking whether there was more than one hit on the middle wire. Real noise hits can be separated from afterpulses by applying cuts on the hit timing. The results of this study (with minimally ionising particles) are shown in figure 16.1.

The amount of ionisation created in the chamber depends on the specific energy loss  $dE/dx$  of a particle and its path length per drift cell. This leads to a higher efficiency for low momentum kaons than for low momentum pions and a characteristic  $\vartheta$  dependence, which reflects in the track efficiencies, as shown in figure 16.2. The gain of the CJC was

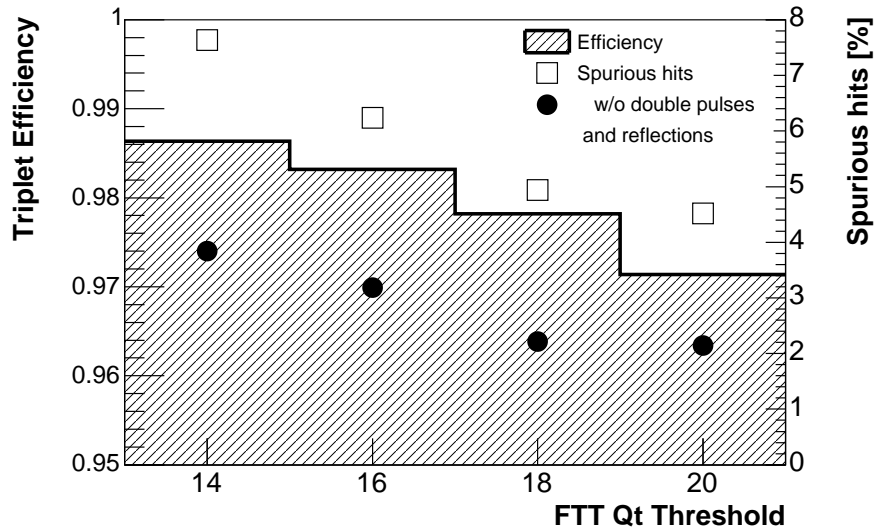


FIGURE 16.1: *Single hit efficiency as determined by the triplet method (histogram, left scale) and percentage of triplets with additional spurious hits on the middle wire before (open squares, right scale) and after removal of double pulses and signal reflections (filled circles, right scale). Determined with cosmic muons. Taken from [276].*

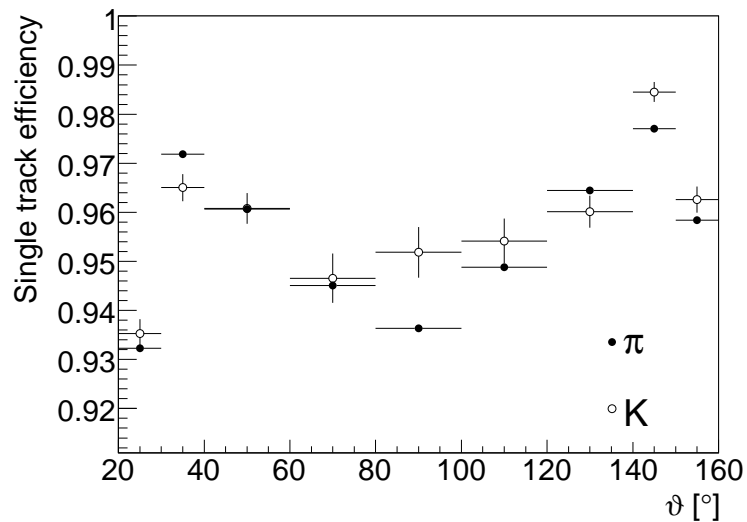


FIGURE 16.2: *FTT single track efficiency for pions and kaons versus the polar angle  $\vartheta$  of the track. The efficiencies were determined applying the matching algorithm described in [17] to the  $\phi$  trigger sample described in 6.2. The particles were selected using their specific energy loss  $dE/dx$ .*

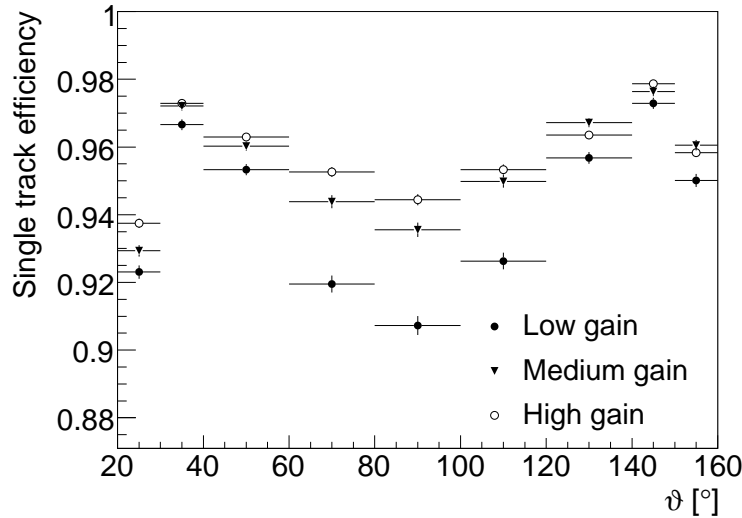


FIGURE 16.3: Gain dependence of the FTT single track efficiency versus the polar angle  $\vartheta$  of the track. The efficiencies were determined for pions with transverse momenta less than 1 GeV using the matching algorithm described in [17]. The three gain settings correspond to the run periods described in section 6.2.

raised twice during the 2005 running period (and once more during 2006) – this reflects directly in the FTT efficiencies<sup>1</sup> (see figure 16.3).

If a track leaves a hit on all three wires of a trigger group, the corresponding segment is found in the large majority of the cases; the segment finding efficiency is thus very well approximated as the third power of the single hit efficiency. If at least two out of four segments are present, a track may be found - the linking is however not 100% efficient. The combined segment finding and linking efficiency is shown in figure 16.4. The reduced efficiency in the first layer is only seen in  $ep$  running. The higher flux of charged particles close to the beam will produce more ionisation in the chamber and thus more space charge, locally lowering the gain of the wires. The space charge effect can be clearly seen when plotting the track finding efficiency versus the product of the beam currents (which in turn is on average proportional to the flux of charged particles in the chamber), as shown in figure 16.5.

A comparison of the FTT with its predecessor, the  $DCr\varphi$  trigger, was performed for the  $\rho^0$  analysis. The much lower  $p_T$  threshold of the FTT allows to trigger on both tracks and thus removes the biases from demanding one track with a  $p_T$  above 400 MeV as was necessary before. The  $p_T$  and invariant mass spectra for a  $DCr\varphi$  and a FTT triggered sample are compared in figure 16.6.

## 16.2 Performance of the Level 2 FTT

### 16.2.1 Track Finding Efficiencies

The track finding efficiency on level 2 is mainly determined by the single hit efficiency as in the case of the level 1 efficiency. The finer masks and the finer linking provide higher

<sup>1</sup>This increase in the FTT efficiencies was the main reason to raise the gain.

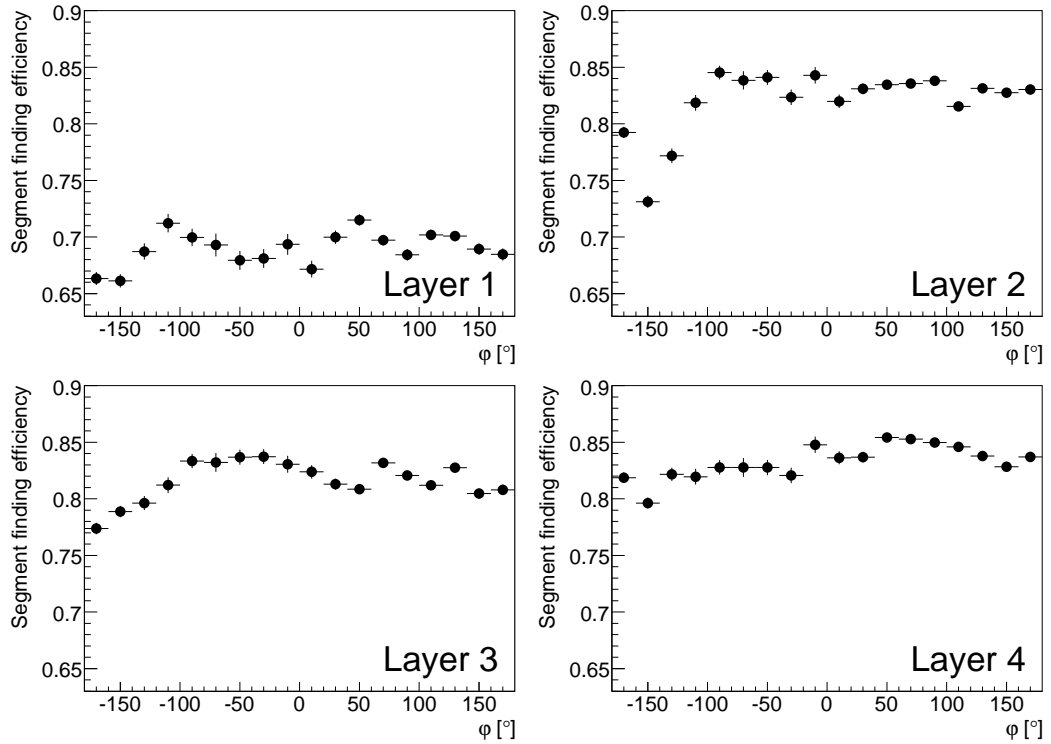


FIGURE 16.4: *Segment finding and linking efficiency: Fraction of long tracks found by the offline reconstruction with a segment found in the indicated FTT layer. The lower efficiency in the first layer is mainly due to space charge effects. The variations in  $\phi$  are mainly caused by malfunctioning pre-amplifiers. Determined from the  $\phi$ -meson trigger sample described in the first part of this thesis.*

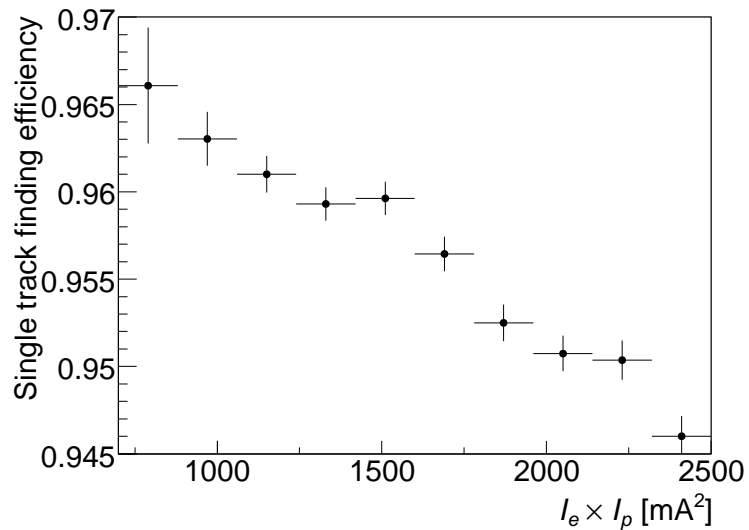


FIGURE 16.5: *The FTT single track finding efficiency for pions is shown versus the product of the electron and proton currents stored in HERA. Determined from the  $\phi$ -meson trigger sample described in the first part of this thesis.*

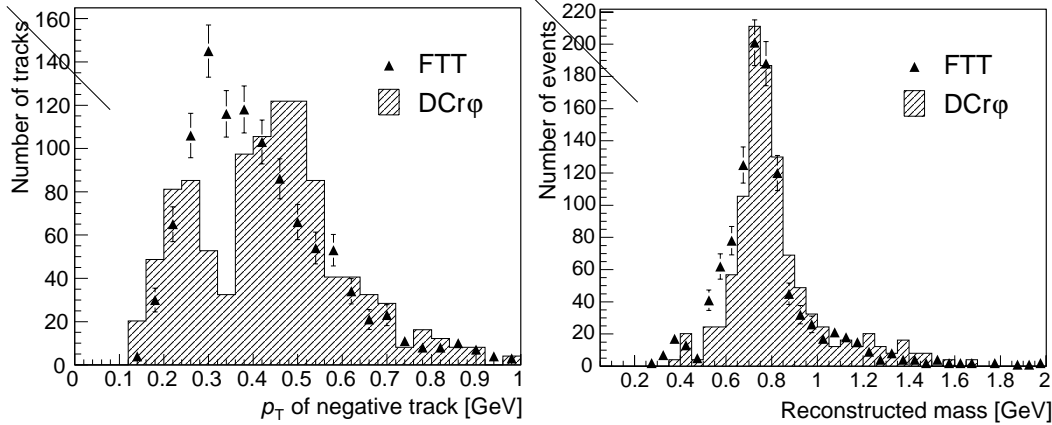


FIGURE 16.6: The transverse momentum distribution for the negatively charged tracks and the offline reconstructed mass of triggered  $\rho$  meson candidates are shown for events triggered with the FTT and with the old drift chamber trigger (DCr $\phi$  – normalised to the FTT histogram). Taken from [276].

resolution but can also lead to a loss of tracks if the masks are not perfectly in accordance with the current operation parameters of the CJC<sup>2</sup>.

The single track finding efficiencies for pions are shown against transverse momentum and polar angle in figures 16.7 and 16.8.

### 16.2.2 Performance of the L2 $z$ Vertex Finder

Due to the fact that the L2  $z$  Vertex Finder algorithm (see chapter 14) completely neglects entries outside of the histogram and uses the weights in the peak bin, it has the tendency of reconstructing the vertex both in the middle of the histogram and in the middle of a bin. Whilst the first is a desired property, as it naturally incorporates the a-priori knowledge about the vertex distribution (a gaussian centered in the origin with a  $\sigma$  of roughly 10 cm), the second property is more of a nuisance, slightly deteriorating the resolution for forward- and backward laying vertices. Resolution and correlation plots for both a normal run and a run where the vertex was shifted in the forward direction due to bad machine timing are shown in figures 16.9 and 16.10.

### 16.2.3 Resolution

For a sample taken in 2006 triggered by the calorimeter, offline reconstructed tracks were matched to the FTT reconstructed tracks and the corresponding resolutions determined. As the difference distributions in  $1/p_T$ ,  $\varphi$  and  $\vartheta$  have larger tails than a gaussian distribution, they were fitted once with the sum of two gaussian distributions, see figure 16.11. An area-weighted mean of the width of the two gaussians is then taken as the resolution. For  $1/p_T$ , only tracks with  $p_T > 2$  GeV were considered in order to reduce the influence of energy loss and multiple scattering.

<sup>2</sup>This could be observed when the drift velocity and lorentz angle in the CJC changed by about 20 % after the gas composition changed due to a leak in the gas supply system. The level 1 efficiency was basically unaffected by the incident whereas the level 2 efficiency dropped to around 60 % and recovered again when the gas composition was restored to the original values.

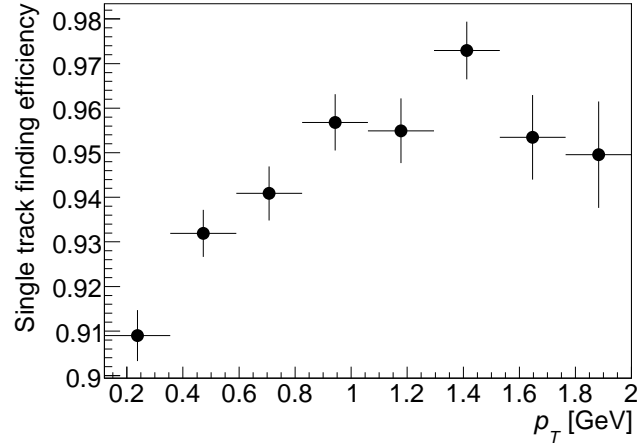


FIGURE 16.7: *FTT L2* single track finding efficiency versus track transverse momentum  $p_T$  for pion tracks. The efficiency was determined for a sample taken in 2005 which triggered a level 1 two-track trigger and has two offline reconstructed tracks.

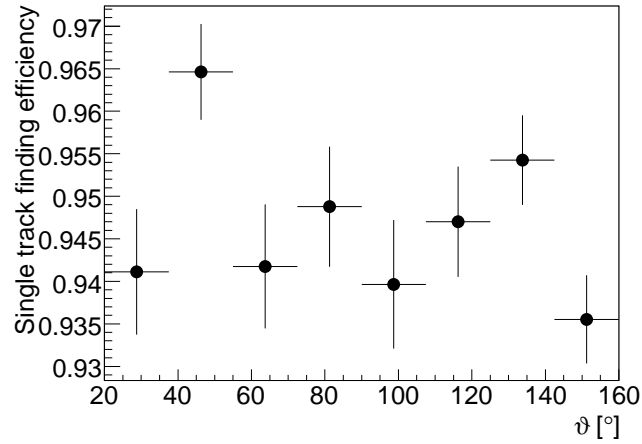


FIGURE 16.8: *FTT L2* efficiency versus track polar angle  $\vartheta$  for pion tracks. The efficiency was determined for a sample taken in 2005 which triggered a level 1 two-track trigger and has two offline reconstructed tracks.

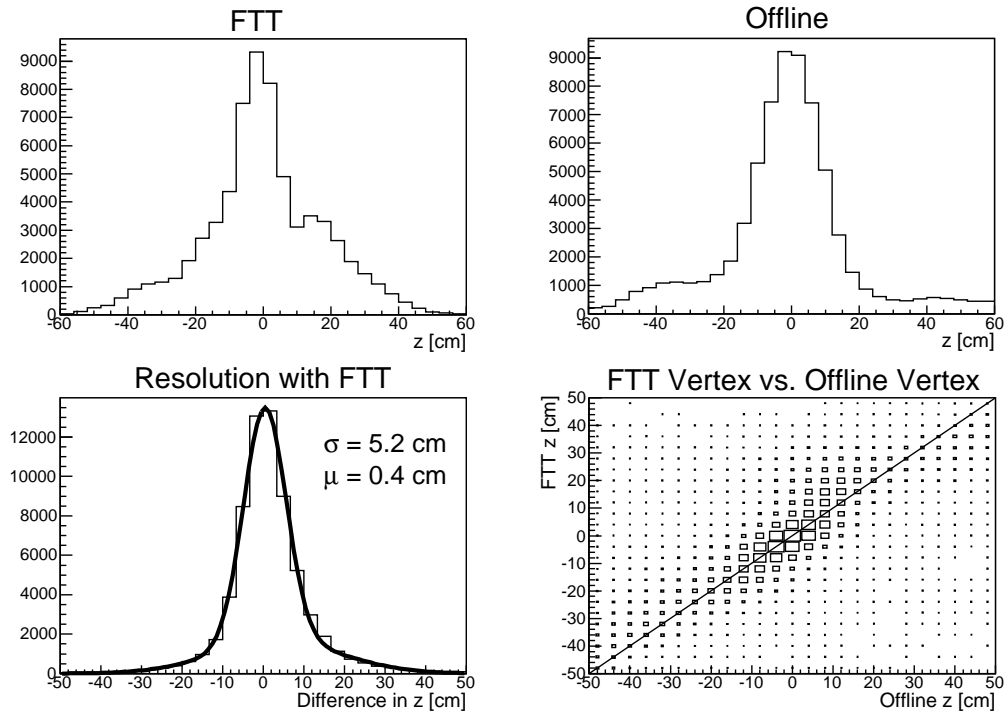


FIGURE 16.9: Performance of the FTT L2z algorithm. Top left: Vertex distribution as seen by the FTT, top right: as seen by the offline reconstruction. Bottom left: Difference between the FTT determined vertex and the offline vertex, fitted with a gaussian. Bottom right: Correlation FTT vertex - offline vertex.

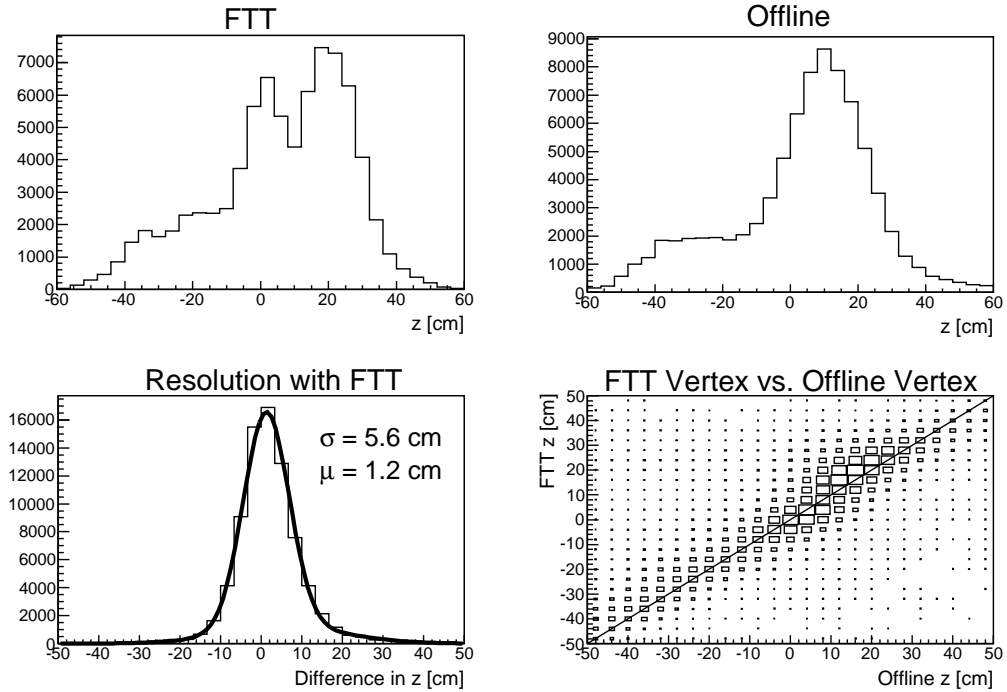


FIGURE 16.10: Performance of the FTT L2z algorithm for a run with a vertex shifted into the forward direction. Top left: Vertex distribution as seen by the FTT, top right: as seen by the offline reconstruction. Bottom left: Difference between the FTT determined vertex and the offline vertex, fitted with a gaussian. Bottom right: Correlation FTT vertex - offline vertex.

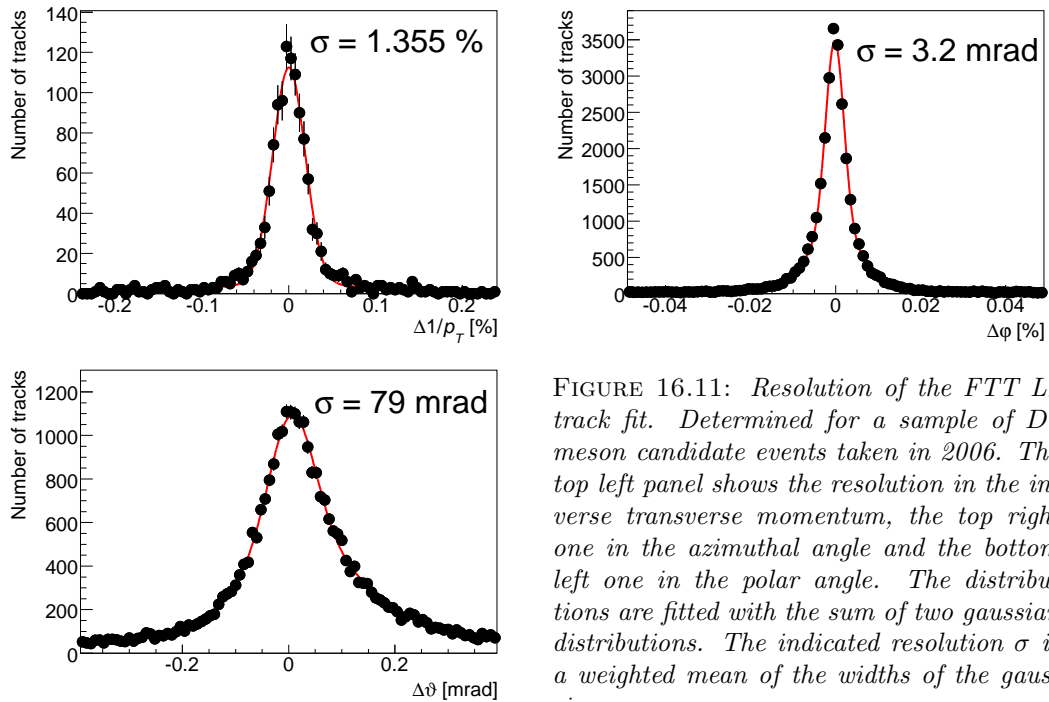


FIGURE 16.11: Resolution of the FTT L2 track fit. Determined for a sample of  $D^*$  meson candidate events taken in 2006. The top left panel shows the resolution in the inverse transverse momentum, the top right one in the azimuthal angle and the bottom left one in the polar angle. The distributions are fitted with the sum of two gaussian distributions. The indicated resolution  $\sigma$  is a weighted mean of the widths of the gaussians.

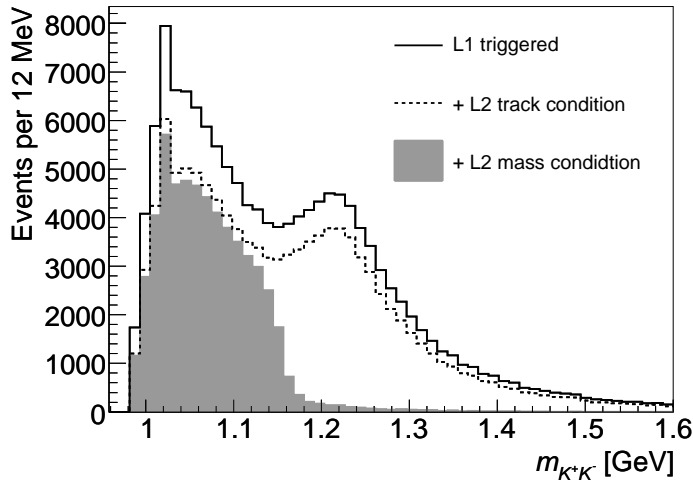


FIGURE 16.12: Reconstructed invariant mass distribution for events with the level 1  $\phi$  trigger condition fulfilled (sample from 2006 positron running). The standard  $\phi$  selection described in section 6.5 without the  $dE/dx$  cut was applied. Overlaid are the same distribution after applying the level 2 two-track condition and the invariant mass condition with an upper limit of 1.15 GeV.

The resolutions found thus are 3.2 mrad in  $\varphi$  (dominated by energy loss and multiple scattering), 1.36% in  $1/p_T$  and 79 mrad in  $\vartheta$ . The resolution of the track fit is dominated by the uncertainty in the knowledge of the vertex position. In the transverse plane, the beam spot constraint is used, which varies slowly with time and has an accuracy to fractions of a millimetre, whereas the  $z$  vertex is known to a few centimetres. This, together with the worse hit resolution in  $z$  explains the bad resolution in  $\vartheta$ . The  $\vartheta$  resolution is also the determining factor for the invariant mass resolution. For a detailed study of the resolution of the level 2 system, see [275].

### 16.3 Performance of the Level 2 Invariant Mass Finder

The level 2 invariant mass finder was applied to the  $\phi$  meson trigger soon after it became operational. An upper cut on the mass of 1.15 GeV suppresses the  $\rho^0$  background, which made up for more than half of the triggered events before the introduction of the cut. The influence of the cut on the invariant mass distribution is shown in figure 16.12. If the level 2 FTT sees both tracks, it will reconstruct them with parameters accurate enough for the mass finder with high efficiency, see figure 16.13. The addition of the mass condition has two main advantages: It approximately doubles the number of triggered  $\phi$ s by reducing the bandwidth taken up by  $\rho^0$ s in the sample and it increases the purity of the sample entering the analysis.

### 16.4 Performance of the Level 3 FTT

As for the level 2 invariant mass finder, the precision of the invariant mass reconstruction in the level 3 system is determined by the resolution of the track reconstruction at level 2. This in turn is dominated by the  $\vartheta$  resolution. Cut scenarios, efficiencies and rejection

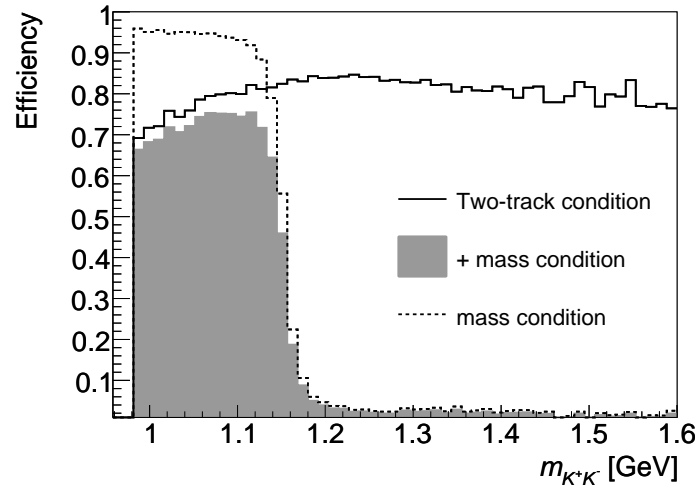


FIGURE 16.13: Efficiency of the level 2  $\phi$  trigger. For a sample from the 2006 positron running with the level 1  $\phi$  trigger condition fulfilled, the efficiency of the two-track condition, of the mass condition and the combined efficiency are shown versus the reconstructed invariant mass.

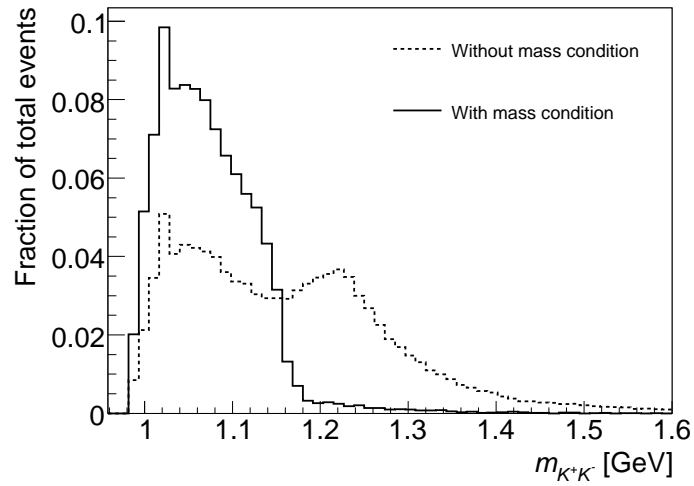


FIGURE 16.14: Purity of the  $\phi$  sample with level 1 and 2 conditions applied. The fraction of events at a certain mass fulfilling the selection cuts is an indication of the purity of the triggered sample. The addition of the invariant mass condition dramatically increases the fraction of events in the analysed range ( $m_{K^+K^-} < 1.1$  GeV).

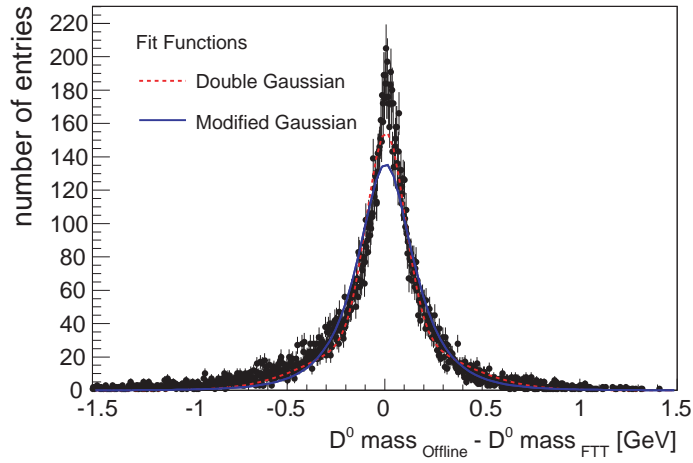


FIGURE 16.15: Resolution for the reconstruction of the  $D^0$  mass.

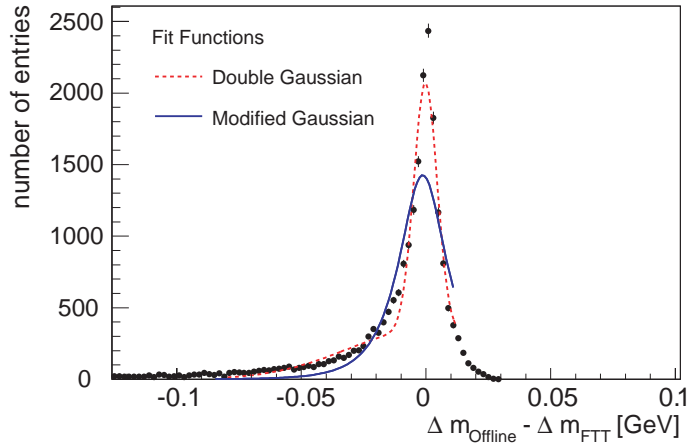


FIGURE 16.16: Resolution for the reconstruction of the  $\Delta m$  variable.

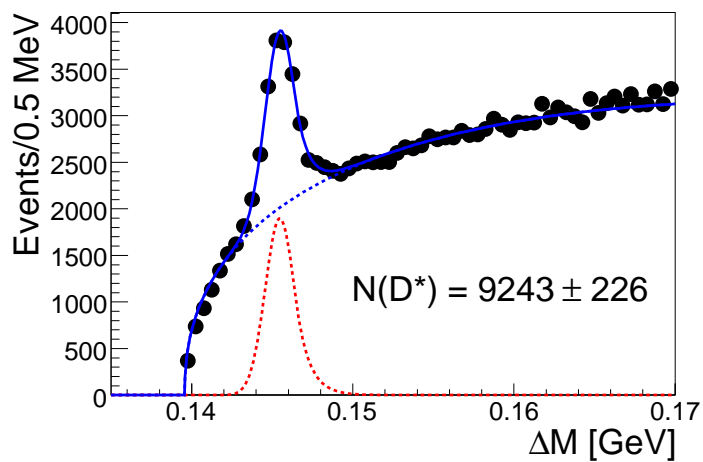


FIGURE 16.17: Mass difference distribution for  $L3$  triggered  $D^*$  candidates.

factors have been studied in detail in [275]. In figures 16.15 and 16.16 the resolutions for the reconstructed  $K\pi$  mass ( $D^0$  mass) and the resolution for  $\Delta m$ , the difference between the reconstructed  $K\pi$  and  $K\pi\pi_s$  mass ( $m_{D^*} - m_{D^0}$ ) are shown.

## Chapter 17

# A Graphical User Interface for the FTT

百闻不如一见

CHINESE PROVERB<sup>1</sup>

*A common mistake people make when trying to design something completely foolproof is to underestimate the ingenuity of complete fools.*

DOUGLAS ADAMS [277]

### 17.1 Introduction

The FTT consists of over 300 electronic cards, about 150 of which are equipped with FPGAs or processors. The configuration, testing and monitoring of such a vast system requires both a high degree of automation and flexibility. Especially the access to several 10'000 VME registers via a command line tool, giving the explicit address, or the en- and decoding of register contents and messages is not only tedious and slow for an expert but also impracticable for a non-expert such as the shift crew.

#### 17.1.1 A Short History of the FTT Graphical User Interface

The FTT design included a Graphical User Interface (GUI) from the very beginning. It was also recognised that the PowerPC processors in each FTT crate should provide a high degree of automation. A first version of the FTT GUI was developed based on the Motif GUI library in C on the Linux Operating System [278]. In the course of this work, also a simple but flexible interface to the PowerPCs as well as a the code base for the communication between the PowerPCs and the VME cards were developed.

During the test and commissioning phase of the FTT, the number of parts to be monitored and the demands on the GUI quickly grew. It was realised that especially the implementation of new graphical displays into the program was time-consuming and could ultimately not keep up with the progress of the project. It was therefore decided to change

---

<sup>1</sup>To see something once is better than to hear about it a hundred times.

to a different framework for the graphical user interface whilst only slightly modifying the underlying communication protocol. Parts of the FTT hardware had been tested using National Instruments LabView framework. This graphical programming language is designed for the monitoring and readout of electronics in scientific experiments. As the user interface and many often needed functions are provided with the program package, much less actual programming has to be done and changes or new features can be implemented very quickly. LabView has the additional benefit of being platform independent – the same project can be run on the Linux, Microsoft Windows and Apple Macintosh platforms.

As the FTT project developed, so did the graphical user interface. The features of LabView and a quickly growing library of FTT specific functionalities allowed the development of new functionalities ahead instead of during the corresponding hardware tests. At least two new versions of the FTT GUI package, introducing new and improving on old functionalities, were released per week for more than two years. During all this development, the core functionalities ran stably and crashes of the program package were extremely rare.

### 17.1.2 Demands on the FTT Graphical User Interface

There are three main scenarios where the FTT graphical user interface can be of assistance:

- The H1 shift crew intends to check the functionality of the FTT or to cure a problem with the system.
- A FTT expert wants to monitor or configure the functionality of a specific detail of the FTT.
- A FTT expert wants to test a part of the FTT, e.g. by emulating another part of the system.

These three scenarios put completely different demands on the user interface. None the less, the decision was taken to implement them in a single program. Besides simplifying the development cycle, this has the additional advantages that the borders between the three scenarios can easily be transcended – the shift crew can reconfigure the FTT e.g. after a power cut, or an expert can test a new configuration etc.. Thus the FTT GUI has to provide at the same time a quick and unambiguous overview of the system status to the shift crew as well as the most detailed information and configuration possibilities to the expert.

For the shift crew, the GUI has to act as an expert system, collecting all the available information and digesting it to clear instructions on what actions (e.g. resets) to perform in case of problems. For the expert on the other hand, the challenge is to display vast amounts of information (e.g. on the relative synchronisation of 150 FPGAs) on a single screen, allowing for the identification of problems at the first glance. If critical actions are taken, this should be noted in a log.

At a lower level, the different parts of the GUI should be as independent as possible, i.e. user action or updating the screen contents should not interfere with the communication part of the program and vice versa. There are also performance and bandwidth constraints to take into account. For every functionality a decision has to be taken on which parts to implement on the PowerPCs and which parts to implement in the GUI program itself. Moving tasks to the PowerPCs usually makes them faster and independent of the GUI, but complicates the communication interface, whereas moving them to the GUI tends to slow them down slightly, but keeps the interface simple and allows for quicker development and debugging.

Byte	8	7	6	5	4	3	2	1	0
PowerPC to FTTMASTER									
Standard message	—	Type	Slot	Payload					
Log message	—	Type	Bytes in log message	Level					
<i>Followed by the log message in ASCII code</i>									
FTTMASTER to GUI									
Standard message	PowerPC	Type	Slot	Payload					
Log message	PowerPC	Type	Bytes in log message	Level					
<i>Followed by the log message in ASCII code</i>									

TABLE 17.1: *Message protocol between the PowerPCs, the FTTMASTER and the GUI. Type is a code for the message content, Slot indicates to which card the message information is related. For messages containing human readable text, the log message format is used. Level indicates the severity of the message.*

## 17.2 Technical Implementation of the GUI

### 17.2.1 LabView

The FTT GUI was developed using the LabView graphical programming toolkit produced by National Instruments [279,280]. This toolkit provides both a powerful, easy to use graphical user interface library and a wealth of commonly used back end functionality such as TCP/IP connection handling. The user interface is modelled after electronic hardware and provides virtual LEDs, dials, switches, thermometers etc.. The different windows of an user interface are called *Virtual Instruments* (VIs) and consist of a *Front Panel*, where data are displayed and user commands are received and a *Block Diagram* where the front panel functionality is provided using a graphical programming approach. A LabView application consists of a collection of VIs, some of which are visible to the user and others which serve as a repository for commonly used functionality and are not visible to the user.

### 17.2.2 Threads and Message Queues

LabView facilitates the creation of *threads*, i.e. independent parts of the program which run asynchronously and can be given different priorities. For example the receiving and logging of messages runs independently and at a higher priority than the handling of menu requests by the user. Each VI creates at least one thread, more often there are two, one for handling communication and one for handling user events. The different threads communicate via *message queues*. These are structures which act as inter-thread FIFOs and also allow for synchronisation and optimal resource sharing between different parts of the program. For example there is a thread which waits for incoming TCP/IP messages, parses them and then sends them to a message queue e.g. for log messages. On the other end of the message queue the log window (see section 17.3.1) is activated as soon as there are messages in the queue, which are then displayed on the screen.

### 17.2.3 FTT Communication Scheme

The control and monitoring of the FTT runs over Ethernet [188], using the TCP/IP protocol [270,271]. The PowerPCs controlling the individual crates connect via a switch to a server program called FTTMASTER [281]. This program constantly runs on the FTT control PC in the experimental hall and provides connection ports to both the PowerPCs and GUI programs. The GUI can then be run in multiple instances on any PC and connect to the

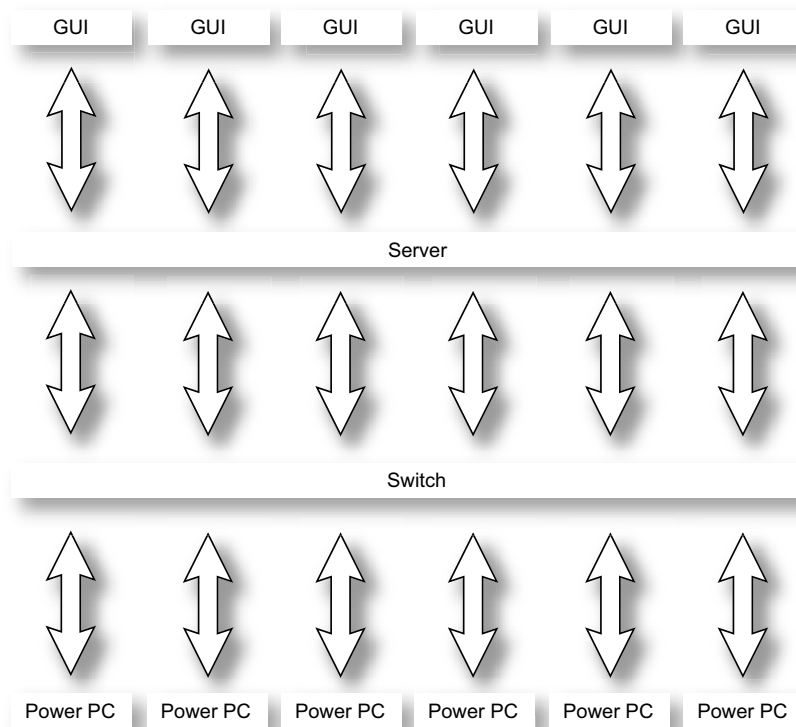


FIGURE 17.1: *Communication in the FTT system. The arrows indicate TCP/IP connections.*

FTTMASTER (see figure 17.1). The whole communication scheme is based on a message protocol described in table 17.1.

#### 17.2.4 Configuration and Customisation

The FTT GUI is run on many different machines, with different production or test setups as communication counterparts. The adaptation to these different environments can be done interactively at runtime. The new, customised settings can then be saved to a file, putting the GUI automatically into the right mode of operation at the next program start. The GUI also has access to a whole file system, also available to the PowerPCs via FTP [282], describing the configuration and calibration settings of the FTT. These files are parsed at program start or when needed and define default settings or lists of choices in many VIs.

#### 17.2.5 Three Layer Structure

The FTT GUI is built up of three layers:

- The communication layer providing TCP/IP connectivity with the PowerPCs via the FTTMASTER server program.
- The message handling layer, parsing and interpreting messages received via TCP/IP.
- The user interface layer, displaying the system status and handling user requests.

Figure 17.2 shows the threads and message queues for incoming messages of a FTT GUI instance. Outgoing messages (user commands) are sent directly to the server, without going

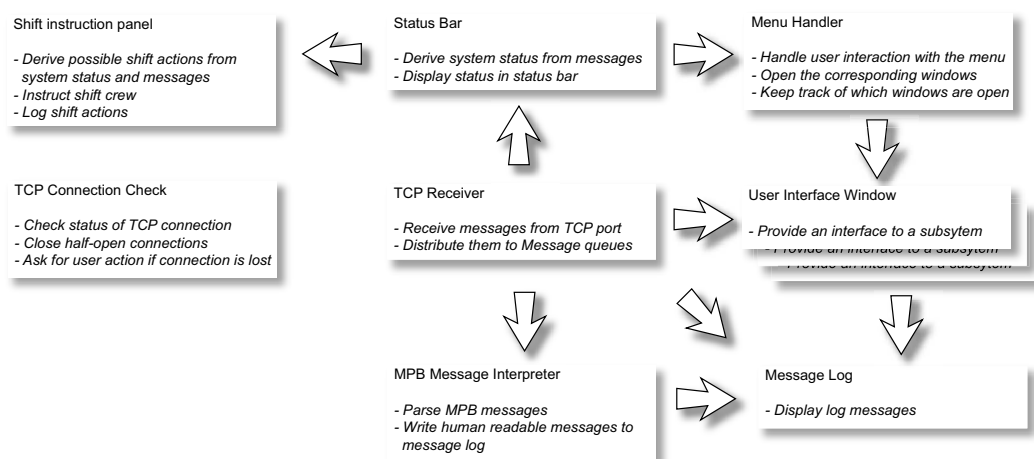


FIGURE 17.2: Overview of the FTT GUI threads, their tasks and their intercommunication via message queues.

through a message queue. In the following, the tasks performed on the different layers are explained in more detail.

### 17.2.6 Communication Layer

After the startup of the GUI, the user has to initiate a connection to the FTTMASTER server program. As soon as this connection is established, the *TCP connection check* and the *TCP receiver* threads begin to run. The first one regularly checks the state of the connection, provides this state to all parts of the GUI via a global variable and closes the connection and frees the port if the connection is lost. The *TCP receiver* is the core thread of the GUI. It reads on the TCP port, according to the protocol specified in table 17.1 and then passes the messages to the message handling layer, partly implemented in the same thread. The speed with which this is accomplished is crucial; it determines on one hand how fast the GUI can read information from the hardware and on the other hand it has to be ensured that the TCP buffer is not filling up, as this could lead to data loss. In practice, the implementation proved to be fast enough (several 100 Hz of messages) and the bottlenecks proved to be the communication round-trip time to the PowerPCs (of the order of 100 ms, depending on the location of the machine running the GUI, the load on the PPCs etc.) and the graphical display of log messages in the GUI (see section 17.3.1).

### 17.2.7 Message Handling Layer

The messages received are sorted according to their *type*, an unique identifier describing the message content (e.g. text log message, reply to a VME register read request or polled MPB message [259]). Depending on the message type, further action is taken:

- Log messages are classified according to severity.
- Error messages are parsed to detect conditions where shift crew action is required.
- MPB messages are decoded and human readable output is produced.
- Status messages are decoded and the connection and system status is updated.

These tasks range from simple and fast (recognising one of five log message severity levels) to rather involved (decoding a MPB message, involving more than one hundred different

cases). As they are only executed when there are messages available and most advanced messages are rare, they are uncritical performance wise.

### 17.2.8 User Interface Layer

The user interface layer is the *raison d'être* of the GUI. Most of the developing effort was spent for the design of front panels collecting all relevant information on a FTT subsystem. Most of the information displayed is gathered by reading of VME registers, so the block diagrams tend to be rather simple. Some of the provided functionalities and the involved user interface design considerations are presented in the next section.

## 17.3 Selected Functionalities of the User Interface

### 17.3.1 Display of Log Messages

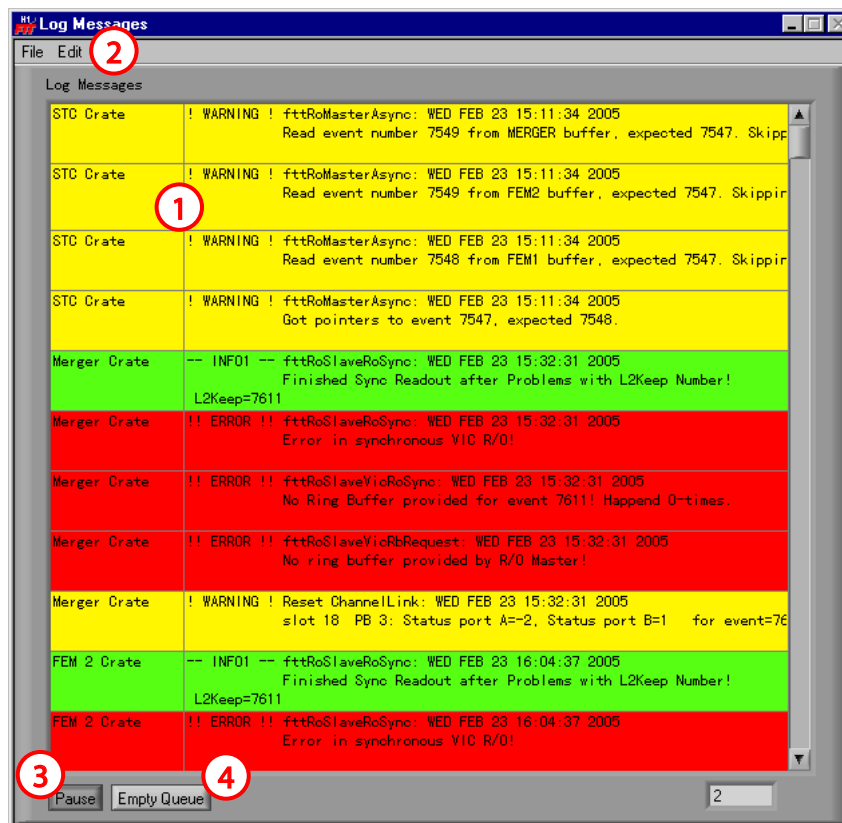


FIGURE 17.3: The log message display. 1 is the message display area, 2 the log menu, 3 the Pause button and 4 the Empty Queue button.

One of the main tasks of the GUI is the display of log messages from the PowerPCs. At a first glance this appears to be an almost trivial task – extract the log string and the log level (*Error*, *Warning* or *Info*) from the PowerPC message and display it on screen. Some comfort for the user is added by displaying not just one but the last one hundred or so messages in a scrollable window and coloring them according to severity (1 in figure 17.3).

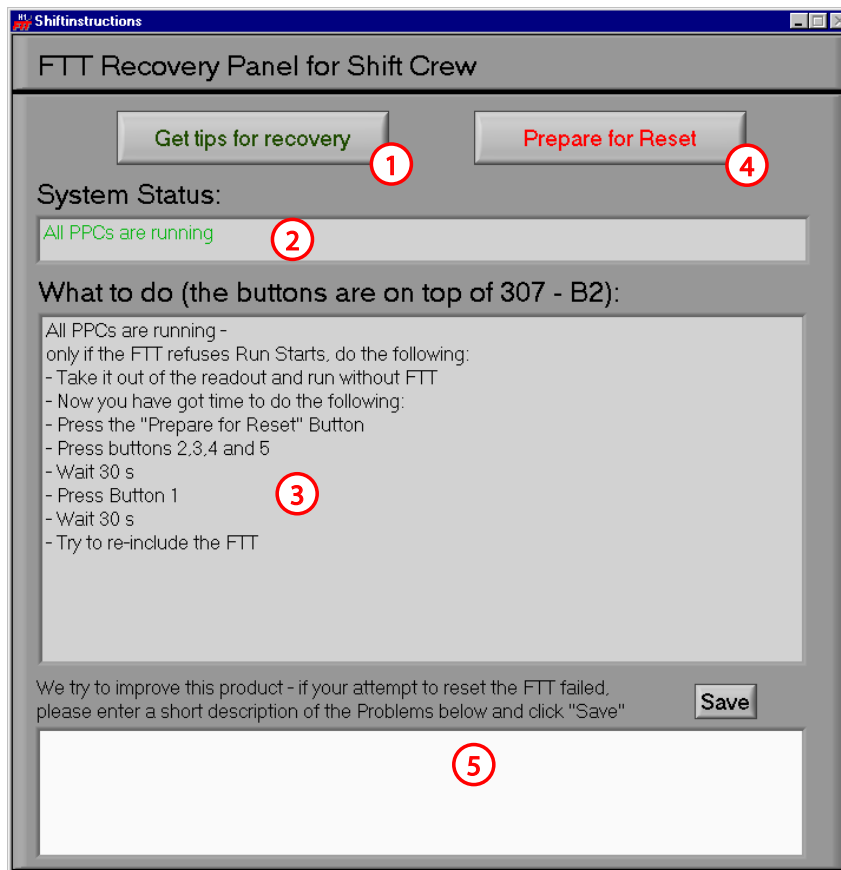


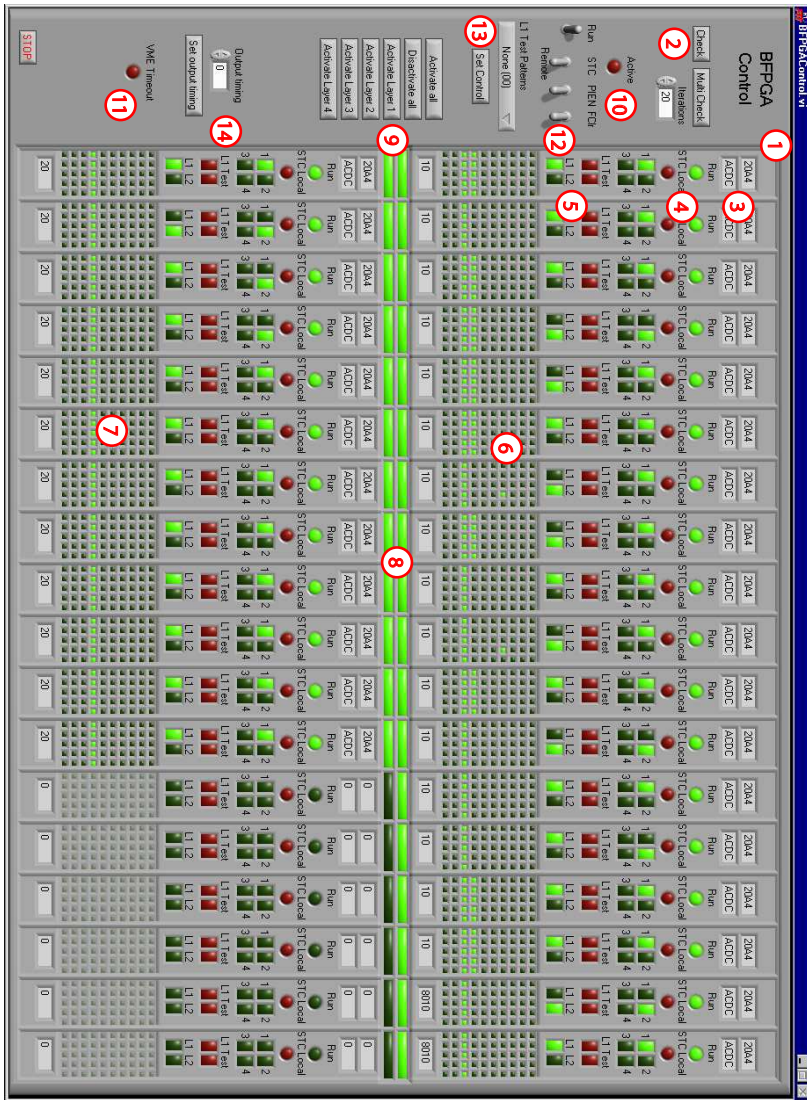
FIGURE 17.4: Automatic shift instructions. Upon pressing the Get Tips for recovery button (1), the GUI analyses the system status, considering alive messages and the content of error messages and then reports the system status in area 2, gives instructions in area 3 and provides buttons needed in the recovery procedure at 4. There is also a possibility for the shift crew to add comments in area 5.

As tastes and requirements on colors differ between users, the possibility to customise the set of colors is supplied (via the menu 2 in figure 17.3).

Printing messages to the GUI has proven an invaluable tool in identifying problems during the commissioning phase. If something goes wrong, the PowerPCs produce as much diagnostic output as possible. This can result in several 10 Hz message rate over extended periods of time. To examine the messages in more detail, the user can stop the output (3 in figure 17.3). The messages are stored in a message queue and displayed on user request. The GUI can display approximately 35 Hz of messages<sup>2</sup> on a machine with a 1 GHz processor. Should the PowerPC output rate be considerably higher, the user has the possibility to skip the messages in the queue (4 in figure 17.3).

<sup>2</sup>This allows for stable operation of an unobserved GUI application even if some error condition in the system leads to a large amount of message output over a prolonged amount of time.

FIGURE 17.5: The BackFPGA Control VI, monitoring 180 VME registers. 1 is the display area, containing representations of the thirty BackFPGAs in the 2 FEM crates. It is updated by pressing the check button 2. For every FPGA, the version and fixed pattern registers (3), the status of the control registers (4) and the operation mode (5) are displayed. The main functionality is the monitoring of the synchronisation of the FrontFPGAs. The start phase of the L1 data relative to the HERA clock is shown at 6 where some stray timestamps are visible, whereas for the FPGAs at 7 the synchronisation is perfect. Which FPGAs should be read out is selected with the switches 8, which can also be activated and deactivated in groups using an array of buttons 9. While the VI is reading registers, the Active LED 10 is on, if there is a timeout during this phase, the LED 11 is lit. The state of the switches 12 is written to the control registers, as soon as the Set Control button 13 is pressed. A new output timing value is written to the FPGAs if button 14 is pressed.



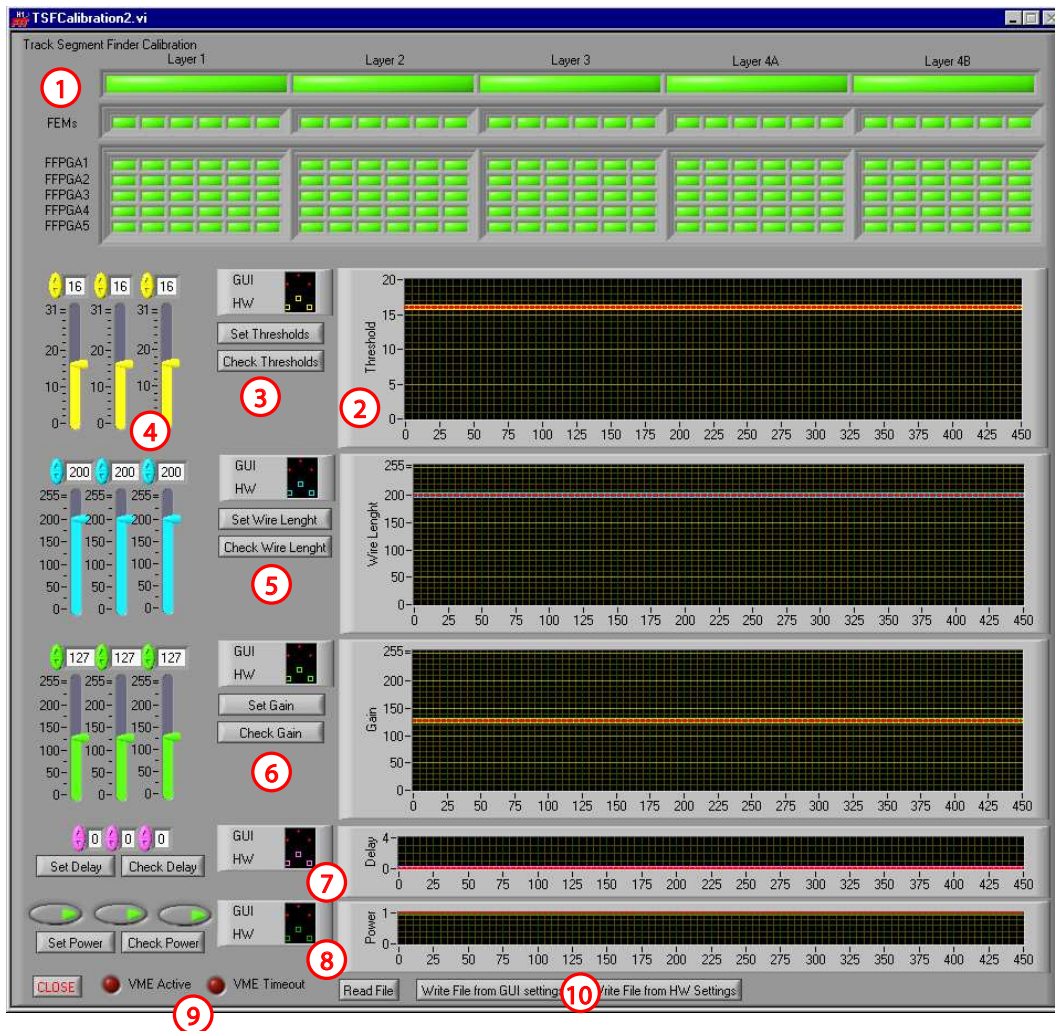


FIGURE 17.6: The Track Segment Finder Calibration VI. On top there is an array of LED switches (1) which selects the TSFs to be calibrated either layer-, FEM- or FPGA-wise. For the Qt-threshold, there is an overlay of two graphs displaying the actual hardware and GUI settings (2), there are two buttons to read and write the settings from and to the FPGAs (3) and there are three slides (4) to manipulate the local (GUI) settings of the active FPGAs. The same exists for the effective wire length (5), relative gain (6), delay (7) and power (8) calibration parameters. Two LEDs (9) show if the GUI is active with reading or writing and whether there were transmission timeouts. There is also the possibility to read and write settings from and to a file (buttons 10).

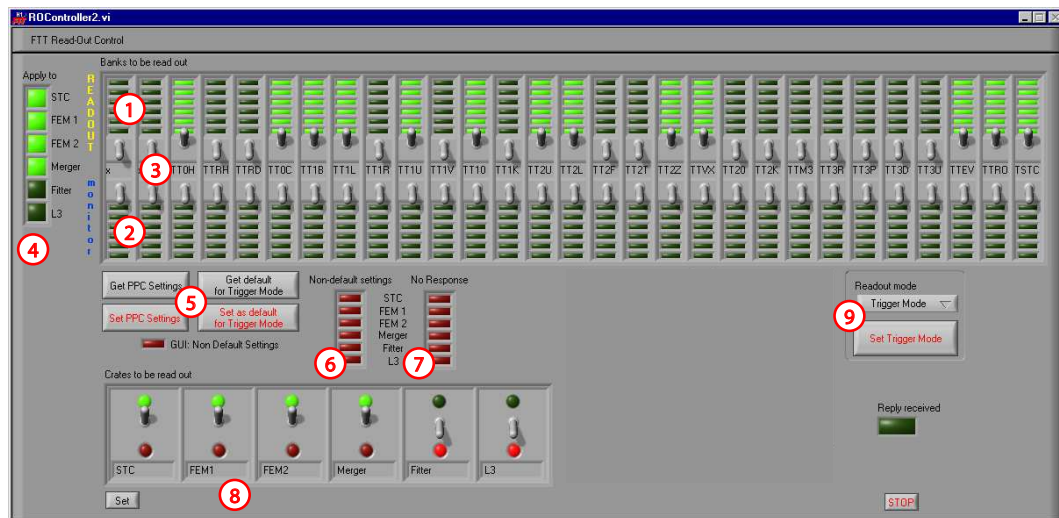


FIGURE 17.7: The readout control VI. The top row (1) shows which banks are read out from the PPCs into the normal readout stream, the bottom row (2) shows the same for the monitor stream. These settings can be manipulated using the switches (3) in the centre row and are applied to the PowerPCs selected with (4) by pressing the Set PPC settings button in the button group 5, where the settings can also be read back, read from a file or written to a file. PPCs with non-default settings are indicated by the LEDs 6, whereas PPCs not responding are shown in 7. The group of switches 8 allows the in- and exclusion of crates from the readout. With the selector and button at 9, the FTT can be put either into raw data or trigger mode.

### 17.3.2 Instructing the Shift Crew

One of the goals of the FTT commissioning phase was to bring the system into a condition, where no more expert interaction is needed and it can be continuously operated by the H1 shift crew. One step toward this aim was to provide the shift crew with a quick diagnosis of the system status and instructions on what actions to take in case of malfunctions. The log messages are not of much use here, as they provide information about internals of the FTT system with which the average shift crew is not acquainted. Instead of writing a lengthy manual, covering all conceivable problems, it was decided to let the GUI act as an expert system and automate the analysis of the system state. This was simplified by the fact that a few simple error conditions provided the lions share of all occurring failures. Dealing with them efficiently and tackling the others in a brute force (rebooting all crates) approach proved effective for day to day running.

The system status analysis first checks whether the GUI is connected to the FTTMASTER - if not, the user is instructed to establish this connection. In a second step, it is checked whether *alive* messages from the crates to be read out (see section 17.3.5) are received - if not, the shift crew is instructed to reboot the corresponding PowerPC. Furthermore, all error messages received are checked against a catalogue containing error messages and specific recovery instructions. If none of the above error conditions is fulfilled, a complete reboot is suggested as the last resort.

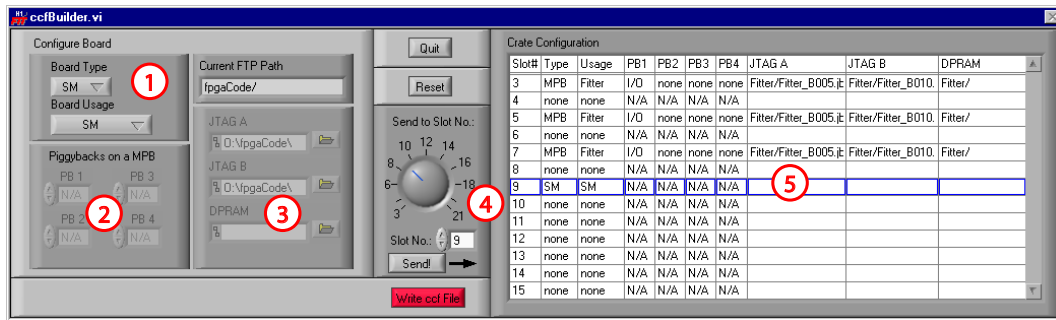


FIGURE 17.8: The crate configuration file builder VI. With 1, the card type is selected, 2 defines the Piggy Back configuration, 3 the set of firmware files and the dial 5 selects the slot of the card. In the table 5, the contents of the file built can be seen.

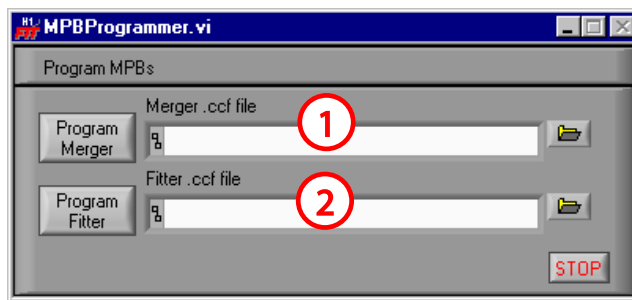


FIGURE 17.9: The crate loading VI provides a very simple front end. Two lines (1 and 2) to select crate configuration files for the merger and filter crate respectively and attached to these .

### 17.3.3 Monitoring of Synchronisation

The synchronisation of different FPGAs connected via buses or channel links is essential for a reliable running of the FTT. Synchronisation thus was one of the main areas of work during the commissioning phase. VIs to monitor the synchronisation of the FrontFPGAs relative to each other and the BackFPGAs as well as the different FEMs relative to the Mergers were valuable tools for this task. A graphical representation using arrays of virtual LEDs showing the phase relative to the raising *HERA* clock edge on the vertical and the different FPGAs on the horizontal axis was developed to this purpose. The relative phase of the L1 data from 150 FrontFPGAs on the BackFPGAs together with some BackFPGA status and timing information is shown in the *BFPGA Control* VI. In the example screenshot (figure 17.5) it can be seen on the first glance that there is a synchronisation problem in the FEM 1 crate (upper row) whereas the FEM 2 crate (lower row) is perfectly in phase.

### 17.3.4 Setting of Calibration Constants

The FTT has 900 analogue input channels, corresponding to the two ends of 450 CJC wires. For every pair of wires, a set of five calibration constants is defined. This front end calibration is stored in a database bank and automatically loaded into hardware by the PowerPCs. For test and control purposes, the GUI offers the possibility to set and read out these values. The main design challenge was the display of 2250 values on a single screen. After some experimentation, the display in graph form, where the calibration constant is

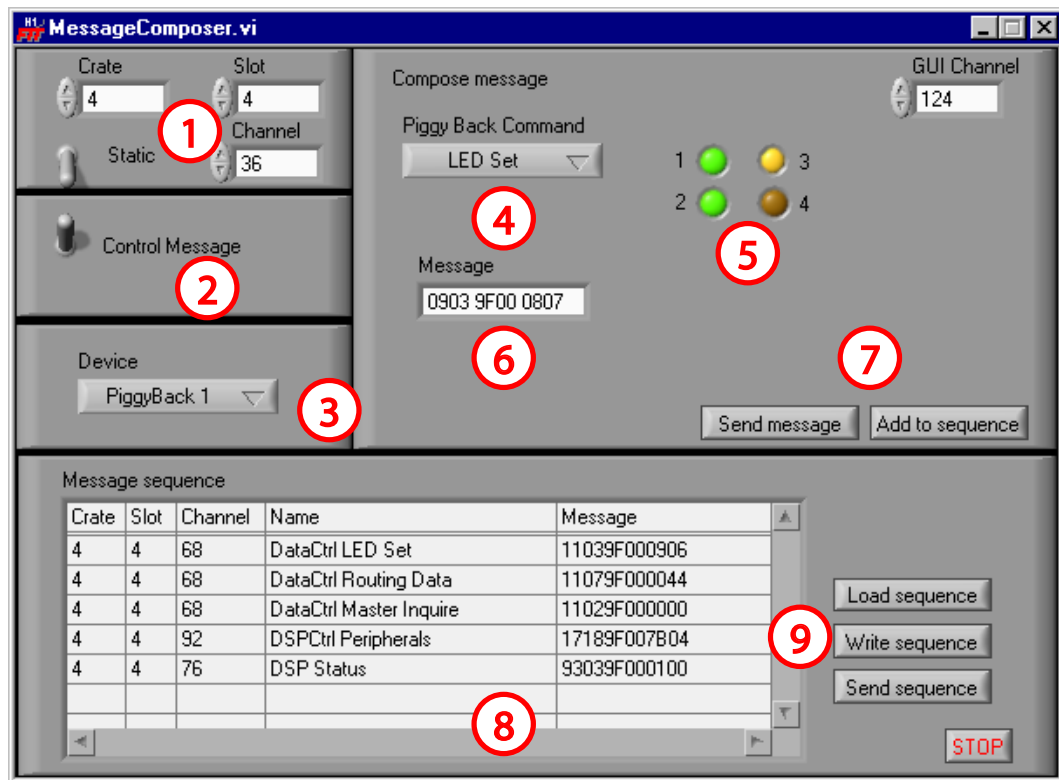


FIGURE 17.10: The MPB Message Composer VI. With the numbers in 1, the message destination is set. The switch 2 selects whether it is going to be a control or data message. 3 selects the target device. 4 chooses the message purpose - the message specific area 5 is changed accordingly. In 6, the actual message is displayed in hexadecimal format for reference and cross checks. With one of the buttons at 7, the message can be sent either to the hardware or to a message sequence (8), which can be written to the hardware or to a file with the buttons 9.

plotted on the vertical and the channel number on the horizontal axis has proven the most effective way. In fact, two graphs are overlaid to show the calibration set in the GUI and the one read from the VME registers so that planned changes (before setting the calibration) and transmission errors (after setting and reading back) become visible, see figure 17.6.

### 17.3.5 Steering Readout

The FTT readout can access a wide variety of information and fill it into BOS banks [187]. Some of these data are needed for physics analysis and are always read out whereas other offer the possibility to survey the FTT system status and are read out at certain intervals or during special runs. In addition, there is a main data stream, which goes to the H1 CDAQ and a secondary (*Monitor*) data stream to the FTT control PC for internal consistency checks. Which banks are written to which stream can be steered individually for each crate with the Readout Control VI (figure 17.7). As the FTT data can become effectively useless if the wrong banks are read out, the emphasis in the design of the Readout Control VI was laid on an unambiguous display of each PowerPCs settings and a clearly visible indication of non-default settings. In addition, all changes made using this VI are protocolled in a

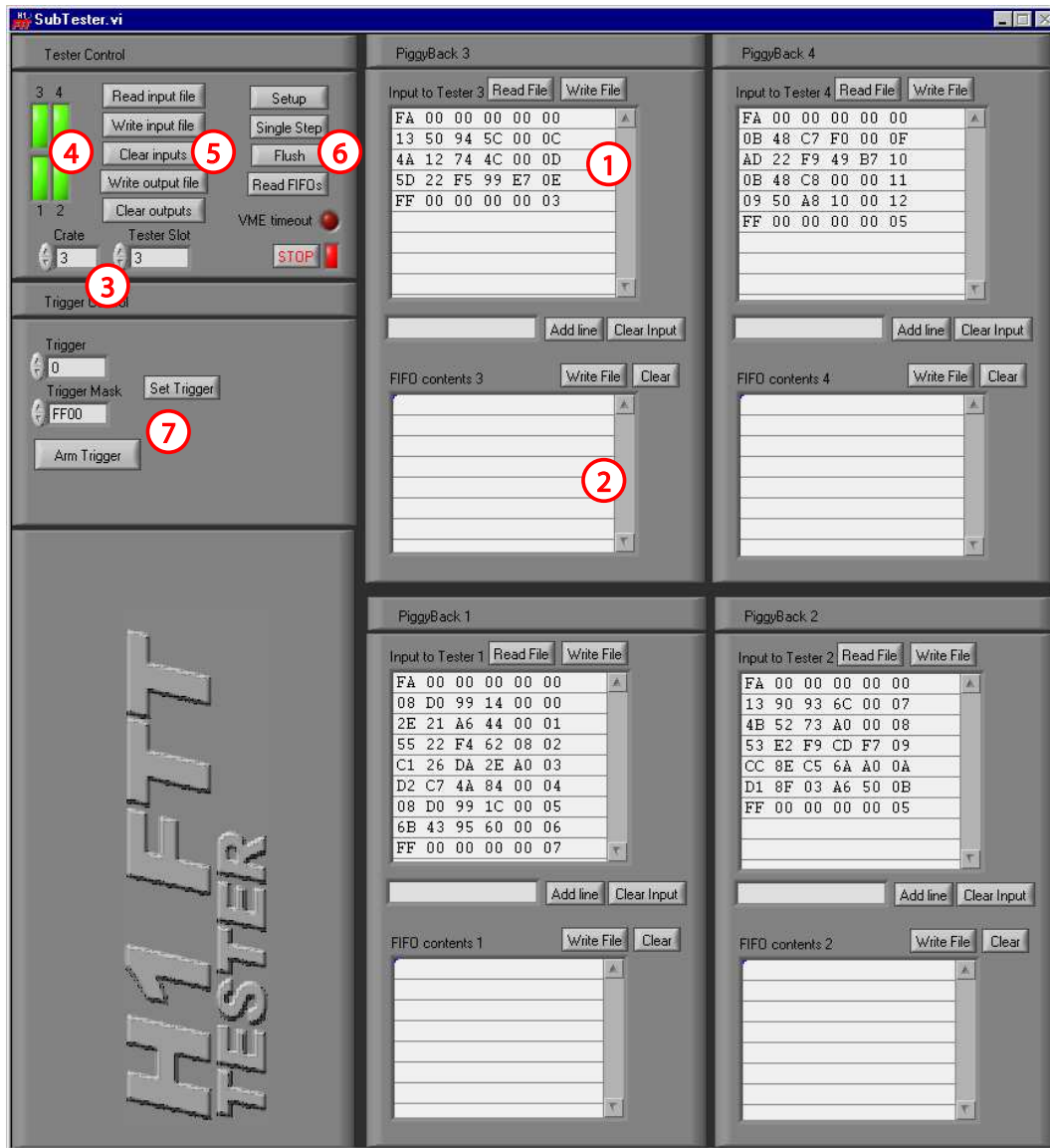


FIGURE 17.11: The FTT Tester VI provides an interface to the Tester firmware suite. The in- and output FIFOs of the four Piggy Backs are represented by two tables, 1 for test data, 2 for captured return data. With 3 the address of the tester in the system is set. The LED switches 4 define which Piggy Backs are to be used. The buttons 5 allow to read from and write to in- and output files and clear the tables for all Piggy Backs. The same functionality is also provided FIFO-wise by buttons placed next to the tables 1 and 2. Writing to hardware, steering the test sequence and reading back is done via the button group 6. The trigger functionality of the tester is steered at 7.

dedicated file.

### 17.3.6 Configuring Crates

The two FTT crates equipped with Multipurpose Processing Boards (MPBSs) contain up to nine such boards, equipped with a varying number of Piggy Back cards. In total, up to 54 FPGAs per crate have to be configured with different firmware versions e.g. after a power cut. The GUI provides a tool (see figure 17.8) to write catalogues of firmware to be loaded, which can then be loaded either from the GUI using a very simple interface (figure 17.9) or directly by the PowerPCs. The corresponding VIs and file formats were developed by a DESY summer student [283].

### 17.3.7 Interfacing to the MPB Message System

Tests and configuration of the fitter crate, where the MPB message system [259] is in operation, are sped up considerably by a tool which builds the messages from user specifications. The knowledge about the details of the message protocol (which channel to use, which bit encodes what etc.) is thus shifted from the user to the program. In addition, graphical representations of e.g. LEDs to be switched or values to be set facilitate the quick recognition of a specific message purpose.

### 17.3.8 Emulating Parts of the FTT

In order to test selected subsystems of the FTT during the commissioning phase, a firmware called *Tester* [284,285] was developed in order to emulate both earlier (data producing) and later (data consuming) system parts to the subsystem under scrutiny. This is simplified insofar as all FTT boards communicate via 48 bit wide LVDS channel links. Consequently, the tester board is a MPB equipped with four I/O Piggy Back cards, each providing one outgoing and one ingoing channel. Test patterns can be loaded to FIFOs on the Piggy Backs, can then be sent over the links and the output from the tested system is stored again in FIFOs on the PiggyBacks. The GUI provides an easy to use interface to the Tester functionality (figure 17.11) including the possibility to read input patterns from files and saving output. For the monitoring of special events in continuous data streams, writing to the FIFO can be optionally triggered on the occurrence of a specific pattern in the data stream.

## Appendix A

# Corrections to the Specific Energy Loss

### A.1 Threshold Correction

The threshold correction  $f_{thresh}$  for a charge per wire of  $C$  is

$$f_{thresh} = \left( \frac{(1 - s_1) \frac{1}{\sqrt{C}}}{\frac{1}{\sqrt{C}} - s_2} \right)^2, \quad (\text{A.1})$$

with

$$s_1 = \frac{1}{2} \left( \operatorname{erfc}(t_2) \left( 1 - \frac{\frac{1}{\sqrt{C}} - q_1}{q_2 - q_1} \right) + \operatorname{erfc}(t_1) \frac{\frac{1}{\sqrt{C}} - q_1}{q_2 - q_1} + (e^{(t_1)^2} - e^{(t_2)^2}) \frac{a\sqrt{\frac{2}{C}}}{\sqrt{\pi}(q_1 - q_2)} \right) \quad (\text{A.2})$$

and

$$s_2 = s_1 \frac{1}{\sqrt{C}} + \frac{1}{2} \left( \frac{a\sqrt{\frac{2}{C}}}{\sqrt{\pi}} \left( e^{(t_2)^2} \left( 1 - \frac{\frac{1}{\sqrt{C}} - q_1}{q_2 - q_1} \right) + e^{(t_1)^2} \frac{\frac{1}{\sqrt{C}} - q_1}{q_2 - q_1} \right) + \frac{a^2 \frac{2}{C}}{q_2 - q_1} \left( \frac{t_1 e^{(t_1)^2} - t_2 e^{(t_2)^2}}{\sqrt{\pi}} + \operatorname{erfc}(t_1) - \operatorname{erfc}(t_2) \right) \right) \quad (\text{A.3})$$

where

$$t_1 = \frac{q_1 - \frac{1}{\sqrt{C}}}{a\sqrt{\frac{2}{C}}}, \quad (\text{A.4})$$

$$t_2 = \frac{q_2 - \frac{1}{\sqrt{C}}}{a\sqrt{\frac{2}{C}}} \quad (\text{A.5})$$

and  $\operatorname{erfc}(x)$  is the complementary error function,

$$\operatorname{erfc}(x) = \int_x^\infty e^{-t^2} dt. \quad (\text{A.6})$$

$q_1$  and  $q_2$  are the inverse squared charges (in units where a minimum ionising particle produces 400 units of charge) defining the threshold region, determined from data [174] to be  $q_1 = 0.0725$  and  $q_2 = 0.1$ .  $a$  parametrises the spread around the mean charge; a value of 0.23 was used.

## A.2 $dE/dx$ Calibration Parameters

Particle	Gain	Charge	$E_0$	$E_1$	$E_2$
Pion	Low	+	2.70	0.0197	-1.25
		-	2.11	0.0208	-1.21
	Medium	+	2.49	0.0200	-1.22
		-	2.54	0.0189	-1.21
	High	+	2.70	0.0203	-1.24
		-	2.46	0.0184	-1.19
Kaon	Low	+	2.40	0.0205	-1.22
		-	2.34	0.0223	-1.24
	Medium	+	2.53	0.0202	-1.22
		-	2.46	0.0201	-1.22
	High	+	2.59	0.0195	-1.22
		-	2.37	0.0194	-1.20
Proton	Low	+	2.58	0.0193	-1.22
		-	2.16	0.0212	-1.22
	Medium	+	2.53	0.0195	-1.21
		-	2.26	0.0196	-1.20
	High	+	2.63	0.0192	-1.23
		-	2.65	0.0178	-1.22

TABLE A.1:  $dE/dx$  resolution parameters.

Gain	$\varphi$ Bin	Charge	$P_0$	$P_1$	$P_2$	$P_3$	$P_4$	$P_5$	$P_6$	$\chi$	$\xi_{pi}$	$\xi_K$	$\xi_p$	
Low	Left	+	2.70	0.0197	-1.25	0.333	9.53	0.667	0.383	303.	0.245	0.141	0.239	
		-	2.11	0.0208	-1.21	0.422	9.68	0.966	0.108	499.	0.140	0.168	0.196	
	Top	+	2.40	0.0205	-1.22	0.394	9.56	0.855	0.254	490.	0.331	0.195	0.211	
		-	2.34	0.0223	-1.24	0.378	9.54	0.816	0.229	500.	0.122	0.191	0.209	
	Right	+	2.58	0.0193	-1.22	0.397	9.50	0.860	0.326	311.	0.230	0.196	0.274	
		-	2.16	0.0212	-1.22	0.410	9.58	0.857	0.185	500.	0.207	0.153	0.188	
	Bottom	+	2.55	0.0198	-1.23	0.410	9.48	0.774	0.276	342.	0.305	0.200	0.237	
		-	2.07	0.0228	-1.21	0.433	9.61	1.00	0.0983	500.	0.126	0.220	0.247	
	Medium	Left	+	2.49	0.0200	-1.22	0.404	9.54	0.838	0.269	277.	0.266	0.258	0.337
			-	2.54	0.0189	-1.21	0.383	9.48	0.750	0.275	344.	0.197	0.164	0.104
		Top	+	2.53	0.0202	-1.22	0.400	9.53	0.836	0.292	304.	0.332	0.281	0.159
			-	2.46	0.0201	-1.22	0.400	9.54	0.701	0.199	500.	0.253	0.248	0.181
Right		+	2.53	0.0195	-1.21	0.408	9.56	0.825	0.286	293.	0.321	0.272	0.277	
		-	2.26	0.0196	-1.20	0.457	9.59	1.01	0.194	499.	0.312	0.263	0.427	
Bottom		+	2.60	0.0200	-1.23	0.404	9.48	0.789	0.303	299.	0.333	0.280	0.372	
		-	2.34	0.0203	-1.21	0.418	9.59	0.881	0.189	397.	0.248	0.264	0.314	
High		Left	+	2.70	0.0203	-1.24	0.374	9.44	0.768	0.399	262.	0.283	0.273	0.380
			-	2.46	0.0184	-1.19	0.411	9.49	0.779	0.248	312.	0.226	0.181	0.178
		Top	+	2.59	0.0195	-1.22	0.389	9.51	0.872	0.379	276.	0.280	0.248	0.194
			-	2.37	0.0194	-1.20	0.445	9.56	0.919	0.209	340.	0.299	0.294	0.318
	Right	+	2.63	0.0192	-1.23	0.408	9.48	0.772	0.354	267.	0.314	0.268	0.278	
		-	2.65	0.0178	-1.22	0.402	9.54	0.827	0.370	308.	0.286	0.226	0.214	
	Bottom	+	2.60	0.0193	-1.22	0.402	9.51	0.795	0.336	268.	0.311	0.284	0.296	
		-	2.51	0.0188	-1.22	0.411	9.55	0.949	0.334	317.	0.270	0.246	0.191	

TABLE A.2: The fitted parameters for the modified Bethe-Bloch equation and the correction functions.



# Appendix B

## Cross Section Tables

Bin		Diffractive $\phi$ photoproduction			
$ t $ GeV <sup>2</sup>	$W$ GeV	$\sigma$	$\delta_{stat}$	$\delta_{sys}$	
			pb <sup>-1</sup>		
0.20 - 0.30	30 - 40	1.36	$\pm 0.03$	+0.14	-0.19
	40 - 65	1.26	$\pm 0.04$	+0.14	-0.19
0.30 - 0.40	30 - 40	1.07	$\pm 0.03$	+0.11	-0.13
	40 - 50	0.72	$\pm 0.03$	+0.09	-0.10
	50 - 58	0.76	$\pm 0.04$	+0.10	-0.11
	58 - 65	1.00	$\pm 0.07$	+0.14	-0.15
0.40 - 0.50	30 - 40	0.653	$\pm 0.020$	+0.070	-0.076
	40 - 50	0.55	$\pm 0.02$	+0.07	-0.07
	50 - 60	0.55	$\pm 0.03$	+0.07	-0.08
	60 - 75	0.71	$\pm 0.03$	+0.10	-0.10
0.50 - 0.65	30 - 40	0.468	$\pm 0.012$	+0.050	-0.052
	40 - 55	0.377	$\pm 0.012$	+0.047	-0.046
	55 - 70	0.463	$\pm 0.015$	+0.067	-0.061
	70 - 80	0.47	$\pm 0.02$	+0.08	-0.07
0.65 - 0.90	30 - 40	0.217	$\pm 0.006$	+0.025	-0.025
	40 - 50	0.202	$\pm 0.007$	+0.027	-0.026
	50 - 60	0.184	$\pm 0.008$	+0.029	-0.026
	60 - 70	0.206	$\pm 0.010$	+0.036	-0.030
	70 - 80	0.228	$\pm 0.012$	+0.044	-0.037
0.90 - 1.50	30 - 50	0.0674	$\pm 0.0017$	+0.0102	-0.0084
	50 - 70	0.069	$\pm 0.002$	+0.013	-0.011
	70 - 90	0.069	$\pm 0.003$	+0.016	-0.012

TABLE B.1: Cross section for diffractive  $\phi$  meson photoproduction.

B. CROSS SECTION TABLES

---

Bin		Elastic $\phi$ photoproduction			
$ t $ GeV <sup>2</sup>	$W$ GeV	$\sigma$	$\delta_{stat}$	$\delta_{sys}$	
			pb <sup>-1</sup>		
0.20 - 0.30	30 - 40	0.70	$\pm 0.02$	+0.07	-0.10
	40 - 65	0.72	$\pm 0.04$	+0.08	-0.11
0.30 - 0.40	30 - 40	0.49	$\pm 0.03$	+0.06	-0.07
	40 - 50	0.44	$\pm 0.04$	+0.06	-0.07
	50 - 58	0.54	$\pm 0.03$	+0.07	-0.08
	58 - 65	0.68	$\pm 0.06$	+0.09	-0.11
0.40 - 0.50	30 - 40	0.304	$\pm 0.018$	+0.035	-0.040
	40 - 50	0.23	$\pm 0.02$	+0.03	-0.03
	50 - 60	0.24	$\pm 0.02$	+0.03	-0.04
	60 - 75	0.29	$\pm 0.02$	+0.04	-0.04
0.50 - 0.65	30 - 40	0.151	$\pm 0.011$	+0.019	-0.022
	40 - 55	0.144	$\pm 0.010$	+0.018	-0.020
	55 - 70	0.151	$\pm 0.012$	+0.019	-0.022
	70 - 80	0.127	$\pm 0.017$	+0.023	-0.025
0.65 - 0.90	30 - 40	0.038	$\pm 0.005$	+0.007	-0.009
	40 - 50	0.038	$\pm 0.006$	+0.008	-0.009
	50 - 60	0.035	$\pm 0.006$	+0.008	-0.009
	60 - 70	0.035	$\pm 0.007$	+0.008	-0.010
	70 - 80	0.042	$\pm 0.009$	+0.010	-0.011
0.90 - 1.50	30 - 50	0.0116	$\pm 0.0015$	+0.0028	-0.0031
	50 - 70	0.0099	$\pm 0.0020$	+0.0026	-0.0032
	70 - 90	0.012	$\pm 0.003$	+0.003	-0.004

TABLE B.2: *Cross section for elastic  $\phi$  meson photoproduction.*

# List of Figures

2.1	Diffraction in optics . . . . .	18
2.2	The diffraction pattern generated by a circular aperture/obstacle. . . . .	19
2.3	Differential cross section for $p - {}^{40}\text{Ca}$ . . . . .	20
2.4	$s$ and $t$ and $u$ channel 2-2 reactions. . . . .	22
2.5	Generic diagram for $ep$ scattering, showing the kinematic variables. . . . .	22
2.6	Generic diffractive reaction. . . . .	23
2.7	The helicity angles $\Phi_h$ , $\phi_h$ and $\theta_h$ . . . . .	25
2.8	$t$ -channel meson exchange scattering . . . . .	30
2.9	Chew-Frautschi plot for mesonic trajectories . . . . .	32
2.10	$t$ -channel reggeon exchange scattering . . . . .	32
2.11	Total $\gamma p$ cross section as a function of the centre of mass energy $W_{\gamma p}$ . . . . .	33
2.12	Two gluon exchange picture of vector meson production. . . . .	34
2.13	Gluon ladder picture of diffractive vector meson exchange. . . . .	35
3.1	$\phi$ meson discovery . . . . .	38
3.2	Illustration of the Zweig rule . . . . .	39
3.3	The vector meson multiplet of $SU(3)_{flavour}$ . . . . .	41
4.1	HERA . . . . .	44
4.2	Side view of H1 . . . . .	47
4.3	The H1 Tracking system . . . . .	48
4.4	Radial view of the H1 central tracker. . . . .	49
4.5	The projective geometry of the CIP . . . . .	50
4.6	Principle of operation of the CIP2000 trigger . . . . .	50
4.7	$z$ -vertex histogram of the CIP 2000 trigger . . . . .	51
4.8	Example of a vertex fit . . . . .	52
4.9	The H1 liquid argon calorimeter . . . . .	54
4.10	The forward muon detector (FMD) . . . . .	56
5.1	Comparison between non-relativistic and relativistic Breit-Wigner . . . . .	62
5.2	Fitted mass and resolution in data and simulation . . . . .	63
6.1	Display of a curling track event . . . . .	67
6.2	Invariant mass for $\pi$ and K energy loss corrections . . . . .	70
6.3	Comparison of energy loss correction algorithms . . . . .	71
6.4	Difference between the reconstructed and the generated $\phi$ mass . . . . .	72
6.5	Di-kaon mass distribution . . . . .	72
6.6	Difference between the reconstructed and the generated $W$ . . . . .	73
6.7	$W$ distribution for selected events . . . . .	74

6.8	The number of $\phi$ meson events in bins of the photon proton centre of mass energy $W$ .	74
6.9	Difference between the reconstructed and the generated $ t $	75
6.10	Average generated $Q^2$ versus reconstructed $ t $	76
6.11	Fraction of events with a high $Q^2$ versus reconstructed $ t $	76
6.12	$ t $ distribution for selected events	77
6.13	The number of $\phi$ meson events in bins of the squared four momentum transfer at the proton vertex $ t $ .	77
6.14	$z$ -vertex distribution	78
6.15	Number of long non-vertex fitted tracks	79
6.16	Unassociated energy	80
6.17	Track transverse momentum.	81
6.18	Track polar angle.	81
6.19	Binning for the pomeron trajectory measurement	82
6.20	Binning for the $t$ dependence measurement	83
7.1	Deviation of the measured $dE/dx$ from the parametrisation vs. $\beta\gamma$	88
7.2	Deviation of the measured $dE/dx$ from the parametrisation vs. $\vartheta$	89
7.3	Kaon likelihood	90
7.4	$dE/dx$ versus momentum	90
7.5	Effect of the OR $dE/dx$ cut on the invariant mass distribution	91
7.6	Effect of the AND $dE/dx$ cut on the invariant mass distribution	91
8.1	Acceptance versus $ t $	94
8.2	Acceptance versus $ W $	95
8.3	Acceptance in $W/t$ bins	95
8.4	Fraction of decaying kaons	96
8.5	$K^+$ –Nucleon cross section measured with the COP/COZ.	97
8.6	$K^-$ –Nucleon cross section measured with the COP/COZ.	98
8.7	Event loss due to the error in the reconstruction software	99
8.8	Efficiency of the $dE/dx$ tag versus track momentum.	100
8.9	Efficiency of the $dE/dx$ tag versus track polar angle.	100
8.10	Single track efficiency of the FTT	102
8.11	Single track efficiency of the FTT after reweight	102
8.12	Reweight of the simulation for the FTT single track efficiency	103
8.13	FTT multiplicity trigger element efficiency	104
8.14	FTT multiplicity trigger element efficiency (reweighted)	104
8.15	FTT topology trigger element efficiency	104
8.16	Efficiency of the CIP trigger conditions versus average transverse momentum	105
8.17	CIP trigger efficiency before and after reweight	106
8.18	Total efficiency versus $ t $	107
8.19	Total efficiency versus $W$	107
9.1	Noise distributions for forward detectors	110
9.2	Correlation of noise in the forward detectors	111
9.3	Number of hit pairs in the FMD	112
9.4	Hits in the FTS stations	112
9.5	Energy measured in the plug calorimeter	113
9.6	Tagging efficiencies versus $\log(M_\gamma)$	114
9.7	Fraction of events tagged versus $ t $	114

9.8	$ t $ spectra with the three forward tags applied . . . . .	115
9.9	$ t $ spectra of events with and without tag . . . . .	115
9.10	Fraction of tagged events in MC and data . . . . .	116
10.1	Fitted $\phi$ peak. . . . .	118
10.2	Invariant mass distributions binned in $W$ and $t$ . . . . .	119
10.3	Change of MC reweight for FTT systematics . . . . .	121
10.4	Systematic variations of the FTT efficiency . . . . .	122
10.5	Systematic errors . . . . .	123
11.1	$\cos\theta_h$ distribution of selected events . . . . .	126
11.2	$\cos\theta_h$ distribution of selected $\phi$ mesons . . . . .	126
11.3	$\phi_h$ distribution of selected events . . . . .	127
11.4	$\phi_h$ distribution of selected $\phi$ mesons . . . . .	127
11.5	Track topologies . . . . .	128
11.6	Inclusive cross section differential in $\cos\theta_h$ . . . . .	128
11.7	Inclusive cross section differential in $\phi_h$ . . . . .	129
11.8	Elastic cross section differential in $\cos\theta_h$ . . . . .	129
11.9	Elastic cross section differential in $\phi_h$ . . . . .	130
11.10	The inclusive angular distribution for $0.25 <  t  < 0.5$ GeV <sup>2</sup> in slices along $\cos\theta_h$ . . . . .	131
11.11	The inclusive angular distribution for $0.5 <  t  < 1.0$ GeV <sup>2</sup> in slices along $\cos\theta_h$ . . . . .	131
11.12	The inclusive angular distribution for $0.25 <  t  < 0.5$ GeV <sup>2</sup> in slices along $\phi_h$ . . . . .	132
11.13	The inclusive angular distribution for $0.5 <  t  < 1.0$ GeV <sup>2</sup> in slices along $\phi_h$ . . . . .	132
11.14	The elastic angular distribution for $0.25 <  t  < 0.5$ GeV <sup>2</sup> in slices along $\cos\theta_h$ . . . . .	133
11.15	The elastic angular distribution for $0.5 <  t  < 1.0$ GeV <sup>2</sup> in slices along $\cos\theta_h$ . . . . .	133
11.16	The elastic angular distribution for $0.25 <  t  < 0.5$ GeV <sup>2</sup> in slices along $\phi_h$ . . . . .	134
11.17	The elastic angular distribution for $0.5 <  t  < 1.0$ GeV <sup>2</sup> in slices along $\phi_h$ . . . . .	134
11.18	Spin density matrix elements for diffractive $\phi$ photoproduction. . . . .	135
11.19	Spin density matrix elements for elastic $\phi$ photoproduction. . . . .	135
12.1	Diffractive differential cross section for $\phi$ meson photoproduction . . . . .	138
12.2	Elastic differential cross section for $\phi$ meson photoproduction . . . . .	139
12.3	$\alpha$ versus $t$ for diffractive $\phi$ photoproduction . . . . .	140
12.4	Pomeron trajectory with errors . . . . .	141
12.5	Error contributions to the pomeron trajectory. . . . .	141
12.6	Comparison of trajectory measurements . . . . .	142
12.7	Result of the global fit, part I . . . . .	145
12.8	Result of the global fit, part II . . . . .	146
12.9	Comparison of pomeron trajectory measurements . . . . .	147
12.10	$t$ dependence of the elastic cross section in bins of $W$ . . . . .	148
12.11	$W$ dependence of the $t$ slope parameter $b$ . . . . .	149
12.12	Elastic $\phi$ photoproduction cross section versus $W$ . . . . .	150
12.13	Vector meson photoproduction cross sections vs. $W$ . . . . .	151

13.1	Memory operation modes . . . . .	160
13.2	The CJC wire layers used by the FTT . . . . .	161
13.3	Illustration of the hit finding technique . . . . .	162
13.4	Schematic representation of the charge integration . . . . .	163
13.5	CJC wire with front end electronics . . . . .	163
13.6	The geometry of an FTT cell . . . . .	164
13.7	Mask generation . . . . .	165
13.8	Illustration of the shift registers and pattern match. . . . .	166
13.9	Picture of a front end module . . . . .	167
13.10	Schematic of the L1 Linker Hough transform . . . . .	168
13.11	Schematic of the L1 Linker algorithm . . . . .	169
13.12	The 78 distinct topologies for a tenfold division in $\varphi$ . . . . .	170
13.13	Hitpatterns constituting $z$ segments . . . . .	172
13.14	Geometry of a level 1 $z$ $\varphi$ sector . . . . .	172
13.15	Linking segments in the $r - z$ -plane. . . . .	173
13.16	Picture of a Multipurpose Processing Board . . . . .	175
13.17	Drift calibration . . . . .	177
13.18	Flow diagram of trigger data in the FTT system (I). Level 1 part. . . . .	180
13.19	Flow diagram of trigger data in the FTT system (II). Level 2 and 3 parts. . . . .	181
14.1	Schematic representation of the L2z algorithm . . . . .	185
14.2	L2z event display . . . . .	186
14.3	Higher multiplicity L2z event display . . . . .	186
15.1	Illustration of the trigonometric function lookup . . . . .	194
15.2	Control mechanism of the invariant mass calculation . . . . .	195
16.1	Single hit efficiency of the FTT . . . . .	198
16.2	FTT single track efficiency for pions and kaons . . . . .	198
16.3	Gain dependence of the FTT single track efficiency . . . . .	199
16.4	Segment finding and linking efficiency . . . . .	200
16.5	FTT single track finding efficiency versus beam currents . . . . .	200
16.6	Comparison between FTT and $DC - r\varphi$ trigger . . . . .	201
16.7	FTT L2 efficiency versus track $p_T$ . . . . .	202
16.8	FTT L2 efficiency versus track $\vartheta$ . . . . .	202
16.9	Performance of the FTT L2z algorithm . . . . .	203
16.10	Performance of the FTT L2z algorithm for shifted vertex . . . . .	204
16.11	Resolution of the FTT L2 track fit . . . . .	204
16.12	Influence of L2 invariant mass cut on mass shape . . . . .	205
16.13	Efficiency of the L2 mass finder . . . . .	206
16.14	Purity of the $\phi$ sample with mass condition . . . . .	206
16.15	Resolution for the reconstruction of the $D^0$ mass. . . . .	207
16.16	Resolution for the reconstruction of the $\Delta m$ variable. . . . .	207
16.17	Mass difference distribution for L3 triggered $D^*$ candidates. . . . .	207
17.1	Communication in the FTT system . . . . .	212
17.2	Overview of the FTT GUI threads . . . . .	213
17.3	The log message display . . . . .	214
17.4	Automatic shift instructions . . . . .	215
17.5	The BackFPGA Control VI . . . . .	216

17.6	The Track Segment Finder Calibration VI . . . . .	217
17.7	The readout control VI . . . . .	218
17.8	The crate configuration file builder VI . . . . .	219
17.9	The crate loading VI . . . . .	219
17.10	The MPB Message Composer VI . . . . .	220
17.11	The FTT Tester VI . . . . .	221



# List of Tables

3.1	$\phi$ meson decay modes . . . . .	39
4.1	Design parameters of HERA II . . . . .	45
4.2	H1 detector components . . . . .	46
4.3	H1 tracker components . . . . .	48
4.4	CJC mechanical parameters . . . . .	50
5.1	DIFFVM generator settings. . . . .	61
6.1	Luminosities of the various subsamples. . . . .	69
6.2	Binning for the pomeron trajectory measurement . . . . .	81
6.3	Binning for the $t$ dependence measurement. . . . .	82
7.1	$\varphi$ bins for the $dE/dx$ calibration. . . . .	87
8.1	$dE/dx$ efficiency parametrisation. . . . .	99
8.2	Parameters used for reweighting the FTT efficiency . . . . .	101
8.3	Cut flow . . . . .	108
12.1	Data sets used for the global fit . . . . .	144
13.1	Timing of the level 1 FTT . . . . .	171
13.2	Data stored in the lookup ROM . . . . .	173
15.1	FTT and single precision float formats . . . . .	190
15.2	Protocol for the invariant mass bus . . . . .	192
17.1	Message protocol . . . . .	211
A.1	$dE/dx$ resolution parameters. . . . .	224
A.2	Fitted parameters for $dE/dx$ parametrisation . . . . .	225
B.1	Cross section for diffractive $\phi$ meson photoproduction. . . . .	227
B.2	Cross section for elastic $\phi$ meson photoproduction. . . . .	228



# List of Acronyms

## A

<b>AC</b>	Alternating Current.
<b>AGS</b>	Alternating Gradient Synchrotron.
<b>APD</b>	Avalanche Photo Diode.
<b>ASCII</b>	American Standard Code for Information Interchange.
<b>ASIC</b>	Application-Specific Integrated Circuit.

## B

<b>BC</b>	Bunch Crossing.
<b>BFKL</b>	Balitsky, Fadin, Kuraev, Lipatov.
<b>BOS</b>	Bank Object System.
<b>BPC</b>	Backward Proportional Chamber.
<b>BR</b>	Branching Ratio.
<b>BSM</b>	Beyond the Standard Model.
<b>BST</b>	Backward Silicon Tracker.

## C

<b>CDAQ</b>	Central Data Acquisition.
<b>CIP</b>	Central Inner Proportional Chamber.
<b>CJC</b>	Central Jet Chamber.
<b>CMD</b>	Central Muon Detector.
<b>CMD-2</b>	Cryogenic Magnetic Detector 2.
<b>CMOS</b>	Complementary Metal-Oxide-Semiconductor.
<b>COP</b>	Central Outer Proportional Chamber.
<b>COZ</b>	Central Outer $z$ Chamber.
<b>CPLD</b>	Complex Programmable Logic Device.
<b>CST</b>	Central Silicon Tracker.
<b>CTL</b>	Central Trigger Logic.

## D

<b>DAQ</b>	Data Acquisition.
<b>DC</b>	Direct Current.
<b>DCR<math>\phi</math></b>	Drift Chamber $r$ - $\phi$ Trigger.
<b>DESY</b>	Deutsches Elektronen-Synchrotron (German electron synchrotron).

<b>DMA</b>	Direct Memory Access.
<b>DOS</b>	Difference Of Samples.
<b>DPIO</b>	Digital Parallel Input Output.
<b>DRAM</b>	Dynamic Random Access Memory.
<b>DST</b>	Detector Summary Tape.

## E

<b>ep</b>	electron-proton.
<b>ESB</b>	Embedded System Block.

## F

<b>FClr</b>	Fast Clear.
<b>FEM</b>	Front End Module.
<b>FIFO</b>	First In First Out.
<b>FMD</b>	Forward Muon Detector.
<b>FNC</b>	Forward Neutron Calorimeter.
<b>FPDP</b>	Front Panel Data Port.
<b>FPGA</b>	Field Programmable Gate Array.
<b>FPS</b>	Forward Proton Spectrometer.
<b>FST</b>	Forward Silicon Tracker.
<b>FTD</b>	Forward Tracking Detector.
<b>FTP</b>	File Transfer Protocol.
<b>FTS</b>	Forward Tagging System.
<b>FTT</b>	Fast Track Trigger.

## G

<b>GUI</b>	Graphical User Interface.
------------	---------------------------

## H

<b>HERA</b>	Hadron Elektron Ring Anlage (Hadron electron ring facility).
-------------	--

## I

<b>IC</b>	Integrated Circuit.
<b>I/O</b>	Input/Output.
<b>IP</b>	Internet Protocol.

## LIST OF ACRONYMS

---

### J

**JTAG** Joint Test Action Group.

### L

**L1** Trigger Level 1.

**L2** Trigger Level 2.

**L2NN** Level 2 Neural Network Trigger.

**L2TT** Level 2 Topological Trigger.

**L3** Trigger Level 3.

**L45** Trigger Level 4/5.

**LAr** Liquid Argon Calorimeter.

**LE** Logic Element.

**LED** Light Emitting Diode.

**LUT** Look-Up Table.

**LVDS** Low Voltage Differential Signalling.

### M

**MPB** Multi Purpose Board or Multipurpose Processing Board.

### P

**PC** Personal Computer.

**PCB** Printed Circuit Board.

**PCI** Peripheral Component Interconnect.

**PiEn** Pipeline Enable.

**PMC** PCI Mezzanine Card.

**PMT** Photo-Multiplier Tube.

**POT** Production Output Tape.

**PPC** PowerPC.

**PQZP** Parallel Quickbus Zero-suppressed Processor.

**PRT** Proton Remnant Tagger.

### Q

**QCD** Quantum Chromo-Dynamics.

**QED** Quantum Electro-Dynamics.

**Qt** Charge - Time.

### R

**RAM** Random Access Memory.

**RFC** Request for Comment.

**RMS** (square) Root of the Mean Squared deviation.

**ROM** Read-Only Memory.

### S

**SCHC** s-Channel Helicity Conservation.

**SM** Service Module.

**SM** Standard Model (of Particle Physics).

**SMD** Surface Mounted Device.

**SND** Spherical Neutral Detector.

**SpaCal** Spaghetti Calorimeter.

**SRAM** Static Random Access Memory.

**ST** Sub-Trigger.

**STC** Subsystem Trigger Controller.

### T

**TCP** Transmission Control Protocol.

**TE** Trigger Element.

**TSF** Track Segment Finder.

### V

**VFPS** Very Forward Proton Spectrometer.

**VHDL** VHSIC Hardware Description Language.

**VHSIC** Very High Speed Integrated Circuit.

**VI** Virtual Instrument.

**VIC** Vertical Crate Interconnect.

**VME** Vesa Module Europe.

### W

**WOM** Write-Only Memory.

### Z

**ZBT** Zero Bus Turnaround.

# Bibliography

- [1] Blaise Pascal, Seizième lettre aux révérends pères jésuites, (Lettre Provinciale XVI), 1656.
- [2] Mercedes Matter, *Alberto Giacometti, photographiert von Herbert Matter*. Benteli, 1988.
- [3] Monty Python, *The Meaning of Life*, 1983.
- [4] Steven Weinberg, *The Quantum Theory of Fields*, volume I-III. Cambridge University Press, 1995-2000.
- [5] S. L. Glashow, “*Partial Symmetries of Weak Interactions*”, Nucl. Phys., **22** 579–588, 1961.
- [6] Steven Weinberg, “*A Model of Leptons*”, Phys. Rev. Lett., **19** 1264–1266, 1967.
- [7] H. David Politzer, “*Reliable Perturbative Results for Strong Interactions?*”, Phys. Rev. Lett., **30** 1346–1349, 1973.
- [8] D. J. Gross and Frank Wilczek, “*Ultraviolet Behavior of Non-Abelian Gauge Theories*”, Phys. Rev. Lett., **30** 1343–1346, 1973.
- [9] T. Regge, “*Introduction to complex orbital momenta*”, Nuovo Cim., **14** 951, 1959.
- [10] G. F. Chew and S. C. Frautschi, “*Regge trajectories and the principle of maximum strength for strong interactions*”, Phys. Rev. Lett., **8** 41–44, 1962.
- [11] I. P. Ivanov, N. N. Nikolaev and A. A. Savin, “*Diffraction vector meson production at HERA: From soft to hard QCD*”, 2004.
- [12] R. Fiore, Laszlo L. Jenkovszky and F. Paccanoni, “*Photoproduction of heavy vector mesons at HERA: A testfield for diffraction*”, Eur. Phys. J., **C10** 461–467, 1999.
- [13] A. Donnachie and P. V. Landshoff, “*Exclusive vector meson production at HERA*”, Phys. Lett., **B348** 213–218, 1995.
- [14] J. J. Sakurai and D. Schildknecht, “*Generalized vector dominance and inelastic electron - proton scattering*”, Phys. Lett., **B40** 121–126, 1972.
- [15] T. H. Bauer, R. D. Spital, D. R. Yennie and F. M. Pipkin, “*The hadronic properties of the photon in high-energy interactions*”, Rev. Mod. Phys., **50** 261, 1978.
- [16] A. Aktas et al., [H1 Collaboration], “*Diffraction photoproduction of  $\rho$  mesons with large momentum transfer at HERA*”, Phys. Lett., **B638** 422–431, 2006.
- [17] Ronald Weber, *Diffraction  $\rho^0$  photoproduction at HERA*, PhD thesis, ETH Zürich, 2006, ETH No. 16709.
- [18] C. Adloff et al., [H1 Collaboration], “*Elastic electroproduction of  $\rho$  mesons at HERA*”, Eur. Phys. J., **C13** 371–396, 2000.
- [19] J. Breitweg et al., [ZEUS Collaboration], “*Measurement of the spin-density matrix elements in exclusive electroproduction of  $\rho^0$  mesons at HERA*”, Eur. Phys. J., **C12** 393–410, 2000.

- [20] J. Breitweg et al., [ZEUS Collaboration], “*Exclusive electroproduction of  $\rho^0$  and  $J/\psi$  mesons at HERA*”, Eur. Phys. J., **C6** 603–627, 1999.
- [21] J. Breitweg et al., [ZEUS Collaboration], “*Elastic and proton-dissociative  $\rho^0$  photoproduction at HERA*”, Eur. Phys. J. C, **2** 247, 1998.
- [22] C. Adloff et al., [H1 Collaboration], “*Proton dissociative  $\rho$  and elastic  $\phi$  electroproduction at HERA*”, Z. Phys., **C75** 607–618, 1997.
- [23] M. Derrick et al., [ZEUS Collaboration], “*The ZEUS leading proton spectrometer and its use in the measurement of elastic  $\rho^0$  photoproduction at HERA*”, Z. Phys. C, **73** 253, 1997.
- [24] D. Westphal, *Measurement of Elastic  $\rho^0$  Photoproduction at HERA*, PhD thesis, Universität Hamburg, 1997.
- [25] S. Aid et al., [H1 Collaboration], “*Elastic Photoproduction of  $\rho^0$  Mesons at HERA*”, Nucl. Phys. B, **463** 3, 1996.
- [26] S. Aid et al., [H1 Collaboration], “*Elastic Electroproduction of  $\rho^0$  and  $J/\psi$  Mesons at large  $Q^2$  at HERA*”, Nucl. Phys., **B468** 3–36, 1996.
- [27] M. Derrick et al., [ZEUS Collaboration], “*Measurement of elastic  $\rho^0$  photoproduction at HERA*”, Z. Phys., **C69** 39–54, 1995.
- [28] A. Aktas et al., [H1 Collaboration], “*Elastic  $J/\psi$  production at HERA*”, Eur. Phys. J., **C46** 585–603, 2005.
- [29] S. Chekanov et al., [ZEUS Collaboration], “*Measurement of inelastic  $J/\psi$  production in deep inelastic scattering at HERA*”, Eur. Phys. J., **C44** 13–25, 2005.
- [30] S. Chekanov et al., [ZEUS Collaboration], “*Exclusive electroproduction of  $J/\psi$  mesons at HERA*”, Nucl. Phys., **B695** 3–37, 2004.
- [31] A. Aktas et al., [H1 Collaboration], “*Diffraction photoproduction of  $J/\psi$  mesons with large momentum transfer at HERA*”, Phys. Lett., **B568** 205–218, 2003.
- [32] S. Chekanov et al., [ZEUS Collaboration], “*Measurements of inelastic  $J/\psi$  and  $\psi'$  photoproduction at HERA*”, Eur. Phys. J., **C27** 173–188, 2003.
- [33] C. Adloff et al., [H1 Collaboration], “*Inelastic photoproduction of  $J/\psi$  mesons at HERA*”, Eur. Phys. J., **C25** 25–39, 2002.
- [34] C. Adloff et al., [H1 Collaboration], “*Inelastic leptonproduction of  $J/\psi$  mesons at HERA*”, Eur. Phys. J., **C25** 41–53, 2002.
- [35] C. Adloff et al., [H1 Collaboration], “*Diffraction photoproduction of  $\psi(2S)$  mesons at HERA*”, Phys. Lett., **B541** 251–264, 2002.
- [36] S. Chekanov et al., [ZEUS Collaboration], “*Exclusive photoproduction of  $J/\psi$  mesons at HERA*”, Eur. Phys. J., **C24** 345–360, 2002.
- [37] C. Adloff et al., [H1 Collaboration], “*Elastic photoproduction of  $J/\psi$  and  $\Upsilon$  mesons at HERA*”, Phys. Lett., **B483** 23–35, 2000.
- [38] C. Adloff et al., [H1 Collaboration], “*Photo-production of  $\psi(2S)$  mesons at HERA*”, Phys. Lett., **B421** 385–394, 1998.
- [39] J. Breitweg et al., [ZEUS Collaboration], “*Measurement of elastic  $J/\psi$  photoproduction at HERA*”, Z. Phys., **C75** 215–228, 1997.
- [40] J. Breitweg et al., [ZEUS Collaboration], “*Measurement of inelastic  $J/\psi$  photoproduction at HERA*”, Z. Phys., **C76** 599–612, 1997.
- [41] S. Aid et al., [H1 Collaboration], “*Elastic and Inelastic Photoproduction of  $J/\psi$  Mesons at HERA*”, Nucl. Phys., **B472** 3–31, 1996.
- [42] M. Derrick et al., [ZEUS Collaboration], “*Measurement of the cross-section for the reaction  $\gamma p \rightarrow J/\psi p$  with the ZEUS detector at HERA*”, Phys. Lett., **B350** 120–134, 1995.

- 
- [43] T. Ahmed et al., [H1 Collaboration], “Photoproduction of  $J/\psi$  mesons at HERA”, Phys. Lett., **B338** 507–518, 1994.
- [44] B. List, *Diffraktive  $J/\psi$ -Produktion in Elektron-Proton-Stößen am Speicherring HERA*, Master’s thesis, Technische Universität Berlin, 1993.
- [45] S. Chekanov et al., [ZEUS Collaboration], “Exclusive electroproduction of  $\phi$  mesons at HERA”, Nucl. Phys., **B718** 3–31, 2005.
- [46] C. Adloff et al., [H1 Collaboration], “Measurement of elastic electroproduction of  $\phi$  mesons at HERA”, Phys. Lett., **B483** 360–372, 2000.
- [47] M. Derrick et al., [ZEUS Collaboration], “Measurement of Elastic  $\phi$  Photoproduction at HERA”, Phys. Lett. B., **377** 259, 1996.
- [48] M. Derrick et al., [ZEUS Collaboration], “Measurement of the Reaction  $\gamma^*p \rightarrow \phi p$  in Deep Inelastic  $e^+p$  Scattering at HERA”, Phys. Lett., **B380** 220–234, 1996.
- [49] Augustin-Jean Fresnel, “Mémoire sur la diffraction de la Lumière”, Mémoires de l’Académie des sciences de l’Institut de France, **5** 393–465, 1818.
- [50] Francesco Maria Grimaldi, *Physicomathesis de lumine, coloribus, et iride, aliisque annexis*. Bologna, 1665.
- [51] U. Amaldi, M. Jacob and G. Matthiae, “Diffraction of Hadronic Waves”, Ann. Rev. Nucl. Sci., **26** 385–456, 1976.
- [52] Bahaa E. A. Saleh and Malvin Carl Teich, *Fundamentals of Photonics*. Wiley-Interscience, 1991.
- [53] George Biddell Airy, “On the Diffraction of an Object-Glass with Circular Aperture”, Trans. Camb. Phil. Soc., **5** 283–291, 1835.
- [54] de Prince Louis-Victor Broglie, *Recherches sur la Théorie des Quanta*, PhD thesis, Université de Paris, 1924.
- [55] C. Davison and L.H. Germer, “The scattering of Electrons by a single crystal of Nickel”, Nature, **119** 558–560, 1927.
- [56] M. Arndt, O. Nairz, J. Voss-Andrae, C. Keller, G. van der Zouw and A. Zeilinger, “Wave-particle duality of  $C_{60}$ ”, Nature, **401** 680–682, 1999.
- [57] G. Alberi and G. Goggi, “Diffraction of Subnuclear Waves”, Phys. Rept., **74** 1–207, 1981.
- [58] P. Ciok, T. Coghén, J. Gierula, R. Holynski, A. Jurak, M. Miesowicz, T. Saniewska and O. Stanisiz, “High-energy interactions in nuclear emulsions”, Nuovo Cim., **8** 166, 1958.
- [59] Giuseppe Cocconi, “Empirical Model for Ultrarelativistic Nucleon-Nucleon Collisions”, Phys. Rev., **111** 1699–1706, 1958.
- [60] M.L. Good and W.D. Walker, “Diffraction dissociation of beam particles”, Phys. Rev., **120** 1857, 1960.
- [61] G. D. Alkhazov, S. L. Belostotsky, O. A. Domchenkov, Yu. V. Dotsenko, N. P. Kuropatkin, M. A. Schuvaev and A. A. Vorobyov, “Nuclear sizes of  $^{40,48}\text{Ca}$  and  $^{32,34}\text{S}$  isotopes determined from 1 GeV proton elastic scattering”, Phys. Lett. B, **57** 47, 1975.
- [62] B.L. Ioffe, “Space-time picture of photon and neutrino scattering and electroproduction cross section asymptotics”, Phys. Lett., **B30** 123, 1969.
- [63] J. J. Sakurai, “Vector meson dominance and high-energy electron proton inelastic scattering”, Phys. Rev. Lett., **22** 981–984, 1969.
- [64] J. J. Sakurai and D. Schildknecht, “Generalized Vector Dominance and Inelastic Electron Nucleon Scattering. 3: The Small  $\omega t$  Region”, Phys. Lett., **B42** 216, 1972.

- [65] J. J. Sakurai and D. Schildknecht, “Generalized vector dominance and inelastic electron-nucleon scattering. the neutron-to-proton ratios”, Phys. Lett., **B41** 489–494, 1972.
- [66] K. Schilling and G. Wolf, “How to analyze vector meson production in inelastic lepton scattering”, Nucl. Phys., **B61** 381–413, 1973.
- [67] E. Fermi, “On the Theory of the impact between atoms and electrically charged particles”, Z. Phys., **29** 315–327, 1924.
- [68] C. F. von Weizsäcker, “Ausstrahlung bei Stößen sehr schneller Elektronen (Radiation emitted in collisions of very fast electrons)”, Z. Phys., **88** 612–625, 1934.
- [69] E. J. Williams, “Nature of the high-energy particles of penetrating radiation and status of ionization and radiation formulae”, Phys. Rev., **45** 729–730, 1934.
- [70] V. M. Budnev, I. F. Ginzburg, G. V. Meledin and V. G. Serbo, “The Two photon particle production mechanism. Physical problems. Applications. Equivalent photon approximation”, Phys. Rept., **15** 181–281, 1974.
- [71] G.F. Chew, *S-Matrix theory of strong interactions*. W.A. Benjamin, New York, 1962.
- [72] Henry P. Stapp, “Derivation of the CPT Theorem and the Connection between Spin and Statistics from Postulates of the S-Matrix Theory”, Phys. Rev., **125**(6) 2139–2162, Mar 1962.
- [73] Alan. R. White, “The past and future of S-matrix theory”, 2000.
- [74] V. Barone and E. Predazzi, *High-Energy Particle Diffraction*. Springer-Verlag, 2002.
- [75] P. D. B. Collins, *An Introduction to Regge Theory and high-energy physics*. Cambridge University Press, 1977, Cambridge 1977, 445p.
- [76] Marcel Froissart, “Asymptotic behavior and subtractions in the Mandelstam representation”, Phys. Rev., **123** 1053–1057, 1961.
- [77] A. Martin, “Unitarity and high-energy behavior of scattering amplitudes”, Phys. Rev., **129** 1432–1436, 1963.
- [78] I.Y. Pomeranchuk, “Equality of the nucleon and antinucleon total interaction cross section at high energies”, Sov. Phys. JETP, **7** 499, 1958.
- [79] Hideki Yukawa, “On the Interaction of Elementary Particles”, Proc.Phys.Math.Soc.Jap., **17** 48, 1935.
- [80] C.D. Anderson and S.H. Neddermeyer, “Note on the Nature of Cosmic-Ray Particles”, Phys. Rev., **51** 884–886, 1937.
- [81] C.D. Anderson and S.H. Neddermeyer, “Cosmic-ray particles of intermediate mass”, Phys. Rev., **54** 88–89, 1938.
- [82] J.C. Street and E.C. Stevenson, “New evidence for the existence of a particle of mass intermediate between the proton and electron”, Phys. Rev., **52** 1003–1004, 1937.
- [83] W. Heisenberg and H. Euler, “Theoretische Gesichtspunkte zur Deutung der kosmischen Strahlung”, Ergebnisse der exakten Naturwissenschaften, **17** 1–69, 1938.
- [84] M. Conversi and O. Piccioni, “Measurements of the Lifetime of the Mesotron”, Nuovo Cimento, **2** 40, 1944.
- [85] M. Conversi, E. Pancini and O. Piccioni, “On the Decay Process of Positive and Negative Mesons”, Phys. Rev., **68** 232, 1945.
- [86] M. Conversi, E. Pancini and O. Piccioni, “On the disintegration of negative mesons”, Phys. Rev., **71** 209–210, 1947.
- [87] O. Piccioni, *History of Original Ideas and Basic Discoveries in Particle Physics*, volume 352 of NATO ASI series. Plenum Press, New York, 1996.
- [88] C.M.G. Lattes, H. Muirhead, G.P.S. Occhialini and C.F. Powell, “Proeses Involving Charged Mesons”, Nature, **159** 694–697, 1947.

- 
- [89] R. Brown, H. Muirhead, U. Camerini, P.H. Fowler, D.M. Ritson and C.F. Powell, “*Observations with electron-sensitive plates exposed to cosmic radiation*”, *Nature*, **163** 47–51, 1949.
- [90] T. Regge, “*Bound states, shadow states and Mandelstam representation*”, *Nuovo Cim.*, **18** 947–956, 1960.
- [91] V. N. Gribov, “*Partial waves with complex orbital angular momenta and the asymptotic behavior of the scattering amplitude*”, *Sov. Phys. JETP*, **14** 1395, 1962.
- [92] G. Veneziano, “*Construction of a crossing - symmetric, Regge behaved amplitude for linearly rising trajectories*”, *Nuovo. Cim.*, **A57** 190–197, 1968.
- [93] L. N. Chang, P. G. O. Freund and Yoichiro Nambu, “*Statistical approach to the veneziano model*”, *Phys. Rev. Lett.*, **24** 628–631, 1970.
- [94] Roger Penrose, *The Road to Reality*. Jonathan Cape, 2004.
- [95] W.-M. Yao et al., “*Review of Particle Physics*”, *Journal of Physics G*, **33**, 2006.
- [96] A. B. Kaidalov, L. A. Ponomarev and K. A. Ter-Martirosian, “*Total Cross-Sections and Diffractive Scattering in a Theory of Interacting Pomerons with  $\alpha_{\mathbb{P}}(0) > 1$* ”, *Yad. Fiz.*, **44** 722–728, 1986.
- [97] E. Gotsman, E. Levin and U. Maor, “*The survival probability of large rapidity gaps in a three channel model*”, *Phys. Rev.*, **D60** 094011, 1999.
- [98] Valery A. Khoze, Alan D. Martin and M. G. Ryskin, “*Soft diffraction and the elastic slope at Tevatron and LHC energies: A multi-pomeron approach*”, *Eur. Phys. J.*, **C18** 167–179, 2000.
- [99] M.G. Ryskin, A.D. Martin and V.A. Khoze, Diffractive processes at the lhc, In *Proceedings of Gribov 75 - Memorial Workshop on Quarks, Hadrons, and Strong Interactions*, 2005.
- [100] A. Donnachie and P. V. Landshoff, “*Elastic scattering and diffraction dissociation*”, *Nucl. Phys.*, **B244** 322, 1984.
- [101] A. Donnachie and P. V. Landshoff, “*Total cross-sections*”, *Phys. Lett.*, **B296** 227–232, 1992.
- [102] Jean Rene Cudell, Kyungsik Kang and Sung Ku Kim, “*Simple Pole Fits to  $pp$  and  $\bar{p}p$  Total Cross Sections and Real Parts*”, *Phys. Lett.*, **B395** 311–331, 1997.
- [103] M. Derrick et al., [ZEUS Collaboration], “*Measurement of elastic  $\omega$  photoproduction at HERA*”, *Z. Phys. C*, **73** 73, 1996.
- [104] A. Donnachie and P. V. Landshoff, “*Small  $x$ : Two pomerons!*”, *Phys. Lett.*, **B437** 408–416, 1998.
- [105] Murray Gell-Mann, “*Symmetries of baryons and mesons*”, *Phys. Rev.*, **125** 1067–1084, 1962.
- [106] Murray Gell-Mann, “*A Schematic model of baryons and mesons*”, *Phys. Lett.*, **8** 214–215, 1964.
- [107] F. E. Low, “*A Model of the Bare Pomeron*”, *Phys. Rev.*, **D12** 163, 1975.
- [108] S. Nussinov, “*Colored Quark Version of Some Hadronic Puzzles*”, *Phys. Rev. Lett.*, **34** 1286–1289, 1975.
- [109] C. Amsler and N. A. Tornqvist, “*Mesons beyond the naive quark model*”, *Phys. Rept.*, **389** 61–117, 2004.
- [110] Felipe J. Llanes-Estrada, Stephen R. Cotanch, Pedro J. de A. Bicudo, J. Emilio F. T. Ribeiro and Adam P. Szczepaniak, “*QCD glueball Regge trajectories and the Pomeron*”, *Nucl. Phys.*, **A710** 45–54, 2002.
- [111] I. I. Balitsky and L. N. Lipatov, “*The Pomeranchuk singularity in quantum chromodynamics*”, *Sov. J. Nucl. Phys.*, **28** 822–829, 1978.

- [112] R. Enberg, J. R. Forshaw, L. Motyka and G. Poludniowski, “*Vector meson photoproduction from the BFKL equation. I: Theory*”, JHEP, **09** 008, 2003.
- [113] G. G. Poludniowski, R. Enberg, J. R. Forshaw and L. Motyka, “*Vector meson photoproduction from the BFKL equation. II: Phenomenology*”, JHEP, **12** 002, 2003.
- [114] A. D. Martin, M. G. Ryskin and T. Teubner, “ *$Q^2$  dependence of diffractive vector meson electroproduction*”, Phys. Rev., **D62** 014022, 2000.
- [115] S. V. Goloskokov and P. Kroll, “*Vector meson electroproduction at small Bjorken- $x$  and generalized parton distributions*”, Eur. Phys. J., **C42** 281–301, 2005.
- [116] Nikolai N. Nikolaev and B. G. Zakharov, “*Colour transparency and scaling properties of nuclear shadowing in deep inelastic scattering*”, Z. Phys., **C49** 607–618, 1991.
- [117] Nikolai Nikolaev and Bronislav G. Zakharov, “*Pomeron structure function and diffraction dissociation of virtual photons in perturbative QCD*”, Z. Phys., **C53** 331–346, 1992.
- [118] Alfred H. Mueller, “*Soft gluons in the infinite momentum wave function and the BFKL pomeron*”, Nucl. Phys., **B415** 373–385, 1994.
- [119] Alfred H. Mueller and Bimal Patel, “*Single and double BFKL pomeron exchange and a dipole picture of high-energy hard processes*”, Nucl. Phys., **B425** 471–488, 1994.
- [120] J. R. Forshaw, R. Sandapen and G. Shaw, “*Further success of the colour dipole model*”, JHEP, **11** 025, 2006.
- [121] Juan M. Maldacena, “*The large  $N$  limit of superconformal field theories and supergravity*”, Adv. Theor. Math. Phys., **2** 231–252, 1998.
- [122] Edward Witten, “*Anti-de Sitter space and holography*”, Adv. Theor. Math. Phys., **2** 253–291, 1998.
- [123] S. S. Gubser, Igor R. Klebanov and Alexander M. Polyakov, “*Gauge theory correlators from non-critical string theory*”, Phys. Lett., **B428** 105–114, 1998.
- [124] Richard C. Brower, Joseph Polchinski, Matthew J. Strassler and Chung-I Tan, “*The pomeron and gauge / string duality*”, 2006.
- [125] L. Bertanza et al., “*Possible resonances in the  $\Xi\pi$  and  $K\bar{K}$  systems*”, Phys. Rev. Lett., **9**(4) 180, 1962.
- [126] A. R. Erwin, G. A. Hoyer, R. H. March, W. D. Walker and T. P. Wangler, “*Experimental Cross Section for  $\pi\pi \rightarrow \bar{K}K$* ”, Phys. Rev. Lett., **9**(1) 34–36, Jul 1962.
- [127] Gideon Alexander, Orin I. Dahl, Laurance Jacobs, George R. Kalbfleisch, Donald H. Miller, Alan Rittenberg, Joseph Schwartz and Gerald A. Smith, “*Final-State Interactions in the  $\pi^- + p \rightarrow K + \bar{K} + N$  Reaction*”, Phys. Rev. Lett., **9**(11) 460–464, Dec 1962.
- [128] P. Schlein et al., “*Quantum numbers of a 1020 MeV  $K\bar{K}$  resonance*”, Phys. Rev. Lett., **10**(8) 368, 1963.
- [129] P.L. Connolly et al., “*Existence and properties of the  $\varphi$  meson*”, Phys. Rev. Lett., **10**(8) 371, 1963.
- [130] J. J. Sakurai, “*Possible Existence of a  $T = 0$  Vector Meson at 1020 MeV*”, Phys. Rev. Lett., **9**(11) 472–475, Dec 1962.
- [131] M. N. Achasov et al., “*Spherical neutral detector for VEPP-2M collider, Nuclear Instruments and Methods in Physics Research Section A: Accelerators, Spectrometers, Detectors and Associated Equipment*”, NIM, **A449** 125–139, 2000.
- [132] G.A. Aksenov et al., “*The CMD-2 Detector*”, Preprint Budker INP, **85** 118, 1985.
- [133] R. R. Akhmetshin et al., [CMD-2], “*Measurement of phi meson parameters in  $K0(L)$   $K0(S)$  decay mode with CMD-2*”, Phys. Lett., **B466** 385, 1999.

- 
- [134] R. R. Akhmetshin et al., [CMD2 Collaboration], “*Study of the processes  $e^+e^- \rightarrow \eta\gamma, \pi^0\gamma \rightarrow 3\gamma$  in the cm. energy range 600-MeV - 1380-MeV at CMD-2*”, Phys. Lett., **B605** 26–36, 2005.
- [135] M. N. Achasov et al., “*Measurements of the parameters of the  $\phi(1020)$  resonance through studies of the processes  $e^+e^- \rightarrow K^+K^-, K_S K_L$ , and  $\pi^+\pi^-\pi^0$* ”, Phys. Rev. D, **63**(7) 072002, Mar 2001.
- [136] Silvan Zenklusen, *Study of  $\pi^+\pi^-\pi^0$  final states at HERA*, Diploma thesis, ETH Zürich, 2006.
- [137] Julian Schwinger, “*A Ninth Baryon?*”, Phys. Rev. Lett., **12**(9) 237–239, Mar 1964.
- [138] P.G.O. Freund, “*Photoproduction of vector mesons as virtual vector meson proton scattering*”, Nuovo Cimento, **A48** 541, 1967.
- [139] H. Joos, “*A remark on the photoproduction of vector mesons*”, Phys. Lett., **B24** 103, 1967.
- [140] K. Kajantie and J. S. Trefil, “*Suppression of the  $\phi$  photoproduction in the quark model*”, Physics Letters B, **24** 106–107, January 1967.
- [141] Vernon D. Barger and D. Cline, “*Inert hadron reaction for the determination of the pomeranchuk trajectory slope*”, Phys. Rev. Lett., **24** 1313–1317, 1970.
- [142] A. Keller, *Infancy of Atomic Physics - Hercules in his Cradle*. Clarendon Press, Oxford, 1983.
- [143] Friedrich Dürrenmatt, *Der Mitmacher. Ein Komplex. Nachwort*. Arche, 1976.
- [144] Deutsches Elektronen Synchrotron DESY, Website, <http://www.desy.de>.
- [145] H1 Collaboration, *ep Physics beyond 1999*, H1 internal report H1-10/97-531, October 1997.
- [146] U. Schneekloth, *Recent HERA results and future prospects*, DESY internal report 98-060, May 1998.
- [147] I. Abt et al., [H1], “*The H1 detector at HERA*”, Nucl. Instrum. Meth., **A386** 310–347, 1997.
- [148] I. Abt et al., [H1], “*The tracking, calorimeter and muon detectors of the H1 experiment at HERA*”, Nucl. Instrum. Meth., **A386** 348–396, 1997.
- [149] D. Pitzl et al., “*The H1 silicon vertex detector*”, Nucl. Instrum. Meth., **A454** 334–349, 2000.
- [150] B. List, “*The H1 central silicon tracker*”, Nucl. Instrum. Meth., **A501** 49–53, 2001.
- [151] B. List, “*The H1 silicon tracker*”, Nucl. Instrum. Meth., **A549** 33–36, 2005.
- [152] G. Charpak, R. Bouclier, T. Bressani, J. Favier and Č Zupančič, “*The use of Multiwire Proportional Counters to Select and Localize Charged Particles*”, NIM, **62** 262–268, 1968.
- [153] Nicole Werner, *Measurement of the Charged Current Cross Section in Positron-Proton Collisions at HERA*, PhD thesis, Universität Zürich, 2004.
- [154] Max Urban, *The new CIP2k z-Vertex Trigger for the H1 Experiment at HERA*, PhD thesis, Universität Zürich, 2004.
- [155] D. Müller and F. Sefkow, *Improving the z-Vertex Trigger*, H1 internal note H1-04/98-539, 1998.
- [156] M. et al. Cuje, *H1 high luminosity upgrade 2000 cip and level 1 vertex trigger*, DESY-PRC 98/02 and H1 internal note H1-01/98-535, 1998.
- [157] J. Becker, *H1 CIP-Vertex-Trigger upgrade - Triggerhardware-Simulation*, Internal note Physikalisches Institut, Ruprecht-Karls-Universität Heidelberg, March 1998.

- [158] A. Schweitzer, *Optimierung eines z-Vertex-Triggers für den H1-Detektor bei HERA*, Diplomarbeit, Ruprecht-Karls-Universität Heidelberg, Heidelberg, February 1999.
- [159] M. Urban, *Ein schneller Trigger für H1 bei HERA*, Diplomarbeit, Ruprecht-Karls-Universität Heidelberg, Heidelberg, May 2000.
- [160] J. Burger et al., “*The Central jet chamber of the H1 experiment*”, Nucl. Instrum. Meth., **A279** 217–222, 1989.
- [161] G. Charpak, D. Rahm and H. Steiner, “*Some Developments in the Operation of Multiwire Proportional Chambers*”, NIM, **80** 13–34, 1970.
- [162] A.H. Walenta, J. Heintze and Schürlein, “*The Multiwire Drift Chamber a new Type of Proportional Wire Chamber*”, NIM, **92** 373–380, 1971.
- [163] H. Drumm et al., “*Experience with the jet chamber of the JADE detector at PETRA*”, Nucl. Instrum. Meth., **176** 333–344, 1980.
- [164] J. Heintze, “*Drift chambers and recent developments*”, Nucl. Instrum. Meth., **156** 227–244, 1978.
- [165] Volker Blobel, Central track reconstruction, Seminar talk, Mai 2004.
- [166] Volker Blobel, Central track reconstruction, Talk given in the H1 tracking group meeting, November 2004.
- [167] Jörn Steinhart, *Die Messung des totalen  $c\bar{c}$ -Photoproduktions-Wirkungsquerschnittes durch die Rekonstruktion von  $\Lambda_c$ -Baryonen unter Verwendung der verbesserten  $dE/dx$ -Teilchenidentifikation am H1 Experiment bei HERA*, PhD thesis, Universität Hamburg, 1999.
- [168] Jörn Steinhart, *Die Bestimmung des Ereignis-Zeitnullpunktes mit der zentralen Spurenkammer am H1-Detektor und seine Anwendung zur Unterdrückung von Untergrund*, Master’s thesis, Universität Hamburg, 1995.
- [169] W.H. Barkas and M.J. Berger, Nat. Acad. Sci.Natl. Res. Council Publ., **1133** 103, 1964.
- [170] S.M. Seltzer and M.J. Berger, Energy loss straggling of protons and mesons, In *In Studies in Penetration of Charged Particles in Matter*, volume 39 of *Nuclear Science Series*. Nat. Academy of Sciences, 1964.
- [171] B. Schorr, “*Programs for the Landau and the Vavilov distributions and the corresponding random numbers*”, Comp. Phys. Comm., **7** 216, 1974.
- [172] R. L. Gluckstern, “*Uncertainties in Track Momentum and Direction due to Multiple Scattering and Measurement Errors*”, Nucl. Instr. Meth., **24** 381–389, 1963.
- [173] Lev Davidowitsch Landau, “*On the energy loss of fast particles by ionization*”, J.Phys., **8** 201, 1944.
- [174] Claus Kleinwort, Private Communication.
- [175] B. Andrieu et al., [H1 Calorimeter Group], “*The H1 liquid argon calorimeter system*”, Nucl. Instrum. Meth., **A336** 460–498, 1993.
- [176] R. D. Appuhn et al., [H1 SPACAL Group], “*The H1 lead/scintillating-fibre calorimeter*”, Nucl. Instrum. Meth., **A386** 397–408, 1997.
- [177] H. Bethe and W. Heitler, “*On the Stopping of Fast Particles and on the Creation of Positive Electrons*”, Proc. Roy. Soc., **A 146** 83, 1934.
- [178] H1 collaboration, Proposal for an Upgrade of the H1 Luminosity System and its Associated Electronics for HERA 2000, Proposal submitted to the DESY PRC 98/05, 1998.
- [179] Niklaus Berger, Fti2, drawing, v2.0, Technical drawing reconstructed from photographs, 2006.

- 
- [180] Michael Dirkmann, *Messung der diffraktiven Strukturfunktion  $F_2^{D(3)}(Q^2, \beta, x_{\mathbb{P}})$  des Protons bei kleinen Impulsübertragen mit dem H1-Detektor*, PhD thesis, Universität Dortmund, 1998.
- [181] F. Sefkow, E. Elsen, H. Krehbiel, U. Straumann and J. Coughlan, “*Experience with the first level trigger of H1*”, IEEE Trans. Nucl. Sci., **42** 900–904, 1995.
- [182] H. C. Schultz-Coulon, E. Elsen, T. Nicholls, J. Coughlan and H. Rick, “*A general scheme for optimization of trigger rates in an experiment with limited bandwidth*”, IEEE Trans. Nucl. Sci., **46** 915–919, 1999.
- [183] T. Nicholls and others., “*Concept, Design and Performance of the Second Level Triggers of the H1 Detector*”, IEEE Trans. Nucl. Sci., **45** 810, 1998.
- [184] H. Kolanoski et al., Concept and design of the fast h1 second level trigger using artificial neural networks, Prepared for International Conference on Computing in High- energy Physics (CHEP 95), Rio de Janeiro, Brazil, 18-22 Sep 1995.
- [185] J. Mock et al., Artificial neural networks as a second-level trigger at the H1 experiment: Performance analysis and results, Prepared for 4th International Workshop on Software Engineering and Artificial Intelligence for High-energy and Nuclear Physics (AIHENP 95), Pisa, Italy, 3-8 April 1995.
- [186] Steffen Udluft, *Protondissoziative Photoproduktion von  $\phi$ -Mesonen am H1-Experiment bei HERA*, PhD thesis, Universität München, 2000.
- [187] Volker Blobel, *The BOS System, Bank Object System*, fourth updated edition, 2001.
- [188] Institute of Electrical and Electronics Engineers, IEEE 802: Standard for Local and Metropolitan Area Networks, 2002.
- [189] Donald E. Knuth, *The Art of Computer Programming*, volume 2: Seminumerical Algorithms. Addison-Wesley, 3rd edition, 1998.
- [190] Jos Visser, Kernel based random number generation in HP-UX 11.00, <http://www.josvisser.nl/hpux11-random/hpux11-random.html>, 2003.
- [191] B. List and A. Mastroberardino, “*DIFFFVM: A Monte Carlo generator for diffractive processes in  $e p$  scattering*”, DESY-PROC-1999-02, page 396, 1998, Prepared for Workshop on Monte Carlo Generators for HERA Physics (Plenary Starting Meeting), Hamburg, Germany, 27-30 Apr 1998.
- [192] Konstantin Goulios, “*Diffractive Interactions of Hadrons at High-Energies*”, Phys. Rept., **101** 169, 1983.
- [193] G. Dissertori, I.K. Knowles and M. Schmelling, *Quantum Chromodynamics: High energy experiments and theory*, number 115 in International Series of Monographs on Physics. Oxford University Press, 2nd edition, 2005.
- [194] Torbjorn Sjostrand, “*PYTHIA 5.7 and JETSET 7.4: Physics and manual*”, 1995.
- [195] G. Breit and E. Wigner, “*Capture of Slow Neutrons*”, Phys. Rev., **49**(7) 519–531, Apr 1936.
- [196] J. D. Jackson, “*Remarks on the phenomenological analysis of resonances*”, Nuovo Cim., **34** 1644–1666, 1964.
- [197] A. Donnachie and P. V. Landshoff, “*Rising total cross-sections*”, Phys. Lett., **B202** 131, 1988.
- [198] J. Breitweg et al., [ZEUS Collaboration], “*Measurement of diffractive photoproduction of vector mesons at large momentum transfer at HERA*”, Eur. Phys. J., **C14** 213–238, 2000.
- [199] CERN Program Library Long Writeup W5013, *GEANT – Detector Description and Simulation Tool*, 1993.

- [200] H. Fesefeldt, “*The  $e/h$  ratio and energy resolution of hadron calorimeters*”, Nucl. Instrum. Meth., **263** 114, 1988.
- [201] W. Erdmann, SV - a package for secondary vertex fitting, <https://www-h1.desy.de/iwork/ibtag/workpages/werdmann/sv/sv.html>, H1 internal.
- [202] Benno List, H1rec63100, Privatel communication/ program code.
- [203] R. M. Sternheimer, “*Density Effect for the Ionization Loss of Charged Particles*”, Phys. Rev., **145**(1) 247–250, May 1966.
- [204] R.M. Sternheimer, “*Density Effect for the Ionization Loss of Charged Particles. II*”, Phys. Rev., **164** 349, 1967.
- [205] Marc Del Degan, *A Search for pentaquarks using the H1 detector at HERA*, PhD thesis, ETH Zürich, In preparation.
- [206] Fred James and Matthias Winkler, MINUIT Users Guide, Technical report, CERN, 2004.
- [207] Mark Strikman, Question concerning inelastic diffraction data, Private communication.
- [208] Daniel Pitzl, Determination of the amount of detector material using photon conversion, Private communication.
- [209] Shiraz Habib, Cip multiplicities, H1 internal presentation.
- [210] Bertrand Russell, Am i an atheist or an agnostic?, Pamphlet, 1947.
- [211] Freeman Dyson, “*A meeting with Enrico Fermi*”, Nature, **427** 297, 2004.
- [212] A. Aktas et al., [H1 Collaboration], “*Measurement and QCD Analysis of the Diffractive Deep-Inelastic Scattering Cross Section at HERA*”, Eur.Phys.J. C, **48** 715–748, 2006.
- [213] Holly Shultz, Hjs studio – where age-old fibers gain a contemporary twist, [www.hjsstudio.com](http://www.hjsstudio.com), 2004.
- [214] K. Schilling, P. Seyboth and Guenter E. Wolf, “*On the Analysis of Vector Meson Production by Polarized Photons*”, Nucl. Phys., **B15** 397–412, 1970.
- [215] Monty Python, Monty Python and the Holy Grail, 1975.
- [216] J. Busenitz et al., “*High-Energy Photoproduction Of  $\pi^+\pi^-\pi^0$ ,  $K^+K^-$ , And  $p\bar{p}$  States*”, Phys. Rev. D, **40** 1, 1989.
- [217] D. P. Barber et al., “*A Study of Elastic Photoproduction of Low Mass  $K^+K^-$  Pairs From Hydrogen in the Energy Range 2.8 GeV to 4.8 GeV*”, Zeit. Phys., **C12** 1, 1982.
- [218] H. J. Behrend et al., “*Elastic and Inelastic  $\phi$  - Photoproduction*”, Nucl. Phys., **B144** 22, 1978.
- [219] Joseph Ballam et al., “*Vector Meson Production by Polarized Photons at 2.8 GeV, 4.7 GeV, and 9.3 GeV*”, Phys. Rev., **D7** 3150, 1973.
- [220] G. McClellan et al., “*Photoproduction of  $\phi^0$  mesons from hydrogen, deuterium, and complex nuclei*”, Phys. Rev. Lett., **26** 1593–1596, 1971.
- [221] Robert L. Anderson et al., “*Neutral Boson Photoproduction on Hydrogen at High Energies*”, Phys. Rev., **D1** 27–47, 1970.
- [222] Galileo Galilei, *Il saggiatore*. Mascardi, 1623.
- [223] Udo Mundt, Spinnenfischen mit Multirolle (Archiv), <http://www.anglerboard.de>.
- [224] ACDC, Shoot to thrill, Song lyrics.
- [225] R. Bernhard et al., editors, *Time 2005 – Proceedings of the 1st Workshop on Tracking in High Multiplicity Environments*, volume 566 of Nucl.Instr.Meth.A, 2005.
- [226] Rudolph Emil Kalman, “*A New Approach to Linear Filtering and Prediction Problems*”, Transactions of the ASME–Journal of Basic Engineering, **82**(Series D) 35–45, 1960.

- 
- [227] Eckhard Elsen, Letter to R. Eichler concerning the feasibility of a Fast Track Trigger, 1999.
- [228] H1 collaboration, A Fast Track Trigger with high resolution for H1, Proposal submitted to the Physics Research Committee, DESY internal report PRC 99/06 and addendum PRC 99/07, 1999.
- [229] D. Müller, D. Meer, J. Müller and M. Heimlicher, H1 Second Level Fast Track Trigger Design Description, Supercomputing Systems, December 2000.
- [230] S.A. Baird et al., Level 1 Fast Track Trigger - Feasibility Study, H1 internal note H1-09/99-576, April 2000.
- [231] H1 Collaboration, H1 Fast Track Trigger - Specification of the L1 System, DESY report PRC 00/05, October 2000.
- [232] N. Berger, *Development of a z-vertex trigger based on drift chamber signals at H1*, Diploma thesis, ETH Zürich, 2002.
- [233] Raphael Baldinger, Srm spezifikation, Technical Note, 2004.
- [234] Thomas Kluge, A synchrotron radiation/ spike research monitor (SRM) for H1, Private communication.
- [235] Peter J. Ashenden, The VHDL cookbook, Dept. Computer Science, University of Adelaide, South Australia, 1990.
- [236] Andreas Mäder, VHDL Kompakt, In German, available from the University of Hamburg VHDL archive at <http://tech-www.informatik.uni-hamburg.de/vhdl/>, 2000.
- [237] Altera Corporation, San Jose, *MAX+PLUS II VHDL*, 7.1 edition, December 1996.
- [238] Altera, Website, <http://www.altera.com>.
- [239] L. Chiswin and R.J. Duckworth, "Content-addressable and associative memory: alternatives to the ubiquitous RAM", IEEE Computer, **22**(7) 51–64, 1989.
- [240] Kostas Pagiamtzis, Content-addressable memory (CAM) primer, Available at: <http://www.eecg.toronto.edu/~pagiamt/>, 2005.
- [241] Altera, Implementing High-Speed Search Applications with Altera CAM, Application Note AN 119, available from [www.altera.com](http://www.altera.com).
- [242] Texas Instruments, *TMS320C6701 FLOATING-POINT DIGITAL SIGNAL PROCESSOR data sheet*, 2004.
- [243] National Semiconductors, *DS90CR483 / DS90CR484 48-Bit LVDS Channel Link SER/DES 33 - 112 MHz data sheet*, 2004.
- [244] Dirk Dodt, *Analysis of the Data Quality of the FTT*, Diplomarbeit, Universität Dortmund, 2005.
- [245] Yves H. Fleming, *The H1 First Level Fast Track Trigger*, PhD thesis, University of Birmingham, 2003.
- [246] André Schöning, The FTT Calibration Concept and Software Scheme, Technical report, FTT internal documentation, 2002.
- [247] Arnold Müller and Philipp Kraft, Mask generation for the FTT, Technical report, Internship report, ETH Zürich, 2004.
- [248] Analog Devices, AD9218 10-Bit, 40/65/80/105 MSPS 3 V Dual A/D Converter Data Sheet (REV. B) , Available from [www.analog.com](http://www.analog.com), 2004.
- [249] Altera, APEX 20K Programmable Logic Device Family Data Sheet, Available from [www.altera.com](http://www.altera.com), 2004.
- [250] André Schöning, Description of the FTT Merging Scheme, FTT documentation 1.04, FTT, 2004.

- [251] David Meer, *Heavy Quark in Photoproduction at HERA, and a linking algorithm for a Fast Track Trigger*, PhD thesis, ETH Zürich, 2004, ETH No. 15875.
- [252] André Schöning, Description of the FTT L1 Linkers, FTT documentation 0.8, FTT, 2005.
- [253] Niklaus Berger, Description of the FTT Linker PiggyBacks, FTT documentation 0.2, FTT, November 2002.
- [254] Paul V. C. Hough, Method and means for recognising complex patterns, U.S. Patent 3'069'654, 1962.
- [255] R. O. Duda and P.E. Hart, "Use of the Hough Transformation to Detect Lines and Curves in Pictures", *Comm. ACM*, **15** 11–15, 1972.
- [256] Volker Michels, *Measurement of the process  $B \rightarrow \mu X$  in electroproduction at HERA*, PhD thesis, Universität Hamburg, In preparation.
- [257] J. Samson,  $\theta$ -fit in the FTT, Presentation at the FTT meeting, October 2001.
- [258] D. Meer et al., "A multifunctional processing board for the fast track trigger of the H1 experiment", *IEEE Trans. Nucl. Sci.*, **49** 357–361, 2002.
- [259] D. Müller and J. Müller, Project FTT - Message System, Technical report, Supercomputing Systems, Zürich, 2002.
- [260] Wenbiao Yan, When do we Reload Masks?, FTT internal note, 2003.
- [261] V. Karimäki, "Effective circle fitting for particle trajectories", *Nucl. Instr. and Meth.*, **A305** 187, 1991.
- [262] Christoph Wissing, *Entwicklung eines Simulationsprogrammes und Implementierung schneller Spurfitalgorithmen für den neuen H1-Driftkammertrigger*, PhD thesis, Universität Dortmund, February 2003.
- [263] André Schöning and Niklaus Berger, Description of the FTT L2 Decider, FTT documentation 1.0, FTT, 2006.
- [264] Jürgen Naumann, *Entwicklung und Test der dritten H1-Triggerstufe*, PhD thesis, Universität Dortmund, 2003.
- [265] Andreas Werner Jung, *Inbetriebnahme der dritten Stufe des schnellen Spurtriggers für das H1-Experiment*, Diplomarbeit, Universität Dortmund, 2004.
- [266] American National Standard Institute and VMEbus Industry Trade Association, ANSI/VITA 17: Front Panel Data Port Standard, 1999.
- [267] Olaf Behrendt, *Entwicklung von Algorithmen zur Identifikation von Vektormeson-Ereignissen mit dem neuen H1-Spurtrigger*, Diplomarbeit, Universität Dortmund, 2002.
- [268] Lea Caminada, *Implementation of a Trigger for the decay  $b \rightarrow eX$  on the third trigger level at the H1 experiment*, Diploma thesis, ETH Zürich, 2006.
- [269] IEEE Standard for a Versatile Backplane Bus: VMEbus, Technical report, IEEE Computer Society/Microprocessors and Microcomputers, 1988.
- [270] Jon Postel, RFC 793: Transmission Control Protocol, DARPA Internet Program, Protocol Specification, 1981.
- [271] Jon Postel, RFC 791: Internet Protocol, DARPA Internet Program, Protocol Specification, 1981.
- [272] Marc-Oliver Bönig, *Dsterne und so (in preparation)*, PhD thesis, Universität Dortmund, 2006.
- [273] IEEE Computer Society, IEEE Standard for Binary Floating-Point Arithmetic, 1985, IEEE Std 754-1985.
- [274] Stephen J. Cannell, The A-Team, Televison series, 1983-1987.

- [275] Kristin Lohwasser, *Optimisation of the selection capability of the H1 Fast Track Trigger*, Diploma thesis, Universität Dortmund, 2006.
- [276] N. Berger et al., First Results from the First Level of the H1 Fast Track Trigger, In J. Anthony Seibert, editor, *Nuclear Science Symposium Conference Record*, volume 3, pages 1976–1980. IEEE, 2004.
- [277] Douglas Adams, *Mostly harmless*. Pan Books, 1992.
- [278] Simon Baumgartner, The FTT Graphical User Interface, Manual webpage.
- [279] National Instruments, *LabView User Manual*, 2001, Version 6.1.
- [280] National Instruments, *Getting Started with LabView*, 2001, Version 6.1.
- [281] Marc-Oliver Bönig, The FTT Master Program, Code Documentation.
- [282] Jon Postel and Joyce Reynolds, RFC 793: File Transfer Protocol, DARPA Internet Program, Protocol Specification, 1981.
- [283] Marko Dragicevic, Graphical User Interface for the Fast Track Trigger FTTGUI2, Summer Students Report and Manual, September 2003.
- [284] André Schöning, Description of the FTT Tester, FTT documentation, Version 0.0, April 2003.
- [285] Niklaus Berger, Description of the FTT Test PiggyBack, FTT documentation, Version 0.2, April 2003.
- [286] Douglas R. Hofstadter, *Gödel, Escher, Bach: An Eternal Golden Braid*. Basic Books, 1979.

## BIBLIOGRAPHY

---

# Acknowledgements

*Nicht der Weg ist das Ziel, sondern der Zwischen-  
aufenthalt*

FREMDENERKEHRSMINISTERIUM DER  
REPUBLIK SLOVENIEN

*Hofstadter's Law: It always takes longer than  
you think, even when you take into account  
Hofstadter's Law.*

DOUGLAS R. HOFSTADTER [286]

Natural science in general and high energy physics in particular is a collaborative effort. Work such as the one presented in this thesis is only possible when hundreds of like-minded people come together to convey, build and operate accelerators and detectors; when they find time to and even take pleasure out of sharing their knowledge, insights and enthusiasm with students like me. I am grateful to everyone who contributed to H1 and HERA; there are however quite a few people whom I would wish to especially mention.

I would like to thank Ralph Eichler for giving me the freedom to perform this research, for asking the right questions again and again and thus ensuring that this work has come to a (happy) end. I am pleased that Günther Dissertori volunteered to co-referee this thesis, and would like to thank him for many stimulating discussions about physics and teaching and the four tenths in Les Marécottes.

Working with André Schöning on the Fast Track Trigger was an inspiring and challenging enterprise. Never relenting in the quest for debugging and improving the FTT or developing new ideas, we spent many late evenings having “just a quick look at a few plots”, resulting in the demise of a major bug or a new insight into the subject at hand.

From Benno List I learned most of what I know about vector mesons, the beauties of good C++ and much more – whenever Benno put his coffee down and stepped up to the whiteboard, his knowledge would mingle with his talent for telling a good story and provide insightful and entertaining lessons.

Most of the code (and the concepts behind it) originate from Ronald Weber. I am greatly indebted to Ron, not only because his hand-to-hand combat with ROOT actually resulted in a corpus of very useful code, but mainly because he was a congenial office mate with whom I could always share a problem or a joke.

Going out in Hamburg was enriched by all three of them; André shares my love of fish and seafood, Benno my liking of a juicy piece of meat and Ron always knows where to get the best rum. This was completed by Raphael Baldinger, with whom I enjoyed memorable concerts and who also taught me a lot about electronics and FPGA programming.

The Fast Track Trigger group has changed quite a bit over the years, but it has always been inspiring to work with such professional and motivated people. Special thanks go

to Christoph Wissing, who also was a great help in obtaining my Monte Carlo (and good Tapas), Marc-Oliver Böning, who delivered us from the VICs, David Meer, who wrote an error-free L2 linker, Simon Baumgartner, who fathered the GUI, Jürgen Naumann, who provided the read-out, Yves Fleming, who wrote the track segment finder, Andreas Jung, who got L3 running, Volker Michels, who built the  $z$ -vertex trigger, Michel Sauter, who made L3 find muons and Katja Krüger, who histogrammed all this.

A lot of support, both technical and moral, also came from the non-FTT, non-vector-meson members of my group, thanks to Christoph Grab, Marc Del Degan, Tobias Zimmermann and Guillaume Leibenguth.

The H1 tracking experts, namely Claus Kleinwort and Daniel Pitzl never hesitated to share their great experience with me. I also enjoyed the support of many members of the H1 diffractive working group, who kept a positive and constructive attitude even through seemingly interminable meetings.

On a more personal note I want to thank Rahel and my parents for their incessant support, their interest in my (sometimes obscure) work and above all their love.

# Curriculum vitae

NIKLAUS EMANUEL BERGER

Born April 10 1978  
in Unterseen, Switzerland

Citizen of Niederurnen (GL)  
and Salez-Sennwald (SG)

## EDUCATION

2002 – 2007	Doctoral studies at ETH Zürich, research at the H1 experiment at DESY, Hamburg
2002	Diploma in Physics at ETH Zürich, diploma thesis “ <i>Development of a z-Vertex trigger based on drift-chamber signals at H1</i> ” in the group of Prof. Ralph Eichler
1998 – 2002	Studies of physics at ETH Zürich
2001	Exchange term at King’s College, London with lectures at University College, and Queen Mary and Westfield College
1998	Compulsory military service in the Swiss army
1998	Eidgenössische Matura Typus C
1995 - 2000	Member of the European Youth Parliament
1994 - 1998	Gymnasium in Interlaken
1985 - 1994	Primary and Secondary School in Interlaken